Scientific Review

Engineering and Environmental Sciences

Przegląd Naukowy
Inżynieria i Kształtowanie Środowiska

Vol. 30 (1)   **2021**   **Nr 91**

Quarterly – Kwartalnik

Spis treści
Contents

PRACE ORYGINALNE
Original papers

PRACE ORYGINALNE
ORIGINAL PAPERS

Kamel Ibrahim ASKER[1], Mohamed Tarek FOUAD[2],
Mohamed Awad BAHR[2], Ahmed Nabil El-ATTAR[1]

[1]Higher Technological Institute, Department of Civil Engineering
[2]Al-Azhar University, Department of Civil Engineering

Minimizing of tunneling effect on existing infrastructure in Egypt

Key words: tunneling, grouting, field measurements, Abaqus, Al-Azhar twin tunnel

Introduction

The construction of two closely distant tunnels under an existing tunnel can cause greater deformation for the existing tunnel and the ground due to the dual disturbances caused by the tunneling process (Jin, Yuan, Li & Zheng, 2018). Several studies have estimated the ground movements as well as the deformation has induced in the existing tunnels by the construction of a new tunnel (Fang, Zhang, Li & Wong, 2015; Zhang, Liu, Kang, Zhong & Chen, 2018; Lin, Chen, Wu & Cheng, 2019). Grout technology is widely used for strengthening the soil and protecting the existing structures in shield tunneling. Li, Zhang and Yuan (2013) presented the case of using jack-

ing as the tunnel protection methodology in case of the tunnel excavation under the existing one. Kimpritis, Smon, Pandrea and Vukotic (2014) explained how jet grouting could be used as the integral part of the complex tunneling projects. They summarized the basic framework for the design and execution of jet-grouting in tunneling.

In this research, the case history of the intersection of Al-Azhar twin tunnel with the CWO sewer is idealized using the three-dimensional numerical model.

Consequently, in this study, a series of parametric studies are conducting by utilizing the verified model of the case history to evaluate the effect of other different protection techniques. The key part of this paper is to investigate the best configuration technique to minimize the tunneling effect on an adjacent structure.

Problem statement

Al-Azhar twin road tunnels were constructed to provide the fast link between the congested parts of downtown Cairo with the eastern parts of the city under the area of old Fatimid Cairo. The intersection of Al-Azhar Road Tunnels was with excavated diameters of 9.40 and 18.70 m spaced, and the CWO sewer 5 m external diameter at Port Said Street as shown in Figure 1. Table 1 summarizes the parameters of soil at the intersection point. According to El-Nahhas (1992), the sewer tunnel was constructed in 1988 with a bentonite slurry shield. Table 2 summarizes the parameters of the twin tunnels

and the CWO sewer. Several measurements were conducted to the several sections of Al-Azhar road tunnels (Abu-Krisha, 2001; El-Sayed, 2001; Ezzeldine & Darrag, 2006). According to Campenon Bernard SGE report (1999), the groundwater table reported at 3.40 m below the ground surface.

Grouting techniques are highly evolved methods used in most tunneling projects as a stabilization method or as sealing to the structures. Before the launch of tunneling work, two slurry walls were injected to confine the sides of the CWO and the road tunnel. The characteristics of the grouted wall are summarized in Table 3. According to
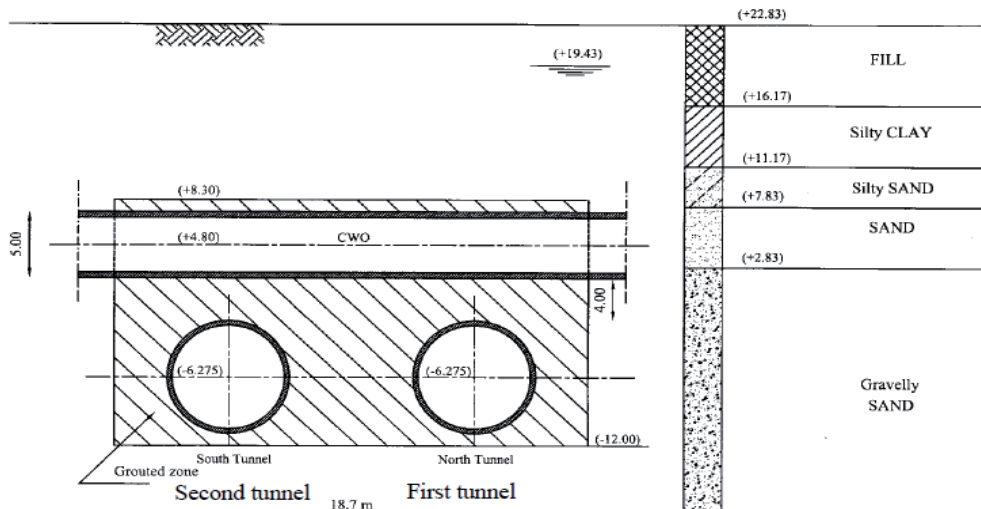
FIGURE 1. Subsurface conditions at the site of the intersection (El-Sayed, 2001)

TABLE 1. Soil properties (Abu-Krisha, 2001)

Layer	Thickness [m]	γ [kN·m^{-3}]	φ [°]	C [kPa]	E [kN·m^{-2}]	v	Ψ [°]
Fill	6.70	16.50–6.50	23	0.20	8 300	0.40	0
Silty clay	5.00	8.00	15	10.50	11 000	0.35	0
Silty sand	3.40	9.00	30	–	50 000	0.35	0
Sand	5.50	9.50	35	–	75 000	0.30	5
Gravelly sand	extend	9.50	41	–	80 000	0.30	11

Campenon Bernard SGE report (1999), the required instrumentation to evaluate the tunnel effect on the adjacent CWO sewer shown in Figure 2.

TABLE 2. Twin tunnel and CWO sewer properties (Abu-Krisha, 2001)

		outer diameter	9.40 m	shield thickness	50 mm
	geometry	inner diameter	8.35 m	gap thickness	75 mm
		lining thickness	0.40 m	grouting thickness	125 mm
Twin tunnel		type	E [kN·m^{-2}]	ν	γ [kN·m^{-3}]
		lining	$1.4 \cdot 10^7$	0.15	25
	mechanical properties	shield	$2.1 \cdot 10^8$	0.3	78
		gap	1 000	0.3	–
		grouting	vary	0.15	25
CWO sewer	geometry	outer diameter	5.00 m	limning thickness	32.80 cm
		inner diameter	4.15 m	grouting thickness	26.20 mm
	mechanical properties	type	E [kN·m^{-2}]	ν	γ [kN·m^{-3}]
		lining	$1.4 \cdot 10^7$	0.20	25
		grouting	$1 \cdot 10^5$	0.15	25

TABLE 3. Grouted walls geometry and properties (Abu-Krisha, 2001)

Height = 20.30 m	Length = 38.50 m	Thickness = 2.00 m	ν = 0.23
$E = 250 \cdot 10^3$ kN·m^{-2}	$C = 100$ kN·m^{-2}	$\varphi = 35°$	q_c = 1.5 MPa
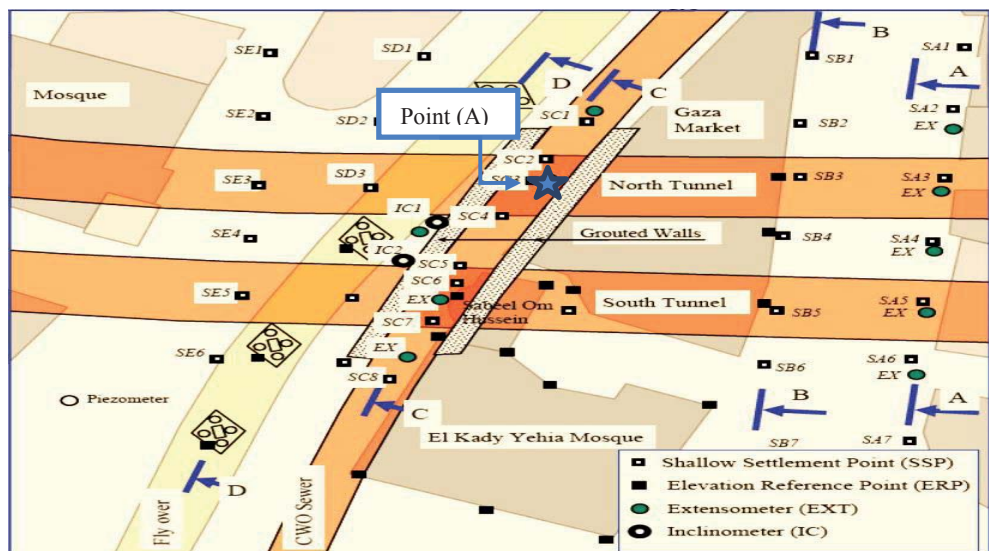
FIGURE 2. Instrumentation layout (Ezzeldine & Darrag, 2006)

Numerical model

To investigate the tunneling effect on the induced ground response, a three-dimensional model with a circular twin-tunnel configuration was developed by using the general-purpose finite element suite Abaqus/CAE (Dassault Systèmes Simulia, 2016).

Soil section with five distinct layers and grout components modeled as solid element, the material utilized in this model is employing elastic-perfectly plastic (the Mohr–Coulomb criterion), while lining, grouting, gap, shield and CWO elements are modeled as solid element by adopting elastic material.

The choice of sufficient mesh dimensions should not affect the tunneling process Moller (2006). Accordingly, the scope of the model was chosen to be in the transverse direction is 100 m, 76 m in the longitudinal direction, and 60 m in the depth. Figure 3 shows the three-dimensional model for the numerical analysis considered in this study.
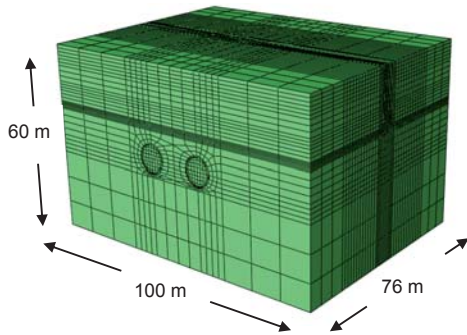
FIGURE 3. The three-dimensional finite element model for the intersection point

The typical excavation of tunneling activities is simulated step by step by taking into consideration the rate of tunnel advancement as 0.5 to 1.5 m·h⁻¹. This simultaneousness of tunneling is as following:

– Removing the length of soil equal to 1.5 m per step, conducting TBM shield with surrounding gap and applying excess face pressure 160 kPa to sustain the shield length of 9 m.

– Deactivating the TBM shield with surrounding gap element and the face pressure.

– Activating lining and grout elements with pressure of 300 kPa taking into consideration the setting time of the grout. The initial stiffness of the grout is 1,000 kPa. This stiffness increases with the rate which is depending on the time from the liquid state to the harding state. It is also relating to the compression strength by the developed empirical formula (Eq. 1), according to ACI 318-11 Building Code (American Concrete Institute [ACI], 2011).

$$E = 4730\sqrt{(f_c)}[kPa] \qquad (1)$$

Numerical model results

Results from the finite element study were compared with the field monitoring data to evaluate the capability of the proposed model to simulate the complex between the soil – CWO sewer – tunneling interaction.

Prediction of deformation field

The observed deformation trend of the soil was well depicted by the Abaqus model after the execution of the north tunnel and after the respective execution of both tunnels as shown in Figures 4 and 5.

K.I. Asker et al.
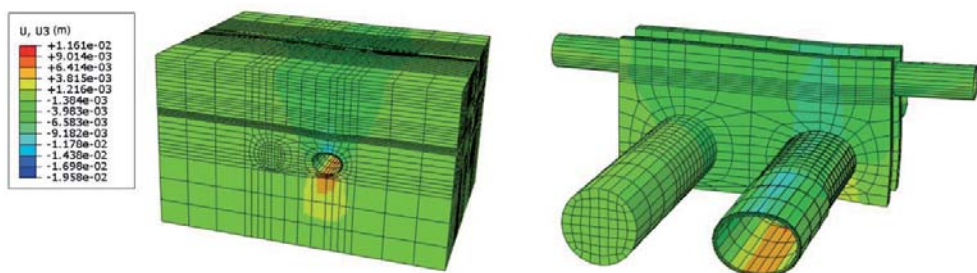
FIGURE 4. Vertical deformation after the execution of the north tunnel
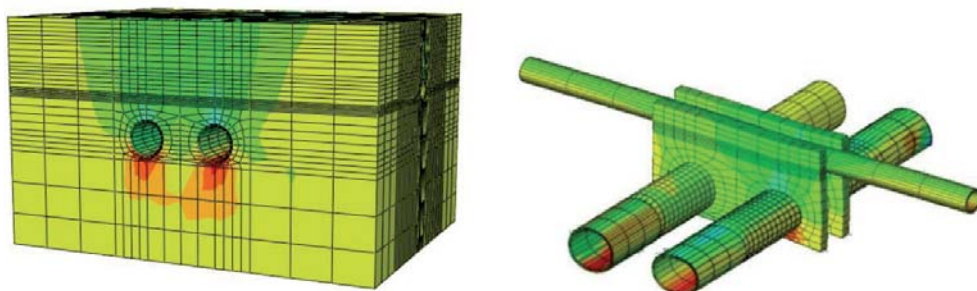
FIGURE 5. Vertical deformation after the execution of south tunnel

It can be noted that the soil deformation increases towards the tunnel vicinity as a result of tunnel cutting over.

Settlement trough

Figure 6 shows that the surface settlement was estimated in the region of the untreated zone after running the north tunnel. The results indicated that the computed ground surface displacement was about 14% more than that of field displacement.

Also, the ordinate of surface settlement trough was not symmetrical about the tunnel vicinity due to the existence of CWO in the global interaction system.
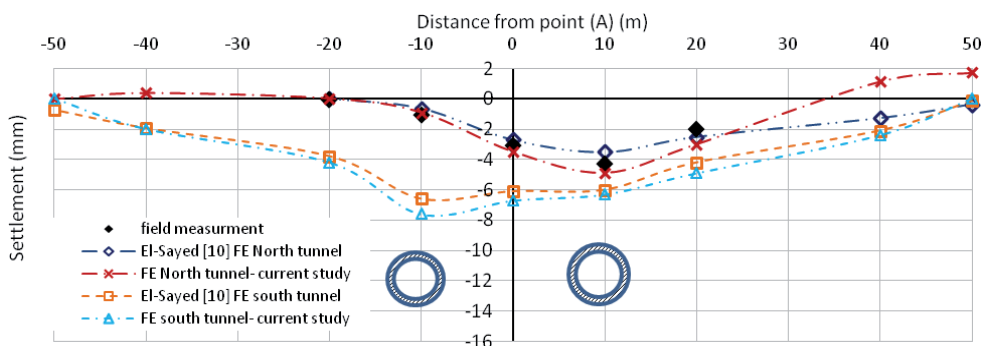
FIGURE 6. Surface settlement trough of the untreated ground

Generally, the comparison indicated the good signs of the agreement between the computed ordinates and the measured values. However, the idealization of the second tunnel after setting up the final field of the ground movements associated with the construction of the first tunnel as shown in Figure 5. Also, the settlement through has estimated and represented in the same figure from another numerical model adopted by El-Sayed (2001).

It can be noticed that the through has reported the maximum settlement of approximately 8 mm as it was compared with the estimated one by El-Sayed (2001). The general trend of the displacement curve appears to agree with the other finite element model simulation conducted by El-Sayed (2001) about 15%. Furthermore, the maximum computed settlement is 24% less than the allowable settlement documented by the Campenon Bernard SGE report (1999) as no more than 8 mm.

Parametric study

A series of parametric studies were carried out to investigate the most effective technique in reducing the tunneling effect, as an alternative technique instead of using the two grouted wall method. Table 4 summarized all cases of the protection techniques conducted in the parametric studies to reduce the tunneling effects.

Analysis 1 is the reference case that is developed without any protection method which indicates efficiency of all other techniques used to minimize the tunneling effect.

TABLE 4. The protection techniques used in parametric studies

Analysis	Protection technique
1	No protective method
2	Two grouted walls (executed case)
3	Slurry piles
4	Secant piles wall
5	Grouted block of slurry beneath the CWO sewer

Analysis 2 investigates the effect of using two grouted walls. The development of the two grouted wall is based on the case study, as shown in Figure 7.

Figure 8 illustrates the protection method of the third analysis by using 38 adjacent slurry piles of diameter 1.0 m distributed in two rows around CWO sewer with length of 35 m from the ground level. The distance between piles C.L. to C.L. is about 2.00 m. The slurry piles are modeled by adopting Mohr––Coulomb with $E = 7.9{\cdot}10^5$ kN·m^{-2}, $v = 0.26$, $C = 780$ kPa, and $\varphi = 30°$.

Analysis 4 investigates the effect of using a total 34 reinforced concrete piles with slurry piles (secant piles) with length of 24 m. The distance between piles C.L. to C.L. is about 2.00 m with a diameter of 1.00 m. The pile's tip level is approximately 0.5 m above the tunnel crown to avoid the damage of the piles when TBM advance. The concrete piles are modeled as an elastic material with $E = 140{\cdot}105$ kN·m^{-2}, $v = 0.15$. The slurry piles modeled like (Analysis 3) as shown in Figure 9.

Analysis 5 demonstrates the use of the grouted block. It confines the twin tunnels with the following dimension $38.50 \times 14.50 \times 9.00$ m. The grouted block is modeled as elastic perfectly
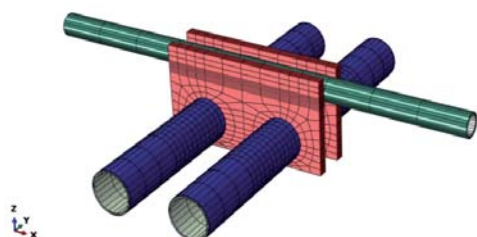
FIGURE 7. Analysis 2
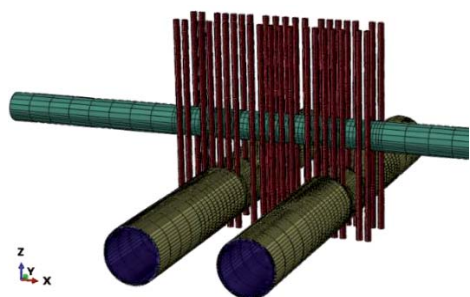
FIGURE 8. Analysis 3
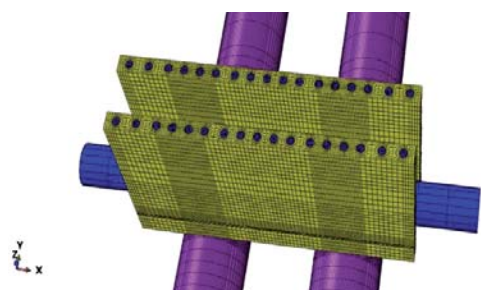
FIGURE 9. Analysis 4
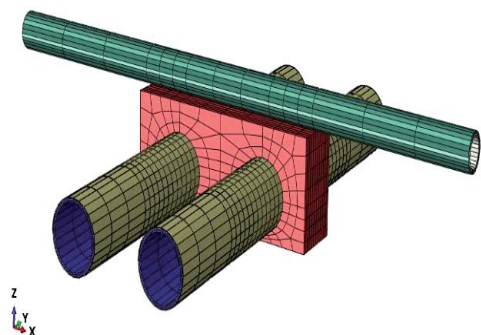
FIGURE 10. Analysis 5

plastic Mohr–Coulomb material like the two grouted walls as shown in Figure 10.

Results of numerical models and discussion

The results of numerical models clarified the effect of the different protection technique on the surficial settlement, CWO sewer settlement, CWO sewer cross-section, longitudinal deformations, principles stresses, bending moment developed on CWO sewer.

Surficial settlement

Figure 11 illustrates the induced maximum surficial settlement curves which are presented for different protection configurations. The figure indicates that using a deep grouted wall or grouted block had almost the same effect on the surficial ground settlement. Also, the induced surface settlement in the case of (Analysis 4) is less than that induced in (Analysis 1) by about 60%. This may be due to the upper portion of the tunnel. It has a larger over-cutting than that of the lower portion. The restraining effect takes place at the lower portion by the restrained secant piles.

Figure 12 demonstrates a comparison between the induced surficial settlements in different analyses associated with the tunnel advancement at the location of the points (A). The maximum settlement is detected after the TBM has passed the point A by the distance of 22.5 m. Also, the results indicate that the ground surface vertical movements measured at the point A start to take place when the TBM ap-
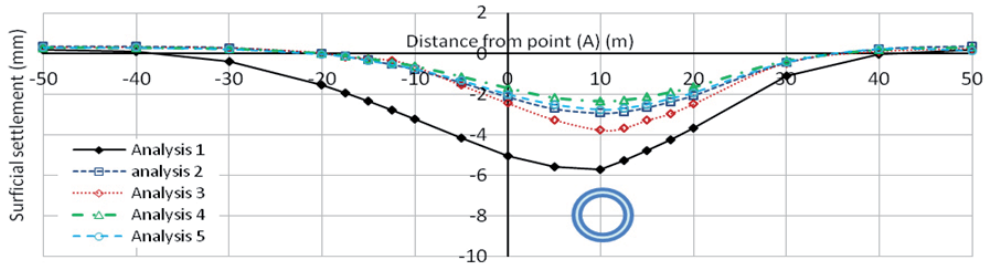
FIGURE 11. Induced surficial settlement relative to different protection configuration
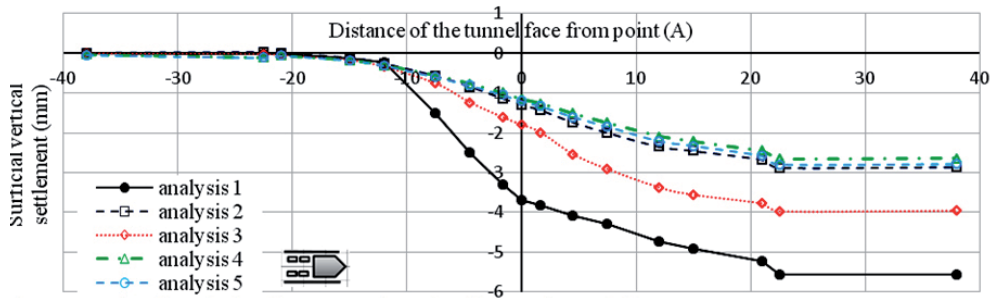
FIGURE 12. Induced vertical settlement at point A for all protection techniques

proaches before point A by the distance of about 1.2 times tunnel diameter, after that the rate increases up to distance 1.2 times tunnel diameter. However, after the distance of 2 times tunnel diameter, there is no increase in the rate of settlement associated with the tunnel advancement.

CWO sewer settlement

Determining the displacement induced from the tunnel is an important parameter to evaluate the construction qual-

ity and the structural stability of the CWO sewer. Figure 13 shows the induced settlement at the level of the crown of CWO at point A, as shown in Figure 2 after the excavation of the north tunnel.

Using the secant piles and the grouted block (Analyses 4 and 5) are more effective method in reducing the CWO sewer settlement by approximately 63% more than that induced in Analysis 1. Generally using any protection methods reduce the CWO settlement less than the allow-
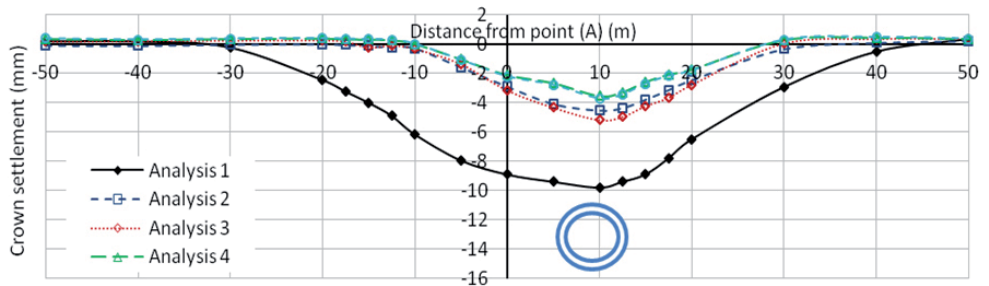
FIGURE 13. Induced CWO sewer settlement after excavation of north tunnel at section C–C

able settlement (8 cm). According to the economic view, using the adjacent slurry pile (Analysis 3) is saving time and cost regardless the settlement.

CWO sewer cross section deformation

Figure 14 shows the crown, invert, and spring line deformations. Realistically, the shape of CWO oval due to the effect of the soil own weight. Away from the CWO shape, the tunneling process causes additional displacement in the CWO sewer. The maximum offset of the CWO sewer is pushed in the diagonal axis which is detected when the tunnel face advancement is ahead of the point A by approximately 24 m or 39 m behind the tunnel. The observed trend of the CWO deformation matched with the documented by Jin, Yuan, Li and Zheng (2018).

Also, there is a difference between the left and right springline deformation caused by the effect of the tunnel face pressure pushing the CWO sewer away from the tunnel. This pushing force causes left springline moves laterally more than the right springline. This can be attributed to the restraining effect of soil against the right springline movement.

The invert deformation of CWO is heave when the TBM head is behind the CWO by 15 m. Then the invert deformation changes from the inward to the outward deformation as the tunnel excavation proceeded. This change in deformation is due to the soil losses resulted from the TBM over-cutting.

Vertical and lateral stresses developed on CWO sewer

Figure 15 sheds light on all changes in the vertical and lateral stresses induced after the tunneling process concerning (Analysis 1). By comparing, the induced lateral and vertical stresses developed in the crown, invert, and springline by that are developed in the un protected case, it can be detected that the maximum reduction about 33% is developed in crown vertical in case of employing the grouted bock (Analysis 5). While conducting adjacent slurry piles (Analysis 3) cause an increase in crown stress about 104%. This change in crown stress can be attributed to the rigidity of the confining method around either tunnel vicinity or CWO.

On the other hand, conducting secant pile is more effective technique in reducing the lateral stress induced along crown, invert, and springline by approximately 15%, 15%, and 19% of that developed in Analysis 1. While utilizing other methods causes an increase in spring line lateral stresses. This can be attributed to the decrease in crown force, which is transferred by arch action to spring line.

Summary and conclusions

The effects of tunneling on the infrastructure have great concern of this research by developing a 3-D numerical model using the finite element program Abaqus (ver. 6.16).
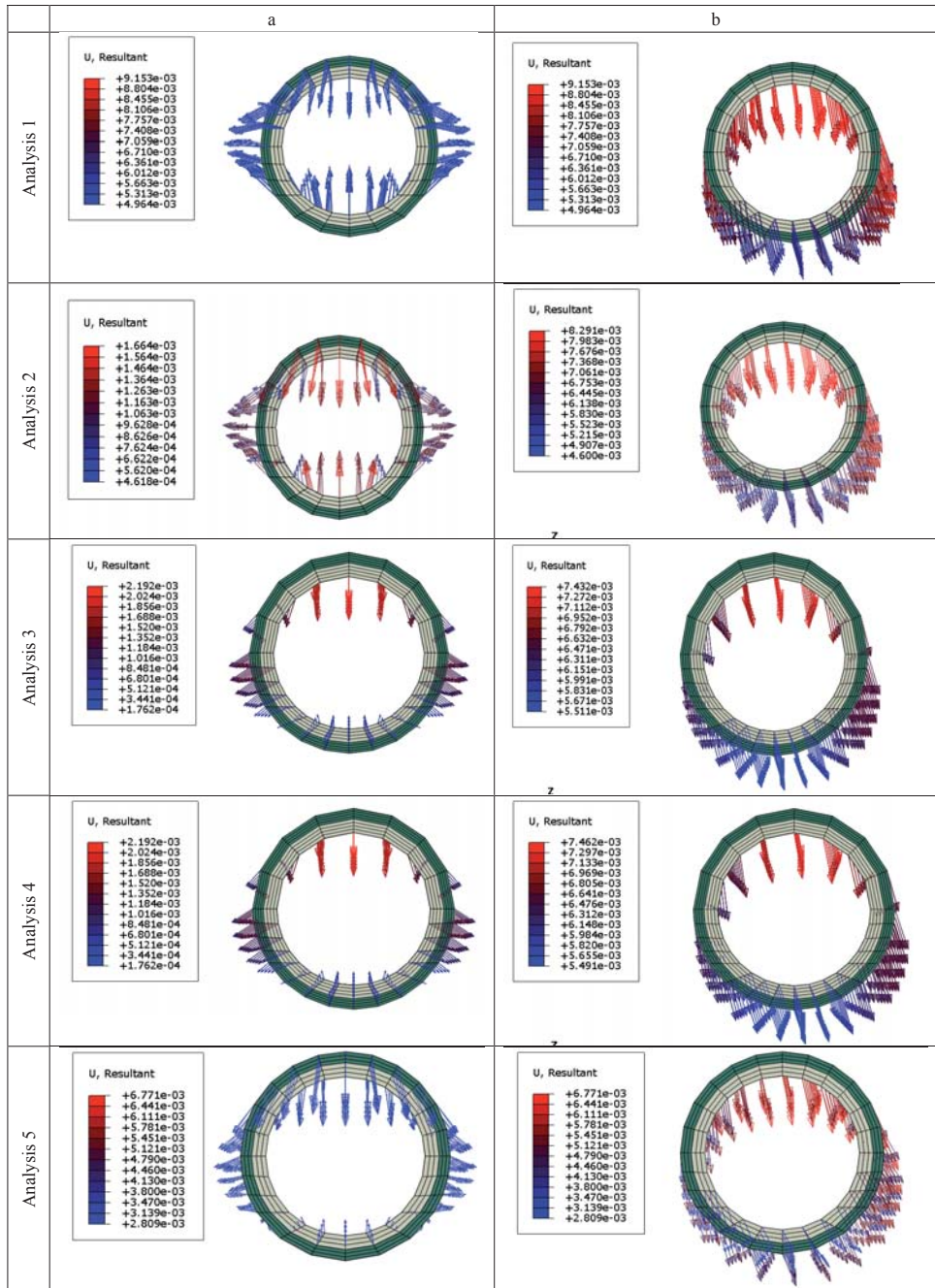
FIGURE 14. Deformation of the CWO sewer at the intersection with the north tunnel: a – before tunneling process; b – after executing of the north tunnel
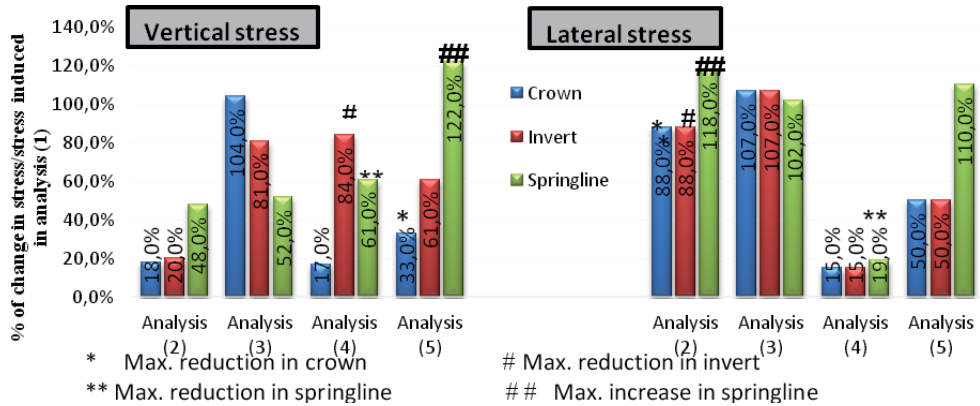
FIGURE 15. The percentage of vertical stress and lateral stresses induced on CWO sewer with respect to Analysis 1

1. The gained surficial settlement from the numerical model fairly agree with field data obtained from monitoring the advanced Al-Azhar twin tunnel during crossing the main sewer of Cairo.

2. Modeling such complicated interaction features is a typical 4D problem

A set of parametric studies is conducting with the same model of the verified case to investigate the effective sealing method of the CWO sewer from the tunneling effect regarding the sealing configuration. 4-different types of mitigation methods were adopted to seal the CWO sewer from the tunneling effect. Based on the results of parametric studies the following may be concluded:

– By comparing the displacement resulted in (Analyses 2 and 3), it can be demonstrated that using the slurry piles (Analysis 3) increases the developed CWO displacements at the crown and invert by 2%, and 34% respectively of that are recorded in (Analysis 2). However, all protection methods are effective in reducing the CWO settlement less than that are

developed in Analysis (1) by 50%, 35%, 60%, 25% in the crown, invert, springline right, and springline left respectively.

– The comparative analyses of the CWO stresses show that using the slurry piles as protection technique reduces the invert stress by 81% of that are induced in the (Analysis 1). While the TBM face pressure, as well as grouted pressure is transferred by the arch action to the CWO crown causing an increase in stresses by 104% of that is induced in Analysis 1.

– Using of the adjacent slurry pile to reduce the tunneling may be considered an effective method in reducing the tunneling effect by the careful selection of the shield. In addition, from an economic view, it is considered that the most sophisticated method (regarding saving time and cost) as the CWO deformation does not exceeded the permissible value.

– Using the grouted block and secant pile (Analyses 4 and 5) are the most effective technique in reducing the

tunneling effect regarding the CWO displacement and stresses.

– The only negative result of using the grouted block below the CWO is increasing spring line vertical and lateral stress by 122% and 110% respectively of that induced in Analysis 1.

– The induced axial stress in the CWO sewer is unexpectedly large in the crown than that induced in the invert. The tensile stress is developed in invert is due to hanging and sagging moments. However, the rigid lining face support can resist the separation force.

References

Abu-Krisha, A. (2001). Settlement control of CWO sewer tunnel during boring El-Azhar road tunnels in Cairo. In *Proceedings of International World Tunnel Congress: International World Tunnel Congress: Milano, Italy 10-13 June 2001*. Bologna: Pàtron Editore.

American Concrete Institute [ACI] (2011). *Building Code Requirements for Structural Concrete and Commentary* (ACI 318-11). Farmington Hills (MI): American Concrete Institute.

Campenon Bernard SGE (1999). *Tunneling at the CWO Crossing, Results of Monitoring* (El Azhar Road Tunnels Project, Detailed Design). Egypt: National Authority for Tunnels.

Dassault Systèmes Simulia (2016). *Abaqus/CAE user's guide*. Version 6.16. Providence, R.I.: Dassault Systèmes Simulia Corp.

El-Nahhas, F. (1992). Ground settlement above urban tunnels constructed using bentonite slurry machines. In *Proceedings of the International Symposium on Current Experiences in Tunneling: International Symposium on Current Experiences in Tunneling, Cairo, Egypt, January 1992* (pp. 61-73).

El-Sayed, S. (2001). *Elasto-plastic three-dimensional analysis of shielded tunnels* (unpublished PhD thesis). Geotechnical and Foundation Engineering, Ain Shams University, Cairo.

Ezzeldine, O.Y. & Darrag, A.A. (2006). Instrumentation at the CWO Crossing – El Azhar Road Tunnels and its use in the Design of Future Projects. In *International Symposium on: Utilization of underground space in urban areas: Sharm El-Sheikh, Egypt 6 November 2006* (pp. 6-7).

Fang, Q., Zhang, D., Li, Q. & Wong, L.N.Y. (2015). Effects of twin tunnels construction beneath existing shield-driven twin tunnels. *Tunnelling and Underground Space Technology*, *45*, 128-137.

Jin, D., Yuan, D., Li, X. & Zheng, H. (2018). An in-tunnel grouting protection method for excavating twin tunnels beneath an existing tunnel. *Tunneling and Underground Space Technology*, *71*, 27-35.

Kimpritis, T., Smon, W., Pandrea, P. & Vukotic, G. (2014). Jet grouting – a solution to problems in tunneling – examples from Europe. In *2nd Eastern European Tunnelling Conference: Athens, 28 September – 1 October 2014*. Athens: Greek Tunneling Society.

Li, X.G., Zhang, C.P. & Yuan, D.J. (2013). An in-tunnel jacking above tunnel protection methodology for excavating a tunnel under a tunnel in service. *Tunnelling and Underground Space Technology*, *34*, 22-37.

Lin, X.T., Chen, R.P., Wu, H.N. & Cheng, H.Z. (2019). Deformation behaviors of existing tunnels caused by shield tunneling under-crossing with oblique angle. *Tunneling and Underground Space Technology*, *89*, 78-90.

Moller, S. (2006). *Tunneling induced settlements and structure forces in linings* (unpublished PhD thesis). Stuttgart University, Stuttgart.

Zhang, P., Liu, Y., Kang, X., Zhong, K. & Chen, R.P. (2018). Application of horizontal MJS piles in tunneling beneath existing twin tunnels. In *Proceedings of the 2nd International Symposium on Asia Urban Geoengineering: 2nd International Symposium on Asia Urban Geoengineering: Changsha, China 24-27 November 2017* (pp. 323-331). Singapore: Springer.

Summary

Minimizing of tunneling effect on existing infrastructure in Egypt. A set of parametric studies by using the Abaqus software is conducting to investigate the effective method to seal the CWO sewer from the tunneling process. These methods include: (i) two deep grouted walls, (ii) adjacent slurry piles, (iii) bored reinforced concrete piles assisted with slurry piles, and (iv) grouted block confining the twin tunnel wall. Based on the results of parametric studies. Most of the protective studied technique was effective on reducing the tunneling effect on the ground movements.

Authors' address:
Kamel Ibrahim Asker – corresponding author
(https://orcid.org/0000-0001-8884-4520)
Ahmed Nabil El-Attar
(https://orcid.org/0000-0002-8941-2815)
Higher Technological Institute
Department of Civil Engineering
Cairo, Egypt
e-mail: kamelasker2004@hti.edu.eg

Mohamed Tarek Fouad
(https://orcid.org/0000-0001-9628-9707)
Mohamed Awad Bahr
(https://orcid.org/0000-0002-6994-2827)
Al-Azhar University
Department of Civil Engineering
Cairo, Egypt

Labeeb S. Al-YASSRI, Munaf A. Al-RAMAHEE, Alaa M. Al-KHEKANI
University of Al-Qadisiyah, College of Engineering

Experimental investigations on concrete beams reinforced with equivalent service steel pipe

Key words: duct, flexural, opening, steel pipe, reinforced concrete beams

Introduction

With modern construction, the passage of utility connections (electricity, communication, etc.) through structural members has become a common technique. The process of transferring service tubes through the structural elements is done by making holes in the body of the structural element. Numerous researches have been carried out to investigate these openings effects and the factors affecting them on the behavior of structural elements. The openings can be categorized according to their shape (rectangular, circular, etc.), their size (small or large), their location within the element, and their direction (transverse or longitudinal). Different studies have considered these properties experimentally (Prentzas, 1968; Somes & Corley, 1974; Mansur, Tan & Lee, 1984; Ha-snat & Akhtanizzaman, 1987; Herrera, Anacleto-Lupianez & Lemnitzer, 2017; Al-Khekany, Al-Yassri & Abbas, 2018; Al-Yasri, Al-Khekany & Abbas, 2018; Makki, Jassem & Jassem, 2018).

Ashour and Rishi (2000) investigated the effect of web reinforcement, size, and position of the rectangular opening using 16 two-span continuous deep beams. Two positions of rectangular openings were considered, with outer and inner shear span.

The opening location controlled mainly the failure mode where the maximum decrease in the load capacity occurred when the opening was in the interior shear span. Yang, Eun and Chung (2006) investigated the effect of the rectangular opening with different sizes on the performance of reinforced concrete (RC) deep beams. Different concrete compressive strength was considered in the study. Different shear span-to-depth (a/d) ratios were considered in this study. The effect of vertical web reinforcement was found to have more impact

on the load-carrying capacity of deep beam than the horizontal reinforcement. Amin, Agarwal and Aziz (2013) studied the opening properties on the shear strength behavior of deep beams with the lack of web reinforcement. Their results showed that the location of openings has a significant effect when openings are located at shear zone where the ultimate shear strength was significantly decreased. However, the opening located at mid-span of the beam had a slight effect where the shear strength increased with the decrease of the openings size. Campione and Minafò (2012) investigated the behavior of RC deep beams with different positions of openings and low shear span-to-depth ratio. The experimental results showed that the position of the opening along the beam length affected the structural behavior of the deep beam.

The presence of openings in different building structural members is important in some cases, but most of codes of practice (Canadian Standard Association [CSA], 2004; Arya, 2009; American Concrete Institute [ACI], 2014) do not suggest any procedure for the design of such type of members. Most investigational experiments in the literature conducted experimental researches on beams with the transverse opening only.

Few studies considered the effect of the longitudinal openings on the structural behavior where beams with an opening along the longitudinal axis has a constant section. Since these openings are considered a weak property, the plane of failure usually goes within these openings. Therefore, in this study, a test of RC beams with steel pipe as main reinforcement as an equivalent to the traditional reinforcement and have a constant cross-section along the beam was presented. The equivalency of reinforcement based on the moment equivalent under the service load between the two types of reinforcing from beam section analysis. Therefore, the reinforcing pipes were employed also as ducts to allow all services to pass through the beam without any need to cover the utilities by a suspended ceiling. Moreover, the overall weight of building can be reduced by adopting a large steel pipe as a main reinforcement especially for a multistory building.

Design and experimental work

Four beams were prepared. Two of them were manufactured with traditional reinforcement while the other two beams were manufactures with equivalent circular pipes. The pipes geometries were selected based on the equivalent sectional moment. From the sectional analysis, the nominal moment at tensile reinforcement was calculated first for the traditional reinforcement based on section equilibrium, and then the resulted moment was used for the designing of the steel pipe reinforced beams. The cross section of all tested beams were 200X and 250 mm (b, h) and overall length (L) was 1,500 mm. The selection of reinforcing bars was based on the target of the failure mode which is set to be a flexural tensile failure. The first traditional reinforced beam TRB1 was reinforced with 3 ø12 mm as the main reinforcement. The second traditional reinforced beam TRB2 was mainly reinforced with 2 ø12 mm and 1 ø16 mm. The first pipe reinforced

beam PRB1 was reinforced with 2 ø50 mm as the main reinforcement while it was reinforced with 1 ø75 mm for the second pipe reinforced beams (PRB2). The thickness of all pipes was 3 mm. All four beams were reinforced with ø10 mm@150 mm c/c for the shear reinforcement. All beams were reinforced with ø12 mm top reinforcement for practical consideration. Table 1, Figures 1 and 2 show the tested beam details. To prevent the bond failure of the steel pipes, the smooth surface of the pipes was welded with around the outer diameter and along the beam to create a coarse surface to work as mechanical ribs and ensure the interaction between and concrete and pipes as shown in Figure 3.

All beams were cast using a proportion of 1 : 1.5 : 3 (cement : sand : aggregate). Locally produced commercial Portland cement (PC) type I the follows the the standard IQS 5/1984 requirements (Central Organization for Standardization and Quality Control [COSQC], 1984a). The fine and the coarse aggregate were selected to satisfy the standard IQS 45/1984 (COSQC 1984b). The 19 mm size rounded gravel were used as coarse aggregate with 2.64 specific gravity. Natural sand of 2.60 specific gravity was used. The mechanical properties of reinforcing bars used in this research are listed in Table 2. The beams were cast using pre-cleaned ply-wood molds as shown in Figure 4. Finally, after demolding, the samples were painted

TABLE 1. Beam reinforcement details

Beam symbol	Opening size [mm]	Longitudinal bar	Transverse bar	Equivalent beam
TRB1	–	3 ø12	ø10@150 mm	–
TRB2	–	2 ø12 + 1 ø16	ø10@150 mm	–
PRB1	2 ø50	2 ø50 steel pipe	ø10@150 mm	TRB1
PRB2	1 ø75	1 ø75 steel pipe	ø10@150 mm	TRB2
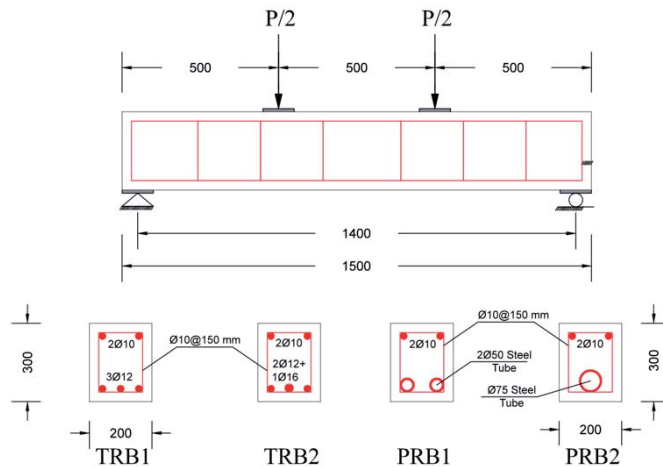
FIGURE 1. Details of tested beams

FIGURE 2. Reinforcement arrangement of the tested beams
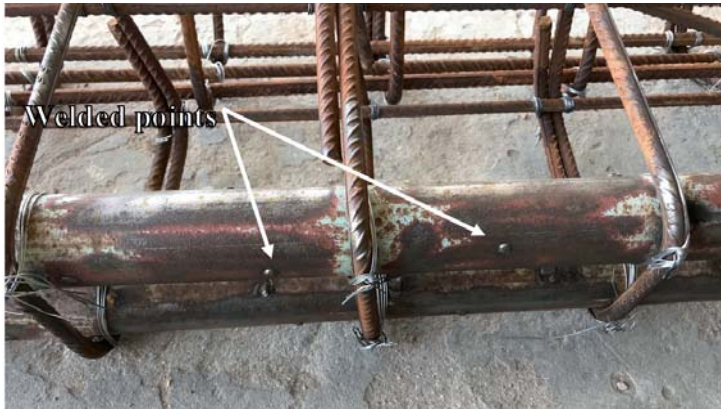
FIGURE 3. Welded points along the pipe

TABLE 2. Reinforcement properties

Reinforcement type	Diameter [mm]	Yield strength [MPa]	Ultimate strength [MPa]
ø12 mm steel bar	11.93	423	637
ø16 mm steel bar	15.88	450	666
ø50 mm steel pipe	50.00	268	396
ø75 mm steel pipe	75.00	268	396

prior to the test to easily recognize the formulation of cracks during different loading stages along the beam. The average 28-day concrete compressive strengths was 30.6 MPa based on $150 \times 150 \times 150$ cubes.

All beams were loaded monotonically until failure using a universal testing machine with a capacity of 1,000 kN as shown in Figure 5. All beams were tested using a four-point load configuration under loading control. The preparation, curing, and test were conducted at the Concrete Lab of Civil Engineering Department in Al--Qadisiyah University. The mid-span displacement was recorded using an LVDT connected to a data logger system with a sampling frequency of 2 Hz.

FIGURE 4. Samples preparation

FIGURE 5. Test set up

Results and discussion

From a typical load-deflection relationship, usually, three stages can be observed. In the first stage which is known as cracking stage, as the specimens are loaded monotonically, a linear increase in the vertical displacement is recorded. After that, there is a curvature in a load--displacement curve up to failure where the slope of the load-deflection curve will be decreased significantly with a large increment in displacement and a small increase in the applied loading up to failure. The flexural cracks were detected initially in middle region between the applied loads. These flexural cracks were speared along the shear span as the load increased.

The mode of failure of all tested beams was a flexural tension except for PRB2 where the failure mode was anchorage failure at the left support. Final failure was occurred by the opening and widening of flexural cracks due to reaching the ultimate tensile strain by the main reinforcement. Horizontal cracks appeared first on the tension reinforcement level and then expanded to the beam end with loading increase. This failure mode

L.S. Al-Yassri, M.A. Al-Ramahee, A.M. Al-Khekani

has specified a diagonal tension crack which is described as a main crack ranging from bottom main reinforcement to the loading point (Sethunarayanan, 1960). Table 3 summarizes the results in terms of load and deflection at cracking and ultimate stages.

and widen with a loss in the beam stiffness. The dominant failure mode as mentioned was the yielding of tension reinforcing steel, following by the concrete crushing under points load at the ultimate load about 192 kN. The load--displacement relationship for TRB1 and

TABLE 3. Summary of results

Beam	Load [kN]		Deflection [mm]	Mode of failure
	cracking	ultimate		
TRB1	30	192	8.49	flexural tensile
TRB2	30	204	8.50	flexural tensile
PRB1	25	161	8.30	flexural tensile
PRB2	22	184	8.01	end anchorage

The first visible crack for TRB1 was recorded in the zero-shear area at a load level of 30 kN. With loading increase, additional flexural cracks initiated, and diagonal shear cracks appeared close to the supports. At the load level of 165 kN, the cracks between loading points at the tension face of the beam began to widen. After that, cracks continued to develop

crack pattern at ultimate load are shown in Figures 6 and 7, respectively.

Beam PRB1 was fabricated as an equivalent for TRB1 based on the moment from the sectional analysis. As mentioned earlier, it was reinforced with a 2 ø50 mm steel pipe as the main reinforcement. The visible crack was recorded as a load level of 25 kN. It can be
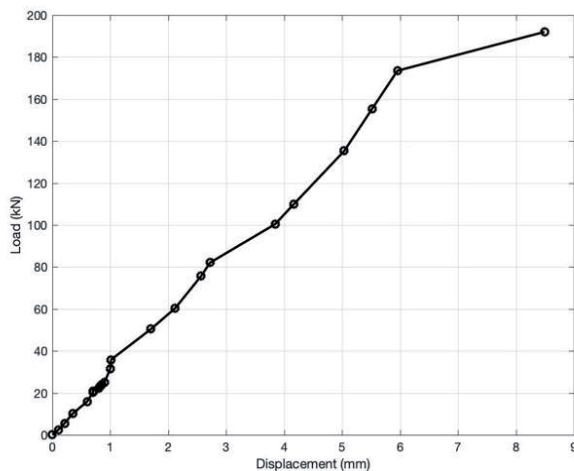
FIGURE 6. Load-displacement for TRB1

FIGURE 7. Crack pattern at ultimate load for TRB1

observed there is a reduction in cracking load of about 5 kN comparing to TRB1. The reason behind this reduction is due to the decrease in uncracked moment of inertia (gross moment of inertia) due to the presence of opening. More flexural and diagonal shear cracks began to initiate with the increasing of a load on the tension face throughout the beam. As the load increased, a major crack widened and propagated to the compression top fiber and flexural tensile failure occurred at a load level of about 161 kN. Figures 8 and 9 show the load-displacement relationship and crack pattern at the ultimate load for PRB1, respectively. Figure 10 shows the comparison between TRB1 and PRB1. As shown from Figure 10, it can be noticed, there is a decrease in the ultimate load of PRB1 compared to TRB1 about 16% due to the smoothness of the pipe that led to the decrease in the strength of the beam. Also, it can be observed from Figure 10 that the after cracking stiffness of PRB1 larger than the reference TRB1 this behavior can
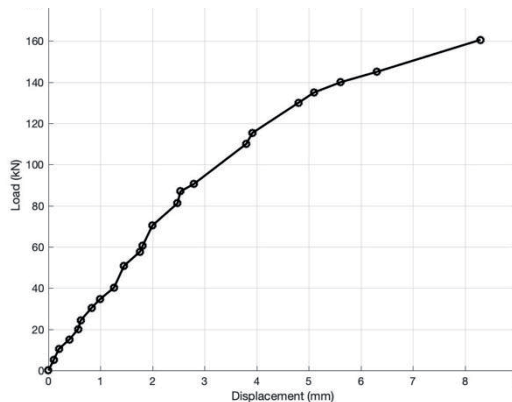
FIGURE 8. Load-displacement for PRB1

L.S. Al-Yassri, M.A. Al-Ramahee, A.M. Al-Khekani
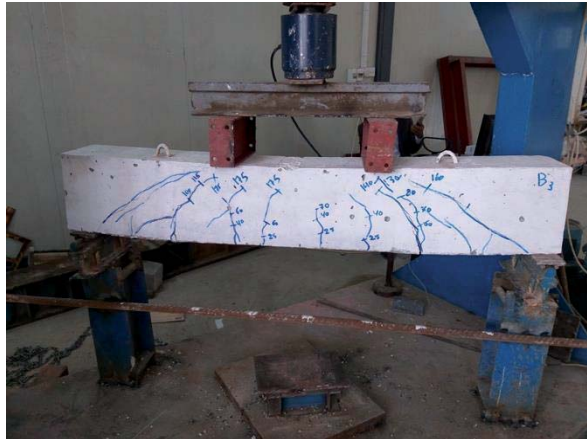
FIGURE 9. Crack pattern at ultimate load for PRB1
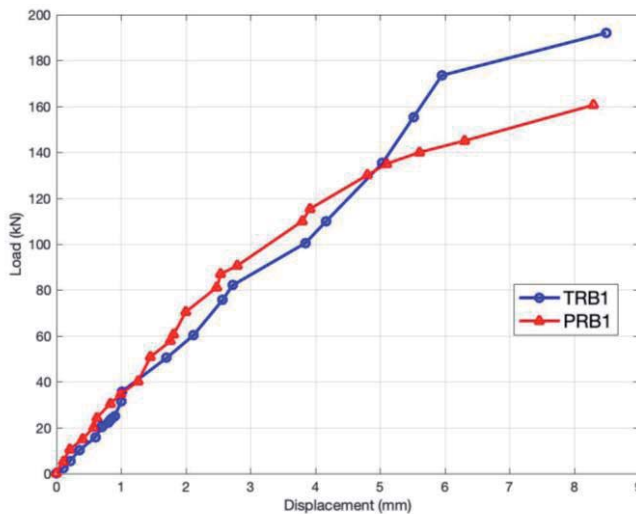
FIGURE 10. Comparison of TRB1 and PRB1

be attributed to the increase in stiffness of steel pipes with respect to traditional steel bars as well as the bond strength along the steel pipes is larger than the bond strength along the traditional steel rebars due to the surface area.

The first visible crack for the second traditional reinforced beam TRB2 was also recorded between the two-point load at a load level of 30 kN. In the same manner to TRB1, more flexural cracks initiated with the increase of the applied load. At the load level of 80 kN, the diagonal shear cracks started to appear in the shear span. After that, cracks continued to develop and widen with a loss in the beam stiffness. The load-displacement relationship for TRB2 is shown in
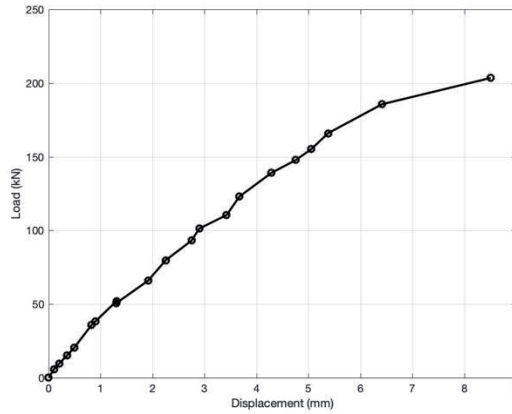
FIGURE 11. Load-displacement for TRB2

Figure 11. The failure mode for this beam was the flexural tensile failure followed by the crushing of concrete in extreme compression fiber at a load level of 203 kN as shown in Figure 12.

the fact that the beam with an open section has a lower gross moment of inertia and an effective moment of inertia that led to a decrease in the strength of the beam. At the load level of 184, an anchorage

FIGURE 12. Crack pattern at ultimate load for TRB2

Beam PRB2 which is equivalent to TRB2 based on the same concept above was reinforced with 1 ø75 mm steel pipe as the main reinforcement. The visible crack was recorded as a load level of 22 kN which is less by 25% compared to TRB2. This difference is related also to

failure occurred in the right support of the beam led to a beam failure. This failure is due to the large size of the opening with respect to the section's width that provided insufficient surrounding concrete around the steel pipe. Figures 13 and 14 show the load-displacement rela-
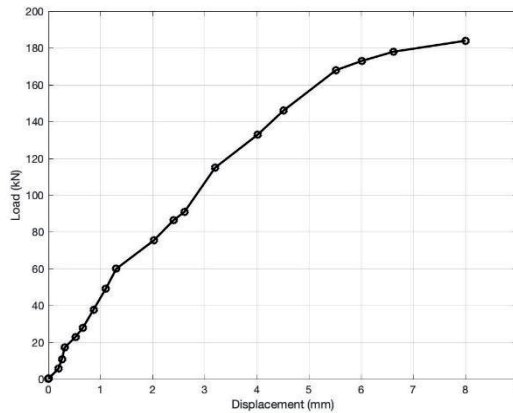
FIGURE 13. Load-displacement for PRB2

FIGURE 14. Crack pattern at ultimate load for PRB2

tionship and crack pattern at the ultimate load for PRB2, respectively.

As shown from Figure 15, which represents the comparison between TRB2 and PRB2, a good agreement in the behavior of the two beams prior to the failure of PRB2. The difference in the ultimate load was about 10% which is due to anchorage failure in PRB2. It can be observed from Figure 15, that after cracking, the stiffness of PRB2 larger than the reference TRB2. This behavior can be attributed to the larger stiffness of steel pipes with respect to the traditional reinforcement as well as the bond strength along the steel pipes is larger than the bond strength along the traditional steel rebars which have a smaller surface area.

Conclusions

Based on the results and observations of current study that implemented for the tested RC beam, the following conclusions can be drawn:
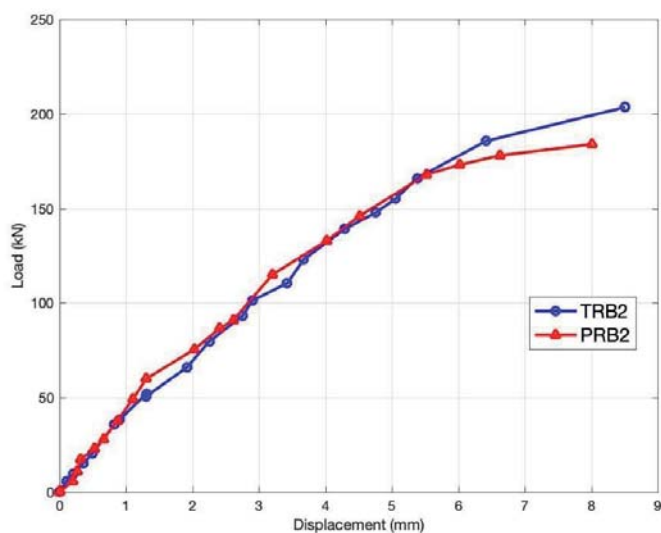
FIGURE 15. Comparison of TRB2 and PRB2

– Replacement of traditional rebars by an equivalent steel pipe with respect to flexural capacity shows a promising result of ductility, cracking pattern, ultimate strength and mode of failure compared to the reference beam with traditional reinforcement with the benefit from all advantages of longitudinal voids mentioned previously.

– The difference in ultimate strength capacity between specimens reinforced with traditional rebars and with those reinforced with steel pipes may be related to the difference in elastic properties between the used reinforcements.

– The steel pipe reinforce beam stiffness after cracking stage is larger than the stiffness of equivalent beams reinforced with rebars because of the large stiffness of steel pipes with respect to traditional rebars as well as the bond strength along the steel pipes is larger than the bond strength along the traditional steel rebars which have a smaller surface area.

– Large size openings provided by large size steel pipes need more confinement by either increasing surrounding concrete or increasing of stirrups at the ends.

References

Al-Khekany, A.M., Al-Yassri, L.S. & Abbas, H.S. (2018). An experimental investigation of hollow composite column reinforced by multi-skin square and round steel tube. *International Journal of Civil Engineering and Technology*, *9*(11), 784-793.

Al-Yassri, L.S., Al-Khekany, A.M. & Abbas, H.S. (2018). Experimental study of replacement the tension reinforcing bars in concrete beams by steel pipes. *International Journal of Engineering and Technology*, *7*(4.20), 229-234.

American Concrete Institute [ACI] (2014). *Building Code Requirements for Structural Concrete and Commentary* (ACI 318-14).

Farmington Hills (MI): American Concrete Institute.

Amin, H.M., Agarwal, V.C. & Aziz, O.Q. (2013). Effect of opening size and location on the shear strength behavior of RC deep beams without web reinforcement. *International Journal of Innovative Technology and Exploring Engineering*, *3*(7), 28-30.

Arya, C. (2009). *Eurocode 2: Design of concrete structures*. In *Design of Structural Elements*. (pp. 314-374). New York: Taylor & Francis.

Ashour, A.F. & Rishi, G. (2000). Tests of reinforced concrete continuous deep beams with web openings. *Structural Journal*, *97*(3), 418-426.

Campione, G. & Minafò, G. (2012). Behaviour of concrete deep beams with openings and low shear span-to-depth ratio. *Engineering Structures*, *41*, 294-306.

Canadian Standards Association [CSA] (2004). *Design of concrete structures* (CSA A23.3--04). Mississauga, Ontario: Canadian Standards Association.

Central Organization for Standardization and Quality Control [COSQC] (1984a). *Portland cement* (IQS 5/1984). Baghdad: Central Organization for Standardization and Quality Control.

Central Organization for Standardization and Quality Control [COSQC] (1984b). *Aggregates from natural sources for concrete and building construction* (IQS 45/1984). Baghdad: Central Organization for Standardization and Quality Control.

Hasnat, A. & Akhtanizzamam, A.A. (1987). Beams with small rectangular opening under torsion, bending, and shear. *Journal of Structural Engineering*, *113*(10), 2253-2270.

Herrera, L., Anacleto-Lupianez, S. & Lemnitzer, A. (2017). Experimental performance of RC moment frame beams with rectangular openings. *Engineering Structures*, *152*, 149-167.

Makki, R.F., Jassem, A.T. & Jassem, H.A.A.L. (2018). Non-linear analysis of Reactive Powder Concrete (RPC) deep beams with openings strengthened by CFRP. *Al-Qadisiyah Journal for Engineering Sciences*, *11*(2), 176-196.

Mansur, M.A., Tan, K.H. & Lee, S.L. (1984). Collapse loads of R/C beams with large openings. *Journal of Structural Engineering*, *110*(11), 2602-2618.

Prentzas, E. (1968). *Behavior and reinforcement of concrete beams with large rectangular apertures*. Sheffield: University of Sheffield.

Sethunarayanan, R. (1960). Ultimate strength of pre-tensioned I-beams in combined bending and shear. *Magazine of Concrete Research*, *12*(35), 83-90.

Somes, N.F. & Corley, W.G. (1974). Circular openings in webs of continuous beams. *Special Publication*, *42*, 359-398.

Yang, K.H., Eun, H.C. & Chung, H.S. (2006). The influence of web openings on the structural behavior of reinforced high-strength concrete deep beams. *Engineering Structures*, *28*(13), 1825-1834.

Summary

Experimental investigations on concrete beams reinforced with equivalent service steel pipe. Different techniques were employed for the passage of different utilities through structural elements. The reduction of the overall building weight was the main concern that needs to be achieved, especially for a multistory building. It can be done with the eliminating of a suspended ceiling with a portion of the beam's weight by taking the advantages of the hollow sections. In this study, an equivalent reinforcement to the traditional ribbed reinforcement was employed to fabricate a reinforced concrete (RC) beam with a hollow section along the length of the beam. A steel pipe was used based on the equivalent moment from section analysis. Two diameters were selected of steel pipes as an equivalent to the commercial reinforcement. A total of four RC beams were cast and tested, two of them with traditional reinforcement and the other with steel pipe reinforcement. The comparison showed a promising result in terms of ductility, cracking pattern, ultimate strength, and mode of failure compared to the reference beam. The peak loads for the specimens with steel pipe were 160.6 kN and 184 kN, while they were 192 kN and 203.5 kN for the beams with traditional reinforcement.

Authors' address:
Labeeb S. Al-Yassri
(https://orcid.org/0000-0002-2664-1506)
Munaf A. Al-Ramahee
(https://orcid.org/0000-0002-1922-9871)
Alaa M. Al-Khekani
(https://orcid.org/0000-0001-8474-6798)
University of Al-Qadisiyah
College of Engineering
Civil Engineering Department
e-mail: labeeb.husein@qu.edu.iq
      Munaf.alramahee@qu.edu.iq
      alaa.alkhekany@qu.edu.iq

Zainab A. NEAMAH, Munaf A. Al-RAMAHEE

University of Al-Qadisiyah, College of Engineering

Strengthening of bi-axially loaded RC slab-column connection using steel plates and stiffeners

Key words: bi-axial loads, eccentric load, flat slab, strengthening, steel plates

Introduction

Reinforced concrete flat slabs are slabs that rest directly on columns without beams. Flat slabs are widely used in multi-storey buildings such as garages and office buildings, due to their many benefits, including ease of construction, simple reinforcements and freedom of architectural design, etc. The slab-column connection regions are the most important part due to its failure by punching shear. Punching shear failure occurs suddenly without any signs due to the transmission of high loads and moments greater than the design resistance which comes from the change in design or using bad constructions materials. Some of these loads are eccentric due to the influence of winds, creep, unbalanced loads, different shrinkage and unequal spans. Punching shear can be avoided by increasing the ultimate strength of the slab.

Different methods have been employed to increase the ultimate strength of flat slabs, including internal and external strengthening (Al-Khekany, Al--Ramahee & Al-Yassri, 2020). The internal strengthening involves; increasing the thickness of the slab, increasing the flexural reinforcement, and using the shear reinforcement. On the other hand, the external strengthening includes the use of fiber reinforced polymer (FRP) strips, the use of drop panel or the column capitals, and the use of steel plates (Al-Ramahee, Chan, Mackie, Ghasemi & Mirmiran, 2017). Shaaban (2013), Abbas, Abadel, Almusallam & Al-Salloum (2015), Meisami, Mostofinejad and Nakamura (2015) investigated the effect of using FRP strips as a strengthening method with different shapes and numbers. This method was effective to increasing the ultimate capacity of flat slab. Marzouk, Emam and Sameh Hilal (1998), Inácio, Ramos, Lùcio and Faria

(2013) experimentally studied the effect of increasing the concrete strength on the behavior of flat slab through using high concrete strength. This method was good for increasing the stiffness of flat plates. Alam and Amanat (2013), Inácio et al. (2013), Jang and Kang (2019) investigated the effect of increasing the flexural reinforcement of flat slab with different ratios. They concluded that the increasing in the flexural reinforcements has a good effect on the behavior of flat plates. Abdelaziz, El-Nawawy, El-Karmoty and Abu-Beah (2019) investigated the behavior of RC flat slab that strengthened with added of ultra-high strength concrete drop panel with different dimensions of drop panels. This method showed a good result, where when the thickness of drop panel was increased, the ultimate load and stiffness increased. Ebead and Marzouk (2002) investigated the effect of using steel plates and steel bolts with different numbers of steel bolts and shapes on the ultimate capacity of slabs. Their results showed the using of steel plates is a good effective strengthening technique. Elbakry and Allam (2015) studied the effect of using externally bonded steel plates with different thickness and different numbers of shear studs on the slab behavior. The use of this method was considered a good method to strengthened flat slab against punching shear stresses. Kadhim and Ammash (2019) investigated the effect of using steel stiffeners and column capital with different dimensions and different numbers of stiffeners. They found that the using of steel plates improve the behavior of slab-column connection.

Available literature shows that the strengthening of slab-columns connec-tions using steel plates and steel stiffeners has not got enough attention previously. Also, there was very little researchers studied the effect of bi-axial loads on punching shear behavior of slab-columns connections. This paper investigates the enhancing the punching shear strength of slab-column connection by using steel plates and stiffeners under the bi-axial loads. Different plates and stiffeners sizes were included in this study.

Experimental program

The experimental program included testing of four RC slabs under bi--axial load. One slab was tested as control slab without strengthening, and other three RC slabs were test with the benefit of applying steel plate and stiffeners to enhance the slab-column region against punching shear failure. The dimensions of slabs are $1{,}600 \times 1{,}600$ mm with a total thickness of 100 mm. The RC column dimensions are 200×200 mm with a height of 300 mm. A column cap is used at the top of the column to avoid crushing the columns and highlighting the biaxial loads. A column cap dimensions are 500×500 mm with thickness of 200 mm. The flexural reinforcement ratio was used to be 1.26%. The details of tested specimens are shown in Table 1. The letters SS referred to strengthened slab. The first number (0, 6, and 8) that follow the letter S refers to the steel plates dimensions (0, 600 and 800 mm). The second number (0, 2 and 3) refers to number of stiffeners. The reinforcement details for slab, column and column's cap for SS00 slab are shown in Figure 1. These details are identical for other

TABLE 1. Specimens details

Symbol	Compressive strength [MPa]	Flexural reinforcement ratio [%]	Total dimensions of slab plates [mm]	Number of stiffeners	Stiffener's dimensions [mm]
SS00	33	1.26	–	–	–
SS62			600 × 600	2	200 × 200
SS63			600 × 600	3	200 × 200
SS83			800 × 800	3	300 × 300

SS00
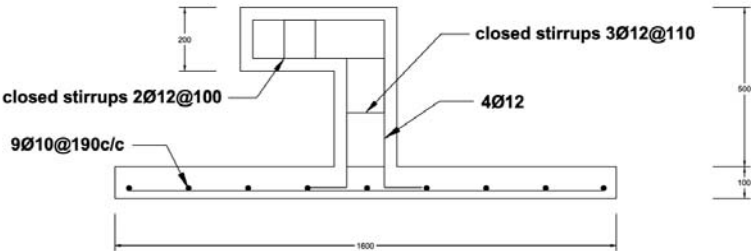
SS62
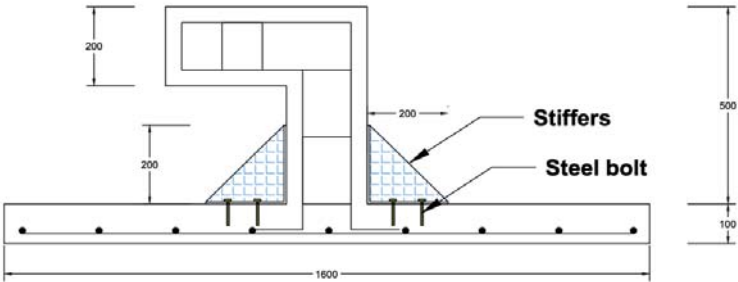
SS83
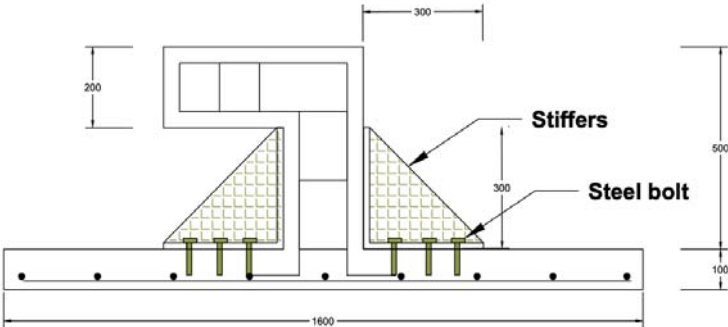
FIGURE 1. Specimens geometry and reinforcement details (all dimensions in mm)
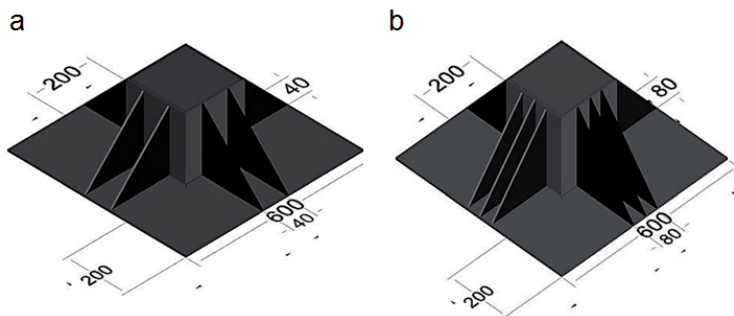
FIGURE 2. Details of steel plate and stiffeners (all dimensions in mm): a – plate with two stiffeners; b – plate with three stiffeners

specimens. Three slabs are strengthened using steel plates and steel stiffeners. The thickness of the steel plates is 6 mm. The dimensions of the steel plate was 600×600 and 800×800 mm in the slab-column connection region and it was fixed to the slab using steel bolts. The steel stiffeners are cut in the form of a right-angled triangle with dimensions of 200×200 and 300×300 mm. Figure 2 shows the sketch of the steel plate and stiffeners. The stiffeners are placed and welded to link the column plates and the slab plates.

Experimental test

A total of four simply supported specimens of RC slab-column connection under biaxial load were tested in this study. One of these slabs was examined as a reference slab (SS00), and the other three slabs were strengthened using steel plates and stiffeners. The specimens are rested along the four edges on knife edges placed on steel frames. The load was applied on 40-mm thick steel plate using load-controlled hydraulic jack with a capacity of 1,000 kN. A linear variable
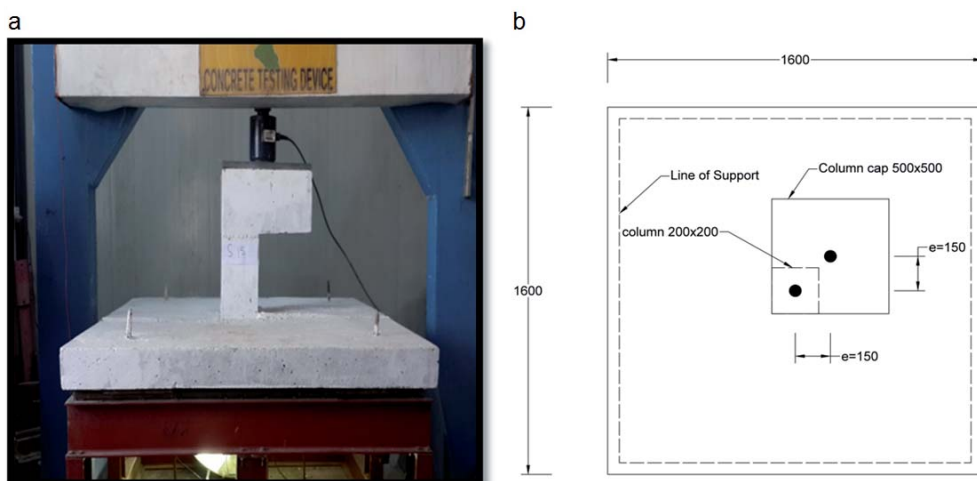
FIGURE 3. Test set-up under biaxial load: a – test set-up; b – top view sketch (all dimensions in mm)

displacement transformer (LVDT) was used to record the central deflection of the slabs. The top and bottom face of all specimens were observed for cracks development. The test continued until an excessive deflection was recorded and the column had penetrated the slab. A computerized data acquisition device was used to record the test results. The test setup and sketch for bi-axially loaded slabs is shown in Figure 3.

Results and discussion

Ultimate load and deflection

The results obtained from experimental tests of the slab column connections strengthened with steel plates and stiffeners under bi-axial load showed that the ultimate loads for SS62, SS63 and SS83 increased by about 71, 72 and 111%, respectively when compared with SS00. Also, the steel plate and stiffeners delayed the first crack load 114% for SS62, 90% for SS63 and 29% for SS83 as shown in Table 2. This enhancement can be related to the fact that the strengthening method was effective to increase the critical section which mean increased area that resist the high stresses. Also, it increases the flexural

rigidity for the connection region. The deflection at ultimate load there was an increasing by about 54% for SS62, 75% for SS63 and by about 94% for slab SS83. Also, the deflection at cracking load level there was increased by about 252%, 148% and 44% for SS62, SS63 and SS83, respectively when compared with SS00.

Failure mode

All slabs in this study have the same behavior of the failure. As the applied load increased, the cracks begin to form, and they extended from the edges of the specimens towards the center and it is intersected with the locations of bolts in the strengthened specimens. It can be observed that the failure of strengthened specimens became more ductile than the reference slab SS00 (Figs. 3 and 4). Also, the slabs strengthened with steel plates (SS62, SS63 and SS83) have cracks width less than the reference slab.

Load deflection relationship

The load-deflection curves for the slabs SS62, SS63, SS83 compared to SS00 are shown in Figures 5 and 6, respectively. It can be shown that the specimens strengthened with steel plates have more stiffness, more ductile fail-

TABLE 2. Summary of test results

Slab	First crack load [kN]	Cracking deflection [mm]	Ultimate load [kN]	Ultimate deflection [mm]	Increasing in ultimate load [%]	Increasing in ultimate deflection [%]
SS00	21	0.64	103	15.42	–	–
SS62	45	2.27	176	23.73	71	54
SS63	40	1.59	177	26.94	72	75
SS83	27	0.93	217	29.91	111	94
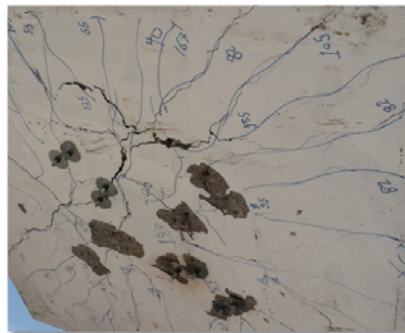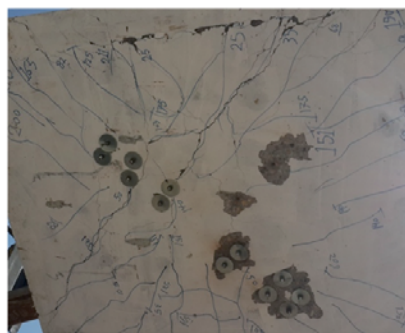
FIGURE 4. Cracks patterns

ure, and higher ultimate load compared to reference specimens (SS00). The increasing in the number of stiffeners from two stiffeners in SS62 to three stiffeners in SS63 has no significant effect on the behavior of specimens for 600 mm steel plate strengthened specimens. Figure 7 shows the comparison between the strengthened slab column connection behavior using 600- and 800-mm steel plate. It can be noticed that when steel plates dimensions increased, the ultimate load increased by about 23% for SS83 when compared with slab SS62 and SS63. Also, when the dimensions of steel plates increased, the stiffness and ductility of connection region increased.

This enhancement of strengthening because of steel plates worked as a column capital which lead to an increasing in the critical sections of column which mean increasing the area that resist the high stresses transformed form column to slab.

Conclusions

Strengthened slab-column connection with the steel plates and stiffeners enhanced both the stiffness, also the failure mode of the slab-columns connection became more ductile.

The connection region that subjected to bi-axial load and strengthened with
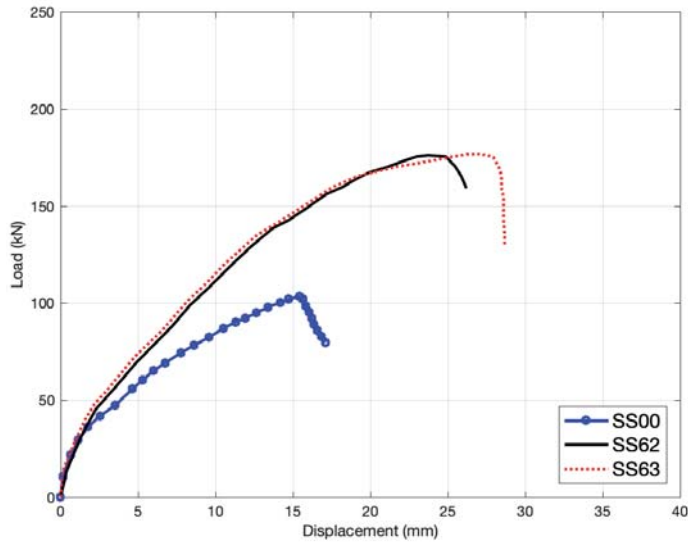
FIGURE 5. Comparison results of 600-mm steel plate
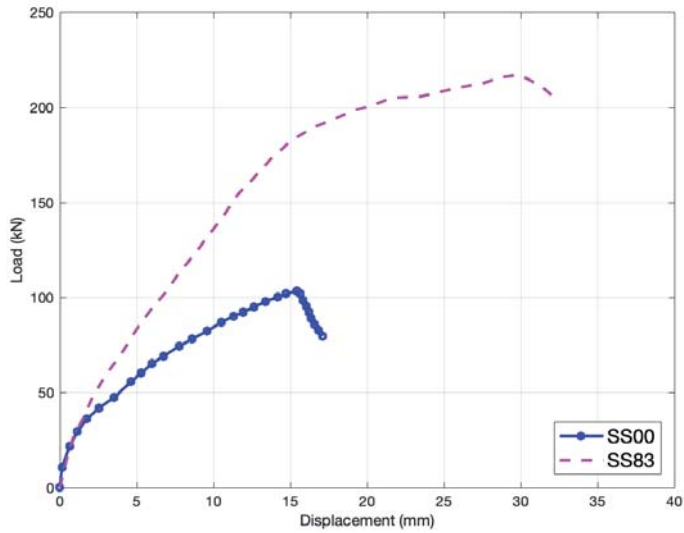
FIGURE 6. Comparison results of 800-mm steel plate

steel plate and stiffeners have ultimate capacity more than the reference specimen by about 71% for SS62, 72% SS63 and 111% for SS83.

It can noticed that the connection with steel plates dimensions 800×800 mm (SS83), the ultimate load and deflection increased by about 23% and 26%, respectively when compared to SS62 and by about 23% and 11%, respectively when compared to SS63 which they strengthened by a 600×600 mm steel plate.
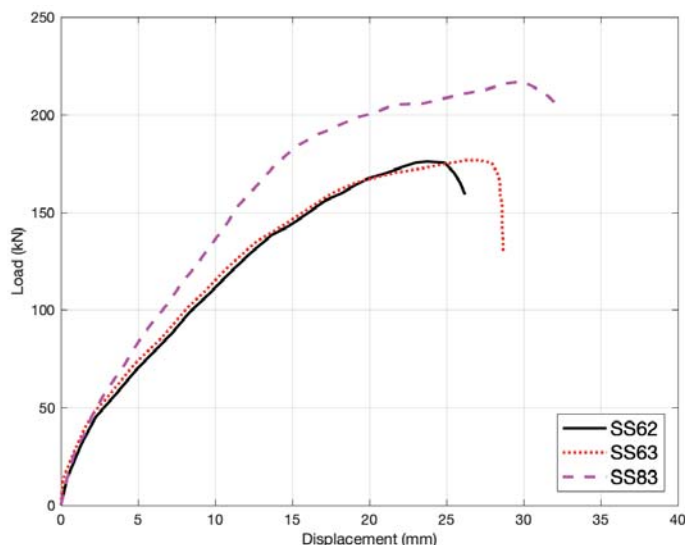
FIGURE 7. Comparison results of 600- and 800-mm steel plate

It can be observed from the results that the larger steel plate (SS83), the less the cracks width compared to the specimen with 600 × 600 mm steel plate despite of the number of stiffeners.

The results showed the using three stiffeners instead of two stiffeners with 600 × 600 mm plate has no significant effect on the ultimate load and the behavior of slab column connection.

References

Abbas, H., Abadel, A.A., Almusallam, T. & Al--Salloum, Y. (2015). Effect of CFRP and TRM strengthening of RC slabs on punching shear strength. *Latin American Journal of Solids and Structures*, *12*(9), 1616-1640.

Abdelaziz, H., El-Nawawy, O., El-Karmoty, H. & Abu-Beah, A. (2019). Behavior of flat slabs using ultra high strength concrete under the effect of eccentric punching shear. *International Journal of Scientific and Engineering Research*, *10*(4), 528-540.

Alam, A.M.J. & Amanat, K.M. (2013). Fe analysis on the effect of flexural steel on punching shear of slabs. *International Journal of Engineering Research and Technology*, *2*(6), 2878-2901.

Al-Khekany, A.M., Al-Ramahee, M.A. & Al--Yassri, L.S. (2020). Experimental and numerical investigations of composite concrete steel flexural members with angle shear connectors under negative moment. *Periodicals of Engineering and Natural Sciences*, *8*(4), 2107-2117.

Al-Ramahee, M.A., Chan, T., Mackie, K.R., Ghasemi, S. & Mirmiran, A. (2017). Lightweight UHPC-FRP composite deck system. *Journal of Bridge Engineering*, *22*(7), 04017022. https://www.doi.org/10.1061/(ASCE)BE.1943-5592.0001049

Ebead, U. & Marzouk, H. (2002). Strengthening of two-way slabs using steel plates. *Structural Journal*, *99*(1), 23-31.

Elbakry, H.M. & Allam, S.M. (2015). Punching strengthening of two-way slabs using external steel plates. *Alexandria Engineering Journal*, *54*(4), 1207-1218.

Inácio, M., Ramos, A., Lúcio, V. & Faria, D. (2013). Punching of high strength concrete flat slabs – experimental investigation. In *Proceedings of the Fib Symposium Tel Aviv 2013*. https://www.doi.org/10.13140/2.1.3251.5849

Jang, J.I. & Kang, S.M. (2019). Punching Shear Behavior of Shear Reinforced Slab–Column Connection with Varying Flexural Reinforcement. *International Journal of Concrete Structures and Materials*, *13*(1), 1-14.

Kadhim, S.S. & Ammash, H.K. (2019). Steel stiffeners for enhancement of slab-column connections. *Al-Qadisiyah Journal for Engineering Sciences*, *12*(4), 199-206.

Marzouk, H., Emam, M. & Sameh Hilal, M. (1998). Effect of high-strength concrete slab on the behavior of slab-column connections. *ACI Structural Journal*, *95*, 227-237.

Meisami, M.H., Mostofinejad, D. & Nakamura, H. (2015). Strengthening of flat slabs with FRP fan for punching shear. *Composite Structures*, *119*, 305-314.

Shaaban, I. (2013). Strengthening of reinforced concrete slab-column connection subjected to punching shear with FRP systems. *International Journal of Engineering and Technology*, *5*(6), 657-661.

Summary

Strengthening of bi-axially loaded RC slab-column connection using steel plates and stiffeners. This paper presented a strengthening technique for enhancement reinforced concrete (RC) slab-column connection behavior using steel plates and steel stiffeners. A bi-axial load was applied with an eccentricity of 150 mm in both x and z directions. Four specimens with dimensions of $1{,}600 \times 1{,}600 \times 100$ mm were tested in this research. The steel plate dimensions were chosen to be 600×600 and 800×800 mm with 6 mm thickness. The steel stiffeners are used to support and enhance the steel plate that it is extended from column to the slab-column connection with different dimension. The results showed an improvement in the stiffness of slab and increasing in the ultimate capacity. Also, when the steel plates dimensions increased, the ultimate capacity and stiffness increased.

Authors' address:
Zainab A. Neamah
Munaf A. Al-Ramahee
(https://orcid.org/0000-0002-1922-9871,
ResearcherID W-7313-2018)
University of Al-Qadisiyah
College of Engineering
e-mail: civil.post11@qu.edu.iq
          Munaf.alramahee@qu.edu.iq

Yevhen FORNALCHYK[1], Ivan KERNYTSKYY[2], Oleh HRYTSUN[1], Yuriy ROYKO[1]

[1]Lviv Polytechnic National University, Transport Technology Department
[2]Warsaw University of Life Sciences – SGGW, Institute of Civil Engineering

Choice of the rational regimes of traffic light control for traffic and pedestrian flows

Key words: pedestrian flow, traffic flow, traffic intensity, speed of movement, volume-capacity ratio, traffic light control, traffic simulation

Introduction

An important direction for transport problems solving is the formation of cities' road networks with increased capacity, improvement, and provision of conditions for public transport movement (separate lanes allocation and provision the priority in movement). It is quite hard to take into account simultaneously these factors, especially for cities with a historical road network. It is possible to solve this problem with the help of the implementation of modern technologies, automated traffic control systems, in particular, to improve the traffic light control system at the intersections (pedestrian crosswalks). Such management should satisfy the requests of road users, based on objective functions – safety and speed of movement.

Traffic light control systems at the intersections in existing conditions have limited time parameters by regulatory documents, although they operate both in adaptive (flexible) and fixed-time regimes. Such systems mainly consider the needs of traffic flows, giving minimal duration for serving pedestrian flows. The existing approach to the balancing of traffic light duration does not always take into account the peculiarities of the pedestrian movement who try to cross the roadway in every convenient moment in time, even in conditions of risk. As result, traffic safety at grade level pedestrian crosswalks reduces (deteriorates).

Analysis of literature and problem statement

During the design of the traffic light cycle duration, to determine the rational control regime, minimal time, which provides crossing the roadway by pedes-

trians, takes into account. In recommendations, the methodology for determining the duration of crossing the roadway by pedestrians is given. The majority of these methodologies are based on assumptions about the average speed of pedestrian movement. That way, in recommendations of the Transportation Research Board (2000), the speed of pedestrian movement is considered 1.2 m·s^{-1}; in the manual of Japan Society of Traffic Engineers (2006), the speed is 1.0 m·s^{-1}; in the studies of Ukrainian researchers – 1.3–1.4 m·s^{-1}.

For the investigation of the speed of pedestrian flows at the grade crosswalks, several techniques are developed, but the majority of them do not consider the impact of counterflow. Various authors developed the model of the duration of crossing the roadway by pedestrians, considering the length and width of the crosswalk, and also the density of conflicting flow (Alhajyaseen, Nakamura & Catbagan, 2008; Alhajyaseen & Nakamura, 2010; Iryo-Asano & Alhajyaseen, 2017; Wang, Zhao, Cao, Lu & Chen, 2017). During pedestrian flows simulation, the method was used which considers pedestrian delays which had formed in result of counterflow impact (the group of pedestrians with a maximal density which had formed at pedestrian crosswalks). The investigation showed that with the intensity approximately equal at each side of the crosswalk (dense flow), pedestrian speed decreases to one third with the comparison to the flow, which moves in one direction. As result, the conclusion was that the impact of conflicting flows is significant and should be reviewed during the design of traffic light control systems to determine

the optimal time needed for crossing the roadway by the groups of pedestrians.

In the study by Alhajyaseen and Nakamura (2012), the method of the determination of traffic light cycle duration taking into account the length of the pedestrian crosswalk, which allows minimizing traffic and pedestrian delays, is given. This method considers the density, intensity, speed of traffic and pedestrian flows, and geometric parameters of the roadway. During the calculation of the traffic light cycle duration, two limitations are considered: optimal duration of permissive signal for traffic flow and minimal duration for the pedestrian.

The main restrictions, which are used during the calculation of traffic light system, are the minimal duration of permissive signal for traffic flow and maximal duration of restrictive signal for pedestrian flow (Transportation Research Board [TRB], 2000; Vrubel, 2003; Levashev, Mykhailov & Holovnykh, 2007; Vasylieva, 2007; Polishchuk & Bakulich, 2012). An experience of the investigation of pedestrian behavior at signalized intersections shows that the duration of patient waiting of green signal by them can be within 30–90 s (Vrubel, 2003; Xiong, Xiong, Deng & Wang, 2014). With such values of restrictive signal, the number of violators is no more 15% (Gong, Xiao & Xu, 2019; Ma, Lu & Zhang, 2020). By the duration of the patient waiting for a green traffic light signal by pedestrians means maximal time, which the pedestrian is ready to spend to wait for such signal.

Many researchers establish the values of limits of traffic light cycle duration by empirical dependencies. Vrubel (2003) investigated that the cycle du-

ration should be no less than 70 s for two-phase control; no less than 90 s for three-phase control; no less than 110 s for four-phase control.

In recommendations by Polishchuk and Bakulich (2012), the limitations of minimal duration of the traffic light cycle are given (no less than 25 s). It is explained by the fact that with a short cycle duration, delays in traffic flow increases and capacity decreases.

Analysis of literature data established many factors: minimal time, needed to pedestrians for crossing the roadway, the duration of the permissive and restrictive signal of the traffic light, intensity, density, speed of traffic an pedestrian flows, geometric parameters of intersection – crosswalk (Zhyvohliadov, 2012). However, such factors are not taken into account as a pedestrian discipline, location of the crosswalk relatively functional zone of the city, the designed purpose of pedestrian movement, climate conditions, and determination the distance between pedestrian crosswalks. Given factors, determine the behavior of pedestrians in compliance with the traffic rules.

Based on the above, the problem of choosing the rational regimes of traffic light control for traffic and pedestrian flows remains topical.

Aim and tasks of the research

The aim of the study is an investigation of traffic and pedestrian flows for choosing the rational regimes of traffic light control.

To achieve the goal, such tasks are formed to:

- reveal the regularities and methods of research of road users indicators;
- investigate road users indicators and pedestrian behavior at signalized intersections;
- choose rational regimes of traffic light control for traffic and pedestrian flows;
- justify the recommendations about the choice of rational regimes of traffic light control for signalized intersections of different types.

Research techniques

Experimental determination technique

To evaluate quantitatively the duration of patient waiting by pedestrians it is necessary to research the process of crossing the roadway by pedestrians. Obtained results will allow determining the factors, which have a direct impact on the time of pedestrians' patient waiting. But, it is necessary to consider such indicators as traffic intensity, density, and composition, traffic light control regime, roadway geometric parameters, district type where the intersection is located (residential, central, and suburb district of the city), climate conditions, etc.

To measure the duration of pedestrians' patient waiting, we used the method, which is based on the investigation of pedestrian behavior during crossing the roadway by them.

On the primary stage of the research conduction, we determined:

- geometric parameters of the roadway (crosswalk), and the duration of permissive and restriction signals of a traffic light;

Y. Fornalchyk et al.

– recorded the number of pedestrians who crossed the crosswalk in such sequence: recorded the number of persons who crossed the roadway while turning on the permissive signal of the traffic light; recorded the moment of the crossing of the last pedestrian on the permissive signal; recorded the number of pedestrians who crowded during the restrictive signal of a traffic light; recorded the number of pedestrians who crossed the roadway during the restrictive signal;
– while turning on the permissive signal of a traffic light for transport, we recorded the number of vehicles that cross the stop-line.

In the next stage, we determined the type of traffic light control (fixed-time or adaptive) and climate conditions.

In the final stage, we determined the speed, with which the pedestrians cross the roadway. To obtain this indicator (speed of pedestrians), we recorded the time which pedestrians spent crossing the roadway with the help of a stopwatch. The experiment was carried out no less than 20 times for different age categories of pedestrians (young, middle age, and old) on each of the investigated objects, and after we calculated the average speed of pedestrian flow.

It was established that the duration, necessary for pedestrians to cross the roadway depends on the length and width of the crosswalk, and pedestrian flow intensity.

Simulation modeling technique

To evaluate operation regimes of traffic and pedestrian flows, there are many foreign and domestic programs and projects, within which the research, modeling, and analysis of cities' road network condition are carried out. Both powerful software package PTV Vissim and simple mathematical models can be distinguished.

To develop a transport model in PTV Vissim software, it is necessary to carry out such operations:
– to calibrate the map of research objects, build streets which approach the research objects, set the appropriate widths and the number of lanes;
– due to the results of field research, to create incoming traffic flows on every approach to the intersection (crosswalk), specify respectively their composition and allowed movement directions. Speed of vehicle movement is specified separately for every type, and restrictions on turns are set;
– as the movement of traffic and pedestrian flows is controlled by the traffic light signalization, it is necessary to create signal groups and specify the duration of permissive and restrictive signals for each phase;
– while crossing the traffic flows in one control phase, it is necessary to enter appropriate priorities for specific flows;
– to determine traffic flow delays (in s·vehicle^{-1}) and vehicle queue length (in m), it is necessary to set measuring points on each approach to the intersection (crosswalk).

At signalized intersections (crosswalks), it is necessary to carry out pedestrian flow simulation similarly to the traffic flow. For the proper operation of such model, it is necessary to set the incoming pedestrian flow and (for needs) pedestrian routes of movement.

The main parameters of pedestrian movement within at-grade crosswalks are intensity, density, and speed of pedestrian movement; the number of crosswalks; the presence of points of attraction near the investigated research object.

Research results

Pedestrian behavior model depending on the movement intensity and crosswalk length

Experimental measurements of traffic and pedestrian flow indicators were carried out on sections of road network of Lviv city. In the primary stage of this research, the range of objects was chosen – signalized intersections and crosswalks beyond intersections. Chosen objects differed by the width of the roadway on approaches to the stop-line (from lane to three lanes on the direction), distance between adjacent stop-lines (about from 50 to 700 m) and signalized intersections – by the number of pedestrians (from 3 to 5). Intersections, where pedestrian behavior was investigated, were considered with fixed-time traffic light cycle. All investigated intersections were conditionally divided into three types relative to their location on the city territory: type I – near transport junctions; type II – central zone; type III – residential zone (Table 1).

Based on the goal, task, and method of experimental measurement, eight signalized intersections and pedestrian crosswalks of each type were chosen for its conduction. Taking into account the fact that indicators of traffic and pedestrian flows are characteristic for the change during the day, measurements were car-

TABLE 1. Types of signalized intersections and pedestrian flows relative to their location on the city territory

Intersection type	Location on the city territory	Peculiarities of pedestrian flow movement	Peculiarities of traffic flow movement	Presence of flows generation center
I	near transport junctions	permanent intensive in peak periods; oriented in the direction to and from generation centers	large heterogeneity of traffic flow (up to 70% of cars); significant share of urban public transport, maneuverability at the car parking	trade establishments, bus stations, and railway stations
II	central zone	permanent intensive during daylight	significant homogeneity of traffic flow (up to 95% of cars)	precise generation center is absent, distribution of pedestrian flows by the territory is steady
III	residential zone	changeable, evenly directed in all zone	share of cars is 80–85%, urban public transport – up to 10%, freight transport almost absent	stopping points of urban public transport

Y. Fornalchyk et al.

ried out for peak (morning and evening) and inter-peak periods. For each period, appropriate indicators were fixed during 50 traffic light cycles. It is important that during these measurements recordings from surveillance cameras from the Center of traffic management of Lviv city were used, which allowed fixating traffic indicators and pedestrian behavior (number of violations) simultaneously with involvement of small number of researchers. We consider this as an advantage of this method.

The operation of signalized intersections and crosswalks was analyzed to investigate pedestrian behavior taking into account their intensity and crosswalk width. On such intersections, the duration of restrictive signal for pedestrians changed from 26 to 115 s. Results of this research are processed in the MS Office Excel software. Experimental dependencies of the number of violations of the traffic rules by pedestrians, which cross the roadway in risk conditions from traffic flow intensity, expressed through the volume-capacity ratio, are obtained (Fig. 1). Volume-capacity ratio (z) was determined as interrelation of traffic intensity (N) to capacity (P): $z = N / P$. Maximum permissible capacity of one lane on intersections of type I is 750–850 pcu·h^{-1}; for type II – 800–900 pcu·h^{-1}; for type III – 800–1,000 pcu·h^{-1}. Traffic intensity determines by results of experimental measurements. Here, it is not indicated how the number of violations of traffic rules by pedestrians will
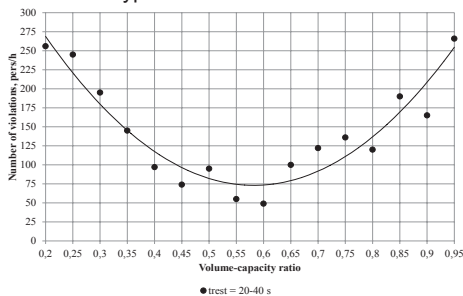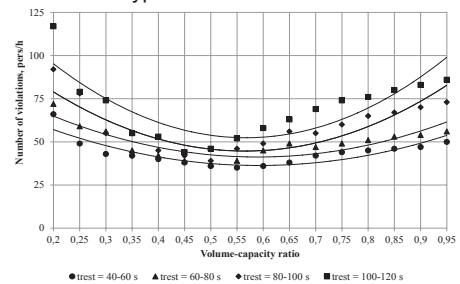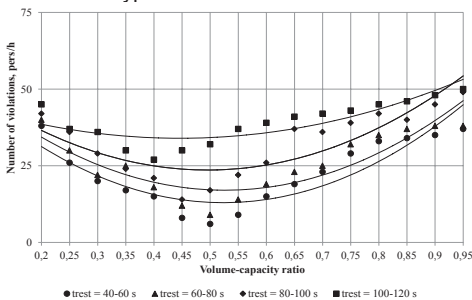
FIGURE 1. Experimental and approximated dependencies of the number of violations the traffic rules by pedestrians from street volume-capacity ratio before stop-line for intersections types (t_{rest} – duration of the restrictive signal of a traffic light for pedestrians)

change depending from the lane width as it lays within 3.0–4.0 m. Lane width has no impact on pedestrian behavior but it depends from the roadway width (pedestrian crosswalk length). Average values of the number of violations the traffic rules by pedestrians for different day periods (with the aim to investigate the change of violations at the intersection with different volume-capacity ratio) is given on Figure 1.

Based on the obtained results, the tendency of decrease of the number of violations by pedestrians while crossing the roadway by street volume-capacity ratios is established: 0.50–65 for intersections of type I (duration of restrictive signal for pedestrians is 20–40 s); 0.40–0.65 for type II (duration of restrictive signal for pedestrians is 40–100 s); 0.45–0.55 for type III (duration of restrictive signal for pedestrians is 40–100 s). For the intersection of type III, with the duration of the restrictive signal of a traffic light for pedestrians is 100–120 s, an increase of the number of violations of the traffic rules by pedestrians regardless of roadway volume-capacity ratio is observed.

Research showed that street volume-capacity ratio and control regime are determinant factors in making a decision by pedestrians about crossing the roadway in risk conditions. With roadway volume-capacity ratios from 0.20 to 0.40, large intervals between vehicles are observed, pedestrians, feeling their relative safety, cross the roadway in risk conditions (especially such thing is observed during long restrictive signal). With the increase of roadway volume-capacity ratios (0.40–0.60), intervals between vehicles density, vehicles structure by composition on the lanes. This leads

to that pedestrians do not risk violating the traffic rules (cross the roadway on the restrictive traffic light signal). With volume-capacity ratios 0.80–0.95 (vehicle movement due to traffic jams is almost absent), the prevailing majority of persons decide to cross the roadway on the restrictive signal. In these conditions, the number of persons who wait for safe roadway crossing, i.e. with abidance of traffic rules, decreases.

Dependence of the number of violations of the traffic rules by pedestrians ($N_{violations}$), i.e. crossing the roadway during restrictive signal, from roadway volume-capacity ratio (z) is non-linear and can be described by the quadratic equation:

$$N_{violations} = a \cdot z^2 + b \cdot z + c \text{ [person·h}^{-1}]$$

where:
a, b, c – coefficients of the power function.

Numerical values of coefficients are determined in the MATLAB software. Obtained results of the dependence of the number of violations the traffic rules by pedestrians from streets volume-capacity ratio for three types of intersections are given in Table 2.

Based on obtained dependencies for the second and third intersection types, we can confirm that the largest number of violators is observed with the duration of restrictive signal for pedestrians above 80 s – respectively about $N_{violations}$ is 90 and 50 person·h^{-1}. This phenomenon appears for several reasons. The first is that due to the long waiting time for permissive signal, pedestrians decide crossing the roadway in risk conditions because at the intersection three or four-phase traffic light cycle operates. The second

Y. Fornalchyk et al.

TABLE 2. Dependence of the number of violations of the traffic rules by pedestrians in the zone of signalized intersections operation

Duration of the restrictive signal of the pedestrian traffic light [s]	Formulas	R^2	Number of formula
Intersection type I			
20–40	$N_{\text{violations}} = 1\,341.3 \cdot z^2 - 1\,562.6 \cdot z + 527.55$	0.89	2
Intersection type II			
40–60	$N_{\text{violations}} = 135.64 \cdot z^2 - 160.43 \cdot z + 83.757$	0.78	3
60–80	$N_{\text{violations}} = 156.23 \cdot z^2 - 184.17 \cdot z + 95.505$	0.74	4
80–100	$N_{\text{violations}} = 257.28 \cdot z^2 - 290.76 \cdot z + 126.83$	0.71	5
100–120	$N_{\text{violations}} = 318.14 \cdot z^2 - 360.83 \cdot z + 154.7$	0.70	6
Intersection type III			
40–60	$N_{\text{violations}} = 175.21 \cdot z^2 - 183.32 \cdot z + 60.92$	0.79	7
60–80	$N_{\text{violations}} = 162.68 \cdot z^2 - 171.22 \cdot z + 62.09$	0.77	8
80–100	$N_{\text{violations}} = 148.25 \cdot z^2 - 146.81 \cdot z + 59.96$	0.74	9
100–120	$N_{\text{violations}} = 75.63 \cdot z^2 - 67.45 \cdot z + 49.01$	0.73	10

is that with the increase of the number of persons which crowded near traffic light object waiting for the permissive signal most frequently a situation appears when one of the pedestrians decide crossing the roadway on the restrictive signal and a group of other pedestrians follows after him.

Determination of rational control parameters

Based on the results of field research indicators of traffic and pedestrian flows, and road network parameters, the choice of rational control regimes is justified. The rational regime of traffic light control was determined by such indicators as a share of the restrictive signal on the lane in traffic light cycle for traffic flow (respectively, permissive for pedestrians), street volume-capacity ratio, and maximal queue length on the approach to the stop-line. Maximal queue length was determined to determine the potential impact of traffic flow delay on the adjacent intersections. We carried out the verification of correctness of listed indicators using the PTV Vissim software. Besides, we considered pedestrian behavior (number of violations the traffic rues by them) for three intersection types. With this aim, the model of a one--lane segment on the approach to the intersection (crosswalk) was created.

The research was carried out in the PTV Vissim software, where a one-lane roadway (3.75 m) was built with the length of 1,000 m, mixed traffic flow with the share of cars (for intersection type I – 70%; for II – 95%; for III – 80––85%) was created.

Primary data for traffic simulation were set, the intensity of vehicles in passenger car units changed from 50 to

700 pcu·h^{-1}. Lane capacity on the approach to the intersection was accepted 800 pcu·h^{-1}.

Traffic light object was created with one group of signals and the duration of the cycle was set 120 s with the structure red-green. The share of restrictive signal for traffic flow on the lane in the control cycle was determined by the equation – $\beta = t_g / T_c$ (the duration of restrictive signal changed from 10 to 105 s). Besides, normative restriction $25 \leq T_c$ 120 s was taken into account, and the value of the main time duration for transport was no less than $t_g \geq 7$ s. The transitional interval of the pedestrian phase did not change, as the geometric parameters of the roadway are constant.

To determine the maximal queue length of vehicles before stop-line in different traffic light control regimes, we simulated traffic and pedestrian flows at intersections of three types (types I, II, and III).

Changes of the maximal queue length of vehicles depending on street volume-capacity ratio before stop-line and the share of restrictive signal duration on the lane in the control cycle are given in Figure 2.

Interrelation between satisfactions of pedestrian needs, based on the criterion of minimal number of violations, and traffic flow condition (by the criterion of vehicle queue length), based on planning features of roadway and traffic light control indicators for each type of signalized intersections and crosswalks is given in Figure 2.

Share of pedestrians that cross the roadway on the restrictive signal of a traffic light for intersections type I increases with the increase of restrictive signal duration. It indicates the need for

adjustment of traffic light cycle duration near the places of a large generation of pedestrian flow. Besides, reduction of permissive signal duration for pedestrians reduces waiting time for traffic flow what, within the intensity above 500 pcu·h^{-1} by one lane, causes the formation of the vehicular queue by the length of more than 100 m with the restrictive signal 40 s (point A, Fig. 2).

As simulation results show of the change of maximal queue length of vehicles before stop-line for different intersection types (Fig. 2), its maximal value is observed for intersection type I (near transport junctions) – 504.56 m with roadway volume-capacity ratio – 0.88 and the share of the restrictive signal on the lane in control cycle – 0.83 (point B in Fig. 2). If in analogical traffic light control regimes to compare the values of maximal queue length for intersection type II (central zone) and type III (residential zone), then we can confirm that vehicular queue length reduces and is respectively 353.65 m (point C in Fig. 2) and 257.88 m (point D in Fig. 2).

Discussion

While choosing the rational regime of traffic light control, the necessary condition is considering psychophysiological and physical properties of people and forecasting their behavior.

Based on the results of experimental research (Fig. 1), simulation modeling (Fig. 2), and on the criterion of optimization of traffic flow delays, we developed recommendations about the choice of rational regimes of traffic light control

Intersection type I
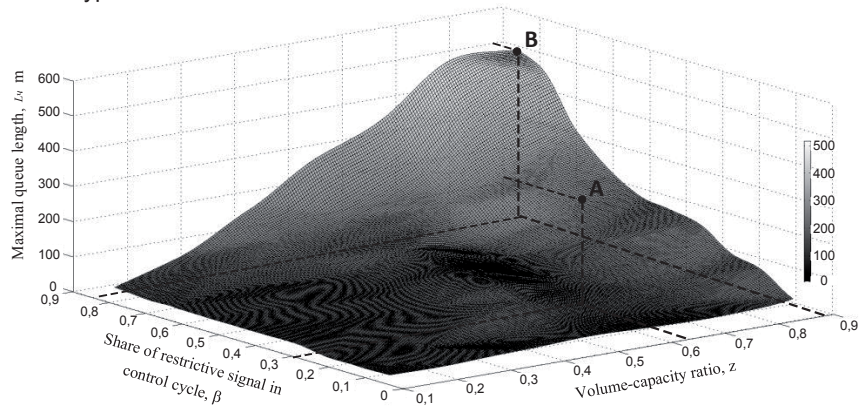
Intersection type II
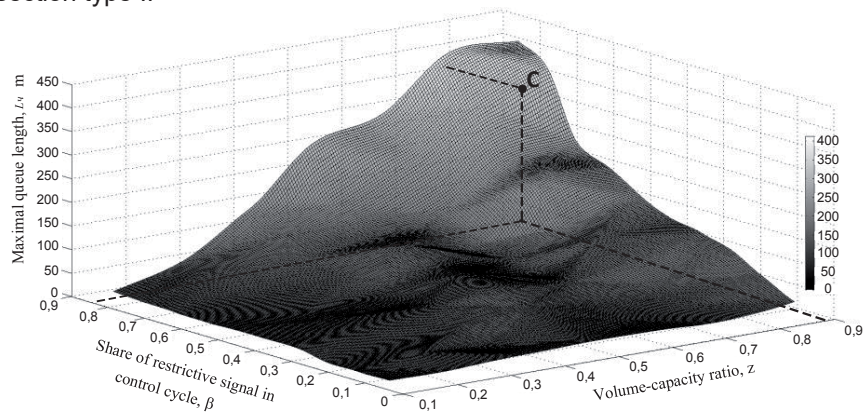
Intersection type III
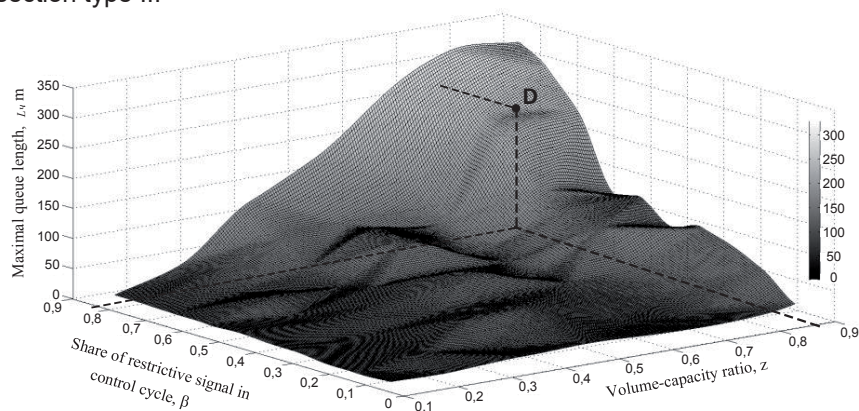
FIGURE 2. Changes of maximal queue length of vehicles depending on roadway volume-capacity ratio before stop-line and the share of restrictive signal duration on the lane in the control cycle

TABLE 3. Recommendations about the choice of rational regimes of traffic light control depending on traffic delay and pedestrian behavior

Street volume-capacity ratio (z)	Recommended duration of the restrictive signal of a traffic light for pedestrians [s]		
	intersection type I	intersection type II	intersection type III
Two phases			
z < 0.2	10–15	10–20	10–25
0.2 ≤ z < 0.45	10–20	10–30	10–30
0.45 ≤ z < 0.7	15–30	30–50	30–50
0.7 ≤ z < 1.0	25–30	45–55	50–65
Three phases			
z < 0.2	10–20	10–30	10–30
0.2 ≤ z < 0.45	15–25	20–45	25–50
0.45 ≤ z < 0.7	20–35	35–50	40–60
0.7 ≤ z < 1.0	35–40	40–65	60–90
Four phases			
z < 0.2	10–20	10–35	10–40
0.2 ≤ z < 0.45	20–30	25–50	40–75
0.45 ≤ z < 0.7	30–40	40–60	60–95
0.7 ≤ z < 1.0	40–50	60–90	75–110

(duration of restrictive signal for pedestrians) taking into account pedestrian behavior (Table 3).

Based on the data, given in Table 3, the least amount of violations of the traffic rules by pedestrians while crossing the roadway and the average vehicular queue length on one approach to the signalized intersection will be observed under the condition of limitation of the duration of restrictive signal for pedestrians:
– for two-phase control: intersection type I – to 30 s, type II – to 55 s, type III – to 65 s;
– for three-phase control: intersection type I – to 40 s, type II – to 65 s, type III – to 90 s;
– for four-phase control: intersection type I – to 50 s, type II – to 90 s, type III – to 110 s.

Such recommendations are advised to provide in current regulatory documents about the regulation of traffic light control implementation at the intersections of city streets and roads, as for today only minimal and maximal limitations of traffic light cycle duration operate, which are 25 s and 120 s respectively. It should be noted that principles of design of traffic and pedestrian phases are justified only by criteria of absence of conflict and limitations of minimal traffic intensity (to 120 pcu·h^{-1}) and pedestrian intensity (to 900 person·h^{-1}).

Conclusions

1. For signalized intersections with different conditions of traffic and pedestrian flows, it is established that these conditions depend on the location relative to the territory of the city. Considering this, intersections are grouped by movement peculiarities (traffic flow intensity and composition, the existence of centers of pedestrian flow generation) on three types: type I – near transport junctions; type II – central zone; type III – residential zone.

2. It is determined by results of experimental measurements that for different intersection types in existing movement conditions, the smallest number of violators among pedestrians with the duration of restrictive traffic light signal for pedestrians 40––60 s is by roadway volume-capacity ratio 0.50–0.65 for intersection type I; 0.40–0.65 for type II; 0.45–0.55 for type III.

3. By results of simulation results, it is determined for intersection type I that the largest vehicular queue is 504.56 m by roadway volume-capacity ratio 0.88 and the share of restrictive signal for traffic on the lane – 0.83. If at these traffic light control regimes, to compare the values of maximal queue length for intersection type II (central zone) and type III (residential zone), then queue length reduces and is about 353.65 m and 257.78 m respectively.

4. By results of experimental research and simulation of the passage signalized sections of city streets by traffic flow (using the PTV Vissim and the MATLAB software) considering the needs for pedestrian movement, and, taking into account the regularities of vehicular queue formation, it is established that limitation of restrictive signal for pedestrians, regardless of the number of control phases, should not be more than: on the sections of type I – 50 s; type II – 90 s; type III – 110 s. Such time limitations of traffic light control parameters meet the criteria of delay minimization for traffic flows and the least amount of violations the traffic rules by pedestrians.

References

Alhajyaseen, W.K.M., Nakamura, H. & Catbagan, J. (2008). A Proposed methodology for modeling pedestrian crossing time at signalized crosswalks considering bi-directional flow. *Proceedings of Infrastructure Planning*, *38*, 1-18.

Alhajyaseen, W.K.M & Nakamura, H. (2010). Quality of pedestrian flow and crosswalk width at signalized intersections. *IATSS Research*, *34*(1), 35-41.

Alhajyaseen, W.K.M. & Nakamura, H. (2012). Design criteria for crosswalk width and position at signalized intersections. *Journal of Civil Engineering and Architecture*, *6*(6), 844-857.

Gong, Q., Xiao, L. & Xu, M. (2019). Pedestrian violations crossing behavior at signal intersections: A case study in Anning District of Lanzhou. *IOP Conference Series: Materials Science and Engineering*, *688*(4), 044006. https://www.doi.org/10.1088/1757-899X/688/4/044006

Iryo-Asano, M. & Alhajyaseen, W. (2017). Consideration of a pedestrian speed change model in the pedestrian–vehicle safety assessment of signalized crosswalks. *Transportation Research Procedia*, *21*, 87-97.

Japan Society of Traffic Engineers [JSTE] (2006). *Manual of traffic signal control*. Tokyo: Japan Society of Traffic Engineers.

Levashev, A.G., Mykhailov, A.Yu., Holovnykh & I.M. (2007). *Proektyrovanye rehulyruemykh peresechenyi: ucheb. Posobye* [*Design of rendered intersections*]. Irkutsk: Izd-vo IrHTU.

Ma, Y., Lu, S. & Zhang, Y. (2020). Analysis on illegal crossing behavior of pedestrians at signalized intersections based on Bayesian network. *Journal of Advanced Transportation*, 2675197. https://doi.org/10.1155/2020/2675197

Polishchuk, V.P. & Bakulich, O.O. (ed.) (2012). *Orhanizatsiia ta rehuliuvannia dorozhnoho rukhu: pidruchnyk* [*Traffic organization and management*]. Kyiv: Znannia Ukrainy.

Transportation Research Board [TRB] (2000). *Highway Capacity Manual*. Washington, DC: TRB.

Vasylieva, H.Yu. (2007). *Metody minimizatsii zatrymok transportu na mahistralnii vulychno-dorozhnii merezhi mist Ukrainy* [*Methods of minimization of transport delays on road network of cities of Ukraine*]. Kyiv: KNUBA.

Vrubel, Yu.A. (2003). *Potery v dorozhnom dvyzhenyy* [*Traffic losses*]. Minsk: BNTU.

Wang, Z., Zhao, L., Cao, N., Lu, Y. & Chen, M. (2017). A modified total crossing time model of bidirectional pedestrians at signalized crosswalks. *Discrete Dynamics in Nature and Society*, *1*, 2190724. https://doi.org/10.1155/2017/2190724

Xiong, H., Xiong, L., Deng, X. & Wang, W. (2014). Evaluation of the impact of pedestrian countdown signals on crossing behavior. *Advances in Mechanical Engineering*, *6*, 518295. https://doi.org/10.1155/2014/518295

Zhyvohliadov, V.G. (2012). *Teoryia dvyzhenyia transportnykh y peshekhodnykh potokov*. Rostov na Donu: Izdatelstvo zhurnala.

Summary

Choice of the rational regimes of traffic light control for traffic and pedestrian flows. The method for the choice of rational regimes of traffic light control is developed based on the minimization of the number of violations the requirements of traffic light signals by pedestrians depending on the volume-capacity ratio of traffic lanes and control of vehicular queue on the approach to the stop-line. Assessment of rationality is carried out considering the simultaneous impact of such factors as roadway volume-capacity ratio, traffic light restrictive signal duration, the number of violations of the traffic rules by pedestrians, and maximal queue length of vehicles. The model of the change of the number of violations of the rules of crossing the roadway by pedestrians depending on the volume-capacity ratio of different intersection types is developed in this paper. The model of determining the maximal vehicular queue length before intersections depending on the volume-capacity ratio and the share of the restrictive signal on the lane in the control cycle is developed. Recommendations about the choice of rational regimes of traffic light control depending on traffic delay, planning parameters of the road network, and pedestrian behavior are proposed.

Authors' address:
Yevhen Fornalchyk
(https://orcid.org/0000-0003-4137-0625)
Oleh Hrytsun
(https://orcid.org/0000-0001-8391-9642)
Yuriy Royko
(https://orcid.org/0000-0003-0055-9413)
Lviv Polytechnic National University
Department of Transport Technologies
st. Stepan Bandera 12, 79000 Lviv
Ukraine
e-mail: yevgen.fornaltchyk@gmail.com
        oleggrutsyn1993@gmail.com
        jurij.rojko@gmail.com

Ivan Kernytskyy
(https://orcid.org/0000-0001-6084-1774)
Szkoła Główna Gospodarstwa Wiejskiego
w Warszawie
Instytut Inżynierii Lądowej
ul. Nowoursynowska 159, 02-776 Warszawa
Poland
e-mail: ivan_kernytskyy@sggw.edu.pl

Bulat Zh. UNAIBAYEV[1], Bulat B. UNAIBAYEV[2], Violetta ANDREYACHSHENKO[1]

[1]Ekibastuz technical and engineering institute named after the academician K. Satpayev, Faculty of Engineering and Economics
[2]Karaganda Technical University, Faculty of Architecture and Construction

Cast-in-situ piles encasements based on oil-bituminous rocks (kirs) in saline soils

Key words: corrosion, foundation, protective shell (encasement), mastic

Introduction

The SN RK 2.01-01-2013 standard (Komitet tekhnicheskogo regulirovaniya i metrologii Ministerstva torgovli i integratsii Respubliki Kazakhstan [KTRM MIR RK], 2013) regulate anti-corrosion protection of piles in aggressive soils with optimally viscous and maintaining continuity materials (bitumen, polymer materials, petrolatum, fuel oil). The use of these recommendations is hampered by the inevitable decreasing of the bearing capacity of the pile along its lateral surface when arranging the coating. So, for example, when coating with bitumen piles immersed to the depth of 13.3–22.7 m, their bearing capacity decreases from 30 to 80% de-pending on fluctuations in soil and the air temperature. In addition, over time, bitumen so-called aging is observed, which is accompanied by delamination, crumbling and loss of the coating water-proofing (Ongarbayev, Imanbayev, Ti-leuberdi, Krivtsov & Golovko, 2019).

The specifics of manufacturing cast--in-situ and bored pile foundations using traditional technologies makes it diffi-cult to solve the issues of their anti-cor-rosion protection, because in the course of arranging it is difficult to maintain the continuity of the coating and concrete of the structure or sufficient density of concrete and the integrity of the film pro-tection along the barrel of the cast-in-situ bored pile.

The construction of buildings and structures (BS) on territories composed of saline silty-clayey soils (SSCS) (Iman-bayev et al., 2017; Tileuberdi, Akkazyn, Ongarbayev, Imanbayev & Mansurov,

2018), in accordance with the current regulatory and legislative framework, is accompanied by inevitable increasing the costs by 5–25%, which are dictated by the danger of SSCS manifestation and the absence of reliable and effective constructive-technological solutions (CTS) within the framework of construction and operation of the geotechnical system "base–foundation–structure" (BFS) in changing conditions under the impact of natural and man-made factors. Consequently, construction and operation of the gas station on SSCS is not provided with a proper quality. This is confirmed by the numerous emergency subsidence of BS on SSCS in the cities of Yerevan, Volgodonsk, Novy Uzen, Zhezkazgan, Balkhash, Karaganda, etc. The expenses for restoration, repair and reinforcement of emergency facilities are often 1.5–2 times higher than the initial estimated cost of construction.

To increase the bearing capacity and durability of the pile foundation in SSCS, there were developed a number of new geotechnologies based on combining well-known but fundamentally different approaches to solving the problem (Fig. 1), namely:

– formation of a protective and supporting shell (encasement) around the pile (Zaharov, 1999; Unaibayev & Zhussupbekova, 2001; Unaibayev, Arsenin & Unbayev, 2018; Unaibayev & Unbayev, 2018);
– compaction or consolidation of saline soil around the pile in order to increase its strength and deformation characteristics, structural and suffusion resistance, water resistance, etc. (Gimmerling, 1986; Komitet po delam stroitel'stva, zhilishchno-kommunal'nogo khozyaystva i upravleniya zemel'nymi resursami Ministerstva national'noy ekonomiki Respubliki Kazakhstan [KDSiZhKKh MNE RK], 2011);
– increasing the density and corrosion resistance of the pile structure concrete by means of using modified additives in concrete, etc. (Gavshin & Dzektser, 1982; Unaibayev & Unbayev, 2019).

The proposed CTS, in addition to increasing the bearing capacity and corrosion resistance of the pile foundation on SSCS, are also relatively economical solutions, since they suggest the use of substandard materials (kirs, natural bitumen, fly ash, etc.).
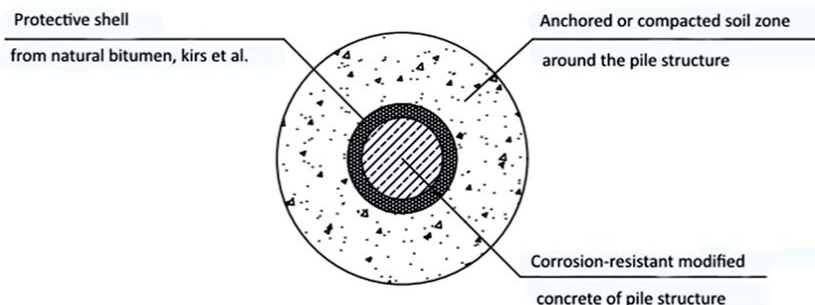
FIGURE 1. Working hypothesis for solving the problem of increasing the bearing capacity and durability of the pile in SSCS

Methods

It seems efficient to arrange a protective and load-bearing shell for cast-in-situ piles in punched and drilled wells and foundations in rammed pits (Figs. 2 and 3). So when driving a well or foundation pit by periodically dropping the dredge, in contrast to drilling a well with an auger, soil compaction is observed around the structure. Compaction leads to improving the physical and mechanical properties of the soil, and consequently to increasing the bearing capacity of the foundation. In this case, water permeability of the compacted soil layer around the structure, depending on the type of compacted soil, decreases tens and hundreds times.

It should be noted that when arranging a bored pile, soil compaction around the structure does not occur; at best, its natural structure is preserved, and at worst, if the technology is violated, the filtration and mechanical properties of the soil around the pile deteriorate, because during "dry" drilling or construction widening, loosened soil crumbles into the well face. In this case, in the well face and therefore, under the bored pile a highly compressible soil layer with increased permeability is formed, which leads to decreasing the bearing capacity of the foundation. It seems efficient the proposed formation of a protective shell of the foundation in the rammed foundation pit and a punched hole by additional ramming into the walls and base of the punched hole or foundation pit of waterproof and corrosion-resistant materials (kirs) or applying heated natural bitumen to their surface by spraying for additional protection of the structure
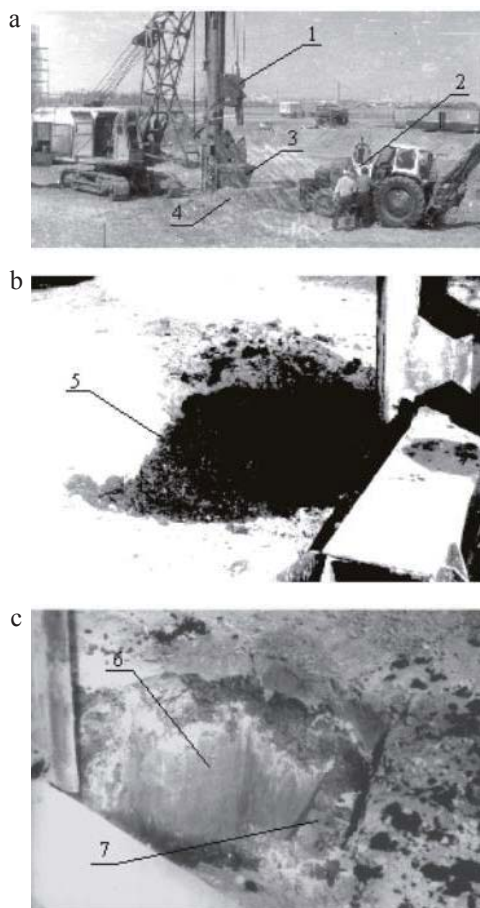
1 – OVK-2 equipment in combination with EO--2621; 2 – loader based on MTZ-80; 3 – rammer; 4 – crushed stone; 5 – kirs; 6 – rammed foundation pit; 7 – the protective shell made of kirs

FIGURE 2. Fragment of testing the technology of arranging a foundation structure with a protective and supporting shell made of kirs in SSCS of the Kulsary urban-type settlement, microdistrict 3: a – general view of the work production; b – filling the rammed pit with kirs; c – a type of the protective shell

from corrosion (Figs. 2 and 3). In this case, after placing and shaping the concrete, the protective coating turns out to be hermetically packed between the reinforced concrete monolithic foundation
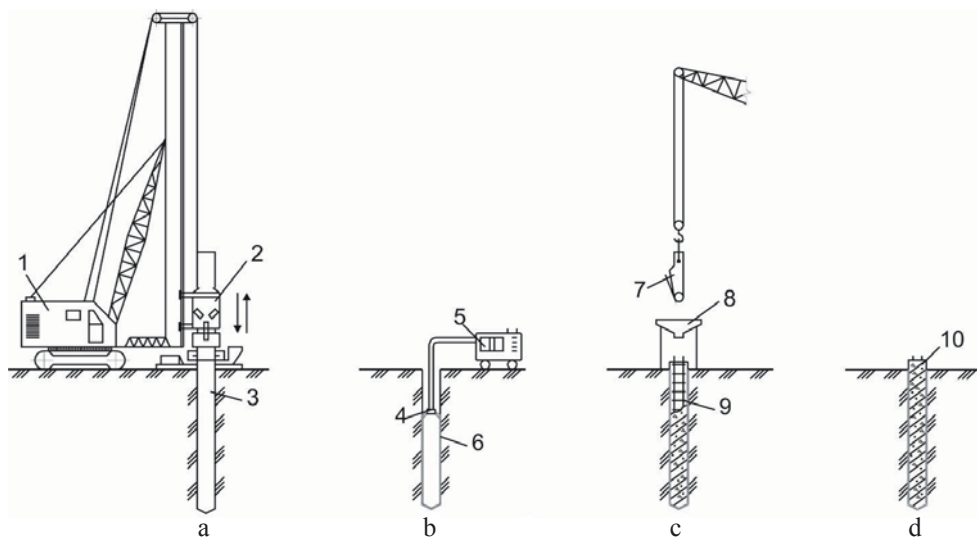
1 – pile driver; 2 – tip; 3 – dredge; 4 – nozzle; 5 – unit for applying bitumen mastic; 6 – protective shell; 7 – vibratory tub; 8 – receiving funnel; 9 – reinforcing cage; 10 – pile

FIGURE 3. Technological diagram of the arranging cast-in-situ piles in drilled wells with the use of a protective shell made of natural bitumen to the well walls: a – immersion and extraction of the dredge; b – applying natural bitumen mastic to the borehole walls; c – reinforcing and concreting the well; d – finished pile

structure and the dense waterproof layer of soil around it compacted by ramming. The latter contributes to the continuity, long-term preservation and durability of the protective coating and consequently, durability and corrosion resistance of the concrete foundation structure.

Protection of a pile foundation structure in contact with an aggressive water-salt soil environment (AWSSE) in the base made of SSCS, by using for this purpose various corrosion-resistant coatings and materials made on the basis of substandard oil-bituminous rocks and natural bitumen extracted from it, significantly reduces the material consumption. The use of natural bitumen as a coating, which in comparison with industrial bitumen has a higher chemical resistance, adhesion value, low cost

and non-scarcity, as well as good adhesion, penetrating ability, etc., can significantly increase the structure durability (Mahsimov, 1986). The technology of extracting bitumen from kirs and technical specifications for the use of kirs for construction purposes were tested by us in industrial conditions and proved to be positive (Ahmetov & Zhurikov, 1988).

Experiments on the extraction of natural bitumen from kirs for construction purposes were carried out with oil-bituminous rocks: kirs from the Munayly-Mola field of the Atyrau region in Kazakhstan with the organic content of 14–22%. The mineral part of the kirs is mainly represented by fine-grained sand with the fraction of 0.1–0.25 mm. The initial raw materials (kirs) were ground in an aqueous medium, and the concen-

tration of the pulp with modifiers and flotation of the organic component was carried out at an elevated temperature. Grinding the feedstock was carried out by mixing the pulp in a Na_2CO_3 solution at an elevated temperature.

In contrast to the traditional technologies of grinding kirs based on impact, compression, rupture or cutting, there was used the ability of kirs in aqueous salt solutions to self-grind or disintegrate into small pieces at elevated temperatures. This process is especially intense with stirring in aqueous solutions of salts. The experiment has shown that in solutions the self-grinding of kirs proceeds 5–6 times more intensely than in water, and the grinding speed increases with the increased concentration.

The process is carried out as follows. Oil-bituminous rock and Na_2CO_3 are loaded into the pneumo-mechanical laboratory flotation machine with the chamber capacity of 1.0 l, filled with water in the required proportions at an appropriate temperature and mixed within 20––30 min; the organic component of kirs (natural bitumen) is floated. The process is controlled by the organic matter content in the sands (tailings) and in the organic component (bitumen concentrate), which is determined by the combustion method after drying the samples at the constant temperature of 85°C.

The resulting natural bitumen was used to prepare a bitumen emulsion paste. Mastics are a mixture of bitumen emulsion pastes with mineral powdered fillers and various additives. Thus, a bitumen paste serves as the main component of the protective composition manufactured at the factory. The mastic itself is prepared at the construction site immediately before its application.

Bitumen emulsion pastes consist of the main organic binder, natural bitumen, an emulsifier, a finely dispersed mineral powder and various additives to water as a dispersed medium in which natural bitumen is dispersed. To prepare a bitumen paste, a laboratory paddle mixer is used.

At first, the emulsifier suspension heated to 80–90°C is loaded into the paste-mixer, and then natural bitumen and water are alternately fed: at first natural bitumen until the mixture thickens, and then water to liquefy it, and so gradually there is introduced the estimated amount of bitumen and water. Bitumen should be evaporated or dehydrated, cleaned of dirt and debris and heated to the operating temperature of 150–160°C. Quicklime, screening from the Temirtau Electrometallurgical Plant and carbide powder lime, waste of the same plant were used as emulsifiers. Before use, the quicklime lump was slaked into powder lime.

The compositions of bitumen pastes based on this lime do not meet the requirements to bitumen pastes for waterproofing purposes, namely, the pastes are not stable and quickly exfoliate, there is no complete emulsification of bitumen. In lump quicklime there are many impurities in the form of unquenched grains, clay inclusions, etc. To obtain high-quality bituminous pastes based on such lime, additional processing of lime is needed, increasing its dispersion by additional grinding, vibration grinding, or introducing additives of highly plastic clays. All these activities require additional costs, so we refused working with this emulsifier. Another emulsifier

used in the work was carbide fluff lime, waste of the Temirtau Electrometallurgical Plant JSC.

When selecting the compositions of bitumen pastes based on natural bitumen, the known paste compositions that are widely used in practice were taken as the base. Since we used waste as an emulsifier, we had to adjust the compositions of bitumen pastes. The results of this work are shown in Table 1.

Table 1 shows that the most high-quality bitumen paste based on natural bitumen is composition number 7. Since the paste of composition number 7 is stable, homogeneous, does not delaminate. Carbide powder lime is the waste that has some impurities, the activity of lime does not exceed 70% therefore, to obtain a stable paste and to increase the bitumen content in the paste, the emulsifier is taken in a larger amount than is needed theoretically.

In the future, the optimal composition of the paste will be marked as follows: BL-42 (bitumen–lime paste with the 42% content of natural bitumen.

BL-42 lime–bitumen paste has the following characteristics:
– cone mobility according to Stroy-CNIL – 13–15 cm;
– the paste density – 1.42 g·cm^{-3};
– the ability to dilute with water – 10 times the amount;
– water absorption of dried paste – 5–7%;
– swelling of the dried paste by volume – 3–5% by weight.

Cold bitumen mastics prepared by mixing bitumen paste with fillers are recommended for applying to the surface of punched and drilled wells for piles, coating strip prefabricated foundations and grillage on pile heads. Lime powder was used as fillers, fly ash of KarGRES-1, Portland cement M-400.

The method of selecting the compositions of cold asphalt mastics was as follows. First, the composition of the bitumen paste was selected, on which base the mastic was prepared. The finished mastic in the liquid and solidified form was tested according to the known technique.

TABLE 1. Characteristics of the bitumen pastes compositions based on natural bitumen

Composition	Natural bitument [%]	Powder lime [%]	Water [%]	Note
1	45	12	43	Water separation 1 h after preparation
2	48	15	37	Delamination of the paste, not all bitumen has been emulsified
3	50	16	34	Coagulation of bitumen has occurred
4	48	18	34	Partial delamination
5	40	20	40	Water separation
6	35	25	40	Water separation
7	42	24	34	The paste is stable, homogeneous, does not delaminate
8	40	25	35	Partial delamination

B.Zh. Unaibayev, B.B. Unaibayev, V. Andreyachshenko

In the liquid state cold asphalt mastics are tested like bituminous pastes: their density, cone mobility according to the StroyCNIL, and heterogeneity are determined. However, when selecting the composition of the mastic, it is necessary to test them additionally for stability during storage. In the plastic state for cold asphalt mastics the bulk density, porosity, water absorption and swelling are determined. In addition, when selecting the composition of the mastic, the samples dried to constant weight at 40°C within 5 days were subjected to all the above tests.

For these samples, water resistance is determined when they are kept in water within 30 days. Finally, by monitoring the composition of the cold asphalt mastic coating, its moisture and bitumen content are determined.

The bulk density of cold asphalt mastics is determined on samples 5×5 cm in size and 1–1.5 cm thick by weighing in air and water.

Determining the bulk density is the main method of the laboratory quality control of the finished coatings, mastic composition and coating density. Water absorption of cold asphalt mastic samples is determined in the accelerated way by saturating them with water during evacuation or keeping the samples in water within 15 days with the constant increasing of the water level within the first three days by one third of the sample per day.

Water resistance of mastics is determined only by a control test when selecting the composition of the mastic. The tests are carried out on standard instruments for determining water resistance of concrete. On the basis of the obtained BL-42 lime–bitumen paste, the compositions of mastics with various types of fillers were selected.

The already known compositions of waterproofing mastics were taken as a base. Mastics based on lime–bitumen paste and II-20 lime filler have a dense structure after drying and stabilization. Testing the mastics has shown that their properties are not inferior to the mastics already used in construction practice.

To increase mechanical strength of the mastic, Portland cement M-400 and fly ash were introduced into its composition. The compositions of mastics IIC-20, IZ-20, IZC-20, IIC-25 were obtained.

Stabilization of mastics with Portland cement occurs faster due to the reaction of cement hydration with water that is a part of the bitumen paste. Indeed, these mastics with two binders, organic and hydraulic, are characterized by increased strength and elastic brittle properties.

Results and discussion

The results of experiments on extraction of natural bitumen from kirs indicate that in an aqueous medium without the addition of Na_2CO_3, the oil-bituminous rock separation into organic and mineral components is low in terms of the quality of the product being reduced. The optimal technological parameters were obtained experimentally and are as follows: the concentration of Na_2CO_3 is 7––10 g·l^{-1}, the stirring time is 20–30 min, the temperature with stirring is 80–85°C, the flotation time is 5 min. The ratio of solid to liquid is 1 : 20. It is undesirable to increase the time for more than 30 min, since the indicators of the qual-

ity of the extracted product do not improve, and increasing the time leads to decreasing the productivity of the process as a whole.

The improved protective properties of cold bitumen compositions based on natural bitumen extracted by the proposed method, when compared with compositions based on industrial bitumen, are explained by the fact that no paraffin was found in these bitumen, which is known to reduce the adhesion properties of the protective coating.

Due to the fact that bitumen mastics are the simplest and most effective traditional means of protecting reinforced concrete structures against corrosion in soils, one of the cold asphalt mastics proposed is a mixture of bitumen mastic based on natural bitumen with mineral powder fillers. Cold asphalt mastics fundamentally differ in their properties from traditional hot asphalts in that after preparing they have increased water absorption compared to the original bitumen or hot asphalt mastics. Long-term tests of bitumen mastics based on natural bitumen indicate that in these mastics the process of water absorption gradually fades over time, and after two to three years of operation these mastics become more waterproof than traditional mastics based on industrial bitumen.

Cold asphalt mastics based on natural bitumen due to good waterproofing properties, such as resistance to water, heat, frost, weather and corrosion, as well as sufficiently high strength under static and dynamic loads, reliable adhesion to concrete can be recommended for anticorrosive protection of concrete, building structures in the conditions of SSCS leaching, marine, sulfate, magnesian, carbonic and alkaline aggressiveness of water-environment, as well as for anti-corrosion protection of overhead metal structures.

The compositions of the obtained cold asphalt mastics and their main characteristics are shown in Table 2. The compositions of cold mastics were selected by the method of mathematical planning of the experiment.

Waterproofing coatings made of mastic based on natural bitumen were tested, applied by spraying onto the walls of drilled wells and rammed pits (Fig. 1) as the secondary protection of cast-in-situ piles in punched and drilled wells and foundations in rammed pits from the aggressive effects of saline soils and saline waters in Atyrau and Kulsary urban-type settlement.

The following composition of cold bitumen mastic is recommended, in percentage by weight:
– natural bitumen – 40%;
– powder lime – 12%;
– asbestos, VI–VII grade – 8%;
– solar (diesel) – 40%.

The efficiency of the developed CTSs is confirmed by technical and economic calculations and experimental and industrial testing. However, the main criterion that determines the efficiency of the proposed CTSs is reducing the subsequent operating costs. Post-construction subsidence of BSs on traditional prefabricated strip foundations and driven piles without a protective shell exceed the subsidence of similar buildings on foundations and piles with a protective shell. This is due to the fact that BSs on strip foundations are not protected from suffusion and deformation processes and therefore, during operation, they require

---

B.Zh. Unaibayev, B.B. Unaibayev, V. Andreyachshenko

TABLE 2. Compositions of cold asphalt mastics (based on natural bitumen extracted from kirs) and their main characteristics

Mastic type	Mastic composition in percent by weight	Density [g·cm^{-3}]	Residual moisture [%]	Water absorption [%]	Swelling [%]
II-20	Lime–bitumen paste BI-42 – 80 Limestone powder – 20	1.38	7.0	6.0	0.5
IIC-20	Lime–bitumen paste BI-42 – 70 Limestone powder – 20 Portland cement M400 – 10	1.4	5.0	3.3	1.1
IZ-20	Lime–bitumen paste BI-42 – 80 Fly ash – 20	1.1	4.0	10.0	2.5
IZC-20	Lime–bitumen paste BI-42 – 75 Fly ash – 15 Portland cement M400 – 10 Water (over 100%) – 5	1.3	6.0	8.0	0.6
IIC-25	Lime–bitumen paste BI-42 – 55 Limestone powder – 20 Portland cement M400 – 25 Water (over 100%) – 5	1.5	7.0	5.0	0.5

annual post-construction repairs. When using foundations and piles in punched and drilled wells with a protective and bearing shell, BSs do not practically undergo post-construction subsidence. This is evidenced by many years of experience in construction and operation of BSs on foundations and piles with a protective and load-bearing shell in Karaganda, Atyrau, Aktobe, Temirtau, Kulsary urban-type settlement, Tengiz and others.

The proposed list of technologically advanced (Figs. 1, 2 and 3) that have passed approbation in the industrial conditions allows reliable and efficient erecting BSs in the territories formed by SSCS.

Conclusions

1. A comprehensive technology of arranging foundations and piles in drilled wells in SSCS with a protective and bearing shell based on natural bitumen-containing materials has been proposed, which makes it possible to increase the durability and bearing capacity of the foundation structure.

2. A method of extracting natural bitumen from kirs has been developed. The use of this method makes it possible to exclude the difficult operation of mechanical grinding the feedstock, which is expensive and energy-intense, as well as to reduce the reagents consumption and to improve the quality of the extracted natural bitumen. The copyright, the novelty and efficiency of the technology are confirmed by A.C. No 16867550 dated 24 November 1988.

3. The compositions of cold mastics based on natural bitumen with the addition of industrial waste have been developed. The compositions of the obtained mastics based on natural bitumen are not inferior in their properties to the known

compositions of waterproofing cold mastics based on industrial bitumen, and the use of waste reduces their cost.

References

Ahmetov, K.N. & Zhurikov, K. (1988). *Sposob izvlecheniya organicheskoy sostavlyayushchey neftebituminoznykh porod flotatsiyey* [*A method of extracting the organic component of oil-bituminous rocks by flotation*]. USSR Copyright Certificate No 16867550 [transl. from Russian].

Gavshin, Z.P. & Dzektser, Ye.S. (1982). *Usloviya podtopleniya gruntovymi vodami zastrayevayemykh territoriy* [*Conditions for underflooding of built-up areas by groundwater*]. Moskva: Stroyizdat [transl. from Russian].

Gimmerling, V.O. (1986). *Opredeleniye nesushchey sposobnosti buronabivnykh svay v zagipsovannykh glinistykh gruntakh pri vyshchelachivanii soley iz osnovaniya* [*Determination of the bearing capacity of bored piles in gypsum clay soils with leaching of salts from the base*]. Moskva [transl. from Russian].

Imanbayev, Y.I., Ongarbayev, Y.K., Tileuberdi, Y., Mansurov, Z.A., Golovko, A.K. & Rudyk, S. (2017). Supercritical solvent extraction of oil sand bitumen. *AIP Conference Proceedings*, *1879*(1), 050003. https://doi.org/10.1063/1.5000473

Komitet po delam stroitel'stva, zhilishchno-kommunal'nogo khozyaystva i upravleniya zemel'nymi resursami Ministerstva national'noy ekonomiki Respubliki Kazakhstan [KDSiZhKKh MNE RK] (2011). *Proyektirocvaniye zdaniy na zasolennykh gruntakh* [*Designing of buildings at saline soils*] (NTP RK 07-01.1-2011). Astana: Komitet po delam stroitel'stva, zhilishchno-kommunal'nogo khozyaystva i upravleniya zemel'nymi resursami Ministerstva national'noy ekonomiki Respubliki Kazakhstan [transl. from Russian].

Komitet tekhnicheskogo regulirovaniya i metrologii Ministerstva torgovli i integratsii Respubliki Kazakhstan [KTRM MIR RK] (2013). *Zashchyta stroytel'nykh konstruktsyy ot korrozyy* [*Construction structures corrosion protection*] (SN RK 2.01-01-2013). Nur-Sultan: Komitet tekhnicheskogo regulirovaniya i metrologii Ministerstva torgovli i integratsii Respubliki Kazakhstan [transl. from Russian].

Mahsimov, K.N. (1986). *Eksperimental'no-teoreticheskiye issledovaniya raboty korotkikh zabivnykh svay v zasolennykh gruntakh* [*Experimental and theoretical studies of the work of short driven piles in saline soils*]. Kyiv [transl. from Russian].

Ongarbayev, Y.K., Imanbayev, Y., Tileuberdi, Y., Krivtsov, E.B. & Golovko, A.K. (2019). Thermal cracking of natural bitumen in presence of activating additives. *Journal of Chemical Technology and Metallurgy*, *54*(3), 564-570.

Tileuberdi, Y., Akkazyn, Y.A., Ongarbayev, Y.K., Imanbayev, Y.I., Mansurov, Z.A. (2018). Production of petroleum bitumen by oxidation of heavy oil residue with sulphur. *IOP Conference Series: Materials Science and Engineering*, *323*(1), 012004. https://www.doi.org/10.1088/1757-899X/323/1/012004

Unaibayev, B.Zh., Arsenin, V.A. & Unaibayev, B.B. (2018). *Svai v zasolennykh gruntakh* [*Piles in saline soils of Kazakhstan*]. Almaty: Evero [transl. from Russian].

Unaibayev, B.Zh. & Unaibayev, B.B. (2018). *Fundamentostroyeniye na zasolennykh gruntakh (Teoriyai praktika)* [*Fundamentals on saline soils (Theory and practice)*]. Almaty: TechSmith [transl. from Russian].

Unaibayev, B.Zh. & Unaibayev, B.B. (2019). *Deshevyy dom dlya molodoy sem'i* [*Cheap home for a young family*]. Pavlodar: Pavlodarskiy Gosudarstvennyy Universitet Imeni S. Toraygyrova [transl. from Russian].

Unaibayev, B.B. & Zhussupbekova, A.Zh. (2001). *Rekomendatsii po proyektirovaniyu i ustroystvu nabivnykh svay s zashchitnoy obolochkoy v probitykh skvazhinakh* [*Recommendations for the design and installation of jacketed piles in drilled wells*]. Astana: Kazakhskiy Geotekhnicheskiy institut Izyskaniy [transl. from Russian].

Zaharov, N.I. (1999). *Fundamenty na prosadochnom osnovanii* [*Foundations on a subsidence basis*]. Ust'-Kamenogorsk: Vostochno-Kaza-

khstanskiy gosudarstvennyy tekhnicheskiy universitet imeni Dauleta Serikbayeva [transl. from Russian].

Summary

Cast-in-situ piles encasements based on oil-bituminous rocks (kirs) in saline soils. A technology of building a pile foundation in saline soils with a protective and load-bearing shell based on bituminous rocks (kirs) is proposed that makes it possible to eliminate water permeability, to increase suffusion resistance and bearing capacity of the soil, as well as durability. The method of extracting natural bitumen from bituminous rocks (kirs) is based on the ability of kirs to self-grind or disintegrate into small parts at elevated temperatures in aqueous salt solutions. The proposed method excludes mechanical grinding and allows reducing the consumption of reagents and improving the quality of extracted natural bitumen. The compositions of the obtained mastics based on natural bitumen are not inferior in their properties to the known compositions of waterproofing cold mastics based on industrial bitumen at a lower cost.

Authors' address:
Bulat Zh. Unaibayev
(https://orcid.org/0000-0002-4186-0010)
Ekibastuz technical and engineering institute named after the academician K. Satpayev
Faculty of Engineering and Economics
Department of "Construction"
54A Energetikov Street, 141200 Ekibastuz
Kazakhstan
e-mail: Ubks@mail.ru

Bulat B. Unaibayev
(https://orcid.org/0000-0002-1593-2842)
Karaganda Technical University
Faculty of Architecture and Construction
Department of "Building materials
and technologies"
56 Bulvar Mira, 100027 Karaganda
Kazakhstan
e-mail: U-danicbks@mail.ru

Violetta A. Andreyachshenko – corresponding author
(https://orcid.org/0000-0001-6933-8163)
Ekibastuz technical and engineering institute named after the academician K. Satpayev
Faculty of Engineering and Economics
Department of "Metallurgy and natural science disciplines"
54A Energetikov Street, 141200 Ekibastuz
Kazakhstan
e-mail: Vi-ta.z@mail.ru

Hassnen JAFER[1], Ibtehaj JAWAD[1], Zaid MAJEED[1], Ali SHUBBAR[2]
[1]University of Babylon, College of Engineering
[2]Liverpool John Moores University, Department of Civil Engineering

The development of an ecofriendly binder containing high volume of cement replacement by incorporating two by-product materials for the use in soil stabilization

Key words: soil stabilization, eco-friendly binder, ordinary Portland cement, ground granulated blast furnace slag, cement kiln dust, cement replacement

Introduction

The use of cement, in the treatment of weak soils, induces chemical reactions that improve the geomechical properties of the treated soils significantly. Hence it has been widely used for soil stabilization. It can be utilized for the stabilization of any type of soil apart from those with pH values less that 5.3 or organic contents of more than 2% (Saride, Puppala & Chikyala, 2013; Ma, Chen & Chen, 2016). The demand for ordinary Portland cement (OPC) is increasing on a daily bases because of the industrialization and urbanization. Consequently, the cement industry has grown significantly in recent years. It

has been reported by van Ruijven et al. (2016) that the global cement production is predicted to grow annually by 5%. However, the OPC manufacturing have several environmental issues particularly the carbon dioxide (CO_2) emission and intensive energy consumption (Jafer, Atherton, Sadique, Ruddock & Loffill, 2018a).

Worldwide nowadays, the global warming as well as the climate changes represent a major concern to the mankind. These phenomenon are related to the green-house gases produced by different sectors of industry which their increased emissions adversely impacting the environment. The carbon dioxide represents one of the main gases contributing to the harmful gasses, being normally emitted by the process of incineration from various industrial factories (Hermawan, Marzuki, Abduh & Driejana, 2015). Meanwhile, the manufacturing of cement is a major sector of industry contributing

to the emission of carbon dioxide, with a global CO_2 emission of 7–9% (Zainab, Zainab, Jafer, Dulaimi & Atherton, 2018). Hence, to minimize the environmental influences of cement, researches have investigated the possibilities of utilizing new materials as alternative to cement. These materials substitute cement partially or totally to make binders used in various construction sectors such as mortars, concrete and soil stabilization (Jafer, Atherton, Ruddock & Loffill, 2017; Jafer, Atherton, Sadique, Ruddock & Loffill, 2018b; Majdi et al., 2020).

Supplementary cementitous materials (SCMs) are the named given to these materials that are wastes or by-products incorporated partially as cement substituents. Supplementary cementitous materials have been utilized since approximate 300 years before century in Roma when volcanic ash was incorporated with lime in building roads (Aïtcin, 2016). Supplementary cementitous materials either induce pozzolanic activity due to having a significant amount of silica such as palm oil fly ash (POFA), rice husk ash (RHA), and fly ash (FA) (Aprianti, 2017), or possess considerable contents of calcium oxide to work like cement while being blended with water such as ground granulated blast furnace slag (GGBFS), sewage sludge ash (SSA) and cement kiln dust (CKD) (Majdi et al., 2020).

Ground granulated blast furnace slag (GGBFS) is a by-product produced from the manufacturing processes of iron industry. In terms of the chemical compositions, GGBFS has chemical oxides such as lime, aluminates and silicates similar to those available in the Portland cement but in different proportions (Oner & Akyuz, 2007). It was reported that most of mineral phases of GGBFS are in the glass phases making them easy to react with water during the hydration process (Zhao, Wang, Yan, Zhao & Zhang, 2016). Despite of that GGBFS was highly utilized in soil stabilization. It was confirmed by previous research that GGBFS in its own have low cementitous reactivity. Hence, lime or OPC are mixed with GGBFS in order to accelerate the hydration of GGBFS via activation that involves supplying enough alkalinity (Higgins, 2005).

Cement kiln dust (CKD) is produced as a by-product during cement manufacturing retrained in the incineration gasses transferred via the kiln. The chemical composition of CKD consists primary of non-calcined and calcined raw and feed materials used in the processes of cement manufacturing in addition to fine clinker and rich alkali compositions (Kunal, Siddique & Rajor, 2014). In spite of the fact that the CKD resulted from cement industry has been lowered subs-considered due to the utilization of new advanced methods in cement manufacture, the discard of CKD is a considerable issues in term of environmental and economic aspects in cement industry (Wild, Kinuthia, Robinson & Humphreys, 1996).

Based on the literatures, there is a limited number of researches investigated the effect of cement replacement using binary blending of GGBFS and CKD on the performance of the produced binders, particularly for the use in fine grained soil stabilization. In this research, GGBFS and CKD were incorporated as replacements to the conventional binder (OPC). Hence, the OPC was replaced at different levels: 15, 30, 45, 60 and 75%. The Atterberg limits,

compaction parameters, and unconfined compressive strength (*UCS*) tests were employed to evaluate the produced mixtures and compare to the reference mixture (soil – 100% OPC binder). To understand the improvement gained in different soil geotechnical properties, the scanning electron microscopy (SEM) technique was utilized by examining the microstructure of the paste of the most logical mixture that exhibited a closed performance to the reference binder.

Materials and methods

Soil samples

The soil samples were obtained from the main campus of University of Babylon, Babylon, Iraq. They were collected from a depth of about 0.5 m below natural ground surface. The particle size distribution curve obtained from carrying out both sieve and hydrometer analysis is shown in Figure 1. This curve shows that the main fraction of the soil is clay while; the silt falls in the second order. Table 1 recapitulates some geotechnical properties of the

soil, while the soil micrograph image obtained from the SEM test. It appeared as flocks and platy shape particles reflecting the existance of clay minerals.

TABLE 1. Some geotechnical properties of the soil

Property	Unit	Value
Liquid limit (*LL*)	%	42
Plastic limit (*PL*)	%	21.5
Plasticity index (*PI*)	–	20.5
Sand	%	11
Silt	%	41
Clay	%	48
Specific gravity (G_s)	–	2.66
Maximum dry density (*MDD*)	$Mg \cdot m^{-3}$	1.61
Optimum moisture content (*OMC*)	%	21.5
Unconfined compressive strength (*UCS*)	kPa	144

Binder materials

The materials used to produce the binders were: OPC which was obtained from a local factory located in Babylon
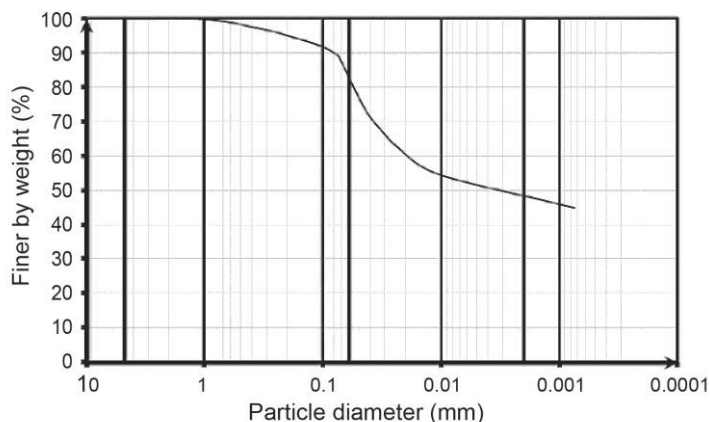
FIGURE 1. Grain size distribution curve for obtained soil

Province, Iraq, ground granulated blast furnace slag (GGBFS); supplied from Hanson Heidelberg Cement Group, Skuthorpe, UK, and cement kiln dust (CKD) which was provided by local cement factory.

The chemical compositions of the candidate materials are listed in Table 2. These compositions were obtained by conducting X-ray fluorescence (XRF) analysis using Shimadzu's EDX-720 Energy Dispersive X-Ray Fluorescence Spectrometer. It is important to observe that the percentages of calcium oxide CaO in GGBFS and CKD were more than 42% and 57% respectively, which are considerable values for the desired objective. On the other hand, the content of silica oxide (SiO_2) available in the composition of GGBFS was high enough to be an alternative pozzolanic source of the replaced cement. In the same view, the source of alumina (Al_2O_3) provided by GGBFS and CKD surpassed that available in cement.

Figure 2 presents the SEM images of binder materials along with virgin soil in their powder states. The EDX Oxford In-

ca x-act detector and FEI SEM models Inspect S instrument was employed for SEM imaging using voltages acceleration of 5–20 kV. For utmost image clarity, a sputter cater was used to coat the specimen by palladium thin layer. It can be seen that the GGBFS appeared as irregular shapes, while CKD shows agglomerated particles. An instrument used laser particle size analyzer was employed to disclose the gradation of binder materials. The grain size distribution curves of OPC and the replacement materials used are illustrated in Figure 3. It can be perceived that GGBFS is finer than the OPC which gave an opportunity to make the chemical reaction faster and more reactive.

Laboratory program

The laboratory program involved three main stages: The untreated soil classification experiments in addition, the unconfined compression test (*UCS*) were carried out in the first stage. The second stage included the process of preparing the specimens of the soil treated with different binder mixtures contained OPC, GGBFS, and CKD with different proportions as illustarted in Table 3. At this stage, Atterberg limits, compaction parameters, and *UCS* test were conducted. In all complementary mixtures, the strategy of replacement comprised using GGBFS of two folds of CKD so that the total replacement began with 15% from the total OPC. Then, the 15% was increased to be 30, 45, 60 and 75%.

Tests of Atterberg limits were made according to standard BS 1377-2:1990 (British Standard Institution [BSI], 1990a). The adopted procedure of standard Proctor compaction test matched with

TABLE 2. The major chemical compositions of the candidate materials

Item	OPC	GGBFS	CKD
CaO [%]	65.89	42.27	57.23
SiO_2 [%]	24.71	41.29	16.52
Al_2O_3 [%]	1.71	5.14	4.2
Fe_2O_3 [%]	1.61	–	3.8
MgO [%]	1.32	4.06	0.8
Na_2O [%]	1.36	3.13	0.23
K_2O [%]	0.83	0.72	6.72
SO_3 [%]	2.54	1.29	4.31
TiO_2 [%]	–	1.01	0.21
pH [-]	12.93	11.65	12.75
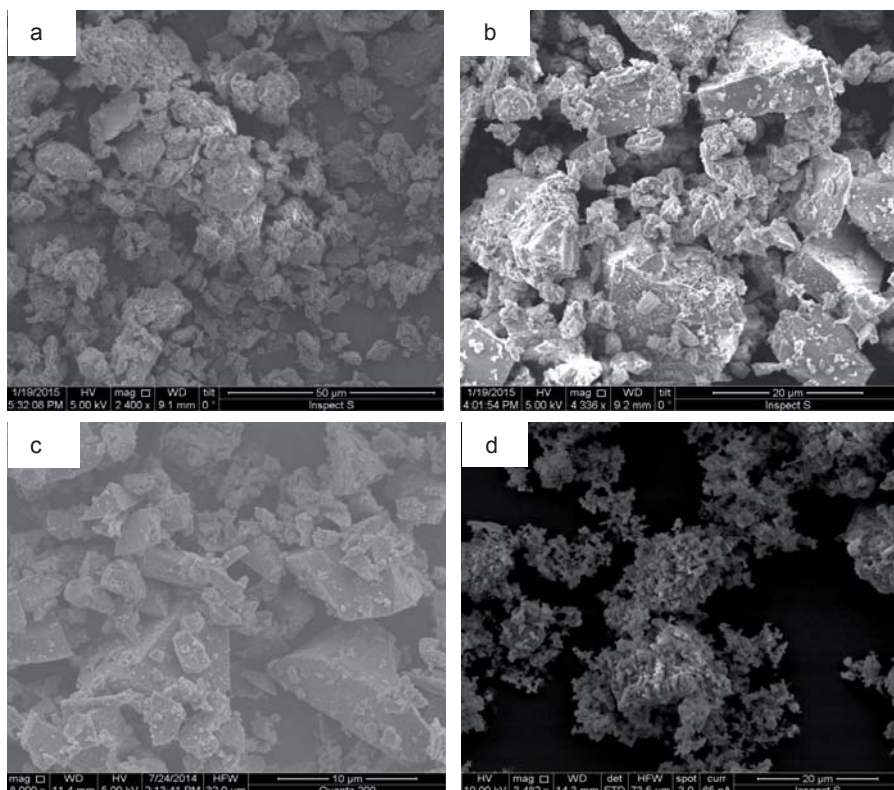
FIGURE 2. SEM magnification of (a) virgin soil, (b) OPC, (c) GGBFS and (d) CKD
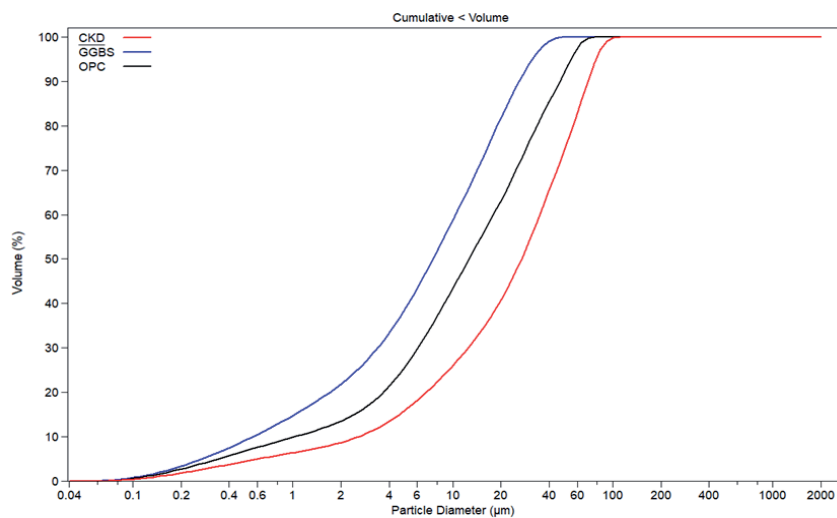
FIGURE 3. Gradations of GGBSF, CKD and OPC

TABLE 3. Mixing procedure adopted in this project

No	Replacement [%]	Mix. ID	Percentages by the total binder [%]		
			OPC	GGBFS	CKD
1	0	US	0	0	0
2	0	RF	100	0	0
3	15	OGC1	85	10	5
4	30	OGC2	70	20	10
5	45	OGC3	55	30	15
6	60	OGC4	40	40	20
7	75	OGC5	25	50	25

standard BS 1377-4 (BSI, 1990b). Strain controlled triaxial testing machine with zero lateral stress (σ_3) was employed to performed *UCS* in which the standard BS 1377-7 (BSI, 1990c) was adopted for *UCS* test. The samples prepared for this test were made at densities and moisture contents corresponding to maximum dry density and optimum moisture content obtained for each mixture. All specimens were prepared with dimensions of 38 and 76 mm in diameter and height respectivily, then wrapped by polyethylene plastic film to maintain the moisture of soil sample while stored during the curing time.

At the third stage, and to identify some mechanisms of treatment along chemical reactions took place over curing periods, a series of scanning electron magnification analyses, for specimens of the most promising binder, after each curing time was performed. Same apparatus and procedure mentioned in section 2.3 were used for this purpose.

Results and discussion

Atterberg limits

The results obtained from Atterberg limits test for the virgin soil (US) were 42, 21.5 and 20.5% for *LL*, *PL*, and *PI* respectively. Since the *PI* is greater than 17, US is considered as a high plasticity soil. The results experienced some increase in *LL* and *PL* in the case of RF specimen whereas, a noticeable reduction in *PI* was obtained, and the *PI* was lowered towered 13.8%. These results agreed with the previous studies (Al-Zoubi, 2008; Jafer et al., 2018b) where the increments in *LL* and *PL* were justified by the increase in the water demand necessary for the cement hydration. Table 4 shows the results of Atterberg limits of primary and complementary mixtures. In the view of this table, it can be inferred that partially replacement of OPC by GGBFS and CKD induced slightly increases in the values of both *LL* and *PL* for all mixtures tested in this study. On

TABLE 4. Results of Atterberg limits

No	Mix ID	*LL*	*PL*	*PI*
1	US	42	21.5	20.5
2	RF	46.8	33	13.8
3	OGC1	46	32	14
4	OGC2	46.3	32.7	13.6
5	OGC3	47	33.6	13.4
6	OGC4	47.6	34	13.6
7	OGC5	48.4	35.2	13.2

the other hands, *PI* values were seeing to slightly increase in the case of OGC1 and then little decrease for the other mixtures when compared with those of RF. It should be noted that the binder OGC5 indicated the lowest value of *PI* (13.2) among all other mixtures.

Compaction parameters

Regarding the results of compaction, the *MDD* and *OMC* for US were 1.61 gm·cm^{-3} and 20.5% respectively. Due to adding OPC in the case of RF mixture, a reduction took place in the value of *MDD* to be 1.52 gm·cm^{-3}. Furthermore,

a considerable growth in the value of *OMC* can be observed for RF specimen which became 27%. The reduction in *MDD* is due to flocculation and agglomeration in clay particles to make them coarser leading to increase the void ratio (Hayano, Dong & Morikawa, 2013). Moreover, the formation and crystallization of cementitious gel after a series of chemical reactions between soil minerals and OPC components formed needle structures which were in turn forms rough texture. This texture characterized by void ratio greater than that in US and less density (Hayano et al., 2013). Figure 4 presents the change in *MDD* and *OMC* for all studied mixtures. The results of compaction tests also indicated an increase in the *MDD* accompanied with a reduction in the *OMC* after the inclusion of GGBFS and CKD particularly with the use of OGC1. This could be attributed to the reduction in the water demand due to the decrease occurred in the active lime after the cement replacement as well as the high fineness of GGBFS replaced the OPC in the aforementioned
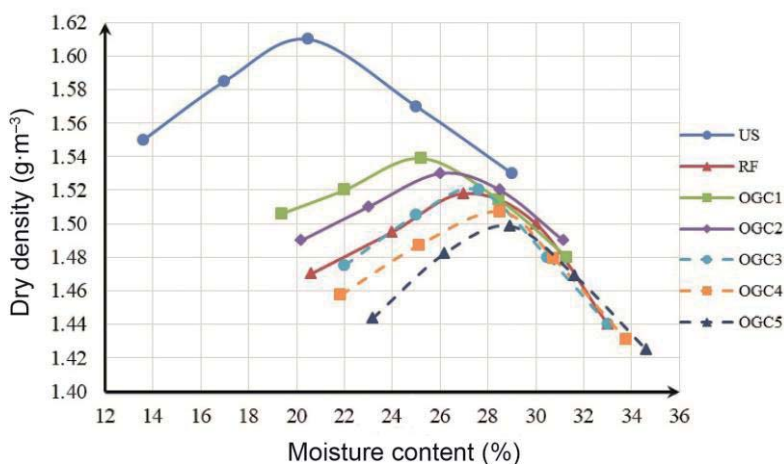
FIGURE 4. Dry densities – moisture contents for US, RF, and all complementary mixtures

H. Jafer et al.

binder (Eyo, Ng'ambi & Abbey, 2020). However, the values of *MMD* then decreased and *OMC* increased with the continuous increase the portion of cement replacement in the used binder as shown in Figure 4.

Results of *UCS* test

Figure 5 illustrates the outcomes of unconfined compressive strength tests. Based on the obtained results, the strength of US specimens was 144 $kN \cdot m^{-2}$. As per the *UCS* test results, the strength of treated soil after cement replacement experienced significant growth compared with the RF strength. The partial replacement of OPC using 2 : 1 mixing proportions of GGBFS and CKD succeed in generating the cementitious gel which plays the main role of strength evolution. This inference is clarified from Figure 5, where *UCS* developed generally in the same trend over curing time for the mixtures OGC1, OGC2, and OGC3. However, the strength gain demonstrated lower trends in the OGC4 and OGC5 mixtures. This significant growth in the strength can be attributed to the formation of cementitious gel which bonded soil particles together in one side and crystallized more and more over time on the other side (Pourakbar, Asadi, Huat & Fasihnikoutalab, 2015; Eyo et al., 2020). These two mechanisms make the soil strength developed over curing period.

Moreover, the strength of the first three mixtures gained at rate higher than that of the other mixtures particularly at the short and medium term curing periods. Where, the *UCS* reached values between 1,300 and 1,281 $kN \cdot m^{-2}$ at the age of 28 days. At the long term curing, the results hovered from 1,376 to 1,350 $kN \cdot m^{-2}$ at age of 90 days which almost closed to that of RF. But the results showed noticeable reduction particularly in the case OGC5 for all curing periods compared with RF strength. This is may be due to the OPC as activator became not enough for chemical reaction of GGBFS and CKD and in turns induced
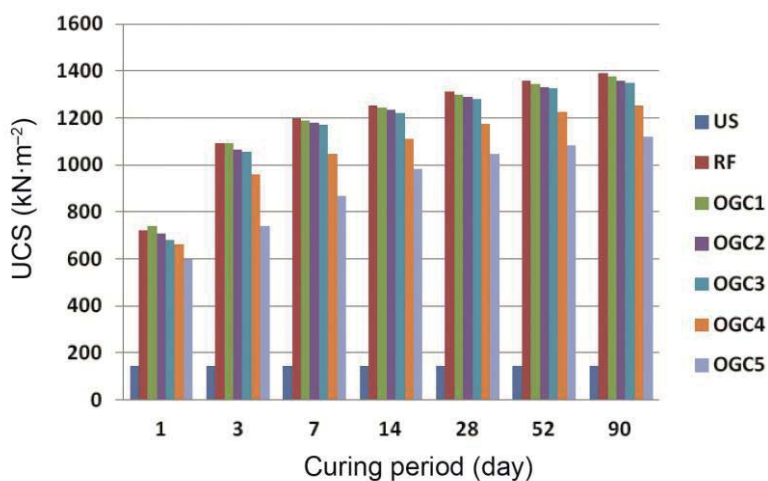
FIGURE 5. Strength developments over curing periods for all mixtures

low creation of cementitious gel (Rahman, Abo-El-Enein, Aboul-Fetouh & Shehata, 2016; Shubbar et al., 2020).

These results of *UCS* indicated that the OPC can be replaced up to 45% by GGBFS and CKD (2 : 1) and got almost same results of strength of the soil – 100% OPC mixture. However, the replacement of OPC with 60% using the combination of GGBFS and CKD (OGC4) indicated accepted results to improve most of the geotechnical properties of the stabilized soil in this study in comparison to those gained from using the binder 100% OPC. The proper percentages of calcium oxide, alumina, and silica included in the chemical composition of GGBFS and CKD gave appropriateness to partial exchange the OPC.

SEM analysis results

Figure 6 presents the results of microscopic analysis and images of SEM of 45% replacement mixture (OGC3) after 6 periods of curing; 1, 3, 7, 28, 52, and 90 days. The analysis pursued the products of chemical reaction results over the mentioned curing periods. The reaction in the short term (in the first day up to 7 days) produced a texture of needle like shape which belongs to ettringite material. Hexagonal shape particles can be detected in the mentioned ages of reaction which were Portlandite production (CH). In addition, at 3 and 7 days of curing, calcium silicate hydrate (C-S-H) can be observed which is the essential cementitious gel responsible for binding the soil particles to each other and strengthen the whole mass of soil. The formation of these materials reflects the reactivity of the proposed materials (CKD and GGBSF) to produce the de-sired cement characteristics (Sadique, Al-Nageim, Atherton, Seton & Dempster, 2013). At the medium age of curing, the Ettringite and CH disappeared under SEM microscope which revealed that they were consumed in chemical reactions at this age to produce more C-S-H gel to be the only materials covered the scene. Similar findings were reported by Jha and Sivapullaiah (2015) and Shubbar et al. (2020). Finally, the long term aging (52 and 90 days of curing) showed that the C-S-H gel began to get high crystallization so that it became solid and very dense matrix. The formation of this dense crystal matrix explains the gain of compressive strength of soil – cement mixture along the curing periods.

Conclusions

In view of previous results, the following conclusions can be extracted:
- The plasticity index decreased significantly when adding 9.0% OPC compared with untreated soil. Cement replacement using GGBFS and CKD as waste materials can give relatively same reduction in plasticity of soil.
- A reduction in maximum dry density and increment in optimum moisture content were experienced in the treated soil by OPC and similar trend of results was found in the mixtures where replacement was made.
- The outcomes of strength evolution showed that the strength of OGC1, OGC2, and OGC3 mixtures gained at a rate higher than that of OGC4 and OGC5 particularly at the short and medium term of curing periods.
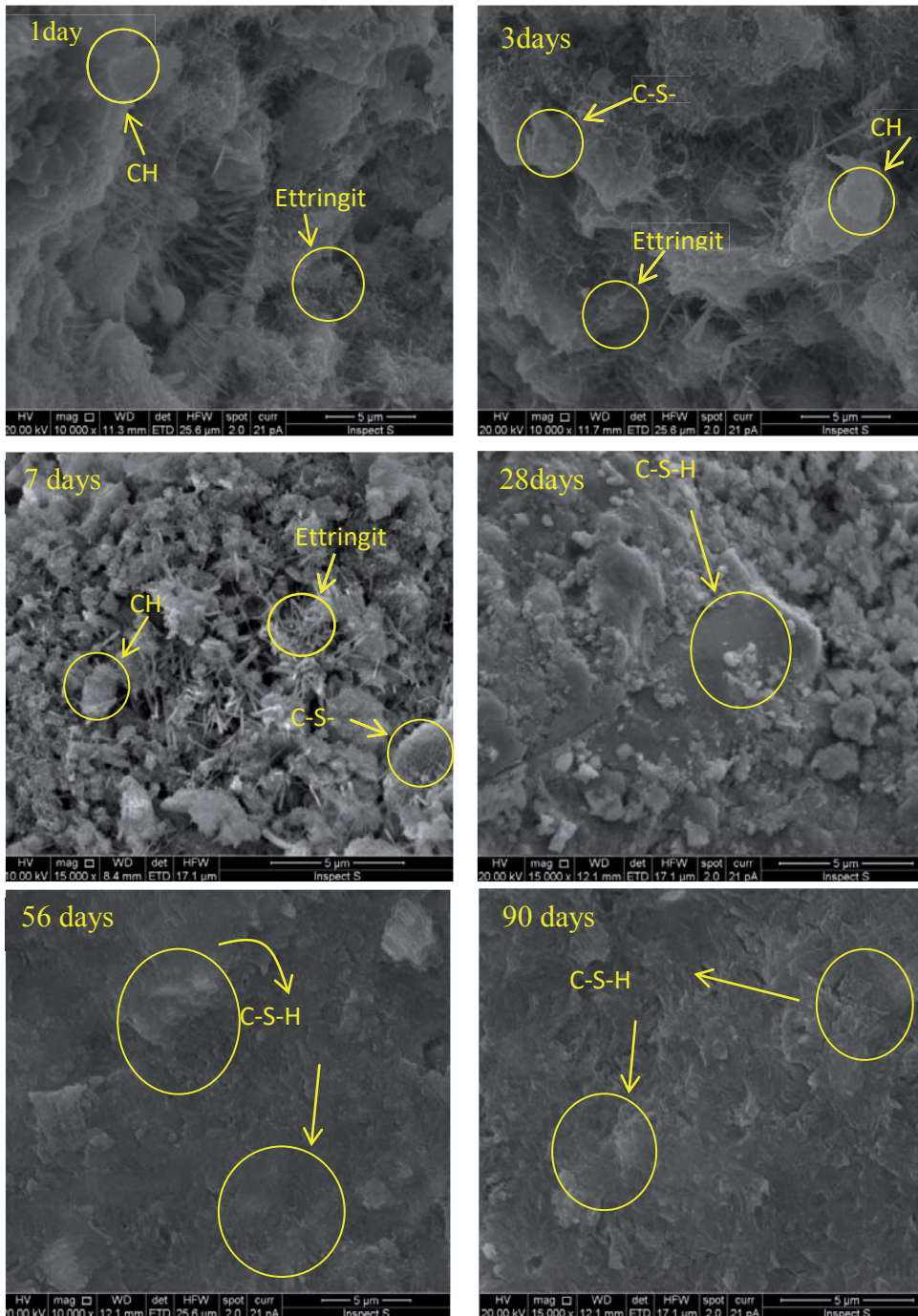
FIGURE 6. SEM microphotographs of binder paste containing 45% cement replacement

Furthermore, the first three mixtures got strength values close to that of RF specimen even in the long term curing.

– The SEM microscopic analysis results of 45% replacement binder showed that formation of needle like shape of Ettringite production and plate like shape of Portlandite formation at the short term curing (1–7 days). The formation of calcium silicate hydrate (C-S-H) can be observed at this age as well. At the medium and long term curing time, the images of SEM presented the only C-S-H formation and absence of CH and Etringite reflected dramatic changes in the microstructure of the hydrated paste of the tested binder along the time of curing. Moreover SEM images indicated that the C-S--H got more and more crystallisation over time.

– Finally, the outcomes of this study revealed that GGBFS and CKD can comfortably be used for cement replacement at levels between 45 and 60% with grantee results close to those that could be obtained from the conventional binder; cement.

Acknowledgements

References

Aïtcin, P.C. (2016). Supplementary cementitious materials and blended cements. In *Science and Technology of Concrete Admixtures* (pp. 53-73). Sawston: Woodhead Publishing.

Al-Zoubi, M.S. (2008). Undrained shear strength and swelling characteristics of cement treated soil. *Jordan Journal of Civil Engineering*, *2*(1), 53-62.

Aprianti, E. (2017). A huge number of artificial waste material can be supplementary cementitious material (SCM) for concrete production – a review part II. *Journal of Cleaner Production*, *142*, 4178-4194.

British Standard Institution [BSI] (1990a). *Methods of test for soils for civil engineering purposes. Part 2: Classification tests* (BS 1377-2:1990). London: British Standard Institution.

British Standard Institution [BSI] (1990b). *Methods of test for soils for civil engineering purposes. Part 4: Compaction-related tests* (BS 1377-4:1990). London: British Standard Institution.

British Standard Institution [BSI] (1990b). *Methods of test for soils for civil engineering purposes. Part 7: Shear strength tests (total stress)* (BS 1377-7:1990). London: British Standard Institution.

Eyo, E.U., Ng'ambi, S. & Abbey, S.J. (2020). Performance of clay stabilized by cementitious materials and inclusion of zeolite/alkaline metals-based additive. *Transportation Geotechnics*, *23*, 100330. https://doi.org/10.1016/j.trgeo.2020.100330

Hayano, K., Dong, P.H. & Morikawa, Y. (2013). Physical and mechanical properties of cement-treated granular soils with respect to geotechnical application. *AIP Conference Proceedings*, *1542*(1), 301-304.

Hermawan, Marzuki, P.F., Abduh, M. & Driejana, R. (2015). Identification of source factors of carbon dioxide (CO_2) emissions in concreting of reinforced concrete. *Procedia Engineering*, *125*, 692-698.

H. Jafer et al.

Higgins, D.D. (2005). *Soil stabilisation with ground granulated blastfurnace slag*. London: UK Cementitious Slag Makers Association (UK CSMA).

Jafer, H.M., Atherton, W., Ruddock, F. & Loffill, E. (2017). The stabilization of a soft soil subgrade layer using a new sustainable binder produced from free-cement blending of waste materials fly ashes. In A. Loizos, I.L. Al-Qadi, T. Scarpas (eds.), *Bearing Capacity of Roads, Railways and Airfields* (pp. 1053--1060). London: CRC Press.

Jafer, H.M., Atherton, W., Sadique, M., Ruddock, F. & Loffill, E. (2018a). Development of a new ternary blended cementitious binder produced from waste materials for use in soft soil stabilisation. *Journal of Cleaner Production*, *172*, 516-528.

Jafer, H.M., Atherton, W., Sadique, M., Ruddock, F. & Loffill, E. (2018b). Stabilisation of soft soil using binary blending of high calcium fly ash and palm oil fuel ash. *Applied Clay Science*, *152*, 323-332.

Jha, A.K. & Sivapullaiah, P.V. (2015). Mechanism of improvement in the strength and volume change behavior of lime stabilized soil. *Engineering Geology*, *198*, 53-64.

Kunal, Siddique, R. & Rajor, A. (2014). Strength and microstructure analysis of bacterial treated cement kiln dust mortar. *Construction and Building Materials*, *63*, 49-55.

Ma, C., Chen, B. & Chen, L. (2016). Effect of organic matter on strength development of self--compacting earth-based construction stabilized with cement-based composites. *Construction and Building Materials*, *123*, 414-423.

Majdi, H.S., Shubbar, A.A.F., Nasr, M.S., Al--Khafaji, Z.S., Jafer, H., Abdulredha, M., Al Masoodi, Z., Sadique, M.M. & Hashim, K.S. (2020). Experimental data on compressive strength and ultrasonic pulse velocity properties of sustainable mortar made with high content of GGBFS and CKD combinations. *Data in Brief*, *31*, 1-11.

Oner, A. & Akyuz, S. (2007). An experimental study on optimum usage of GGBS for the compressive strength of concrete. *Cement and Concrete Composites*, *29*(6), 505-514.

Pourakbar, S., Asadi, A., Huat, B.B. & Fasihnikoutalab, M.H. (2015). Stabilization of clayey soil using ultrafine palm oil fuel ash (POFA) and cement. *Transportation Geotechnics*, *3*, 24-35.

Rahman, A. A., Abo-El-Enein, S.A., Aboul-Fetouh, M. & Shehata, K. (2016). Characteristics of Portland blast-furnace slag cement containing cement kiln dust and active silica. *Arabian Journal of Chemistry*, *9*, 138-143.

Ruijven, B.J., van, Vuuren, D.P., van, Boskaljon, W., Neelis, M.L., Saygin, D. & Patel, M.K. (2016). Long-term model-based projections of energy use and CO_2 emissions from the global steel and cement industries. *Resources, Conservation and Recycling, 112*, 15-36.

Sadique, M., Al-Nageim, H., Atherton, W., Seton, L. & Dempster, N. (2013). Mechano-chemical activation of high-Ca fly ash by cement free blending and gypsum aided grinding. *Construction and Building Materials*, *43*, 480-489.

Saride, S., Puppala, A.J. & Chikyala, S.R. (2013). Swell-shrink and strength behaviors of lime and cement stabilized expansive organic clays. *Applied Clay Science*, *85*, 39-45.

Shubbar, A.A., Jafer, H., Abdulredha, M., Al--Khafaji, Z.S., Nasr, M.S., Al Masoodi, Z. & Sadique, M. (2020). Properties of cement mortar incorporated high volume fraction of GGBFS and CKD from 1 day to 550 days. *Journal of Building Engineering*, *30*, 101327. https://doi.org/10.1016/j.jobe.2020.101327

Wild, S., Kinuthia, J.M., Robinson, R.B. & Humphreys, I. (1996). Effects of ground granulated blast furnace slag (GGBS) on the strength and swelling properties of lime-stabilized kaolinite in the presence of sulphates. *Clay Minerals*, *31*(3), 423-433.

Zainab, S.A.K., Zainab, A. M., Jafer, H., Dulaimi, A.F. & Atherton, W. (2018). The effect of using fluid catalytic cracking catalyst residue (FC3R) as a cement replacement in soft soil stabilisation. *International Journal of Civil Engineering and Technology*, *9*(4), 522-533.

Zhao, J., Wang, D., Yan, P., Zhao, S. & Zhang, D. (2016). Particle characteristics and hydration activity of ground granulated blast furnace slag powder containing industrial crude glycerol-based grinding aids. *Construction and Building Materials*, *104*, 134-141.

Summary

The development of an ecofriendly binder containing high volume of cement replacement by incorporating two by--product materials for the use in soil stabilization. The development of an ecofriendly binder containing high volume of cement replacement by incorporating two waste materials for the use in soil stabilization. This paper investigates the possibility of replacing ordinary Portland cement (OPC) by two waste and by-product materials for the use of a silty clay soil stabilization purpose. The soil was treated by 9.0% OPC where this mixture was used as a reference for all tests. Two by--product materials: ground granulated blast furnace slag and cement kiln dust were used as replacement materials. Consistency limits, compaction and unconfined compression strength (*UCS*) tests were conducted. Scanning electron microscopy (SEM) analysis was carried out for the proposed binder to investigate the reaction of products over curing time. Seven curing periods were adopted for all mixtures; 1, 3, 7, 14, 28, 52, and 90 days. The results showed that the strength development over curing periods after ce- ment replacement up to 45–60% was closed to those of the reference specimens. The microphotographs of SEM analysis showed that the formation of Ettringite and Portladite as well as to calcium silicate hydrate gel was obvious at curing periods longer than 7 days reflected that the replacing materials succeed to produce the main products necessary for binder formation.

Authors' address:
Hassnen M. Jafer
(https://orcid.org/0000-0001-8740-9535)
Ibtehaj Jawad
(https://orcid.org/0000-0003-0940-9681)
Zaid Majeed
(https://orcid.org/0000-0002-5057-6003)
University of Babylon
College of Engineering
Department of Civil Engineering
Al-Hillah – Al-Najaf Road
Babylon, Iraq
e-mail: eng.hassnen.mosa@uobabylon.edu.iq

Ali Shubbar
(https://orcid.org/0000-0001-5609-1165)
Henry Cotton Building
15-21 Webster Street
Liverpool L3 2ET, UK

Konrad PODAWCA[1], Agata GRZYMAŁA[2]
[1]Warsaw University of Life Sciences – SGGW, Institute of Environmental Engineering
[2]independent researcher

Comparative analysis of selected features of traditional and photocatalytical paving stones

Key words: technical properties, traditional and photocatalytical paving stones, cement TioCem®, smog

Introduction

The matter of ecology of urbanised areas appeared in the 1970s, but recently the interest in the issue has considerably increased. Currently, the subject of scientific and social consideration is atmospheric air pollution associated with so-called low emissions. Concrete is a building material that predominantly shapes the urban landscape. Increasingly, it is also replacing asphalt used on road surfaces. Concrete paving stones are used on lower-ranking roads and pedestrian traffic routes. According to Łój (2007), cement is responsible for most of the properties of concrete. At the beginning of the 2000s, the cement developed by the HeidelbergCement Group called TioCem® was launched on the market. The product is characterized by pho-tocatalytic properties owing to the use of nanometric titanium dioxide (TiO_2), which affects the removal of harmful compounds from the air and self-cleaning of concrete (Bolte, 2005; Sokołowski & Dziuk, 2008; Sokołowski, Kaczmarek & Szerszeń, 2010).

There are many examples of research on TioCem® cement itself (initial setting time, end of setting time, compressive strength after 2 and 28 days) and products based on it (Brylicki, 2004; Grupa Górażdże, n.d.; Sokołowski, 2008; Sokołowski & Dziuk, 2008; Sokołowski & Kaczmarek, 2009; Lucas, Ferreira & Barroso de Aguiar, 2013; Langier & Pietrzak, 2017). The research is focused on reducing pollution (Bolte, Dienemann & Smolik, 2008; Sokołowski & Dziuk, 2008; Giergiczny & Sokołowski, 2009). Unfortunately, there are not many tests carried out on materials that have been exploited. Most amount to foreign examples from Germany, the United Kingdom or Italy (Ente Italiano di Normazi-one [UNI], 2007; Sokołowski, 2008;

Sokołowski, 2010; Jackiewicz-Rek, 2019). There is a need to check not only reduction of pollution over time, but also technical properties of the paving blocks.

The aim of the analysis

The aim of the research is to determine the main technical characteristics, i.e. absorbability, frost resistance, abrasion and splitting tensile strength concrete materials used for walking and driving routes in cities. The aim of the analysis is to compare the results obtained for traditional and photocatalytic paving stones. In addition, an attempt has been made to determine whether atmospheric conditions and air pollution affect the characteristics of these products.

The analysis was based on the provisions of the PN-EN 1338:2005 standard (Polski Komitet Normalizacyjny [PKN], 2005) and the requirements for concrete paving stones.

Material and methods

It was assumed that test material would be prefabricated paving blocks. The choice of the material for analyses was primarily dictated by various air pollution reduction properties of selected products. They were finally selected for the research:

- rectangular concrete pavement block Mini Trio by Libet from the Monocolor line with nominal area dimensions of 9 × 18 cm and thickness of 6 cm in anthracite colour, made of unreinforced concrete using the vibro-press method, composed of an abrasive layer with minimum thickness of 5 mm and a construction layer, used according to the manufacturer, among others for: private properties, public space, terraces, pavements, alleyways, garden paths, passages, squares, footpaths with a possibility of entry up to 3.5 t and car parks and driveways with light traffic up to 3.5 t;
- rectangular concrete pavement block HOLLAND by ZIEL-BRUK with nominal surface dimensions of 10 × 20 cm and thickness of 6 cm in graphite, made in TX Active® technology with the use of TioCem® cement, according to the manufacturer it is used both on private properties, on pavements and municipal car parks, as well as on surfaces of industrial facilities.

The research material described above was divided into two parts. Half of the paving blocks were stored under laboratory conditions, while the second half was exposed to weather conditions and pollution between December 2018 and March 2019 being stored near the S8 expressway at the Radzymin South junction.

Laboratory tests were carried out in a construction laboratory of the Faculty of Civil and Environmental Engineering of the Warsaw University of Life Sciences – SGGW. The absorbency test of concrete paving stones was carried out in accordance with the PN-EN 1338:2005 standard. Samples were cleaned with a brush at the temperature of 20°C and then immersed in a vessel filled with drinking water at 20°C until mass M_1 was determined. The period of immer-

sion of samples lasted for 7 days. After that two successive weighting rounds were carried out, within an interval of 24 h. The result of weighting between the above mentioned rounds showed no difference of more than 0.1%. In order to remove excess water, surface of samples was cleaned with a damp cloth before each weighing. Then the samples were placed in a dryer and dried at 105°C until constant mass M_2 was obtained. The samples were cooled to room temperature before each weighing.

Test of frost resistance of concrete paving stones was carried out in accordance with Annex N of the PN-B--06256:2018-10 standard (PKN, 2018). All samples were saturated with water until constant mass was obtained. For 10 days the samples were placed in a vessel filled with water at 18°C. The ones intended for freezing were wiped and placed in a freezing chamber. Freezing took place at –18°C. Each freezing period of samples lasted for 5 h, while the thawing period of samples immersed in water at 18°C lasted for 3 h. The study included 25 freeze–thaw cycles.

Abrasion measurement was performed in accordance with Annex H of the PN-EN 1338:2005 standard. The study was carried out on Boehme shield. Square cubes with side length of 71.0 ±1.5 mm were used for the test. The samples were dried at 105°C before testing to constant weight. The samples were loaded with force of 294 N and tested in 16 cycles, each of which consisted of 22 rotations. The abrasiveness was measured by volume loss according to the PN-EN 1338:2005 standard.

Measurement of the splitting tensile strength of concrete paving stones was carried out in accordance with Annex F of the PN-EN 1338:2005 standard. The test was carried out with the use of a testing machine type ZD 40 and washers with width of 15 mm and thickness of 4 mm. Before the beginning of the test, the samples were immersed in water at 20°C for 24 h, then dried and immediately tested. Correction factor for concrete paving blocks amounted to $t = 60$ mm, thickness added up to $k = 0.87$.

Results

The above-described tests were carried out in March 2019. Preparation of the samples for the absorption test was carried out by systematic pouring of water in a cuvette, after maximum water saturation. The samples were graded and then dried in a dryer (Fig. 1). The obtained results are presented in Table 1.

The frost resistance tests were carried out with the use of a chamber (Fig. 2), in which 25 cycles of freezing and defrosting of the samples were performed. The obtained results are presented in Table 2.

The abrasion process was carried out on a Boehme disc (Fig. 3). The samples prepared in accordance with the standard were successively subjected to abrasion cycles. After each completed cycle, shields were cleaned, corundum was poured again and sample was rotated 90°. Each sample was measured along straight lines perpendicular to adopted base and weighted. Loss of height was given as the arithmetic mean height measured at assumed points. The results of the test and of the measurement of abrasion are presented in Table 3.

FIGURE 1. Stages of absorption testing – saturating samples, drying of samples (own photo)

TABLE 1. The results of measurements of water absorption (own study)

Sample	Initial sample weight [kg]	Final sample weight [kg]	Water absorption [%]	Sample	Initial sample weight [kg]	Final sample weight [kg]	Water absorption [%]
Traditional paving stones							
stored in laboratory conditions				stored near the S8 expressway			
1	2.149	2.099	2.38	21	2.166	2.100	3.14
2	2.206	2.160	2.13	22	2.180	2.115	3.07
3	2.169	2.121	2.26	23	2.167	2.096	3.39
Photocatalytic paving stones							
stored in laboratory conditions				stored near the S8 expressway			
11	2.572	2.498	2.96	31	2.594	2.504	3.59
12	2.507	2.430	3.17	32	2.613	2.518	3.77
13	2.490	2.415	3.11	33	2.566	2.468	3.97

FIGURE 2. Frost resistance test chamber (own photo)

Splitting tensile strength was tested on five specimens from each test group prepared in accordance with the requirements. The results of the breaking load and strength *T* are shown in Table 4 and the failure moment and appearance of the sample after the test are shown in Figure 4.

TABLE 2. Weight loss after testing for frost resistance of paving stones (own study)

Sample	Weight of the sample before their first freezing, in a state of saturation with water [g]	Weight of samples after their last thawing, in a state of saturation with water [g]	Weight loss after the test [%]
Traditional paving stones stored in laboratory conditions			
1	2 202	2 176	1.19
2	2 263	2 240	1.02
3	2 220	2 196	1.09
Traditional paving stones stored near the S8 expressway			
21	2 200	2 178	1.01
22	2 215	2 193	1.00
23	2 200	2 178	1.00
Photocatalytic paving stones stored in laboratory conditions			
11	2 633	2 532	3.99
12	2 583	2 547	1.41
13	2 606	2 572	1.32
Photocatalytic paving stones stored near the S8 expressway			
31	2 632	2 608	0.92
32	2 655	2 629	0.99
33	2 603	2 582	0.81

FIGURE 3. Abrasion test on the Boehme disk, sample before and after the test (own photo)

Discussion of the results

The comparative analysis boiled down to presenting the differences in the results of the examined properties in two directions: between different types of paving stones (traditional and photocatalytic) and between paving stones stored under different conditions (stabilized in the laboratory and exposed to weather

TABLE 3. Loss of weight, height and volume after 16 wear cycles of paving stones (own study)

Sample	Average height loss (Δh) [mm]	Loss of weight after 16 wear cycles (Δm) [g]	Density (ρ) [g·mm^{-3}]	Loss of volume after 16 wear cycles (ΔV) [mm^3]	Loss of volume after 16 wear cycles (ΔV) [cm^3]
Traditional paving stones stored in laboratory conditions					
7 A	2.12	22	0.002288	9 615.38	9.62
7 B	1.77	20	0.002288	8 741.26	8.74
10 A	2.28	23	0.002297	10 013.06	10.01
10 B	2.17	25	0.002297	10 883.76	10.88
Traditional paving stones stored near the S8 expressway					
28 A	2.41	23	0.002294	10 026.16	10.03
28 B	2.47	24	0.002294	10 462.07	10.46
30 A	1.53	17	0.002313	7 349.76	7.35
30 B	1.57	18	0.002313	7 782.10	7.78
Photocatalytic paving stones stored in laboratory conditions					
18 A	1.16	13	0.002202	5 903.72	5.90
18 B	1.22	14	0.002202	6 357.86	6.36
19 A	1.89	16	0.002243	7 133.30	7.13
19 B	1.62	16	0.002243	7 133.30	7.13
Photocatalytic paving stones stored near the S8 expressway					
36 A	1.16	14	0.002284	6 129.60	6.13
36 B	1.46	16	0.002284	7 005.25	7.01
39 A	1.21	13	0.002268	5 731.92	5.73
39 B	1.16	12	0.002268	5 291.01	5.29

TABLE 4. Results of the measurement of characteristic tensile strength at splitting (own study)

Sample	Destructive force (P) [N]	Cracking surface (S) [mm^2]	Correction factor (k) [-]	Splitting tensile strength (T) [MPa]
Traditional paving stones stored in laboratory conditions				
4	66 000	10 426		3.51
5	100 000	10 603		5.23
6	85 000	10 541	0.87	4.47
8	120 000	10 634		6.25
9	80 000	10 525		4.21

TABLE 4 cont.

Sample	Destructive force (*P*) [N]	Cracking surface (*S*) [mm^2]	Correction factor (*k*) [-]	Splitting tensile strength (*T*) [MPa]
Traditional paving stones stored near the S8 expressway				
24	92 000	10 603		4.81
25	117 000	10 642		6.09
26	120 000	10 698	0.87	6.22
27	112 000	10 609		5.85
29	84 000	10 540		4.42
Photocatalytic paving stones stored in laboratory conditions				
14	96 000	11 787		4.51
15	94 000	11 644		4.47
16	110 000	11 919	0.87	5.11
17	93 000	11 641		4.43
20	95 000	11 769		4.47
Photocatalytic paving stones stored near the S8 expressway				
34	108 000	11 847		5.05
35	116 000	11 872		5.41
37	109 000	11 850	0.87	5.10
38	102 000	11 810		4.79
40	115 000	11 870		5.37

FIGURE 4. Tensile strength cracking test, sample of traditional and photocatalytic cubes after the test (own photo)

conditions and pollution). Additionally, the obtained results were confronted with the standard requirements (Table 5).

It can be observed that no sample of paving stones exceeded the 6% limit value. Traditional paving stones

---

TABLE 5. Comparative analysis of traditional paving stones and photocatalytic paving stones according to the PN-EN 1338:2005 standard (own study)

Property	Traditional paving stones stored in laboratory conditions	Photocatalytic paving stones stored in laboratory conditions	Traditional paving stones stored near the S8 expressway	Photocatalytic paving stones stored near the S8 expressway	Requirements according to PN-EN 1338:2005/ /PN-B-06265:2018-10
Average water absorption	2.26%	3.08%	3.20%	3.78%	$\leq 6.0\%$
Average weight loss after the testing for frost resistance	1.1%	2.2%	1.0%	0.9%	$< 5.0\%$
Average destructive force of characteristic tensile strength at splitting	508.17 $N \cdot mm^{-1}$	491.88 $N \cdot mm^{-1}$	590.32 $N \cdot mm^{-1}$	552.28 $N \cdot mm^{-1}$	≥ 250 $N \cdot mm^{-1}$
Average strength of characteristic tensile strength at splitting	4.73 MPa	4.60 MPa	5.48 MPa	5.14 MPa	≥ 3.6 MPa
Average of abrasion on Boehme disk	9.81 $cm^3/50$ cm^2	6.63 $cm^3/50$ cm^2	8.90 $cm^3/50$ cm^2	6.04 $cm^3/50$ cm^2	≤ 18 $cm^3/50$ cm^2

achieved the minimum of absorbability, both for samples stored in the laboratory and along the S8 route. It should also be stressed that the samples stored by the expressway were slightly more absorbent than those stored in the laboratory. This may be due to atmospheric factors, mainly low temperatures and precipitation. The frost resistance test of concrete paving stones, carried out in accordance with the PN-B-06265:2018-10 standard for concrete, may be a sure proof of that. This was due to the fact that it was not possible to carry out the test by the method of determining resistance to freeze/ /thawing with de-icing salt recommended by the PN-EN 1338:2005 standard. The analysis of the data from Tables 2 and 5 shows that there has been a loss of mass, which may result in greater absorbability. Regardless of the type and place of storage of the cubes, the loss in mass is 1%, which is negligible in relation to the allowed 5%.

The wear resistance of paving blocks according to the standard for class 4 should be less than 18 cm^3 per 50 cm^3 sample. For all samples the loss in volume shall not exceed the maximum value. Interestingly, samples exposed to weathering show less volume loss after 16 abrasion cycles than samples from the laboratory. The weight of the samples of traditional paving stones after 16 test cycles decreases on average by 22 g, while that of photocatalytic paving stones by 14 g.

With regard to the tensile strength at splitting, the test material met the standard expectations. In all types of the samples the average strength was greater than 3.6 MPa and no single result was less than 2.9 MPa. The average breaking load was twice as high as the mini-
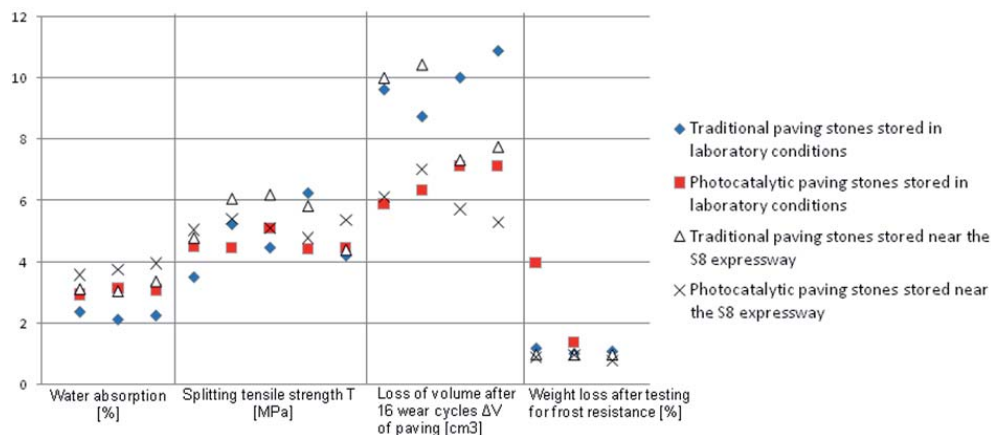
FIGURE 5. Summary of test results depending on the type of paving blocks and their storage method (own study)

mum required by the PN-EN 1338:2005 standard. The strength of traditional paving stones and of photocatalytic paving stones were very similar.

The studies carried out and, above all, the obtained results confirmed the views expressed so far. Compared to the tests carried out by Sokołowski (2010), slightly less absorbability, better abrasiveness, but also less destructive load was obtained when testing tensile strength in splitting. Similarly, in comparison with the experimental results presented by Adamus, Janic and Pietrzak (2016), also the absorbability of the analysed subjects was about 1.5% lower, and the weight loss after frost resistance testing was about 0.5% lower. The authors did not check abrasiveness and tensile strength at splitting in these tests. It should be stressed that research on real material, not experimental material, produced better results. This shows that current manufacturers of paving blocks, including those using TioCem® cement,

try to meet the conditions for such products at a high level.

Conclusions

On the basis of the carried out research synthetic conclusions can be drawn:

– traditional paving stones in the abrasion test were characterized by a higher volume loss than photocatalytic paving stones about 32%;
– based on the average values of split tensile strength, slight increase in the values of strength of the samples used in the vicinity of the S8 expressway can be observed compared to paving blocks stored in the laboratory conditions, regardless of their type;
– the frost resistance of traditional and photocatalytic paving stones is at comparable level, oscillating around 1% weight loss after 25 freeze–thaw cycles;

– the absorbability of the samples that were exposed to weather and pollution between December 2018 and March 2019 increased by about 1% in comparison to the test material stored in the laboratory.

Environmental problems contributed to the creation of a modern product containing nanometric titanium dioxide with photocatalytic properties that reduce harmful substances present in the air and have self-cleaning properties. The production technology of photocatalytic products is identical to the standard version of the products. TX Active® production technology is definitely the technology of the future. The aim of the article, which was to compare selected properties of traditional paving stones and photocatalytic paving stones, was achieved. The laboratory tests show that in analogous storage methods photocatalytic paving blocks slightly exceed the properties of traditional paving blocks. Therefore, it can be assumed that, taking into account the additional properties of pollution reduction and self-cleaning, photocatalytic paving block will replace the traditional one as walking and driving on roads material.

References

Adamus, J., Janic, A. & Pietrzak, A. (2016). Ocena jakości betonu z cementem TioCem® pod kątem możliwości wykorzystania w produkcji kostki brukowej [Quality assessment of concrete of TioCem® cement in terms of the possibilities of using in the production of concrete paving blocks]. *Materiały Budowlane*, *530*(10), 30-32.

Bolte, G. (2005). Photocatalysis in cement-bonded materials. *Cement International*, *3*(3), 92-97.

Bolte, G., Dienemann, W. & Smolik, I. (2008). Can concrete purify the air? In P. Kijowski & J. Deja (eds.), *Dni Betonu. Tradycja i nowoczesność*: konferencja, Wisła 13-15 października 2008 r. Kraków: Stowarzyszenie Producentów Cementu.

Brylicki, W. (2004). Właściwości betonowej kostki brukowej z betonu wibroprasowanego na mieszankach betonowych o niskiej zawartości cementu [Properties of concrete paving blocks made of vibropressed concrete on low-cement concrete mix]. In *Dni Betonu. Tradycja i nowoczesność*: konferencja, Wisła 11-13 października 2004 r. Kraków: Polski Cement.

Ente Italiano di Normazione [UNI] (2007). *Di-terminazione dell'attivita di degradazione di ossidi di azoto in aria de parte di materiali inirganic fotocatalytici* (UNI 11247:2007). Milano: Ente Italiano di Normazione.

Giergiczny, Z. & Sokołowski M. (2009). Fotokatalityczne właściwości betonu zawierającego cement TioCem® [Photocatalytic properties of concrete based on TioCem® cement]. In W.J. Tic et al. (ed.), *Nowe inicjatywy organizacyjne i technologiczne w zakresie chemii przemysłowej* (pp. 73–82). Opole: Oficyna Wydawnicza Politechniki Opolskiej.

Grupa Górażdże (n.d.). *TioCem® Cement ekologiczny*. Retrieved from: https://www.gorazdze.pl/pl/TioCem-Cement-Ekologiczny (access 28.02.2020).

Jackiewicz-Rek, W. (2019). *Beton fotokatalityczny na drodze do poprawy jakości powietrza*. Referat na seminarium *Drogi betonowe. Trwałe i niezawodne rozwiązanie*, Kielce 15 maja 2019 r. [slideshow] Retrieved from: https://www.polskicement.pl/wp-content/uploads/2019/07/04_Beton-fotokatalityczny_Kielce_2019.pdf (access 28.02.2020).

Langier, B. & Pietrzak, A. (2017). Ocena wybranych właściwości kompozytów fotokatalitycznych [Evaluation of some properties of photocatalytic composites]. *Budownictwo o Zoptymalizowanym Potencjale Energetycznym*, *1*(19), 15-20.

Łój, G. (2007). Betonowa kostka brukowa – trwałość i estetyka [Concrete paving blocks – durability and visual appearance]. *Czasopismo Techniczne. Architektura*, *104*(4-A), 139-144.

Lucas, S.S., Ferreira, V.M. & Barroso de Aguiar, J.L. (2013). Incorporation of titanium dioxide nanoparticles in mortars – influence of microstructure in the hardened state properties and photocatalytic activity. *Cement and Concrete Research*, 43, 112-120.

Polski Komitet Normalizacyjny [PKN] (2005). *Betonowe kostki brukowe. Wymagania i metody badań* (PN-EN 1338:2005). Warszawa: Polski Komitet Normalizacyjny.

Polski Komitet Normalizacyjny [PKN] (2018). *Beton. Wymagania, właściwości, produkcja i zgodność. Krajowe uzupełnienie PN-EN 206+A1:2016-12* (PN-B-06256:2018-10). Warszawa: Polski Komitet Normalizacyjny.

Sokołowski, M. & Dziuk, D. (2008). Tiocem – cement z przyszłością. In *Reologia w technologii betonu*: X Symposium Naukowo-Techniczne „Cement – właściwości i zastosowanie" (pp. 17-24). Gliwice: UKiP J&D Gębka.

Sokołowski, M. & Kaczmarek, K. (2009). Nanocement TiOCem w produkcji kostki brukowej [Nanocement TiOCem® in pavement blocks production]. In *Reologia w technologii betonu*: XI Symposium Naukowo-Techniczne „Cement – właściwości i zastosowanie" (pp. 39-48). Gliwice: UKiP J&D Gębka.

Sokołowski, M. (2008). TioCem – ekologiczny cement dla budownictwa [TioCem – ecological cement in civil engineering]. *Materiały Budowlane*, 4(428), 54-55.

Sokołowski, M. (2010). Cement TioCem w produkcji fotokatalitycznej kostki brukowej [TioCem cement in the photocatalytic paving stones production]. *Budownictwo. Technologie. Architektura*, 1(49), 60-63.

Sokołowski, M., Kaczmarek, K. & Szerszeń, K. (2010). Praktyczne zastosowanie cementu TioCem® w produkcji kostki brukowej [Use of cement TioCem® in practice for pavement blocks production]. In P. Kijowski & J. Deja (eds.), *Dni Betonu. Tradycja i nowoczesność*: konferencja, Wisła 11–13 października 2010. Kraków: Stowarzyszenie Producentów Cementu.

Summary

Comparative analysis of selected features of traditional and photocatalytical paving stones. Nature friendly technologies in today's world are the subject of scientific research and the interest of local authorities and the residents themselves. In the context of the city, one of the most important issues is the neutralization of air pollution generated by transport and heating of the premises with the use of solid fuels. The article analyses differences of the response of traditional and photocatalytic paving stones. We analysed water absorption, frost resistance, tensile strength at splitting and abrasion of paving stones. It has been proved that paving stones exposed to atmospheric factors and pollution during one heating season met the assumed quality criteria. In addition, the results obtained for the characteristics analysed were higher than the results of samples tested in laboratory conditions. The results also indicate a slight advantage of photocatalytic cubes in terms of their resistance to abrasion and tensile strength at splitting. Traditional and photocatalytic paving stones withstand well the operating conditions. It seems that products based on TioCem® cement are the future implementation of pedestrian and traffic routes.

Authors' address:
Konrad Podawca
(https://orcid.org/0000-0001-5261-6657)
Szkoła Główna Gospodarstwa Wiejskiego
w Warszawie
Instytut Inżynierii Środowiska
Katedra Teledetekcji i Badań Środowiska
ul. Nowoursynowska 159, 02-776 Warszawa
Poland
e-mail: konrad_podawca@sggw.edu.pl

Saif S. ALQUZWEENI, Afrah A. HASSAN, Rasha S. ALKIZWINI
University of Babylon, College of Engineering

A novel application of building demolition waste for removal benzene from aqueous solutions

Introduction

The environment of the planet of Earth is deteriorating severely nowadays because of the increase in human activities, including industries and agriculture, which results in the production of enormous gaseous and liquid pollutants (Grmasha, Al-Sareji, Salman, Hashim & Jasim, 2020; Zubaidi et al., 2020). For example, the cement industry pollutes the air with a wide range of gases and particulates (Kadhim, Sadique, Al--Mufti & Hashim, 2020) that led to global warming (Salah, Abdulkareem et al., 2020; Zubaidi, Al-Bugharbee, Muhsin, Hashim & Alkhaddar, 2020) and climate change (Salah, Ortega-Martorell et al., 2020). However, water sources are severely polluted due to the recent growth in industrial activities, where several contaminants, including petroleum hydrocarbons, have polluted many water bodies from various industries, such as textile, petroleum, and fertilizers industries (Hashim, Al-Saati, Hussein & Al--Saati, 2018; Omran et al., 2019). Benzene is the commonest compound used for fractions of petroleum in a number of applications, such as raw materials in a number of industries and solvents in a number of industrial processes (Bakather, 2020); nevertheless, benzene is a toxic groundwater pollutant that has adverse impacts on the environment and hence endangers on the health of human. Based on the reports of the U.S. Environmental Protection Agency (EPA), benzene does not exceed 5 $\mu g \cdot L^{-1}$. Therefore, safe, effective methods are needed to remove benzene from water. Benzene and organic matter were removed from water by a number of methods as wet air oxidation, photocatalytic degradation, and adsorption (Elsayed et al., 2017; Alquzweeni & Alkizwini, 2020). Adsorption is one of the areas of surface chemistry that relies on the aggregation of contaminants called adsorbates on the

surface of adsorbents (Bakather, 2020). The literature demonstrates that adsorption is the most powerful and widespread way to remove water contaminants, such as electro-chemical methods (Mohammed et al., 2020; Abdulhadi et al., 2021; Hashim, Shaw, AlKhaddar, Kot & Al-Shamma'a, 2021), coagulation and electrocoagulation (Aqeel et al., 2020; Emamjomeh, Kakavand et al., 2020; Emamjomeh, Mousazadeh et al., 2020; Hashim, Kot et al., 2020), and hybrid methods (Alnaimi et al., 2020; Al-Marri et al., 2020; Zanki et al., 2020). Several adsorbents were used adsorb benzene and components from water, including beer bran (Legrouri et al., 2018), raw and thermally modified lignite (Aivalioti, Pothoulaki, Papoulias & Gidarakas, 2012; Abdulla et al., 2020), and activated carbon (Perrich, 2018; Alyafei et al., 2020), and zeolite (Alenezi et al., 2020; Alhendal et al., 2020), natural adsorbents (Abdulraheem et al., 2020; Alenazi et al., 2020), and industrial by-products (Hashim, Ewadh et al., 2020). However, various waste materials (e.g. biomass and sewage of sludge) were effectively used to minimize the cost of processing nanoporous carbon and controlling the accumulation of atmospheric waste materials (Abdulraheem et al., 2020). Adsorption may, therefore, be used to remove aromatic compounds dissolved in water. With the current trend of using methods that minimize losses and are sufficiently efficient, research has been conducted to evaluate the use of waste or by-products, in particular those generated by industrial processes among the various solid wastes. The prospect of using construction by-products (from the demolition process) as adsorbents would be a significant point for the present study to assess how suitable it is for removing benzene from aqueous solutions.

Materials and methods

Adsorbent and contaminant

The building materials waste from bricks used in this study has been collected and grinded, and then in the oven, drying is done for 24 h at 80°C. The powder was placed in a container for further use. Distilled water is polluted with refined benzene (C_6H_6) at room temperature (purity > 99.5%, produced at a specific concentration by Sinopharm Chemical Reagent Co., Ltd.). This benzene's physical properties are 1,750 mg·L^{-1} water solubility, 0.88 specific gravity, and 35 dynes per 1 cm interfacial tension (Elsayed et al., 2017).

Characterization of building material waste

Figure 1 shows the results of X-ray diffraction, which indicates that O–H ranges from 3,700 to 3,000 cm^{-1}. The very strong and sharp band appearing at 3,644 cm^{-1} corresponds to calcium hydroxide stretching vibrations. The C–H stretching bands measure 3,300––2,800 cm^{-1}. In water solution, however, the C–H vibration frequency is much lower than in non-polar solution. Extending vibration frequencies between hydrogen and other heteroatoms are 2,600–2,000 cm^{-1}, including 2,250––2,100 cm^{-1} Si–H. Regions from 1,300 to 910 cm^{-1} also have skeleton C–O and C–C a contribution to vibration, providing additional molecular structural de-
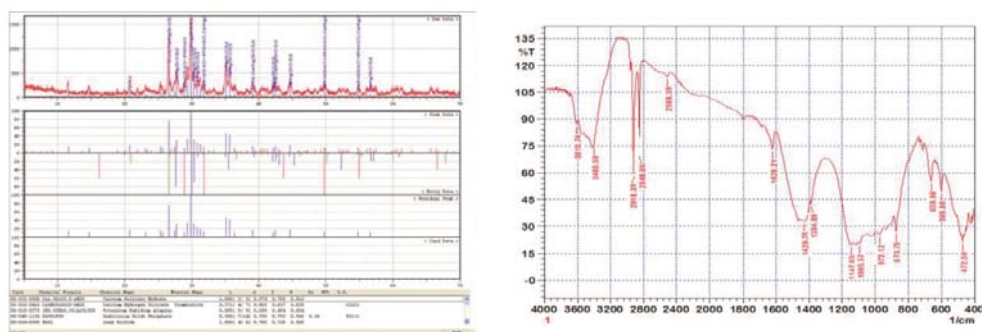
FIGURE 1. XRD and FTIR analysis for natural building material waste

tails relevant to higher frequency regions. Bands between 450 and 600 cm^{-1} are typical features of oxides not detected as major constituents. Due to the complex structure of building material waste, additional structural knowledge from this spectrum area is very difficult to obtain, as the bands characteristic of the various components overlap.

Batch experimental study

It is put in place to get the aforementioned single benzene equilibrium and kinetic data with prepared sorbents. This data will define the best-operating conditions such as initial pH, sorbent dose, and shaking speed for some initial concentration (C_o) that achieves the high performance of the process of treatment. Batch experiments are required for preparing a series of 250 mL flasks, and 100 mL of the contaminated water must be put in every flask with an initial 300 ppm concentration. Different doses of sorbent were applied and the flasks were kept agitated for 180 min at 250 rpm. Then each flask solution was filtered to isolate the water from the solid particles. High-performance liquid chromatography can be used to calculate the residual concentration (C_e) of benzene in the supernatant (HPLC, Shimadzu 2010 Japan). The principle of mass balance can be applied to locate the contaminant sorbed quantity per unit mass of the sorbent. Sorption analysis with pH levels of 3.0–7.0, contact time of 0–180 min and finally C_o at 300–700 mg·L^{-1} was performed. The amounts of pollutants sorbed onto the sorbent (q_e) have been calculated for the best conditions as follows:

$$q_e = (C_o - C_e)\frac{V}{m} \tag{1}$$

where:
V – volume of water in a flask [L],
m – sorbent mass in a flask [g].

The adsorption isotherm is plotted between calculated q_e and C_e.

Equilibrium sorption process models

The model of sorption is the relationship between the quantities of the chemicals sorbed on solids (q_e mg·g^{-1}) and final concentrations of the compound (C_e mg·L^{-1}). At a certain temperature and

pH values were determined; however, several isothermal models, including Freundlich and Langmuir, were fitted.

Freundlich model

The present model may cover multilayer sorption and heterogeneous surfaces but may, generally, be the following (Alquzweeni & Alkizwini, 2020):

$$q_e = K_F C_e^{1/n} \qquad (2)$$

where:
K_F – maximum quantities of contaminant sorbed on reactive material,
$1/n$ (< 1) – indicated by the intensity of the sorption.

Langmuir model

Langmuir developed the following relationship for monolayer sorption and homogeneous surfaces (Alquzweeni & Alkizwini, 2020):

$$q_e = \frac{q_{max} b C_e}{1 + b C_e} \qquad (3)$$

where:
q_{max} – maximum capacity of adsorption [mg·g^{-1}],
b – intensity of contaminants to the solid phase.

Kinetic models

For the design of the appropriate sorption process, the rate of transfer is used from the watery to the solid phase. The following kinetic models predict this rate:

Pseudo-first order model

It has a formula to explain sorption rates as a function of time (Alquzweeni & Alkizwini, 2020):

$$\frac{dq}{dt} = k_1(q_e - q_t) \qquad (4)$$

By applying $q_t = q_e$ at $t = t$ and $q_t = 0$ at $t = 0$, Eq. (2) is integrated to produce the following model:

$$\ln(q_e - q_t) = \ln q_e - k_1 t \text{ or } q_t = q_e\left(1 - e^{-k_t t}\right) \qquad (5)$$

where:
q_t, q_e – amounts of contaminant sorbed on the solid matrix in time t [mg·g^{-1}],
t – time of equilibrium [min],
k_1 – rate constant [min^{-1}].

Pseudo-second order model

The same energy of sorption for un-interacted sorbents and sorbed chemical species, as well as the contaminant's monolayer attached to the sorbent surface, are the general assumptions to guide this model as in Eq. (4):

$$\frac{dq}{dt} = k_1(q_e - q_t)^2 \qquad (6)$$

where:
k_2 – rate constant [g·mg^{-1}·min^{-1}].

Eq. (5) is integrated under the same conditions as the previous model, and the equation will take the forms in Eq. (5):

$$\frac{1}{(q_e - q_t)} = \frac{1}{q_e} + k_2 t \text{ or } q_t = \frac{t}{\left(\dfrac{1}{k_2 q_e^2} + \dfrac{t}{q_e}\right)} \qquad (7)$$

Results and discussion

Effect of adsorbent dosage

The adsorbent dose effect on the adsorption of a fixed benzene concentration is shown in Figure 2a. As the solvent dose increased over the range of 0.4–2.4 g per 100 mL, the percentage of benzene sorbent increased reached 98%. The number of available adsorption sites increases by raising the adsorbent dose, which increases the removal efficiency (Alquzweeni & Alkizwini, 2020). Higher adsorption with the sorbent dose may also be due to increased surface area. These frequent findings with Langmuir's theories that the adsorbent particle is increasingly compatible with organic material with a growing amount of adsorbent particles per unit volume.

Effect of the time of contact

Determining the time of contact needed to achieve an equilibrium status takes into account the possible point of the batch study. Accordingly, as a function of the time of contact, the sorption of benzene on sorbents was controlled, and results were plotted in Figure 2b. Operational conditions include C_o, agitation rate of 300 ppm, and 250 rpm, respectively, adsorbent dose of 1.2 g added at room temperature to 100 mL of polluted water. Figure 2b shows that the removal will increase in the early times of the rapid rate significantly with the contact time, and this rate slows after approximately 150 min. The explanation for slower sorption may be the decline in vacant sites for adopting sorbent. Kinetic data shows that 1 h is sufficient for benzene removal. After this equilibrium period, there is no noticeable shift in the final concentration up to 180 min (Faisal & Naji, 2019).

Effect of initial pH

Effects of the initial pH on benzene's adsorption by the adsorbent were measured at a pH range of 3.0–7.0. As shown in Figure 2b, the pH influences significantly on adsorption of benzene by the adsorbent of 3–6. This means the adsorbent has absorbed benzene. It can be shown that the adsorbent's adsorption capacity decreased rapidly to pH 7.0. It can decrease the driving force of benzene, including the force of van der Waal to the adsorbent's active sites.

Effect of initial benzene concentration

The effect of the initial concentration on benzene's sorption efficiency within the range of 300–700 mg·L^{-1} has been investigated. Figures 2c showed that the removal efficiencies of benzene on a sorbent at (pH 7.0) decreased from (> 90%) to lower values (> 50%) as a result of an increase in the C_o within the range described. The primary explanation for this activity may be the presence of sufficient sites to absorb even more benzene from an aqueous solution. The benzene present in the solution is capable of interacting with lower concentrations of vacant binding sites and, therefore, has been high intake performance relative to higher rates. Thus, the treatment yield can be improved by diluting the water polluted with high benzene concentrations.
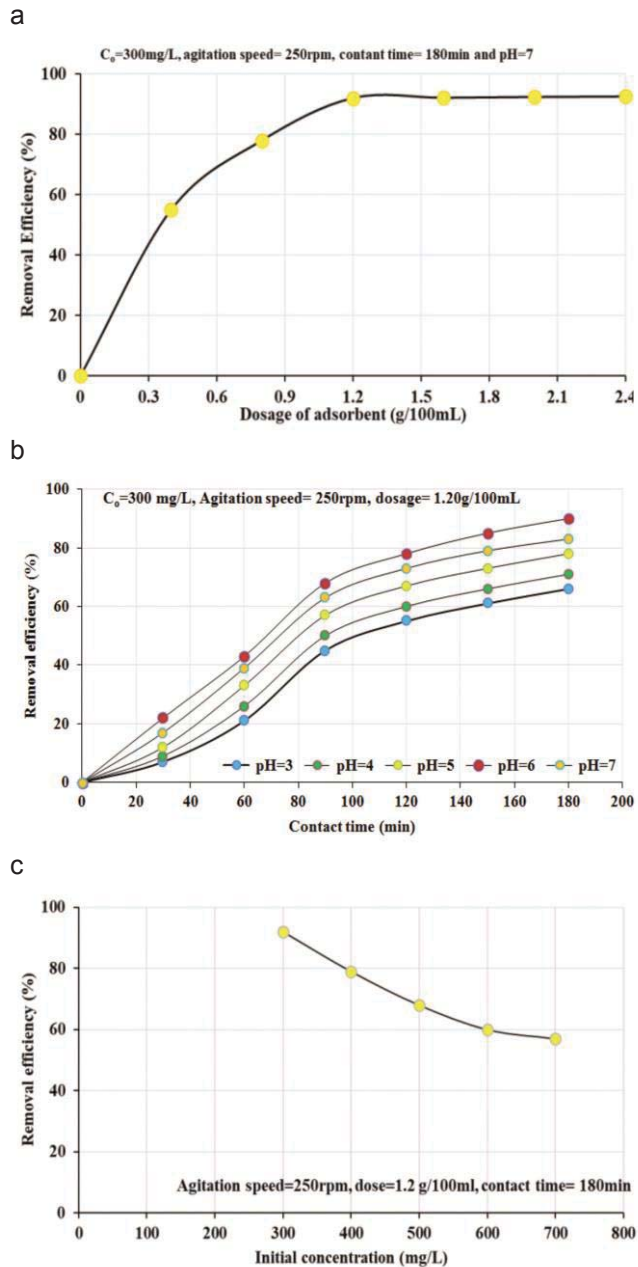
FIGURE 2. The relationship between benzene removal efficiency: a – dose of the adsorbent; b – time of contact, initial pH; c – initial concentration

Kinetic and isotherm analysis

Figure 3 shows the pseudo-first, second-order, and Weber–Morris models that are fitted with kinetic data. For this reason, Microsoft Excel 2016 used the nonlinear regression approach to find the models' constants. The benzene sorption is compatible with (pseudo-first order kinetic) model. This indicates that physical sorption is the primary Sorption mechanism under consideration (Alquzweeni & Alkizwini, 2020). Sorption mechanisms are difficult to characterize based on the previously described kinetic models. This function was thus performed based on (intra-particle diffusion) model concepts. As shown in Eq. (8), the model would be represented empirically where the sorbed quantity changing as a function of $t^{0.5}$ instead of t.

$$q_t = k_{int} t^{0.5} + C \qquad (8)$$

where:
k_i – constant rate of stage i [mg·g^{-1}·h$^{-0.5}$], and is equal to the related slope of q_t to $t^{0.5}$.

The intercept for stage i is also expressed by the value of c_i and reflects the boundary layer's thickness. This implies the greater boundary layer effect can be recognized with the greater intercept value. The intra-particle diffusion occurs if the relationship is associate linearly between q_t and $t^{0.5}$. If the linear plot passes through the origin, the rate-limiting mechanism is defined as the only intra-particle diffusion. Otherwise, other processes of intra-particle diffusion must be considered. The adsorption mechanism is usually considered to include: (i) the mass transfer of adsorbents from bulk to the particulate surface, (ii) surface adsorption, finally (iii) intra-particle diffusion of the adsorbed molecules to an adsorption site through a pore diffusion and/or surface diffusion mechanism. Step (ii) is always presumed to be extremely fast; hence the adsorption of large molecules with long periods of contact to equilibrium is often considered to be regulated by diffusion through external film resistance and/or internal mass transfer of diffusion or intra-particle diffusion. A classical method for evaluating whether intra-particle diffusion regulates an adsorption mechanism is to plot the amount adsorbed versus the square root of time ($t^{0.5}$); when the plot is linear and passes through the origin, it implies that the adsorption rate is regulated by intra-particle diffusion. So, Figure 3 shows the amount of benzene adsorbed for the adsorbents as a function of $t^{0.5}$. It can be shown that the experimental data are satisfactorily fitted by the intra-particle diffusion model, obtaining a linear section that does not pass through the origin, suggesting that benzene adsorption on these adsorbents is not controlled by intra-particle diffusion. Sorption tests are carried out for various concentrations under conditions of pH 7.0, dose = = 1.2 g per 100 mL, speed of 250 rpm, and contact time of 3 h. Freundlich and Langmuir isotherms are shown graphically in Figure 3, and the table lists their constants, which were determined using non-linear fitting of these models with sorption measurements using the Microsoft Excel 2016 Solver option (Alquzweeni & Alkizwini, 2020). Based on Figure 3 and determination coefficient (R^2) in the table, in the definition of sorption measurements, Freundlich model is better than Langmuir one.
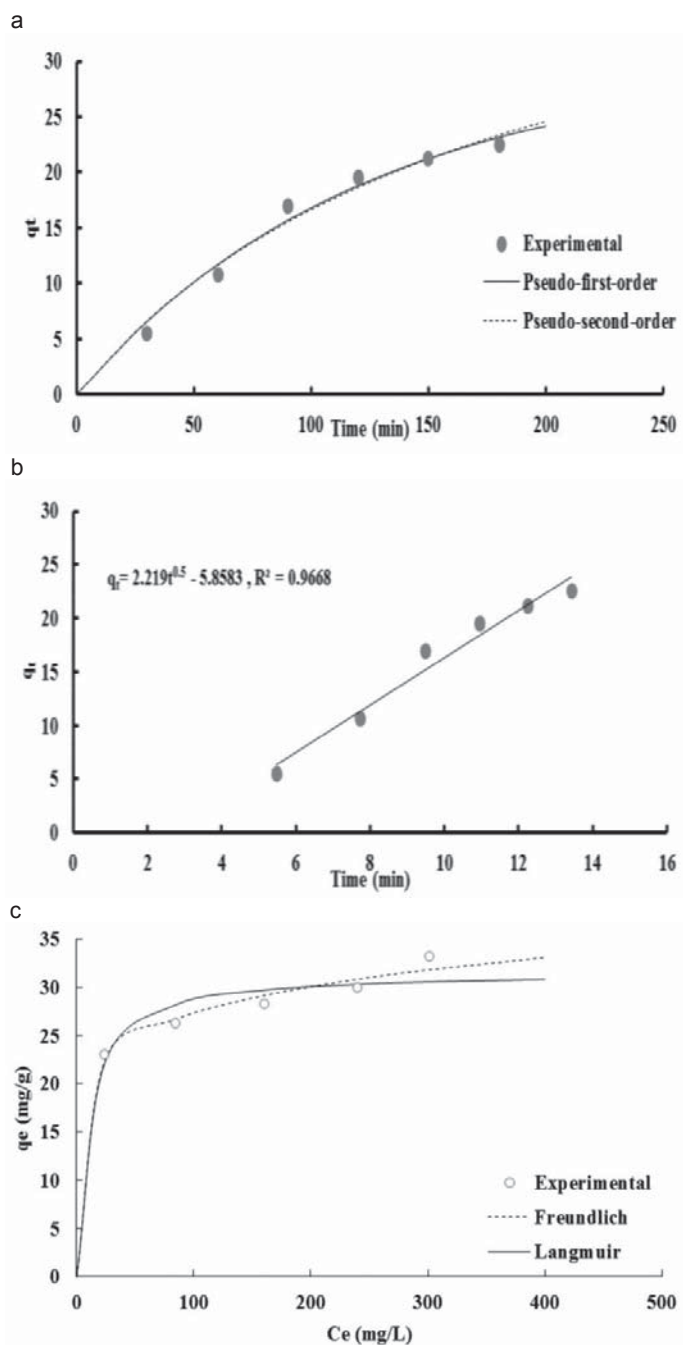
FIGURE 3. Experimental data on sorption fitted with (a) pseudo-first, pseudo-second order models, (b) intra-particle diffusion model, and (c) the isotherm models for the benzene's sorption

TABLE. Isotherm and kinetic modals' constant for benzene's sorption

Model		Parameter	Value
Isotherm	Freundlich	$K_F\,[\mathrm{mg\cdot mg^{-1}}][\mathrm{L\cdot mg^{-1/n}}]$	14.458
		N	7.237
		R^2	0.935
		SSE	13.277
	Langmuir	$q_{\max}\,[\mathrm{mg\cdot g^{-1}}]$	31.602
		$b\,[\mathrm{L\cdot mg^{-1}}]$	0.097
		R^2	0.777
		SSE	3.868
Kinetic	pseudo-first order	$q_e\,[\mathrm{mg\cdot g^{-1}}]$	29.938
		$k_1\,[\mathrm{1\cdot min^{-1}}]$	0.0083
		R^2	0.982
		SSE	4.632
	pseudo-second order	$q_e\,[\mathrm{mg\cdot g^{-1}}]$	47.04
		$k_2\,[\mathrm{g\cdot mg^{-1}\cdot min^{-1}}]$	0.0001
		R^2	0.977
		SSE	5.676
Intra-particle diffusion		$k_{int}\,[\mathrm{mg\cdot g^{-1}\cdot min^{-0.5}}]$	2.219
		R^2	0.967

Conclusion

This has been researched the possible use of building material waste as an adsorbent to benzene. Building material was found to be more effective for removing benzene from the solution; the maximum benzene's adsorption efficiency was 31.601 mg·g^{-1}. The percentage of removal depended strongly on the contact time, the solution's initial pH, and adsorbent dose. Initial pH, contact time, and sorbent dose must be 6, 1 h and 1.2 mg per 100 mL for C_o of 300 mg·L^{-1} and a speed of agitation of 200 rpm, respectively, are the best conditions for achieving these effects. Sorption results are well illustrated by the Freundlich model for the interaction of benzene–water contaminated with sorbent. Finally, the kinetic process is consistent with the pseudo-second order equation.

References

Abdulhadi, B., Kot, P., Hashim, K., Shaw, A., Muradov, M. & Al-Khaddar, R. (2021). Continuous-flow electrocoagulation (EC) process for iron removal from water: experimental, statistical and economic study. *Science of the Total Environment*, *756*(2), 1-16.

Abdulla, G., Kareem, M.M., Hashim, K.S., Muradov, M., Kot, P., Mubarak, H.A., Abdellatif, M. & Abdulhadi, B. (2020). Removal of iron from wastewater using a hybrid filter. *IOP Conference Series: Materials Science and Engineering*, *888*(1), 012035. https://www.doi.org/10.1088/1757-899X/888/1/012035

Abdulraheem, F.S., Al-Khafaji, Z.S., Hashim, K.S., Muradov, M., Kot, P. & Shubbar, A.A. (2020). Natural filtration unit for removal of heavy metals from water. *IOP Conference Series: Materials Science and Engineering*, *888*(1), 012034. https://www.doi.org/10.1088/1757-899X/888/1/012034

Aivalioti, M., Pothoulaki, D., Papoulias, P. & Gidarakos, E. (2012). Removal of BTEX, MTBE and TAME from aqueous solutions by adsorption onto raw and thermally treated lignite. *Journal of Hazardous Materials*, *207*, 136-146.

Alenazi, M., Hashim, K. S., Hassan, A. A., Muradov, M., Kot, P., & Abdulhadi, B. (2020). Turbidity removal using natural coagulants derived from the seeds of *Strychnos potatorum*: statistical and experimental approach. *IOP Conference Series: Materials Science and Engineering*, *888*(1), 012064. https://www.doi.org/10.1088/1757-899X/888/1/012064

Alenezi, A.K., Hasan, H.A., Hashim, K.S., Amoako-Attah, J., Gkantou, M., Muradov, M., Kot, P. & Abdulhadi, B. (2020). Zeolite-assisted electrocoagulation for remediation of phosphate from calcium-phosphate solution. *IOP Conference Series: Materials Science and Engineering*, *888*(1), 012031. https://www.doi.org/10.1088/1757-899X/888/1/012031

Alhendal, M., Nasir, M.J., Hashim, K.S., Amoako-Attah, J., Al-Faluji, D., Muradov, M., Kot, P. & Abdulhadi, B. (2020). Cost-effective hybrid filter for remediation of water from fluoride. *IOP Conference Series: Materials Science and Engineering*, *888*(1), 012038. https://www.doi.org/10.1088/1757-899X/888/1/012038

Al-Marri, S., AlQuzweeni, S.S., Hashim, K.S., AlKhaddar, R., Kot, P., AlKizwini, R.S., Zubaidi, S.L. & Al-Khafaji, Z.S. (2020). Ultrasonic-Electrocoagulation method for nitrate removal from water. *IOP Conference Series: Materials Science and Engineering*, *888*(1), 012073. https://www.doi.org/10.1088/1757-899X/888/1/012073

Alnaimi, H., Idan, I. J., Al-Janabi, A., Hashim, K.S., Gkantou, M., Zubaidi, S.L., Kot, P. & Muradov, M. (2020). Ultrasonic-electrochemical treatment for effluents of concrete plants. *IOP Conference Series: Materials Science and Engineering*, *888*(1),

012063. https://www.doi.org/10.1088/1757-899X/888/1/012063

Alquzweeni, S.S. & Alkizwini, R.S. (2020). Removal of cadmium from contaminated water using coated chicken bones with double-layer hydroxide (Mg/Fe-LDH). *Water*, *12*(8), 2303. https://doi.org/10.3390/w12082303

Alyafei, A., AlKizwini, R.S., Hashim, K.S., Yeboah, D., Gkantou, M., Al Khaddar, R., Al-Faluji, D. & Zubaidi, S.L. (2020). Treatment of effluents of construction industry using a combined filtration-electrocoagulation method. *IOP Conference Series: Materials Science and Engineering*, *888*(1), 012032. https://www.doi.org/10.1088/1757-899X/888/1/012032

Aqeel, K., Mubarak, H.A., Amoako-Attah, J., Abdul-Rahaim, L.A., Al Khaddar, R., Abdellatif, M., Al-Janabi, A. & Hashim, K.S. (2020). Electrochemical removal of brilliant green dye from wastewater. *IOP Conference Series: Materials Science and Engineering*, *888*(1), 012036. https://www.doi.org/10.1088/1757-899X/888/1/012036

Bakather, O.Y. (2020). Adsorption of benzene on impregnated carbon nanotubes. *Ain Shams Engineering Journal*, *11*(4), 905-912.

Elsayed, E., Raya, A.D., Mahmoud, S., Anderson, P.A., Elsayed, A. & Youssef, P.G. (2017). CPO-27 (Ni), aluminium fumarate and MIL-101 (Cr) MOF materials for adsorption water desalination. *Desalination*, *406*, 25-36.

Emamjomeh, M. M., Mousazadeh, M., Mokhtari, N., Jamali, H.A., Makkiabadi, M., Naghdali, Z., Hashim, K.S. & Ghanbari, R. (2020). Simultaneous removal of phenol and linear alkylbenzene sulfonate from automotive service station wastewater: Optimization of coupled electrochemical and physical processes. *Separation Science and Technology*, *55*(17), 3184-3194.

Emamjomeh, M.M., Kakavand, S., Jamali, H.A., Alizadeh, S.M., Safdari, M., Mousavi, S.E.S., Hashim, K. S. & Mousazade, M. (2020). The treatment of printing and packaging wastewater by electrocoagulation–flotation: the simultaneous efficacy of critical parameters and economics. *Desalination and Water Treatment*, *205*, 161-174.

Faisal, A.A. & Naji, L.A. (2019). Simulation of ammonia nitrogen removal from simulated

wastewater by sorption onto waste foundry sand using artificial neural network. *Association of Arab Universities Journal of Engineering Sciences*, *26*(1), 28-34.

Grmasha, R.A., Al-Sareji, O.J., Salman, J.M., Hashim, K.S. & Jasim, I.A. (2020). Polycyclic Aromatic Hydrocarbons (PAHs) in urban street dust within three land-uses of Babylon Governorate, Iraq: distribution, sources, and health risk assessment. *Journal of King Saud University – Engineering Sciences*, *33*, 1-18.

Hashim, K., Kot, P., Zubaid, S., Alwash, R., Al Khaddar, R., Shaw, A., Al-Jumeily, D. & Aljefery, M. (2020). Energy efficient electrocoagulation using baffle-plates electrodes for efficient *Escherichia coli* removal from wastewater. *Journal of Water Process Engineering*, *33*(20), 101079-101086.

Hashim, K.S., Al-Saati, N.H., Hussein, A.H. & Al-Saati, Z.N. (2018). An investigation into the level of heavy metals leaching from canal-dreged sediment: a case study metals leaching from dreged sediment. *IOP Conference Series: Materials Science and Engineering*, *454*(1), 012022. https://www.doi.org/10.1088/1757-899X/454/1/012022

Hashim, K.S., Ewadh, H.M., Muhsin, A.A., Zubaidi, S.L., Kot, P., Muradov, M., Aljefery, M. & Al-Khaddar, R. (2020). Phosphate removal from water using bottom ash: Adsorption performance, coexisting anions and modelling studies. *Water Science and Technology*, *82*(11), 1-17.

Hashim, K.S., Shaw, A., AlKhaddar, R., Kot, P. & Al-Shamma'a, A. (2021). Water purification from metal ions in the presence of organic matter using electromagnetic radiation-assisted treatment. *Journal of Cleaner Production*, *280*(2), 1-17.

Kadhim, A., Sadique, M., Al-Mufti, R. & Hashim, K. (2020). Long-term performance of novel high-calcium one-part alkali-activated cement developed from thermally activated lime kiln dust. *Journal of Building Engineering*, *32*, 1-17.

Legrouri, K., Khouya, E., Oumam, M., Hannache, H., Ezzine, M., Fakhi, S. & Hanafi, N. (2018). Preparation and characterization of activated carbons obtained from molasses by phosphoric acid activation. *Applied Journal of Environmental Engineering Science*, *4*(3), 352-366.

Mohammed, A.H., Hussein, A.H., Yeboah, D., Al Khaddar, R., Abdulhadi, B., Shubbar, A.A. & Hashim, K.S. (2020). Electrochemical removal of nitrate from wastewater. *IOP Conference Series: Materials Science and Engineering*, *888*(1), 012037. https://www.doi.org/10.1088/1757-899X/888/1/012037

Omran, I.I., Al-Saati, N.H., Hashim, K.S., Al-Saati, Z.N., Patryk, K., Khaddar, R.A., Al-Jumeily, D., Shaw, A., Ruddock, F. & Aljefery, M. (2019). Assessment of heavy metal pollution in the Great Al-Mussaib irrigation channel. *Desalination and Water Treatment*, *168*, 165-174.

Perrich, J.R. (2018). *Activated carbon adsorption for wastewater treatment*. Boca Raton, FL: CRC Press.

Salah, Z., Abdulkareem, I.H., Hashim, K.S., Al-Bugharbee, H., Ridha, H.M., Gharghan, S.K., Al-Qaim, F. F., Muradov, M., Kot, P. & Alkhaddar, R. (2020). Hybridised artificial neural network model with slime mould algorithm: a novel methodology for prediction urban stochastic water demand. *Water*, *12*(10), 1-18.

Salah, Z., Ortega-Martorell, S., Kot, P., Alkhaddar, R.M., Abdellatif, M., Gharghan, S.K., Ahmed, M.S., & Hashim, K. (2020). A method for predicting long-term municipal water demands under climate change. *Water Resources Management*, *34*(3), 1265-1279.

Zanki, A.K., Mohammad, F.H., Hashim, K.S., Muradov, M., Kot, P., Kareem, M.M. & Abdulhadi, B. (2020). Removal of organic matter from water using ultrasonic-assisted electrocoagulation method. *IOP Conference Series: Materials Science and Engineering*, *888*(1), 012033. https://www.doi.org/10.1088/1757-899X/888/1/012033

Zubaidi, S., Al-Bugharbee, H., Muhsin, Y.R., Hashim, K. & Alkhaddar, R. (2020). Forecasting of monthly stochastic signal of urban water demand: Baghdad as a case study. *IOP Conference Series: Materials Science and Engineering*, *888*(1), 012018. https://www.doi.org/10.1088/1757-899X/888/1/012018

Zubaidi, S., Ortega-Martorell, S., Al-Bugharbee, H., Olier, I., Hashim, K.S., Gharghan, S.K., Kot, P. & Al-Khaddar, R. (2020). Urban water demand prediction for a city that suffers from climate change and population growth: Gauteng Province case study. *Water*, *12*(7), 1-18.

Summary

A novel application of building demolition waste for removal benzene from aqueous solutions. A novel application of building demolition waste for removal benzene from aqueous solutions. In this research, demolition waste from buildings has been studied for possible use as benzene removal adsorbent from aquatic solution. The effect of adsorbent dosage, contact time, initial benzene concentration, and initial pH on benzene adsorption capacity have been investigated in the batch adsorption experiments. The adsorption effects initially happened very rapidly and achieved equilibrium within 180 min. Benzene removal was observed to decrease by an increase in the initial concentration of benzene of 300–700 mg·L^{-1}, an increase in the adsorbent dose of 0.4–2.4 g per 100 mL, where an optimum adsorbent dose equal to 1.2 g per 100 mL was found. The potential of adsorption increases with pH 3.0–7.0 to reach the maximum removal efficiency at pH 6.0. The findings showed that equilibrium data were adequately adapted and correlated with the Freundlich isotherm models. The average percentage of the removal at room temperature was about 98%. Results suggest that building demolition waste can be used effectively in industrial wastewater treatment for the removal of aromatic hydrocarbon, benzene, as a low--cost option.

Authors' address:
Saif S. Alquzweeni – corresponding author
University of Babylon
College of Engineering
Department of Civil Engineering
40-street, 009647812260838, 51001, Babil
Iraq
e-mail: saifalquzweeni@gmail.com

Afrah A. Hassan
Rasha S. Alkizwini
University of Babylon
College of Engineering
Department of Environmental Engineering
80-street, 009647812835911, 51001, Babil
Iraq
e-mail: eng.afrah.abood@uobabylon.edu.iq
    eng.rasha.salah2018@gmail.com

Zeyad K. ABDULLAD[1], Shatha Y. Al-SAMARRAI[2]

[1]Iraqi Ministry of Oil, North Oil Refineries Company
[2]Tikrit University, College of Science

Modified solid ion-selective electrode for potentiometric determination of sulfide in oil refineries water

Key words: ion-selective electrode, silver sulfide, oil refineries, water

Introduction

A scientist, developed electrode membranes at the beginning of the twentieth century with the discovery of the glass electrode, which is one of the important tools in laboratories, as it response to hydrogen ions (Skoog, Holler & Nieman, 1998). Among the different analytical techniques (Mahajan, Kaur, Sharma & Kumar, 2002) and as a result of the development of research, advances in this area began in the 1960s, when Rokosing and Pungor developed a new type of solid sensor (Cattral, 1997). The field of ion-selective electrodes has experienced rapid growth since the past two decades (Arida, Ahmed & El-Saied, 2003), and chemical sensors are miniature analytical devices that can provide information about the presence of specific compounds or ions in complex samples (Wroblewski, 2009), which are dependent on the development of static electricity potential difference across a membrane. It separates two phases. When placed in a solution containing ions (Cattral, 1997), it is one of the most importantly fast and simple modern electrolysis techniques that require the current passing through them to be equal to zero (Othmer, 1981).

The use of ion-selective membrane electrodes is a good analytical technique. Due to its several advantages over conventional analysis methods for example they provide accurate, repeatable, fast, and often selective identification of different ions (Liu, Zhao, Chen & Che, 2000). Sulfide is an anion that is widely present in both natural, wastewater, and industrial waters, and it is one of the most important factors to monitor in water due to its high toxicity to aquatic organisms. The sulfide toxicity is attributed to the release of hydrogen sulfide (H_2S) (Huang et al., 2010) and hydrogen sulfide (H_2S) is one of the most dangerous highly cor-

rosive media (Lusk, Gupta, Boinapally & Cao, 2008). Because sulfide solutions can attack metals and concrete causing corrosion problems (Shao, Ying & Ping, 2020). It is now known that corrosion can have some effects on the chemistry of the specific process, and the product of corrosion can affect the reaction and purity of the reaction products (Popoola, Grema, Latinwo, Gutti & Balogun, 2013). Recent industrial disasters indicate that many industries have lost several billion dollars as a result of corrosion (Oyelami & Asere, 2011).

The ion-selective sulfide electrode has been applied to monitor sulfide in industrial waters, and Ag/Ag$_2$S electrode is the solid-state that uses this type of ion-selective electrode (S^{-2}) (Zaidan, 2007; Ding, Pan, Huang, Chen & Ye, 2015). These electrodes contain in their crystal membranes only two crystalline compounds, they are the responsible materials for the electrochemical behavior of the membranes, and they are monocrystalline, where the membrane can be got by pressing or dissolving salt powder and then attaching it to the end of the electrode body made so it is not affected by air temperatures and is not subjected to cracking because of heat or rag and resists chemical changes such as the selective fluoride electrode (LaF3). The other such electrodes are the polycrystalline which can be prepared from Ag$_2$S, CuS, CdS, AgCl, AgI, or AgBr powder selective for sulfide ions, chloride, iodide, or bromide respectively (Anfalt & Jagner, 1969; Vesely et al., 1972). These films have been developed to prepare ion-sensitive selective membranes, where they are used to identifying many of the same ions as an internal solution for a con-

ductor (Dulkiewicz, 1989; Bűhlmann, Pretsch & Bakker, 1998).

The aim of this study is to manufacture a selective electrode to determine the sulfur ions prepared from the reaction of sodium sulfide with silver nitrate to form silver sulfide by sedimentation method and apply it to measure sulfur ions in industrial waters in the production units of oil refineries of North Oil Refineries Company, Iraq, and compared with sensitivity and response of Sindie sulfur analyzer (model 7039 G3).

Material and methods

Instrumentations

The following instruments were used: pH/mV meter (3310 Jenway); silver-silver chloride electrode as working electrode (Jenway); reference calomel electrode (Hanna); PVC tubing; balance (BL 210S Sartorius); magnetic stirrer with hotplate (LMS-1003 LabTech); drying oven (Memmert); test sieve (analysensieb) (200 mm, dia. ×50 mm, ASTM E1175 micron) (D-42781 Haan); sulfur analyzer (7039 G3 Sindie).

Reagents and solutions

All reagents were of high purity grade supplied by Fluka, BDH, and MUMBAI. Sodium sulfide 0.1M Na$_2$S was used to prepare the standard solution, nitric acid HNO$_3$, NaOH. The sulfide anti--oxidant buffer SAOB containing 2M NaOH, 0.2M ascorbic acid, and 0.2M disodium EDTA (Dulkiewicz, 1989). Standard staggered ionic solutions were prepared at a concentration of 0.1M of KBr, BaCl$_2$, SnCl$_2$·2H$_2$O, CuSO$_4$·5H$_2$O,

Pb(NO$_3$)$_2$, CrCl$_3$ in a volume of 100 ml distilled water.

Preparation of Ag$_2$S electrodes

The Ag$_2$S electrodes used in this study were fabricated by slow addition of 200 ml of 0.5 ml of silver nitrate solution using a burette, at a rate of 100 drops per minute to 100 ml of 0.5M sodium sulfide solution with continuous stirring, and after completing the addition process, it was filtered. The resulting sediment was washed several times with distilled water, and then with diluted 0.1M nitric acid, the sediment was dried in an oven at 120°C for 3 h. The sediment was collected, milled, and homogenized using ceramic mortar until it became a very fine powder and it was made using a 300 μm sieve, the material was pressed in the form of hard disks using a medicinal pill making machine and it became a compact hard disk with a thickness of 0.7 mm, a diameter of 11.9 mm and a weight of 0.8639 g.

Construction of ion-selective electrodes

A PVC diameter was cut into 3–4 cm long pieces. An Ag$_2$S disk was placed in one end and the other end of the PVC tube was connected to an empty and open Ag/AgCl (Fig. 1).

Cell design and calculation of electrode potential

The selective electrode potential can be calculated depending on the voltage of the membrane that separated different solutions containing the same concentrations of the metal since the response of these membranes depends on the ion

FIGURE 1. The installation of the manufactured electrode

exchanges present in them and has a selectivity of the desired ion. Without the other ions, depending on two main factors the size and charge of the ion, and given that the current passing through these electrodes is equal to zero, the cell used to measure the voltage of this type of electrode is shown in the following:

Ag/AgCl | internal solution of Na$_2$S (10^{-6}M) | membrane (Ag$_2$S) | external solution of Na$_2$S (X M) | SCE

Results and discussion

In this study, the sedimentation method was used to prepare silver sulfide (Ag$_2$S), which is the material from which the membrane electrode is made, because this method works to accomplish chemical reactions in a fast, simple, and highly efficient way Energy and less time consuming and the properties as shown in Table 1.

Z.K. Abdullad, S.Y. Al-Samarrai

TABLE 1. Properties of the prepared electrode

Lifetime/ /month	Response time [s]	Slope [mv·decade^{-1}]	Detection limit [M]	Working pH range	Linear range [M]	Working pH range
4	5-17	28.229	$2.28 \cdot 10^{-7}$	6.0–12.0	10^{-1}–10^{-6}	S^{-2}

Effect of temperature

The best range of temperature without significantly affecting the electrode voltage was 25–35°C, and there is an increase in the voltage difference values at higher temperatures of 35°C, which may occur because of the increase in the movement of S^{-2} in and out of the electrode and the increase in the surface area of the fabricated electrode membrane as the increase in the movement of the solution particles is directly proportional to the increase in the surface area directly with the temperature (Fig. 2).

Response time

Figure 3 shows the response time of the electrode, it could be noticed that the response time within a range of concentrations between 10^{-2} and 10^{-6}M was between 5 and 17 s, and it is noticed that the response time is inversely proportional to the concentration of ions in the external solution. The concentration of ions increases in the external test solution, the response time decreases due to the easy access of the ions to the outer membrane of the electrode, and vice versa, as the concentration of ions decreases, the number of ions in the external solution will decrease, so it takes longer to reach a state of equilibrium in the electrode voltage.

Calibration curve

The standard calibration curve can be measured by preparing a series of solutions in question at concentrations ranging from $0.1 \cdot 10^{-1}$ to $0.1 \cdot 10^{-6}$M, then measuring the voltage by the prepared
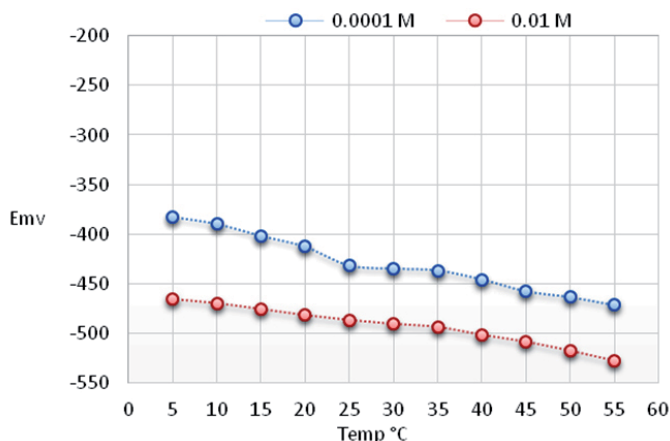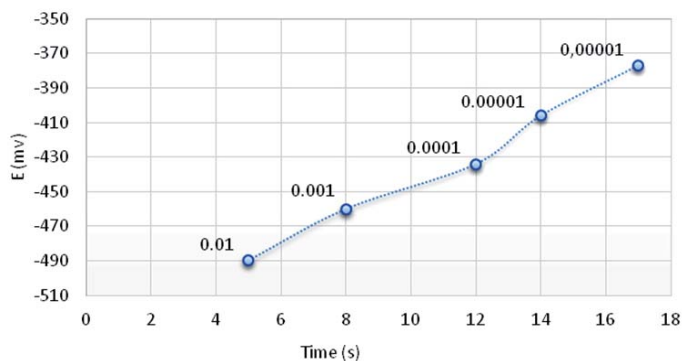

FIGURE 2. Effect of temperature on electrode response

FIGURE 3. The response time of the electrode

selective electrode and drawing the relationship between the electrode voltage versus $-\log[S^{-2}]$, while observing the movement of the model to affect the state of equilibrium. Figure 4 shows the effect of the concentration of the internal filling solution on the electrode response

per decade, which was close to the theoretical value 29.58 mv per decade, to be the concentration, and the electrode calibration curve the linear response of the opposites ranged between $1.00 \cdot 10^{-6}$ and $1.00 \cdot 10^{-1}$M and the minimum Nernst response $2.28 \cdot 10^{-7}$.
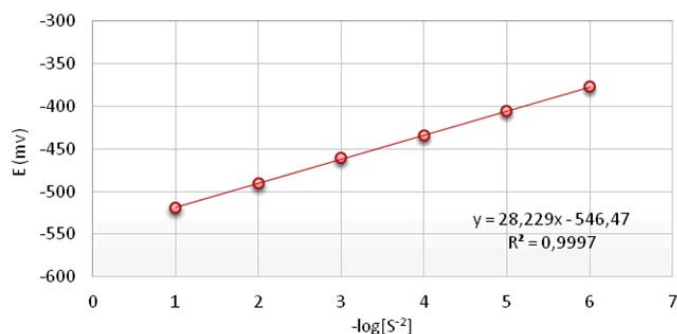
FIGURE 4. Standard curve of an electrode

after fixing the other conditions, temperature and pH where it was observed that the concentrations less than 10^{-6}M did not show any linear response and it was neglected in the subsequent experiments, and the internal filling solution was at concentration 10^{-6}M is the best internal packing solution because the best Nernst slope response 28.229 mv

Selectivity

Selectivity is the most important characteristic that determines the nature of an electrode and the extent to which it can be used successfully. The values of the selectivity coefficient (Table 2) were determined against the number of interfering ions, using the mixed solution method, the selectivity coefficient can be

TABLE 2. Selectivity values of $K_{A,B}^{Pot}$

Concentrations of Na$_2$S [M]		Interfering species 10^{-2}M
$K_{A,B}^{Pot}$ values		
10^{-4}	10^{-2}	
0.0470	0.0390	K^{+1}
0.0046	0.0320	Cu^{+2}
0.0081	0.0300	Zn^{+2}
0.0069	0.0490	Pb^{+2}
0.0053	0.0082	Cr^{+3}
0.0048	0.0270	Cl^{-1}
0.0064	0.0880	Br^{-1}
0.0710	0.0540	SO$_4^{-2}$

expressed by the relative error and concentration of the ion to be analyzed to the interfering ion by Eq. (1):

$$K_{A,B}^{Pot} = \frac{C_{A\min} \cdot P}{C_{B\max} \cdot 100} \tag{1}$$

$K_{A,B}^{Pot}$ – selectivity coefficient of the ion selection electrode (A) in the presence of the interfering ion (B),

$C_{A\min}$– the lowest expected concentration of the ion to be analyzed,
$C_{B\max}$– maximum expected concentration of the interfering ion,
P – permissible relative error when analyzing the ion (A) due to ion interference (B).

Accuracy and precision

Table 3 shows the accuracy and agreement of the results of the standard curve of the electrode, noting that the extent of convergence between the real value and the laboratory values of the concentrations: 10^{-2}, 10^{-4}, 10^{-6}M, and that the percentage recoverable values in

TABLE 3. Accuracy and compatibility of the results of the standard curve of the electrode

%REC	%RE	%RSD	Concentration thoughtful [M]	Electrode
99.9	−0.1	0.5772	10^{-2}	S^{-2}
103.7	3.7	0.7430	10^{-4}	
98.0	2.0	0.6352	10^{-6}	–

TABLE 4. Comparison method between the electrode and sulfur analyzer

%RE	Concentration of S^{-2} [mol·l^{-1}]		Sample
	Ag$_2$S electrode	sulfur analyzer	
3.92	$2.69 \cdot 10^{-2}$	$2.8 \cdot 10^{-2}$	S1
3.44	$3.00 \cdot 10^{-2}$	$2.9 \cdot 10^{-2}$	S2
−5.66	$2.83 \cdot 10^{-3}$	$3.0 \cdot 10^{-3}$	S3
0.50	$1.47 \cdot 10^{-2}$	$1.4 \cdot 10^{-2}$	S4
−3.25	$3.87 \cdot 10^{-4}$	$4.0 \cdot 10^{-4}$	S5
−5.68	$8.96 \cdot 10^{-4}$	$9.5 \cdot 10^{-4}$	S6
−3.88	$3.46 \cdot 10^{-4}$	$3.6 \cdot 10^{-4}$	S7
4.25	$8.32 \cdot 10^{-4}$	$8.0 \cdot 10^{-4}$	S8
6.15	$1.38 \cdot 10^{-3}$	$1.3 \cdot 10^{-3}$	S9
5.38	$2.74 \cdot 10^{-4}$	$2.6 \cdot 10^{-4}$	S10

the range of 98–103.7% for the concentrations chosen from the standard curve, and the highest value of the relative standard deviation (0.7430%). These results indicate high precision and electrode compatibility.

Applications

The method of comparison with the sulfur ion analyzer and the electrode that was the results was very close and the relative error was very small between the two methods, and this gives evidence of good selectivity and high sensitivity of the electrode as shown in Table 4.

Conclusion

The Ag/Ag$_2$S electrode proved to be a suitable tool for measuring the concentrations of sulfur ions in solutions as well as in industrial water that used in the petroleum industries. It is characterized by ease of manufacturing and use, and it has a fast response time, long life, good selectivity, and high sensitivity.

References

Anfalt, T. & Jagner, D. (1969). Effect of acetate buffer on the potentiometric titration of fluoride with lanthanum using a lanthanum fluoride membrane electrode. *Analitica Chimica Acta*, *47*(3), 483-494.

Arida, H.A., Ahmed, M.A. & El-Saied, A.M. (2003). A novel coated graphite rod Th(IV) ion selective electrode based on thorium oxinate complex and its application. *Sensors*, *3*(10), 424-437.

Bühlmann, P., Pretsch, E. & Bakker, E. (1998). Carrier-based ion-selective electrodes and bulk optodes. 2. Ionophores for potentiometric and optical sensors. *Chemical Reviews*, *98*(4), 1593-1688.

Cattral, R.W. (1997). *Chemical Sensors*. Oxford: Oxford University Press.

Ding, Q., Pan, Y.W., Huang, Y. F., Chen, C.T.A. & Ye, Y. (2015). The optimization of Ag/Ag2S electrode using carrier electroplating of nano silver particles and its preliminary application to offshore Kueishan Tao, Taiwan. *Continental Shelf Research*, *111*, 262-267.

Dulkiewicz, R. (1989). An alternative approach to workplace air monitoring. *Analyst*, *114*, 21-25.

Huang, D., Xu, B., Tang, J., Luo, J., Chen, L., Yang, L., Yang, Z. & Bi, S. (2010). Indirect determination of sulfide ions in water samples at trace level by anodic stripping voltammetry using mercury film electrode. *Analytical Methods*, *2*(2), 154-158.

Liu, Y., Zhao, B.T., Chen, L.X., & He, X.W. (2000). Liquid membrane transport and silver selective electrode based on novel bis(3-pyridinecarboxylate) calix[4]arene as ionophore. *Microchemical Journal*, *65*(1), 75-79.

Lusk, D., Gupta, M., Boinapally, K. & Cao, Y. (2008). Armoured against corrosion. *Hydrocarbon Engineering*, *13*(11), 115-118.

Mahajan, R.K., Kaur, I., Sharma, V. & Kumar, M. (2002). Sensor for silver (I) ion based on Schiff-base-p-tertbutylcalix [4] arene. *Sensor*s, *2*(10), 417-423.

Othmer, K. (eds.) (1981). *Encyclopedia of chemical technology*. Hoboken, NJ: John Wiley & Sons

Oyelami, B.O. & Asere A.A. (2011). Mathematical modeling: an application to corrosion in a petroleum industry. In *NMC Proceedings Workshop on Environment* (pp. 48-66). Abuja, Nigeria: National Mathematical Centre.

Popoola, L.T., Grema, A.S., Latinwo, G.K., Gutti, B. & Balogun, A.S. (2013). Corrosion problems during oil and gas production and its mitigation. *International Journal of Industrial Chemistry*, *4*(1), 1-15.

Shao, Y., Ying, Y. & Ping, J. (2020). Recent advances in solid-contact ion-selective electrodes: functional materials, transduction mechanisms, and development trends. *Chemical Society Review*, *49*(13), 4405-4465.

Skoog, D.A., Holler, F.J. & Nieman, T.A. (1998). *Principles of instrumental analysis*. Philadelphia: Saunders College Publishing.

Vesely, J., Jensen, O.J. & Nicolaisen, B. (1972). Ion-selective electrodes based on silver sulphide. *Analitica Chimica Acta*, *62*(1), 1-12.

Wroblewski, W. (2009). *Ion-selective electrodes*. Warsaw: Chemical Sensors Research Group.

Zaidan, T.A. (2007). Evaluation the precision of "doctore test" for mercaptans detection in petroleum products by sulphide ion-selective electrode. *Journal of University of Anbar for Pure Science*, *1*(3), 41-44.

Summary

Modified solid ion-selective electrode for potentiometric determination of sulfide in oil refineries water. A selective electrode was manufactured to determine the sulfur ions by sedimentation method in industrial waters in oil refineries of North Refineries Company, Baiji, Iraq. The linear response on a wide range of concentration (from $1.0 \cdot 10^{-1}$ to $1.0 \cdot 10^{-6}$M) Na_2S with a Nernst response of 28.229 mv per decade, theoretical value for slope of 29.58 mv per decade, correlation factor of 0.9998, detection limit of $2.287 \cdot 10^{-7}$ at 25–35°C, pH 6.0–12.0, and the best concentration of the filling solution of 10^{-6}M with a fast response time (5–13 s). The direct method were %RSD for 0.5772––0.7430, %RE for –0.1, 3.7 and %REC for 99.9, 103.7.

Authors' address:
Shatha Y. Al-Samarrai – corresponding author
(https://orcid.org/0000-0002-0389-1991)
Tikrit University
College of Science
Salahddin, Tikrit
Iraq
e-mail: dr.shatha81@tu.edu.iq

Elanda FIKRI[1, 2], Dhaifina HANIFATI[3], Nurul HIDAYAH[3]

[1]Diponegoro University, Doctorate Program of Environmental Studies
[2]Bandung Health Polytechnic, Center of Excellence
[3]Bandung Health Polytechnic, Department of Environmental Health

Differences in thickness variations of activated carbon in decreasing oil and grease levels using modified grease trap on the canteen wastewater

Key words: canteen wastewater, modified grease trap, thickness, activated carbon, oil, and grease

Introduction

Wastewater is residual water from either or both industrial activities and non-industrial activities. Non-industrial wastewater such as domestic wastewater is derived from human daily life activities related to water use according to the Indonesian Regulation of the Minister of Environment and Forestry No 68 of 2016 concerning domestic wastewater quality standards (Peraturan Menteri Lingkungan Hidup tentang baku mutu air limbah, BNRI No 1323, 2016). Domestic wastewater (greywater) is wastewater originating from kitchen activities, toilets, sinks, and more, which will cause water pollution and impact on the aquatic life when directly discharged into the environment without any prior treatment.

The characteristics of domestic wastewater are generally grouped into physical, chemical, and biological characteristics. The physical characteristics of domestic wastewater include TSS (suspended residue), chemical characteristics include pH, ammonium, COD, and BOD, while organic chemistry includes oil and grease, and biological characteristics such as total coliform according to the aforementioned regulation.

Wastewaters with those parameters are prohibited from being discharged into water bodies if they do not meet the predetermined quality standards. Wastewater quality standards are a tolerable limit or level of pollution in the wastewater that will be disposed or released into the water bodies as a result of either

or both industrial activities and non-industrial activities, according to the aforementioned regulation.

Currently, the most dominant pollutant in water bodies is domestic wastewater with a percentage that can reach up to 60–70%. Domestic wastewater consists of parameters such as BOD, TSS, pH, oil, and grease, when all these parameters are discharged directly into the water body it will cause water pollution (Faulconer & Mazyck, 2017).

Oil and grease are one source of contaminants that have not been handled properly in Indonesia (Abuzar, Afrianita & Notrilauvia, 2012). Oil and grease are one of the parameters with a number of maximum concentrations determined as a requirement for the discharge of industrial wastewater and surface water (Rahmi, 2016). High concentrations of oil and grease can damage aquatic ecosystems (Abuzar et al., 2012). Oil and grease contained in water bodies will form a layer on the surface because the density of oil is lower than the density of water. The layers of oil and grease will block the entry of sunlight thus the aquatic plants could not process photosynthesis. For that, the wastewater should be treated first to meet the predetermined quality standards.

Based on the quality standards used for domestic wastewater, namely the aforementioned regulation concerning the domestic wastewater quality standards, the quality standard for organic chemical wastewater for oil and grease is 5 mg·L^{-1}. This regulation must be applied by the wastewater producer, both industrial wastewater or domestic wastewater producer (Putu & Nieke, 2012).

PT. Sipatex Putri Lestari is a textile industry that facilitates a canteen in the company, the canteen operates every day at 11.00–13.00 Western Indonesian Time, as a result, PT. Sipatex Putri Lestari produces domestic wastewater as a residue of canteen kitchen activities. In February 2020 a laboratory test has been carried out to find out the concentration of oil and grease from the wastewater of residual kitchen activities with a result of oil and grease as 10.40 mg·L^{-1}. The examination was carried out by the West Java Provincial Laboratory using the gravimetric method based on the SNI 6989.10:2011 standard (Badan Standardisasi Nasional [BSN], 2011).

Based on the result, the concentration of oil and grease from the wastewater of residual kitchen activities at PT. Sipatex Putri Lestari does not meet the predetermined quality standards on the aforementioned regulation concerning domestic wastewater quality standards, the quality standard for organic chemical waste for oil and grease is 5 mg·L^{-1}. Therefore, it is necessary to carry out a wastewater treatment before discharging it into the water body.

Rahmi (2016) conducted research related to the reduction of oil and grease levels using various activated carbon, such as by using coconut shells, palm kernel shells, rice husks, and sawdust, with a thickness of 10 cm each. This activated carbon is used as an adsorption medium for domestic wastewater. The results of the research have stated that coconut shells and rice husks activated carbon was able to reduce oil and grease by 66.66%. Meanwhile, palm kernel shells activated carbon was only able

to reduce oil and grease by 29.16% and sawdust activated carbon was very ineffective because it was unable to reduce oil and grease (Rahmi, 2016).

Zaharah, Nurlina and Moelyani (2017) have also conducted research in 2017 related to reducing oil and grease levels using activated carbon modified grease traps. The results of the research stated that there was a decrease in oil and grease level, which was more effective, compared to simple grease traps without modification of activated carbon. The oil and grease in the wastewater that has passed through the grease trap will be passed through the container containing activated carbon and the output will be stored into a container. When passing through a 20 cm PVC pipe containing activated carbon, organic matter from oil and grease is reduced based on the principle of adsorption by activated carbon which can occur due to the pores that the adsorbent.

Activated carbon will be in contact with pollutants, where activated carbon will adsorb pollutant molecules until equilibrium conditions are reached. In this process, particles or molecules of pollutants will attach to the surface of activated carbon, which happened due to the difference in the weak charge between the two, this occurs due to the van der Waals Force (Zaharah et al., 2017). The van der Waals force is founded on the recognition that spontaneous, transient electric polarization can arise at a center due to the motion of electrons, molecular distortion, or molecular orientation. This polarization will act on the surrounding region to perturb spontaneous fluctuations elsewhere (Ninham & Parsegian, 1970). According to Wongth-

anate, Mapracha, Prapagdee and Arunlertaree (2014), modified oil traps have a higher efficiency of reducing TSS, BOD, oil, and grease than simple grease traps.

Based on this research, the researchers are interested in researching the differences in the thickness variation of activated carbon to reduce oil and grease levels using a modified grease trap on the canteen wastewater of PT. Sipatex Putri Lestari because the wastewater contains quite high levels of oil and grease. The modified grease trap is a grease trap reactor modified with activated carbon added to one of its parts, the purpose of modification or adding activated carbon is to increase the amount of reduction in oil and grease levels.

Rahmi (2016) conducted research using various variations of activated carbon with a thickness of 10 cm, the results of the study stated that it could reduce oil and grease levels by 66%. Zaharah et al. (2017) also conducted research using activated carbon, the thickness used was adjusted to the length of the PVC pipe used, which was 20 cm, the results showed the effectiveness in reducing oil and grease levels. Kasman, Riyanti, Sy and Ridwan (2018) also used additional activated carbon in reducing oil and grease levels by using water jasmine (*Echinodorus palaefolius*) with a thickness of activated carbon of 5 cm, but the results showed that the reduction in oil and grease levels was ineffective and it has still exceeded the determined quality standard.

Based on this, the thickness variations that will be used by the researcher are 10, 20 (that has been suggested by previous researchers) and 30 cm because Umar,

Baiquni and Ritohardoyo (2011) have stated that the thicker the media the better the results will be obtained s thus if the thickness is added to the arrangement of the media, it will be better in decreasing the oil and grease levels (Umar et al., 2011). Kasman et al. (2018) research stated that the lower the thickness of the activated carbon used, the less effective it is to reduce the existing oil and grease levels. As a result, the oil and grease levels produced are below the quality standard values that have been determined in the aforementioned regulation concerning domestic wastewater quality standards.

The type of activated carbon that will be used in this research is activated carbon from coconut shells. According to Rahmi (2016), the effective activated carbon in reducing the oil and grease is by using the coconut shell charcoal and rice husk charcoal. Tamado et al. (2013) stated that the use of basic material from coconut shells is not only used because of the affordable price and it's easy to obtain, but also because of the properties and characteristics of the content in the coconut shells both chemically and physically, coconut shells have a high carbon content thus they have the potential to become an alternative renewable energy source. A good coconut shell for activated carbon is an old and dry shell because its carbon content is higher than that of younger ones.

The utilization choice of activated carbon made from coconut shells is because coconut shells activated carbon has a wide surface, lightweight, and it has many pores thus it supports the attaching process of pollutants in the wastewater (Wardhani, Dirgawati & dan Alvina, 2013).

Material and methods

The type of research used is experimental research, which aims to determine the difference in the thickness variations of activated carbon to reduce oil and grease levels using a modified grease trap on the canteen wastewater of PT. Sipatex Putri Lestari. Concentrate on research used true experiment pretest posttest without control. The modified grease trap is a grease trap reactor with activated carbon added to one of its parts, the purpose of modification of activated carbon added is to increase the amount of reduction in oil and grease levels.

Work procedures

Table 1 lists tools and materials used for the research. The wastewater is passed through the modified grease trap with a thickness variation of activated carbon as 10, 20 and 30 cm.

Data processing

The data processing stage is carried out by doing the editing process, such

TABLE 1. Preparation of tools and materials used for research

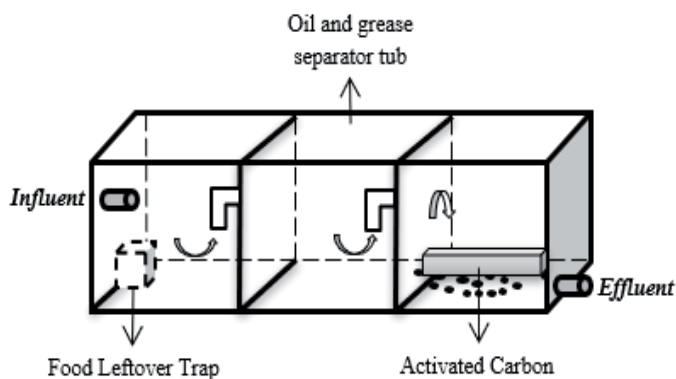| Tools/Materials	Size	Quantity
Grease trap	90 × 30 × 40 (30 × 30 × 40 of each chamber)	1
Pipe	0.0254 m	1 m
Pipe	0.0508 m	1 m
T-pipe	0.0508 m	2
Grill plat	–	0.5 m
Jerrycan	5 L	10
Activated carbon	10 kg	–
Canteen wastewater sample	100 L	–

FIGURE 1. Modified grease trap (Zaharah et al., 2017)

as rechecking the measurement results of the data, the coding process which is coding the measurement data, the data entry process which is entering the measurement results of the data into the data analysis software called SPSS for further analysis and the cleaning process which is the re-checking process of the measured data that has been entered to see any possibility of coding errors and incomplete measurement data for further correction process.

The data analysis used in this research is the univariate analysis and bivariate analysis. In this study, univariate analysis was used to determine the normality of the data using the Shapiro–Wilk test, the mean, minimum and maximum values and standard deviation values of the decreasing levels results in the measurements of oil and grease levels while the bivariate analysis was carried out using the one-way ANOVA test because the data results from the measurement of decreasing oil and grease levels is in the normal distribution.

Results and discussion

Temperature test result

The results obtained in measuring the temperature of the canteen wastewater before and after the treatment was ranging from 24 to 27°C (Fig. 2). The higher the temperature, the lower the viscosity, and density which will cause the liquid to flow quickly. The viscosity of a liquid will cause a certain amount of friction between parts or layers of fluid that move one against another. The friction or resistance that occurs is due to the cohesion force in the liquid, thus the viscosity of a liquid is due to the cohesion force between particles or molecules of the liquid. The change in temperature of the reaction causes the motion of the molecules to accelerate (collisions between reactant molecules increases) (Wahyuni, 2015).

The reduction in oil and grease level is affected by the room temperature that will transform grease into a solid form
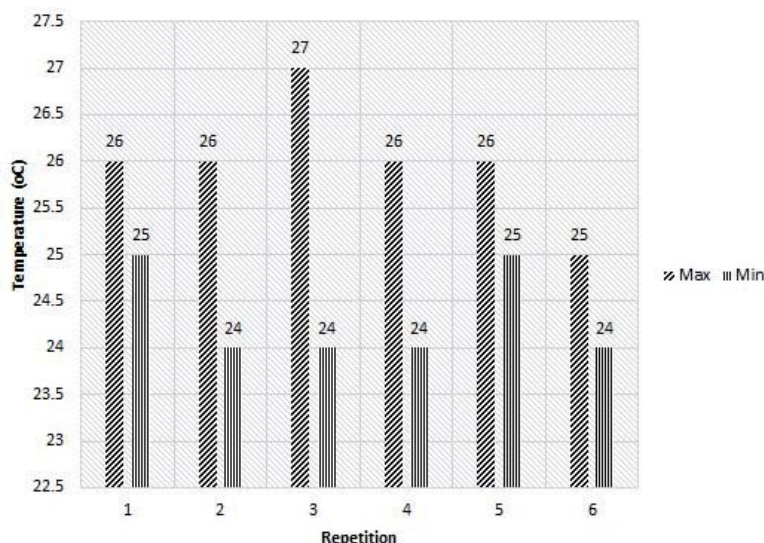
FIGURE 2. The temperature of canteen wastewater in PT. Sipatex Puti Lestari

and oil into a liquid form. When this situation occurs, it will make the adsorption process carried out by activated carbon easier. The temperature measured in this study corresponds to room temperature, which is in the range of 24–27°C.

The pH test result

The pH of wastewater from PT. Sipatex Putri Lestari ranges at 7.0–8.5, thus it can be concluded that the pH of the canteen wastewater tends to be alkaline due to the process of dish-washing using soap. The pH is one of the factors that affect the rate and ability of adsorption. At pH conditions greater than or equal to 7.0, the efficiency of reducing oil and grease concentration increases (Valencia, 2017). The pH of the wastewater is measured from PT. Sipatex Putri Lestari ranges from 7.0–8.5 with that result that the adsorption process to reduce oil and grease levels runs optimally (Fig. 3).
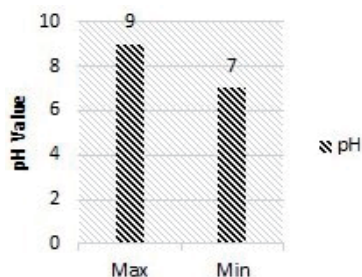

FIGURE 3. The pH test result

Measurement result of oil and grease levels of the wastewater

The oil and grease levels of the canteen wastewater before given treatment was at an average result of 27.4 mg·L^{-1}, and after being treated with a thickness variation of activated carbon using a modified grease trap, the oil and grease levels of activated carbon with a thickness of 10 cm was at an average of 15 mg·L^{-1}, activated carbon with a thickness of 20 cm was at an average of

TABLE 3. Measurement result of oil and grease level on each activated carbon thickness

Specification	10 cm activated carbon thickness		20 cm activated carbon thickness		30 cm activated carbon thickness	
	pretest	posttest	pretest	posttest	pretest	posttest
	$mg \cdot L^{-1}$					
Repitition 1	31.8	18.8	31.5	12.7	31.7	4.2
Repitition 2	23.1	13.2	23.4	11.6	23.8	2.2
Repitition 3	26.6	13.8	26.8	10.8	26.7	3.1
Repitition 4	25.5	12.9	25.7	9.7	25.8	2.8
Repitition 5	29.3	17.3	29.5	11.9	28.8	4
Repitition 6	27.8	14.2	27.9	12.2	27.3	3.5
Average	27.4	15.0	27.5	11.5	27.4	3.7
Max	31.8	18.8	31.5	12.7	31.7	4.5
Min	23.1	12.9	23.4	9.7	23.8	2.2
SD	3.03	2.43	2.85	1.08	2.70	0.66

11.5 mg·L^{-1}, and activated carbon with a thickness of 30 cm was at 3.7 mg·L^{-1} (Table 3).

The average result of the reduction in oil and grease levels with a thickness variation of 10 cm was at 12.32 mg·L^{-1} with a percentage of 49%, an average reduction in oil and grease levels with a thickness variation of 20 cm was at 15.98 mg·L^{-1} with a percentage of 62% and an average reduction in oil and grease levels of 13 cm thickness was at 23.67 mg·L^{-1}. The highest percent-age reduction in oil and grease levels occurred in the third treatment variation, which was the thickness variation of activated carbon at 30 cm with an average result of 86% in the reduction of oil and grease levels (Fig. 4).

Besides, the results of statistical tests, namely the post hoc test, have shown that activated carbon with a thickness of 30 cm obtained the greatest p-value 0.001) at 11.35 (95% $CI = 8.65 – 14.04$), which means that there is a very optimal
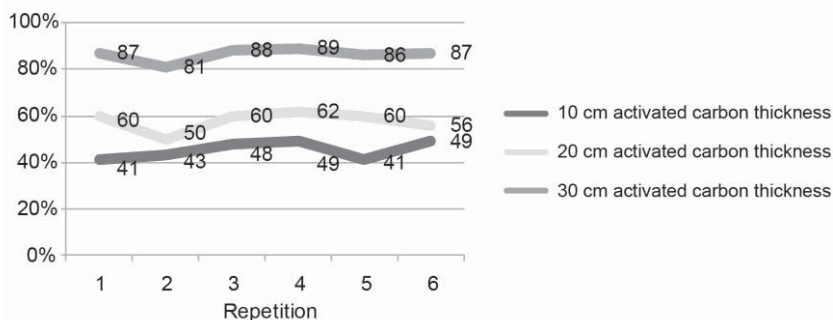

FIGURE 4. Percentage of reduction in oil and grease level

E. Fikri, D. Hanifati, N. Hidayah

difference in this variation. The reduction that occurs after the treatment with the thickness variation of activated carbon using a modified grease trap happened due to the sedimentation process where oil and grease particles will rise to the surface and then followed by the adsorption process where activated carbon will be in contact with the pollutants, activated carbon will adsorb pollutant molecules until equilibrium conditions are reached. The reduction in oil and grease levels of PT. Sipatex Putri Lestari occurs because of the physical processing, namely the sedimentation and adsorption process with activated carbon adsorbents using a modified grease trap. Sedimentation is a deposition process in which these oils and grease will float to the surface of the water because the oil density is lower than the water density. Adsorption is either or both physical and chemical processes in which the substance accumulates on a surface layer of the absorbent substance.

In this process, particles or molecules of pollutants will attach to the surface of the activated carbon which is caused by the difference of the weak charge between the two, this occurs due to the van der Waals force (Zaharah et al., 2017).

Activated carbon is a carbon-based material that has a broad surface and internal porous structure with a pore distribution that varies in size, and a broad spectrum of oxygenated functional groups (Wardhani et al., 2013; Faulconer & Mazyck, 2017; Valencia, 2017). The type of activated carbon used in this study is coconut shell-based activated carbon. Because coconut shells are very easy to obtain and they are one of the abundant renewable resources, one of the efforts made to utilize them is by processing coconut shells into activated carbon. This activated carbon material is widely used in industry, especially in the field of oil, water treatment, gas, food, beverage, medicine, and chemical industry (Rizky, 2017). According to Rahmi (2016), the effective type of activated carbon used in the filtration in reducing the value of oil and grease is coconut shell charcoal and rice husk charcoal.

The particle size of activated carbon used in this study was 8–16 mesh, the type of activated carbon used was coconut shell. In the research of Putu and Nieke (2012), activated carbon with a diameter of 1.19 mm (16 mesh) had the best removal efficiency to reduce oil levels. The smaller the media diameter, the greater the effective surface area, which will increase the ability to absorb organic pollutants. The thicker the activated carbon used, the more activated carbon particles will absorb the levels of oil and grease in the canteen wastewater of PT. Sipatex Putri Lestari, this also affects the increase of contact time of pollutants with activated carbon particles. Therefore, the thickness of activated carbon affects the reduction in oil and grease levels of PT. Sipatex Putri Lestari. The reduction that occurred in the 30 cm thickness variation of activated carbon reached the most optimal and effective point in reducing oil and grease levels of the canteen wastewater at PT. Sipatex Putri Lestari has finally met the requirements whereas the result was following the quality standard because it does not exceed the maximum of 5 mg·L^{-1} based on the aforementioned regulation concerning domestic wastewater quality standards.

The flow rate used in the research was 2.22 L·min^{-1} which is adjusted to the existing flow rate conditions in the industry so that the condition or characteristics of the flowing water will be similar to as it was in the industry.

Conclusions

The reduction in oil and grease level that has occurred was at an average of 12.32 mg·L^{-1} and the percentage of reduction in oil and grease levels of canteen wastewater with thickness variation of activated carbon at 10 cm was 49%, 20 cm was 62% (average: 15.98 mg·L^{-1}), and 30 cm was 89% (average: 23.67 mg·L^{-1}).

Based on the result the most effective reduction of oil and greases levels using the modified grease trap in the canteen wastewater of PT. Sipatex Putri Lestari, was a variation thickness of activated carbon at 30 cm. Because it can reduce the oil and grease levels of the wastewater with a percentage of 89% and the result has met the quality standards which is maximum at 5 mg·L^{-1} based on with the aforementioned regulation concerning domestic wastewater quality standards.

References

Abuzar, S.S., Afrianita, R. & Notrilauvia, N. (2012). Removal of oil and grease from hotel wastewater using corn husk powder. *Journal of Environmental Engineering*, *9*(1), 13-25.

Badan Standardisasi Nasional [BSN] (2011). *Air dan air limbah – bagian 10: cara uji minyak nabati dan minyak mineral secara gravimetri* [*Water and wastewater – Part 10: Gravimetric examination of oil and grease*] (SNI 6989.10:2011). Jakarta: Badan Standardisasi Nasional [transl. from Indonesian]. Retrieved from: http://lib.kemenperin.go.id/neo/detail.php?id=225757

Faulconer, E.K. & Mazyck, D.W. (2017). Effect of surface oxygen activated carbon on adsorption of elemental mercury from aqueous solutions. *Journal of Environmental Chemical Engineering*, *5*(3), 2879-2885.

Kasman, M., Riyanti, A., Sy, S. & Ridwan, M. (2018). Reduksi pencemar limbah cair industri tahudengan tumbuhan melati air (*Echinodorus palaefolius*) dalam sistem kombinasi constructed wetland dan filtrasi [Reduction of the pollution parameters in tofu industry wastewater by water jasmine plant (*Echinodorus palaefolius*) in constructed wetland and filtration combination system]. *Jurnal Litbang Industri*, *8*(1), 39-46.

Nilasari, E., Faizal, M. & Suheryanto, S. (2016). Pengolahan air limbah rumah tangga dengan menggunakan proses gabungan saringan bertingkat dan bioremediasi eceng gondok (*Eichornia crassipes*), (Studi kasus di Perumahan Griya Mitra 2, Palembang) [Household wastewater treatment using a combined process of multi-level sieves and water hyacinth (*Eichornia crassipes*) in bioremediation (case study at Griya Mitra 2 housing complex, Palembang)]. *Jurnal Penelitian Sains*, *18*(1), 18102-18108.

Ninham, B.W. & Parsegian, V.A. (1970). Van der Waals forces: special characteristics in lipid-water systems and a general method of calculation based on the Lifshitz theory. *Biophysical Journal*, *10*(7), 646-663.

Peraturan Menteri Lingkungan Hidup dan Kehutanan Republik Indonesia nomor: P. 68/Menlhk/Setjen/Kum. 1/8/2016 tentang baku mutu air limbah domestik [Regulation of the Minister of Environment and Forestry of the Republic of Indonesia No 68 of 2016 concerning domestic wastewater quality standards]. Berita Negara Republik Indonesia No 1323, 2016 [transl. from Indonesian]. Retrieved from: http://ditjenpp.kemenkumham.go.id/arsip/bn/2016/bn1323-2016.pdf

Putu, A.R.P. & Nieke, K. (2012). *Car wash wastewater treatment with oil separator and activated carbon reactor* (unpublished doctoral

dissertation). Institut Tekhnologi Surabaya, Surabaya.

Rahmi, A. (2016). Wastewater treatment into non--consumptive domestic water with biosand filter activated carbon variations. *Journal of Civil Engineering Cycle*, *2*(1), 58-66.

Rizky, R.Y. (2017). *Wastewater treatment system design in office buildings (case study: 'Mipa Tower' Office Building ITS Surabaya)* (unpublished doctoral dissertation). Institut Tekhnologi Surabaya, Surabaya.

Tamado, D., Budi, E., Wirawan, R., Dwi, H., Tyaswuri, A., Sulistyani, E. & Asma, E. (2013). Sifat termal karbon aktif berbahan arang tempurung kelapa [Thermal properties of activated carbon coconut shell-based charcoal]. *Prosiding Seminar Nasional Fisika (e-Journal)*, *2*(1), 73-81.

Umar, M.A., Baiquni, M. & Ritohardoyo, S. (2011). Peran masyarakat dan pemerintah dalam pengelolaan air limbah domestik di wilayah ternate tengah [Role of community and government in domestic wastewater management in the central ternate region of Yogyakarta]. *Majalah Geografi Indonesia*, *25*(1), 42-54.

Valencia, S.M. (2017). *Study literature: industrial waste oil and grease processing* (unpublished doctoral dissertation). Institut Technologi Sepuluh Nopember, Surabaya.

Wahyuni, S. (2015). Pengaruh suhu proses dan lama pengendapan terhadap kualitas biodiesel dari minyak jelantah [The effect of temperature process and deposition time on the quality of biodiesel from used cooking oil]. *Pillar of Physics*, *6*(3), 33-40.

Wardhani, E., Dirgawati, M. & dan Alvina, I.F. (2013). Kombinati proses presipitasi dan adsorpsi karbon aktif dalam pengolahan air limbah industri penyamakan kulit [The combination process of precipitation and activated carbon adsorption in wastewater treatment tannery industry]. *Lingkungan Tropis*, *7*(1), 39-52. Retrieved from: http://lib.itenas.ac.id/kti/wp-content/uploads/2014/04/6_JLT_v7n1_EKAWARDHANI2.pdf

Wongthanate, J., Mapracha, N., Prapagdee, B. & Arunlertaree, C. (2014). Efficiency of modified grease trap for domestic wastewater treatment. *The Journal of Industrial Technology*, *10*(2), 10-22.

Zaharah, T.A., Nurlina, N. & Moelyani, R.R.E. (2017). Reduksi minyak, lemak, dan bahan organik limbah rumah makan menggunakan grease trap termodifikasi karbon aktif [Reduction of oil, grease, and organic materials from restaurant waste using activated carbon modified grease traps]. *Jurnal pengelolan Lingkungan Berkelanjutan – Journal of Environmental Sustainability Management*, *1*(3), 25-32.

Summary

Differences in thickness variations of activated carbon in decreasing oil and grease levels using modified grease trap on the canteen wastewater. Wastewater is residual water of industrial activities and domestic wastewater that is derived from daily activities of human life related to water usage, such wastewater should not be discharged into water bodies if it has not met the standards based on the regulation. Oil and grease contained in the water bodies will form a layer on the surface because the density of oil is lower than the density of water. The layer of oil and grease will block the entry of sunlight and cause the inability in the photosynthesis process of aquatic plants. The textile industry facilitates canteens within the company which operates daily at 11.00–13.00 Western Indonesian Time, resulting in the domestic wastewater from the canteen kitchen activities. The purpose of this study was to determine differences in the thickness variations of activated carbon to reduce oil and grease levels using modified grease traps on the canteen wastewater at PT. Sipatex Putri Lestari. The type of study used was categorized as a field experiment with a pretest–posttest research design. The population of the study was the entire canteen wastewater of PT. Sipatex Putri Lestari. The sampling technique used the time composite method. The univariate analysis of the study showed the average number of decreases in oil and grease levels in the treatment as 12.32, 15.98 and 23.67 mg$\cdot$L^{-1}. The bivariate data analysis

used the one-way ANOVA test. The results of the experiment on the three thickness variations of activated carbon within six times repetitions resulted in a decrease of oil and grease levels, which is 49% at 10 cm, 62% at 20 cm, and 88% at 30 cm. The conclusion of the study showed differences in the thickness variations of activated carbon to reduce oil and grease levels using a modified grease trap on the canteen wastewater at PT. Sipatex Putri Lestari. Furthur suggestions for this study are to determine the saturation period of activated carbon and periodic maintenance of the tool.

Authors' address:
Elanda Fikri – corresponding author
(https://orcid.org/0000-0001-7196-6011)
Diponegoro University
Doctorate Program of Environmental Studies
Semarang 50241
Indonesia
e-mail: elandafikri@yahoo.com

Pham Thi Hai HA, Nguyen Thi HOA, Pham Tien BINH
National University of Civil Engineering, Faculty of Architecture and Planning

Simple method to improve the TCXDVN 306:2004 indoor climate standard for closed office workplaces in Vietnam

Key words: thermal comfort, artificial indoor environment, standard indoor climatic parameters, office workplaces, energy efficient building, Vietnam

Introduction

People spend 86.9% of the day living, working, and relaxing in indoor environments (Klepeis et al., 2001). Accordingly, indoor thermal comfort is regarded as one of the most significant factors affecting environmental satisfaction (Nasrollahi, Knight & Jones, 2008). Undesirable thermal conditions can lead to occupant dissatisfaction which, in turn, has an adverse effect on their productivity, performance (Budaiwi, 2006). Thermal comfort is also critical to planning for energy efficient building design and overall post-occupancy evaluations.

The ANSI/ASHRAE 55-2017 standard defines the term thermal comfort as the condition of mind that expresses satisfaction with the thermal environment and is assessed by subjective evaluation (American National Standards Institute/ /American Society of Heating, Refrigerating and Air-Conditioning Engineers [ANSI/ASHRAE], 2017). The factors affecting thermal comfort is normally dependent on four environmental parameters (dry bulb temperature, air humidity, air velocity and mean-radiant temperature) and two personal (clothing-insulation and physical activity) parameters (Szokolay, 2004). In office buildings, indoor temperature is one of the main influencing factors: direct (when thermal comfort is not obtained) as well as indirect (when sick building syndrome symptoms occur).

Overview of common assessment measures for thermal comfort worldwide

Initially, the definition of thermal comfort stems from effective temperature (ET), proposed by Houghten and Yagloi (1923). The effective temperature inte-

grates air temperature, air humidity, and wind velocity into one unique environmental indicator. In 1932, the ASHRAE published a nomogram representing the index of effective temperature (*ET*). They used the *ET*, which would be used extensively over the next 50 years.

From the early 1960s there were many researchers working in the field of thermal comfort. The best-known and most influential theory was Fanger's new model (1970). It is the model of thermal comfort – the predicted mean vote (*PMV*), focusing on the relationship between the physical parameters of the environment, the physiological parameters of people and the perception of comfort expressed by people themselves. The *PMV* indicator predicts the level of thermal comfort on a seven-grade sensation scale (−3: cold, −2: cool, −1: slightly cool, 0: neutral, +1: slightly warm, +2: warm, +3: hot). As a follow-up to the *PMV* index, Fanger introduced the index of predicted percentage of dissatisfied (*PPD*), includ-

ing the human factor, showing the majority percentage of respondents who feel either satisfied or unsatisfied with their working or living environment (Fig. 1). This *PMV* is used in the ISO 7730-2005 (International Organization for Standardization [ISO], 2005) and the ANSI/ /ASHRAE 55-2017 standard. This model is often applied to buildings using air conditioning systems when building occupants are allowed to adjust the indoor environmental conditions to the desired level of thermal balance.

During the 1980s, Michael Humphreys initiated discussion about adaptive principles related to thermal comfort. De Dear, Brager and Cooper (1997) developed an adaptive model of thermal comfort: they predicted the temperature of comfort based on new findings of self--regulation of human bodies and applied that to naturally ventilated buildings. This research was subsequently included in both the ANSI/ASHRAE 55-2017 and the BS EN 16798-1:2019 standard (Brit-
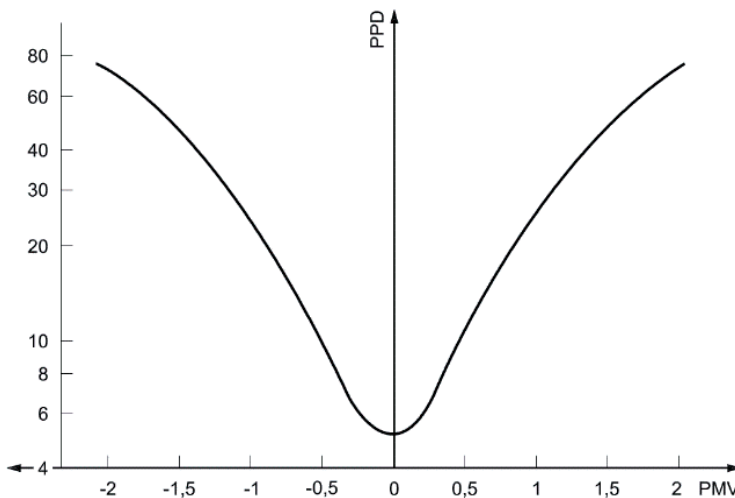

FIGURE 1. The predicted percentage of dissatisfied index (*PPD*) as function of the predicted mean vote index (*PMV*)

ish Standards Institution [BSI], 2019). De Dear and Brager (2002) discussed the process of publishing a new adaptive comfort standard incorporated into the ANSI/ASHRAE 55-2017 standard that allows warmer indoor temperatures for naturally ventilated buildings during summer and in warmer climate zones.

Various field studies on the concept of thermal comfort have been carried out on office buildings with ducted air-conditioning systems by different objectives, methods, and in different climate zone in recent years. Bakhtiari, Akander and Cehlin (2020) study on thermal comfort by on-site measurements, BMS data logging and standardized questionnaire in the historic City Hall of Gävle, Sweden. Szabo and Kajtar (2018) carried on-site measurements in office buildings with different air-conditioning systems during the summer season for thermal comfort analysis, using *PMV*, *PPD* model and the local discomfort based on draught rate (*DR*). De Vecchi, Candido, de Dear and Lamberts (2017) carried the indoor climatic field studies by measurements and online questionnaires in three office buildings with two different environmental control strategies (two with mixed-mode ventilation and one with permanent air-conditioning). The results obtained in this study are used as a baseline for a Brazilian thermal comfort standard. Simons, Koranteng, Adinyira and Ayarkwa (2014) used quantitative survey along with questionnaires to assess the thermal comfort in multi storey (naturally and mechanically ventilated) office buildings in Accra, Ghana, using the *PMV* and the *PPD* models. Tao, Li, Qiu and Zhang (2014) studied the indoor air environmental conditions of three

different typical office buildings in Xi'an (China) by actual measurement and questionnaire survey. This study noticed that there was a remarkable difference between the *PMV* index and actual-measurement thermal sensation vote (*TSV*) in evaluating indoor thermal environments in typical office buildings.

Overview of studies on thermal comfort for Vietnamese people

In the 1960s and 1980s, many scientists in Vietnam conducted research projects on human thermal comfort in houses and low-rise office buildings. Tables 1 and 2 summarize the results.

Dung (1995) in research of human thermal comfort in Vietnam found that the relationship between temperature and humidity greatly impacts human comfort under hot and humid climate conditions. Nguyen (2002) carried out several tests regarding thermal comfort on some students in Hanoi and Vinh city. However, his research outcomes were just about an assessment of an expansion of the thermal comfort zone, especially towards higher air humidity and wind velocity. The research results published by Nguyen, Singh and Reiter (2013) showed a neutral level of temperature in ASEAN countries would be 27.1°C for a naturally ventilated room and 25.9°C for an air-conditioned room, these values approximate those shown in Table 2. In recent years, there were some studies on micro-climate conditions in educational and residential buildings in Ho Chi Minh City and Da Nang and in few office buildings in Hanoi (e.g. Huong, 2001; Khanh, 2011; Nguyen, Singh

TABLE 1. Effective temperature-based limit indicators of thermal comfort in research projects in Vietnam from the 1960s to 1980s

Researcher	Season	Cold	Slightly cold	Comfortable			Slightly hot	Hot
				lower limit	completely comfortable	upper limit		
				°C				
Dang (1981)*	summer	–	–	–	24.4	27.0	28.5	≥ 29.2
	winter	≤ 17.3	18.5	20.0	23.3	26.5	–	–
Con (1985)	summer	–	–	18.8	23.0	27.0	–	–
	winter	–	–	16.7	21.0	24.7	–	–
Anh (1984)	–	–	–	20.0	23.7	27.5	–	–

*The *ET* values investigated by Dang (1981) can be determined by means of *ET* nomogram of the American Society of Heating and Ventilating Engineers (ASHVE).

TABLE 2. Limit values of thermal comfort subject to air temperature in studies in Vietnam from the 1960s to the 1980s

Researcher	Season	Air temperature [°C]			Air humidity [%]	Wind velocity [m·s⁻¹]
		lower limit of comfort	completely comfortable	upper level of comfort		
Dang (1981)	summer	–	25.5	29.5	80	0.3–0.5
	winter	21.5	24.5	29.0	80	
Thiem (1984)	–	23.0	24.0–25.0	26.0–27.0	60–80	0.1
Phong, Uyen, Lanh & Anh (1984)	–	–	–	28.9	84	–

& Reiter, 2012; Tuan & Le, 2015; Tuan, Dung & Vinh, 2016; Nguyen & Tran, 2017). Dung and Kien (2019) provides an overview of situation of energy consumption and indoor conditions of office buildings in major cities of Vietnam, and gives some ideas for improving the energy efficiency and indoor comfort of office buildings.

In Vietnam, there has been so far only one standard – the TCXDVN 306:2004, which determines standard micro-climatic specifications applicable to office workplaces (Ministry of Construction of Vietnam, 2004). Nevertheless, in fact, this standard is rarely used, because of the following shortcomings and disadvantages:

– It specifies the standard values for micro-climate parameters on the basis of the "Scale of thermal comfort for Vietnamese people" proposed by Dang (1981) (as presented in Tables 1 and 2). That comes from an experimental study on 1,100 participants conducted by Dang (1981) in 1966––1967. This scale of thermal comfort corresponds to the 50% probability

of the total number of participants in the *PMV* experiment regarding their thermal comfort, while according to the requirement of the ISO 7730--2005, the ANSI/ASHRAE 55-2017, the standard micro-climate parameters are divided into three categories: Category A (*PMV* = 90%), Category B (*PMV* = 80%), and Category C (*PMV* = 70%).

– It does not specify clearly what kind of indoor environment it should be: natural or artificial;

– It was formulated primarily in reference to Russian standard the GOST 30494-1996 (Standartinform, 1996), while the climate conditions in Russia are very different from those in Vietnam.

Most of the office buildings in Vietnam today are equipped with air-conditioning systems, either local or central systems with various design and installation concepts. Technically, this is the best solution to control the indoor climate in office buildings in a hot and humid tropical country. For this reason, it is necessary to investigate the current situation of indoor climate conditions of workplaces in office buildings in all three regions of Vietnam: North, Central and South, so that the aforementioned Vietnamese standard can be properly adjusted to meet the real demand for thermal comfort as well as for energy efficiency required in a highly comfortable built environment.
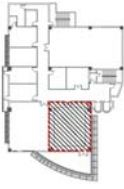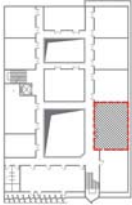
Material and methods

In order to evaluate the current situation of indoor climate conditions and thermal comfort in closed office work-

places, the two methods were used as follows: physical measurements and questionnaires survey. More specifically:

– Area of survey: Five office buildings, of which two buildings are located in Hanoi, one in Da Nang, and two in Ho Chi Minh City. The pictures and data for these five office buildings are shown in Table 3 (exemplary measuring points location in Fig. 2). In each 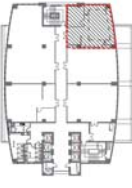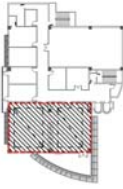office building, two rooms were selected, one on a middle floor and one on an upper floor, or two on the same floor but facing different directions.

– Time of surveys: In Hanoi, there are two distinct seasons (winter and summer) and the worst case time for surveying in Hanoi is during the hottest months of the year (July and August) as well as in the coldest months of the year (January and February). In Da Nang and Ho Chi Minh City, it is warm throughout the year, therefore the time for surveying should also be in July for Da Nang and in April for Ho Chi Minh City. Each office building was measured within one day, during five time intervals: 8:00––8:30, 10:00–10:30, 12:00–12:30, 14:00–14:30, 16:00–16:30.

– One paper questionnaire had been prepared beforehand to evaluate the quality of indoor climate subject to the individual feelings of the occupants working in a room selected for survey.

– Measurement data: Indoor climate conditions, including air temperature – T_{in} [°C], indoor air humidity – φ_{in} [%], indoor air velocity – v_{in} [m·s^{-1}] and mean-radiant room surface temperatures – *TR* [°C]; outdoor weather

TABLE 3. Buildings selected for survey

|	Hanoi		Da Nang	Ho Chi Minh City	
	A1-NUCE	GELEX	EVNCPC	BITEXCO Nam Long	IPC
Photo					
Storeys	6 storeys	22 storeys	9 storeys	12 storeys	20 storeys
Air conditioning	split type air conditioning	semi-central air conditioning	central air conditioning	central air conditioning	central air conditioning
Mode	one-way for cooling	two-way: heating and cooling	one-way for cooling	one-way for cooling	one-way for cooling
Floor plan					
Location	Location of room 205 (in 2rd floor)	Location of room 702 (in 7th floor)	Location of measurement room in 3rd floor	Location of measurement room in 2nd floor	Location of measurement room in 10th floor
Floor plan					
Location	Location of room 602 (in 6th floor)	Location of room 705 (in 7th floor)	Location of measurement room in 5th floor	Location of measurement room in 8th floor	Location of measurement room in 17th floor
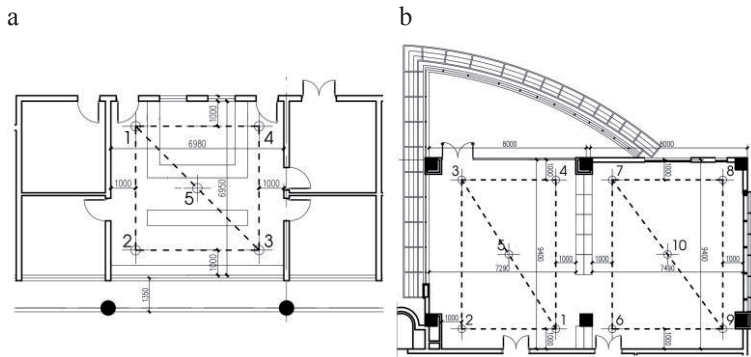
FIGURE 2. Location of measuring points in: a – room 205 of A1-NUCE building; b – room of 5th floor of EVNCPC building

conditions, including air temperature – T_{out} [°C], air humidity – φ_{out} [°C] and air velocity – v_{out} [m·s^{-1}]. The measurements of indoor and outdoor climate conditions were taken in accordance with the TCXDVN 306:2004 standard.

–   Measurement positions: The following parameters T_{in}, φ_{in}, v_{in} were measured at least five points evenly distributed in the room workplaces, at the level of 1.2 m from the floor; parameter TR was measured at the middle point of the room. Outdoor weather conditions were measured one point only, representing the surrounding area of the building, also at 1.5 m level from the ground.

In order to assess thermal comfort, the ET and the PMV indicators were used. The ASHRAE ET nomogram was used to calculate the ET indicators. A program called CBE Thermal Comfort Tool (Tartarini, Schiavon, Cheung & Hoyt, 2020), was used to calculate the PMV indicators.

Results and discussion

Outdoor and indoor climate conditions

In Hanoi, two surveys were conducted in winter of 2018: on January 18th (A1 Building at the NUCE) and on February 5th (GELEX Building) and two surveys were conducted in summer of 2018: on August 21st (A1 Building at the NUCE) and on July 5th (GELEX Building) during working hours (from 8 am to 5 pm).

In Da Nang, a survey was conducted on July 27th 2018 during working hours in EVNCPC Building.

In Ho Chi Minh City, two surveys were conducted in 2018: on April 12th (Bitexco Nam Long Building) and on April 13th (IPC Building) during working hours.

Tables 4, 5 and 6 illustrate the results of outdoor and indoor climate conditions (air temperature, air humidity and air velocity) during working hours in measuring days in Hanoi, Danang and

TABLE 4. The results of outdoor and indoor climate conditions in winter measuring days in Hanoi

January 18th 2018 – cold winter day (A1-NUCE, with doors closed, without heating)			February 5th 2018 – very cold winter day (GELEX, with heating systems)		
Outdoor	Room 205	Room 602	Outdoor	Room 702	Room 705
T_{out} = 16.1–22.4°C	T_{in} = 22.6–23.3°C	T_{in} = 22.6–24.9°C	T_{out} = 12.6–17.0°C	T_{in} = 20.7–24.4°C	T_{in} = 22.7–24.0°C
φ_{out} = 71.8–80.9%	φ_{in} = 73.0–75.8%	φ_{in} = 71.3–75.8%	φ_{out} = 43.8–47.5%	φ_{in} = 30.8–38.2%	φ_{in} = 34.3–38.2%
$v_{out(mean)}$ = 0.96 m·s⁻¹	v_{in} = 0.05–0.1 m·s⁻¹	v_{in} = 0.05–0.1 m·s⁻¹	$v_{out(mean)}$ = 3.3 m·s⁻¹	v_{in} = 0.05–0.1 m·s⁻¹	v_{in} = 0.05–0.1 m·s⁻¹
×	ET = 20.6 – 21.8	ET = 21.0–22.8	×	ET = 17.1–19.9	ET = 18.8–19.7
	PMV = 0.52–0.91	PMV = 0.61–1.19		PMV = (−0.15)–0.45	PMV = 0.23–0.36
	PPD = 11–23%	PPD = 13–35%		PPD = 5–9%	PPD = 6–8%

August 21st 2018 – very hot summer day (A1-NUCE, with split air conditioning systems)			July 5th 2018 – extremely hot summer day (GELEX, with cooling systems)		
Outdoor	Room 205	Room 602	Outdoor	Room 702	Room 705
T_{out} = 32.3–34.5°C	T_{in} = 26.3–27.6°C	T_{in} = 27.1–28.7°C	T_{out} = 35.3–37.1°C	T_{in} = 25.0–26.6°C	T_{in} = 24.4–25.1°C
φ_{out} = 69.0–81.2%	φ_{in} = 59.2–67.9%	φ_{in} = 56.5–60.1%	φ_{out} = 48.3–54.9%	φ_{in} = 48.1–66.3%	φ_{in} = 48.1–55.5%
$v_{out(mean)}$ = 0.6 m·s⁻¹	v_{in} = 0.05–0.1 m·s⁻¹	v_{in} = 0.2–0.4 m·s⁻¹	$v_{out(mean)}$ = 0.6 m·s⁻¹	v_{in} = 0.05–0.1 m·s⁻¹	v_{in} = 0.05–0.1 m·s⁻¹
×	ET = 23.3–24.5	ET = 23.4–24.6	×	ET = 22.2–23.6	ET = 20.8–21.4
	PMV = 0.44–0.63	PMV = 0.8–1.24		PMV = (−0.28)–0.23	PMV = (−0.34)–0.7
	PPD = 9–13%	PPD = 18–37%		PPD = 5–7%	PPD = 5–15%

TABLE 5. The results of outdoor and indoor climate conditions in measuring day in Da Nang

July 27th 2018 – hot day (EVNCPC, with cooling systems)		
Outdoor	Room of 3rd floor	Room of 5th floor
T_{out} = 28.0–29.8°C	T_{in} = 26.6–27.1°C	T_{in} = 25.5–26.4°C
φ_{out} = 69.5–80.7%	φ_{in} = 59.5–63.8%	φ_{in} = 53.5–60.5%
$v_{out(\text{mean})}$ = 0.3 m·s^{-1}	v_{in} = 0.05–0.1 m·s^{-1}	v_{in} = 0.05–0.1 m·s^{-1}
×	ET = 23.5–24.1	ET = 22.1–23.1
	PMV = 0.66–0.76	PMV = 0.08–0.58
	PPD = 14–17%	PPD = 5–12%

Ho Chi Minh City. These micro-climatic survey measurement results have been transformed into ET values and PMV, PPD indicators. Because the office occupants all use computers at work, the research team estimated human metabolic heat to be 1.1 met (typing) as specified in the BS EN 16798-1:2019 and the ANSI/ASHRAE 55-2017 standard while calculating PMV and PPD indicators. Clothes heat resistance would be 0.5 clo during summer, and 1.0 clo during winter, in office rooms with heating systems (GELEX Building), and 1.2 clo in office rooms without heating systems (A1 Building at the NUCE).

The number of questionnaires collected corresponded with the number of officers/staffs working in those office workplaces on their respective survey days. One hundred thirty-two questionnaires were collected. Figure 5 compares results of thermal comfort subject to temperature expressed by the staffs in measured office workplaces during winter and summer times. With regard to air humidity: in office rooms with relative humidity lower than 60%: 87.2% of the staff said that air humidity was at a moderate level, 12.8% felt too dry. In rooms with relative humidity between 60 and 75%:

85% of the staff said that air humidity was at a moderate level while 15% felt too dry. Also with regard to wind velocity: 72.6% said that wind velocity was at a moderate level; 25% said that it lacked air movement, while 2.4% felt that it was windy.

The study results showed that:

– Average relative humidity in office workplaces in buildings with air conditioning systems varied between 46 and 64%. Air velocity distributed within 0.05–0.2 m·s^{-1} (most cases approximately 0.1 m·s^{-1}), this value is similar to the average air velocity (0.04 m·s^{-1}) of the indoor thermal environments survey in three office buildings in the city of Xi'an (Tao et al., 2014). In the meantime, the TCXDVN 306:2004 standard requires that wind velocity should be 0.3–0.5 m·s^{-1} for 80% humidity. Thus, humidity and wind velocity values in the mentioned standard should not apply to air-conditioned buildings.

– Due to adaptation to very humid environment in hot and humid tropical climates, 85% of the staff in rooms with air humidity between 60 and 75% felt comfortable with this hu-

TABLE 6. The results of outdoor and indoor climate conditions during measuring days in Ho Chi Minh City

April 12th 2018 – very hot day (Bitexco Nam Long, with cooling systems)			April 13th 2018 – very hot day (IPC, with cooling systems)		
Outdoor	Room of 2nd floor	Room of 8th floor	Outdoor	Room of 10th floor	Room of 17th floor
T_{out} = 29.7–36.1°C	T_{in} = 23.3–25.8°C	T_{in} = 26.1–27.3°C	T_{out} = 29.7–33.6°C	T_{in} = 24.5–25.9°C	T_{in} = 23.9–26.4°C
φ_{out} = 50.2–65.1%	φ_{in} = 42.1–51.5%	φ_{in} = 35.6–43.7%	φ_{out} = 54.8–64.8%	φ_{in} = 43.7–48.8%	φ_{in} = 41.4–52.4%
$v_{out(mean)}$ = 0.5 m·s⁻¹	v_{in} = 0.05–0.1 m·s⁻¹	v_{in} = 0.05–0.1 m·s⁻¹	$v_{out(mean)}$ = 1.3 m·s⁻¹	v_{in} = 0.1–0.2 m·s⁻¹	v_{in} = 0.05–0.1 m·s⁻¹
×	ET = 19.7–22.1	ET = 21.9–22.8	×	ET = 20.5–22.0	ET = 20.7–22.6
	PMV = (−0.64)–0.59	PMV = (−0.05)–0.34		PMV = (−0.58)–(−0.39)	PMV = (−0.19)–0.38
	PPD = 5–14%	PPD = 5–7%		PPD = 8–12%	PPD = 5–8%

midity, while 60% air humidity is the upper limit of the ASHRAE comfort zone.

– The assessment results based on *ET* and *PMV* indicators in A1 Building at the NUCE (without heating) on January 18th 2018 (cold winter day) brought thermal comfort to building occupants. The opinion survey revealed that most of the staff felt comfortable, in accordance with the *ET* and *PMV*-based evaluation.

– The assessment results based on the *ET* indicator in GELEX Building (with heating) on February 5th 2018 (very cold winter day) exceeded the comfort zone for winter time (slightly cold). Nevertheless, the assessment results based on *PMV* indicator stayed entirely within comfort zone, also in accordance with the opinion survey results of building occupants. It is possible to see that *ET*-based thermal comfort in the TCXDVN 306:2004 standard does not always correspond well to perceived (surveyed) thermal comfort.

– Average daily *ET* values during summer time in office rooms varied between 20.5°C and 23.8°C. These values are lower than *ET* value for completely comfortable 24.4°C in summer months with reference to the mentioned standard.

– Results of the *PMV*-based assessment during summer months indicated that except room 602 with average daily *PMV* = 1.16, beyond comfort zone (rather warm), in remaining rooms the *PMV*-based values all fell within the comfort zone. However, the opinion survey undertaken by staff working in room 602
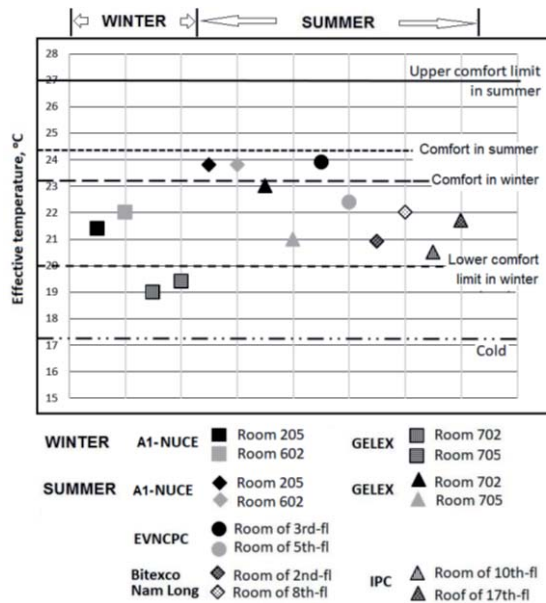
FIGURE 3. Average daily effective temperature value in surveyed rooms in five office buildings (in winter and summer)
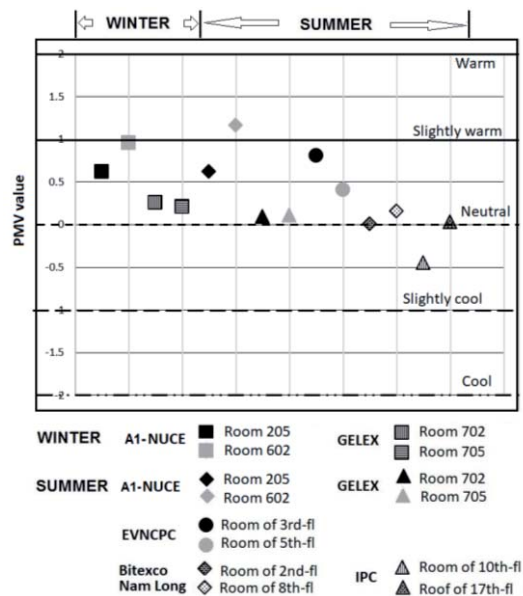

FIGURE 4. Average daily predicted mean vote value in surveyed rooms in five office buildings (in winter and summer)
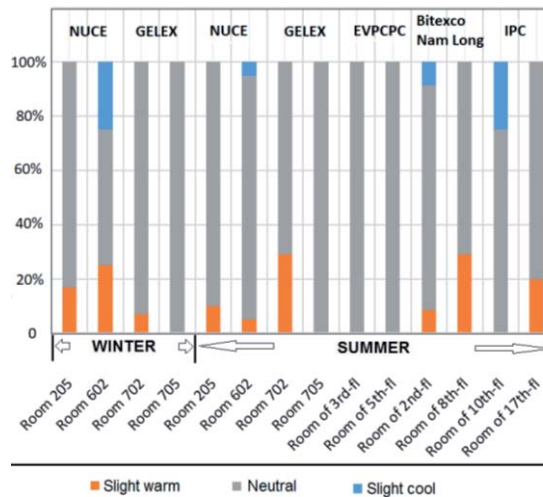
FIGURE 5. Interview results of thermal comfort subject to temperature among the staff working in office rooms measured in winter and summer time

revealed that more than 90% of occupants felt comfortable. Therefore, *ET* thermal comfort during summer time following mentioned standard would be more appropriate for thermal comfort among Vietnamese people than a thermal comfort scale based on *PMV* indicators.

– Although these investigations did not have sufficient samples to establish the confidence level as expected, the survey and measurement results also demonstrate that some micro-climatic parameters in mentioned standard should be adjusted and updated for current use.

Recommendations to update current standards in micro-climate

The TCXDVN 306:2004 specifies standard values of micro-climate on the basis of "Scale of thermal comfort for Vietnamese people" as proposed by Dang (1981). The curve in Figure 6 represents the relationship between the level of thermal comfort (% probability of thermal comfort) for Vietnamese people based on experiments by Dang (1981). The authors add three thermal comfort zones A, B and C to "Scale of thermal comfort for Vietnamese people". This graph considers metabolic heat of a healthy person (reading books, doing office paperwork, undertaking research, etc.) is 1.1 met, and heat resistance for normal clothes is 0.4–0.5 clo during summer, and 0.9–1.0 clo during winter.

Comment on Figure 6: If we extend the winter comfort curve and summer comfort curves in Figure 6 and compare this graph to the curve representing the relationship between *PPD* and *PMV* sensation scale, following theoretical calculations in the ISO 7730-2005 standard from Figure 1, it is possible to see that the two curves are exponentials and quite similar in variability. There is only one difference: one is convex while the other is concave. The reason is given as follows: *PPD* is measured in % according to the
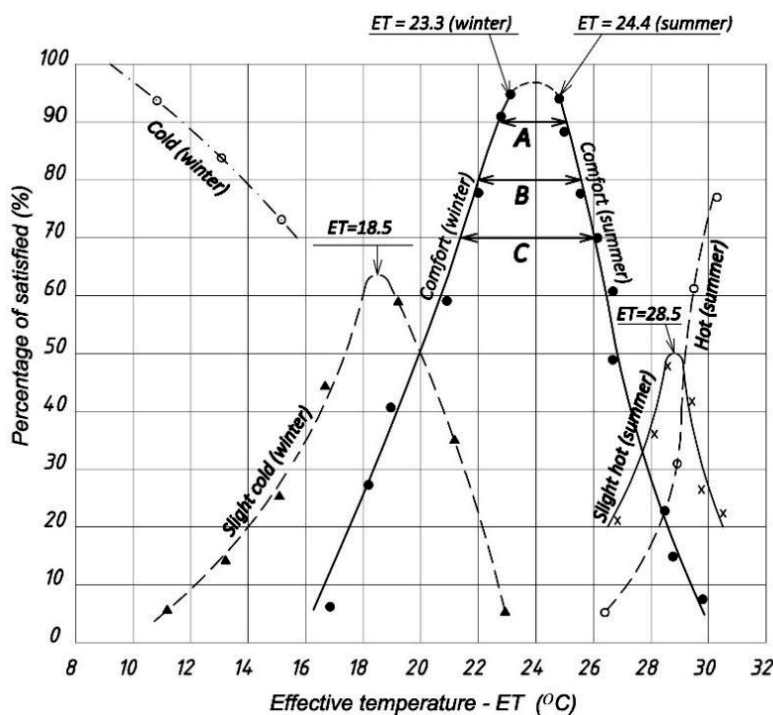
FIGURE 6. Relationship between effective temperature and probability of feeling hot or cold by Vietnamese people (Note: Thermal comfort zones A, B, C have been added)

ISO 7730-2005 standard, and the graph proposed by Dang (1981) uses *PMV* unit [%], whereas *PPD* [%] = 100% − *PMV* [%]. Thus, the graph showing the relationship between *ET* and probability of feeling hot or cold by Vietnamese people proposed by Dang (1981) can be used as a foundation reference to establish the limits of micro-climatic comfort and modify the TCXDVN 306:2004 standard wherever possible, as more comprehensive experimental studies on thermal comfort of Vietnamese people are not available.

As required by the ISO 7730-2005, the ANSI/ASHRAE 55-2017, the BS EN 16798-1:2019 and the GOST 30494-1996 standard, the limits of thermal comfort to be included in building micro-climatic

regulations depend on the function of the building and should be divided in three categories A, B and C, corresponding to three levels of comfort: 90, 80 and 70%.

The research team analysed the experimental outcomes by Dang (1981) in the graphic "Relationship between *ET* and probability of feeling hot or cold by Vietnamese people" in Figure 6 by means of the ISO 7730 method in order to differentiate the levels of thermal comfort on the basis of probability of thermal comfort in categories A, B, C (90, 80 and 70%, respectively). It aims to standardize micro-climatic conditions in consideration of different levels of quality and comfort. The results are presented in Table 7.

TABLE 7. Limits of thermal comfort for Vietnamese people on the basis of effective temperature (*ET*) and combination of parameters of air temperature (*T*), humidity (*φ*) and wind velocity (*v*) for air-conditioned office rooms

Level of thermal comfort – Probability of thermal comfort	ET [°C]	T [°C] ($φ$ = 60%, v = 0.05–0.2 m·s^{-1})	T [°C] ($φ$ = 65%, v = 0.05–0.2 m·s^{-1})	T [°C] ($φ$ = 70%, v = 0.05–0.2 m·s^{-1})
Comfort at 97%	23.8	27.1	26.7	26.3
Grade A, 90%	22.6–25.0	25.8–28.4	25.4–28.0	25.0–27.6
Grade B, 80%	22.0–25.5	25.2–29.0	24.8–28.5	24.4–28.1
Grade C, 70%	21.5–26.0	24.7–29.5	24.3–29.0	23.9–28.6

Conclusions

This research paper reports physical measurements and opinion surveys of current indoor climatic conditions in office workplaces for five representative office buildings in three cities, representing three climate zones in Vietnam: Hanoi, Da Nang and Ho Chi Minh City. Based on the survey and measurement results, and experimental results previously conducted by Dang (1981) the authors propose that the limits of thermal comfort for Vietnamese people should be established by using the classification of comfort of the ISO and the ASHRAE standard (in three levels of comfort: 90, 80 and 70%), in order to standardize micro-climatic conditions in air-conditioned office buildings at different levels of comfort. In future, more experimental investigations into thermal comfort on a larger scale will help validate scales of thermal comfort appropriate for use throughout all climate zones in Vietnam.

Acknowledgements

References

American National Standards Institute/American Society of Heating, Refrigerating and Air--Conditioning Engineers [ANSI/ASHRAE] (2017). *Thermal environmental conditions for human occupancy* (ANSI/ASHRAE 55-2017). Atlanta: American Society of Heating, Refrigerating and Air-Conditioning Engineers.

Anh, N.H. (1984). Bioclimate diagram applied in the design of dwelling house. In *Proceedings of Vietnam-Sweden Symposium*: *Vietnam Building Climatology*. Hanoi (pp. B33-B41) [unpublished].

Bakhtiari, H., Akander, J. & Cehlin, M. (2020). Evaluation of thermal comfort in a historic building refurbished to an office building with modernized HVAC systems. *Advances in Building Energy Research*, *14*(2), 218--237. https://doi.org/10.1080/17512549.2019.1604428

British Standards Institution [BSI] (2019). *Energy performance of buildings. Part 1: Ventilation for buildings. Indoor environmental input parameters for design and assessment of energy performance of buildings addressing indoor*

air quality, thermal environment, lighting and acoustics. *Module M1-6* (BS EN 16798--1:2019). London: British Standards Institution.

Budaiwi, I.M. (2006). An approach to investigate and remedy thermal-comfort problems in buildings. *Building and Environment*, *42*(5), 2124-2131. https://doi.org/10.1016/j.buildenv.2006.03.010

Con, N.H. (1985). *Climatic, Architecture and Human*. Hanoi: Science and Technology Publisher.

Dang, P.N. (1981). *Climatic fundamentals of architectural design*. Hanoi: Science and Technology Publisher.

De Vecchi, R.D., Candido, C., Dear, R. de, Lamberts, R. (2017). Thermal comfort in office buildings: Findings from a field study in mixed-mode and fully-air conditioning environments under humid subtropical conditions. *Building and Environment*, *123*, 672-683. https://doi.org/10.1016/j.buildenv.2017.07.029

Dear, R.J. de & Brager, G.S. (2002). Thermal comfort in naturally ventilated buildings: revisions to ASHRAE Standard 55. *Energy and Buildings*, *34*(6), 549-561.

Dear, R. de, Brager, G. & Cooper, D. (1997). *Developing and adaptive model of thermal comfort and preference* (final report ASHRAE RP-884). American Society of Heating, Refrigerating and Air Conditioning Engineers/Macquarie Research.

Dung, N.H. (1995). Discussions of human thermal comfort in Vietnam. In F. Nicol, M. Humphreys, O. Sykes, S. Roaf (eds.), *Standards for Thermal Comfort: Indoor air temperatures for the 21st century* (pp. 143--148). London: E & FN Spon.

Dung, N.H.N. & Kien, N.T. (2019). Recommendations for the design of an energy-efficient and indoor comfortable office building in Vietnam. In E. Motoasca, A. Agarwal, H. Breesch (eds.), *Energy Sustainability in Built and Urban Environments. Energy, Environment, and Sustainability* (pp. 67-90). Singapore: Springer. https://doi.org/10.1007/978-981-13-3284-5_4

Fanger, P.O. (1970). *Thermal comfort: analysis and applications in environmental engineering*. Vanloese: Danish Technical Press.

Houghten, F.C. & Yaglou, C.P. (1923). Determination of the comfort zone. *Transactions of the American Society of Heating and Ventilating Engineers*, *29*, 165-176.

Huong, N.T. (2001). *Report on research project "Initially assessing the factors which can cause the SBS disease in the offices in Vietnam and proposing solutions to improve the working environment"*. Hanoi [unpublished].

International Organization for Standardization [ISO] (2005). *Ergonomics of the thermal environment. Analytical determination and interpretation of thermal comfort using calculation of the PMV and PPD indices and local thermal comfort criteria* (ISO 7730--2005). Geneva: International Organization for Standardization.

Khanh, N.Q. (2011). *Report on research project "Investigating and assessing the indoor environment quality of the working environment and the health of workers in office buildings. Proposing solutions"* [unpublished].

Klepeis, N.E., Nelson, W.C., Ott, W.R., Robinson, J.P., Tsang, A.M., Switzer, P., Behar, J.V., Hern, S.C. & Engelmann, W.H. (2001). The National Human Activity Pattern Survey (NHAPS): a resource for assessing exposure to environmental pollutants. *Journal of Exposure Science and Environmental Epidemiology*, *11*(3), 231-252. https://doi.org/10.1038/sj.jea.7500165

Ministry of Construction of Vietnam (2004). *Nhà ở và công trình công cộng – Các thông số vi khí hậu trong phòng* [*Dwelling and public buildings – Parameters for micro-climates in the rooms*] (TCXDVN 306:2004). Hanoi: Ministry of Construction of Vietnam [transl. from Vietnamese].

Nasrollahi, N., Knight, I. & Jones, P. (2008). Workplace satisfaction and thermal comfort in air conditioned office buildings: Findings from a summer survey and field experiments in Iran. *Indoor and Built Environment*, *17*(1), 69-79. https://doi.org/10.1177/1420326X07086945

Nguyen, P.D. (2002). *Report on research project „Building databank for architectural design in tropical climate"* [unpublished].

Nguyen, A.T., Singh, M.K. & Reiter, S. (2012). An adaptive thermal comfort model for hot humid south-east Asia. *Building and Environ-*

ment, *56*, 291-300. https://doi.org/10.1016/j.buildenv.2012.03.021

Nguyen, N.T.Q. & Tran, T.C. (2017). Assessing the thermal comfort in non-air conditioned classrooms in Ho Chi Minh City. *Science and Technology Development Journal – Natural Sciences*, *1*(T4), 232-240. https://doi.org/10.32508/stdjns.v1iT4.473

Phong, D.N., Uyen, L.T., Lanh, N.N., Anh, N.H. (1984). Impacts of hot and humid climate on youths in residential buildings, physio-biologically considered. In *Proceedings of Vietnam-Sweden Symposium*: *Vietnam Building Climatology*. Hanoi (pp. C32-C43) [unpublished].

Simons, B., Koranteng, C., Adinyira, E. & Ayarkwa, J. (2014). An assessment of thermal comfort in multi storey office buildings in Ghana. *Journal of Building Construction and Planning Research*, *2*(1), 30-38. https://doi.org/10.4236/jbcpr.2014.21003

Standartinform (1996). *Zdaniya zhilyye i obshchestvennyye. Parametry mikroklimata v pomeshcheniyakh* [*Residential and public buildings. Microclimate parameters for indoor enclosures*] (GOST 30494-1996). Moskva: FHUP Standartinform [transl. from Russian].

Szabo, J. & Kajtar, L. (2018). Thermal comfort analysis in office buildings with different air-conditioning systems. *International Review of Applied Sciences and Engineering*, *9*(1), 59-63. https://doi.org/10.1556/1848.2018.9.1.8

Szokolay, S.V. (2004). *Introduction to architectural science: the basis of sustainable design*. Oxford: Architectural Press.

Tao, P., Li, A., Qiu, G. & Zhang, J. (2014). Field measurement, survey and evaluation on indoor thermal environments in typical office buildings. In A. Li, Y. Zhu, Y. Li (eds.), *Proceedings of the 8th International Symposium on Heating, Ventilation and Air Conditioning* (pp. 77-86). Berlin: Springer.

Tartarini, F., Schiavon, S., Cheung, T. & Hoyt, T. (2020). CBE Thermal Comfort Tool: online tool for thermal comfort calculations and visualizations. SoftwareX 12, 100563. https://doi.org/10.1016/j.softx.2020.100563

Thiem, T.H. (1984). The comfortable microclimate parameters in hot humid conditions. In *Proceedings of Vietnam-Sweden Symposium*:

Vietnam Building Climatology. Hanoi (pp. C21-C26) [unpublished].

Tuan, N.A, Dung, L.T.K. & Vinh, P.T. (2016). Assessment the indoor environmental quality in low-income apartments in Danang in the summer. *Journal of Architectural and Building Sciences*, *23*, 20-24.

Tuan, N.A. & Le, T.K. (2015). Thermal comfort in some naturally-ventilated lecture halls. *Journal of Science and Technology – Danang University*, *1*, 84-88.

Summary

Simple method to improve the TCXD-VN 306:2004 indoor climate standard for closed office workplaces in Vietnam. Thermal comfort is an important parameter of indoor climate, which affects office worker health and productivity, and also aids planning for energy efficient building design and operation. To provide satisfactory thermal comfort in office workplaces under hot and humid outdoor conditions, most contemporary office buildings in Vietnam are fitted with ducted air-conditioning systems. The current Vietnamese standard TCXDVN 306:2004 for indoor climate was derived from thermal comfort research conducted between the 1960s and 1980s. This standard is limited by various drawbacks, including no distinction between natural or artificial environments. In response, this 2018 research provides physical measurements and opinion surveys of current indoor climatic conditions in representative office workplaces in three regions of Vietnam: North, Central and South. The measurement results have been transformed into *ET*, *PMV* and *PPD* indicators, which value demonstrate the shortcomings of the TCXDVN 306:2004 standard, while providing a baseline input for updating this standard to meet the thermal comfort needs of air-conditioned office workplaces, based on the concept of probability comfort, which are integral with the ISO and the ASHRAE standard.

Authors' address:
Pham Thi Hai Ha
(https://orcid.org/0000-0002-7277-7674)
National University of Civil Engineering
55 Giai Phong road, Hai Ba Trung District
Hanoi
Vietnam
e-mail: hapth@nuce.edu.vn

Zahid HUSSAIN[1], Muhammad Siyab KHAN[1], Hamza KUNDI[2],
Kashif ALAM[1], Yasir ULLAH[1]

[1] Sarhad University of Science and Information Technology, Faculty of Engineering
[2] University of Engineering and Technology, Faculty of Civil Engineering

Assessment of integrated indoor environmental air quality parameters in selected church buildings of Faisalabad city: a statistical based comparative study

Key words: indoor air quality, church buildings, particulate matter, public health, air pollution

Introduction

The quality of air is the most vital insight that supports human existence on earth. Some cities of the world are facing the issues related with smog and imperceptible air pollution which are detrimental to the public's health (Al-Dabbous et al., 2019). For instance, particulate matter which is an arrangement of solid bits and liquid droplets measures 10 µm can easily inhaled deep into the respirational system (Shahid et al., 2019). The particulate matter size less than 2.5 µm are considered as fine particles. However, there may create a health risk, if a large portion of these particulates is inhaled (Aung et al., 2019). These particles patent from an assortment of different sources and may be emitted by the conversion of gaseous emissions. How these dangerous fine particles travel through the atmosphere is caused by dispersion creating a plume which spreads over a specific area, hence dropping the concentration of the air contaminants it covers (Behrooz et al., 2017). The common technique use for the gaseous diffusion is the Gaussian dispersion, in which air contaminants disseminated and are supposed to disclose ideal gas performance (Chang et al., 2019). The major force in air pollution transference is the wind causing the air pollutants to move downwind while the highest absorption of air contaminant molecules move laterally the plume centerline (Fernández, 2019). Since these molecules diffuse freely from upper to lower concentration regions, hence the air pollutants emitted constantly making the dispersion and

emission process at a constant rate (Soudagar et al., 2019). Figure 1 shows the mechanism and arrangement of plume and wind sources related to the Gaussian dispersion. Looking through the Cartesian coordinate arrangement, the emission source is located at the starting point while the wind direction at the x-axis. Similarly, the vertical and horizontal dispersion are located the y-axis and z-axis respectively. For instance, as the plume travels downwind, it extents both crosswise and straight up away from the centerline allowing the air molecules to travel from upper to lower concentrations (Kelly & Fussell, 2019). Transection of the air pollutant concentration at both the y and z axes thus take the normal bell shape of Gaussian distribution curves as illustrated in Figure 1. The total effective height (H) is the sum of the vertical distance (h) and the symmetrical heap height (h_s) respectively. The cause of the pollutant spiral is in consequence a source raised above the ground at altitude follows Eq. (1).

$$z = H \tag{1}$$

The downwind attentiveness coming from this prominent source may be written using Eq. (2) (Filbet & Jin, 2010).

$$C(x, y, z) =$$
$$= \frac{Q}{2\pi\upsilon\sigma_y\sigma_z} e^{\frac{y^2}{2\sigma y^2}} e^{\left[\frac{-(z+H)2}{2\sigma x^2} + e^{\frac{-(z-H)2}{2\sigma x^2}}\right]}$$

$$\tag{2}$$

here:
$C(x, y, z)$ – concentration with coordinates x, y, z,
Q – emission rate [gm·s^{-1}],
v – normal wind speed [m·s^{-1}],
σ_y – standard non-conformity of the plume in the horizontal flow [m],
σ_z – standard non-conformity of the plume in the z trend [m] (Gao et al., 2017).

Since particulates matter concentration is normally restrained at earth level ($z = 0$) therefore, Eq. (2) diminishes to:
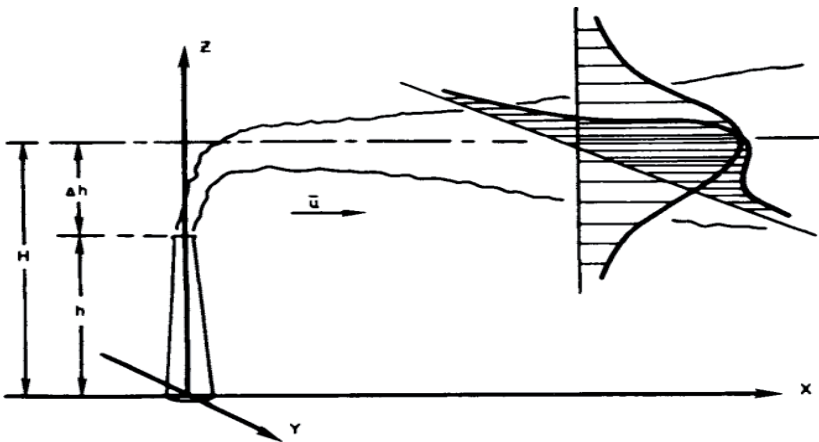

FIGURE 1. Fundamental layout of the Gaussian dispersion

$$C(x,y,0) = \frac{Q}{\pi \upsilon \sigma_y \sigma_z} e\left[\frac{y^2}{2\sigma_{y^2}}\right] e\left[-\frac{H^2}{2\sigma_{z^2}}\right]$$

$$(3)$$

However, the higher value of the concentration in any desired direction is the point of interest hence when $y = 0$, then Eq. (3) reduces to:

$$C(x,0,0) = \frac{Q}{\pi \upsilon \sigma_y \sigma_z} e - \frac{H^2}{2\sigma_{z^2}} \qquad (4)$$

As a final point, in case when $H = 0$ and the concentration at ground level for the air pollutants moving down along the centerline becomes equal to:

$$C(x,0,0) = \frac{Q}{\pi \upsilon \sigma_y \sigma_z} \qquad (5)$$

Rendering to the surveys of the World Health Organization (WHO), people spend around 90% of their time indoors however according to the statement of the EPA, the level of unhealthy concentrations is complex than the outdoor (Chang et al., 2019). Those related to the human contribution include a variety of sources such as industrial processes, apparel of road dust into the air, burning of fossil and wood fuels, demolition and construction activities (Ramírez et al., 2019). The most significant in this case include nitrogen dioxide (NO_2), sulphur dioxide (SO_2), ozone (O_3), carbon monoxide (CO), radon (Rn) and a variety of concentrations (Van den Heede & De Belie, 2012). In church buildings, pollutant matter from different sources affects the comfort, health and routine work of the people in a negative manner (Mitcham &

Briggle, 2009). It is also noticeable that the rank of the quality of air in a church building is significantly influenced by the topographical latitude of the building (Ruffolo et al., 2015). The people who normally stay in the church buildings are pastors, administration staff, secretary, treasurer, Sunday schooling staff, music department staff, and visitors. Making sure that these individuals feel contented with the existing environment, a study on indoor air quality has been needed to be highlighted at church buildings where religious activities are performed (Wang et al., 2018). The environments of church buildings under this study are extremely polluted due to the reasons such as crowded halls, low ventilation during rituals, insufficiency in fresh air supply, lack of ventilation system, presence of impervious windows, and great levels of radon gas.

According to the 2018 world air quality reports based on air quality data from public monitoring sources, Pakistan had been placed at the next utmost contaminated country with an annual $PM_{2.5}$ average of 74.3 µg·m^{-3} (Sultan et al., 2019). There is quite a lack of investigations for studying the particulate matter contaminants in the church buildings located in Faisalabad-Pakistan. In 2019, Faisalabad's air pollution ranked number 3 while the recorded exposure of $PM_{2.5}$ is 274.7 µg·m^{-3} on averages (Alvi et al., 2019). There are additional factors which contribute to increasing the rate of air pollution including huge scale losses of forests and tree for new buildings and furniture (Behrooz et al., 2017). During the summer, the kinetics of O_3 with other organic compound increases which leads to minimizing the O_3 concentrations in

indoor air. Conversely, the concentrations of NO_2, remain similar both in the summer and winter to the concentrations in the air surrounded by the church buildings (Stamp et al., 2020). However, the concentration was normally 2–3 times greater in the winter due to increased emissions from additional sources including agricultural fields' burning. The concentrations of NO_2 were also found higher due to the influence of burning candles inside the church buildings (Yin et al., 2019). During the study on air quality in church buildings, it was observed that the concentration of particulates matter is determined by establishing relationships between them.

Materials and methods

Faisalabad is the third largest city in Pakistan with latitude and longitude coordinates as (31°41'8.7"N, 73°4'35"E) (Ahmad & Nizami, 2015). Figure 2 shows the location of Faisalabad with the surrounding provinces of Pakistan (Muqaddas et al., 2019). Conversely, in January the average lowest and highest temperatures are 3.89°C (39.00°F) and 18.8°C (65.84°F), respectively. On the other hand, ranking between the topmost 10 peak contaminated cities in the world, the quality of air of Faisalabad is inferior to what is deliberated safe by worldwide standards for harmless air quality (Nawaz et al., 2020). The Jesus Pentecostal Church building is located in Faisalabad city. There is a light stream of traffic around the church building as it is located 15 km away from the main city. In the main hall, air circulation is done through electric fans and natural sources.

The tables and benches in the main hall are made up of medium density fibers (MDF) concealed chipboards and two--fold glazed windows in size 140 × 45 cm. The windows are skylight models with an aluminum frame. The covered area of the building is 460 m^2 and for 270 publics. On the other hand, the St. Joseph's Cathedral church building is selected because it is located on the main mall road which is considered as one of the most crowded and commercial area of Faisalabad city. Hence, the church building is highly exposed to particulate matter, dust, smog and air pollution due to dissipating gases from traffic flow affecting the indoor air quality. The building has

FIGURE 2. Location of Faisalabad with the surrounding provinces

single glazed windows in size 120×50 cm. Tables and benches are made up of medium density fibers (MDF) concealed chipboards, wooden doors, classical skylight models windows with steel frame and precast slabs flooring. The covered area of the building is 445 m^2 and 250 publics. Based on study visits, different air quality parameters were investigated and analyzed to explore which specific church building has an extreme level of indoor contaminants.

Data collection and methodology

Comparing the air quality of Faisalabad city with the WHO guidelines, concentrations of different pollutant matter used in this work are represented in Table 1.

The measurements were performed in the middle of October–December 2019 which is the main smog period in Faisalabad city. The physical measurement was carried out in both church buildings at different time periods. The measurements were completed after acknowledged complaints associated with indoor air quality at the church buildings, based on the investigational process as shown in Figure 3. These values confirm

that the hourly concentrations level of different pollutant matter reached 6–7 times the limit set by the WHO guidelines (Colbeck, Nasir & Ali, 2010). Similarly, the level of $PM_{2.5}$, which is mainly from combustion sources, has reached an alarming level, 8–9 times greater than the safe limit (according to the WHO guidelines annual mean of 10 $\mu g \cdot m^{-3}$ and 24-hour mean of 25 $\mu g \cdot m^{-3}$). It further confirms that the air quality of Faisalabad city is very unhealthy. The methodical data collections are extended further by determining the contents of air pollutants and particulate matter accompanied by sampling progression. The specific equipment used includes PCE/RCM-12 for measuring temperature in the range between −20°C and +70°C, humidity level from 0–100%, volatile organic compounds (VOCs) level from 0.00– −5.00 mg·m^{-3} and CO_2 level between 0 and 9,999 ppm respectively. Measurement point was selected near the main halls as the most significant to indoor air pollutants come from the outdoor air. Indicators were set aside at a distance of around 25 cm from the wall and 2.5 m high from the floor. Total numbers of 92 samples were obtained. The measurements were carried out in the course of the normal operating hour, starting from

TABLE 1. Comparison of air quality of Faisalabad with the World Health Organization guidelines

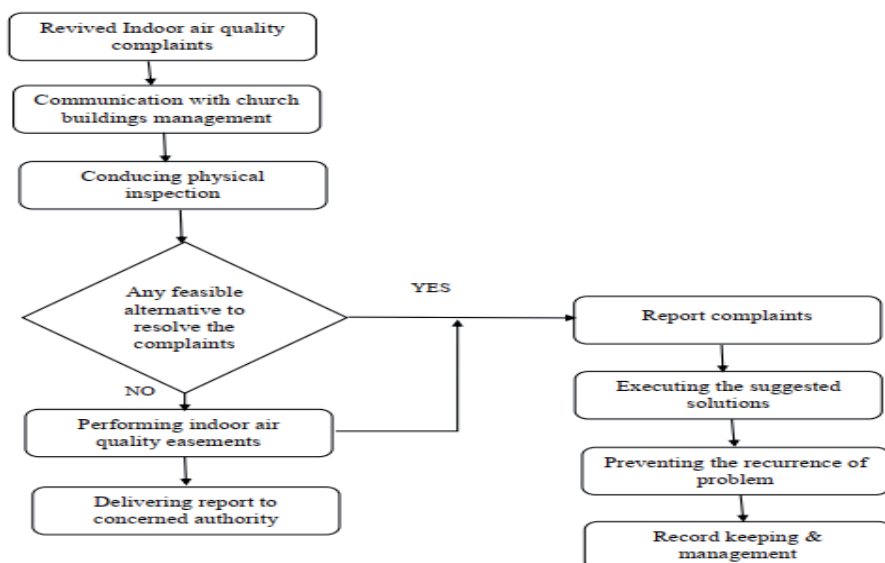| Data collecting time	Temperature [°C]	Humidity [%]	NO_2 [$\mu g \cdot m^{-3}$]	SO_2 [$\mu g \cdot m^{-3}$]	CO [$\mu g \cdot m^{-3}$]	O_3 [$\mu g \cdot m^{-3}$]	$PM_{2.5}$ [$\mu g \cdot m^{-3}$]
00.05–08.00	27	63	89	55	1 342	70	198
08.05–16.00	32	60	101	78	1 470	72	235
16.05–24.00	25	69	95	59	1 370	71	203
24-hour average	28	64	95	64	1 394	71	212
WHO values	–	–	70	20	20	60	25

FIGURE 3. Indoor air quality complaints and exploration process flow chart

8 am and finished at 5 pm, for six days. The data were analyzed considering different air quality parameters.

For data analysis, Minitab 18 and Statgraphics Centurion XVII mathematical software packages were used accordingly. For establishing a mathematical comparison between air quality factors, the Pearson correlation coefficient (r) is used using Eq. (6). This comparison is helpful to scrutinize the existence of a linear correlation among different parameters given that positive norms around the data are contented (Koo & Li, 2016).

$$R_{xy} = \frac{\sum_{i=1}^{n}[y(x_i - \overline{x})]}{[\sum_{i=1}^{n}(y_i - \overline{y})\sum_{i=1}^{n}(x_i - \overline{x})^2]} \quad (6)$$

Being a quantitative extent of the strength of the correlation between the two random variables x and y, if the parameters have a linear correlation with a positive slant, then $R_{xy} = 1$ however $R_{xy} = -1$ will show a negative correlation among the two parameters (Larsen et al., 2007).

Results and discussion

Table 2 shows the descriptive statistics of the measured data. The descriptive statistics parameters based on 92 counts, the mean, standard deviation, minimum, median, maximum and range values were determined. Mean indoor temperature of both the church buildings was recorded as 19.71°C as well as the corresponding range was 9.00°C (such that 24.00 – 15.00 = 9.00°C).

Figure 4 shows that these values are lower than the standards specified by the American National Standards Institute (ANSI) and the American Society of Heating, Refrigerating and Air-Con-

TABLE 2. Descriptive statistics of the measured data

Parameter	Mean	Standard deviation	Minimum	Median	Maximum	Range
Temperature [°C]	19.71	2.71	15.00	20.00	24.00	9.00
Relative humidity [%]	41.61	15.01	19.00	40.00	75.00	56.00
Carbon dioxide [ppm]	1 459.5	714.3	490.00	1300.0	2 900.00	2 410.00
Nitrogen dioxide [ppm]	215.98	36.86	105.00	215.00	300.00	195.00
Sulphur dioxide [ppm]	125	64.73	5.00	110.00	350.00	345.00
$PM_{2.5}$ [$\mu g \cdot m^{-3}$]	69.04	28.42	10.00	70.00	130.00	120.00
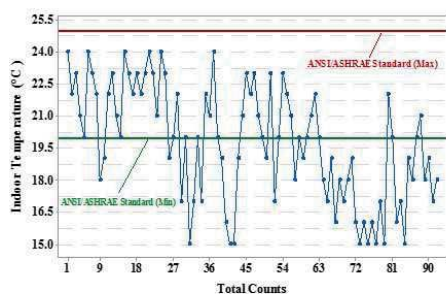
a   b
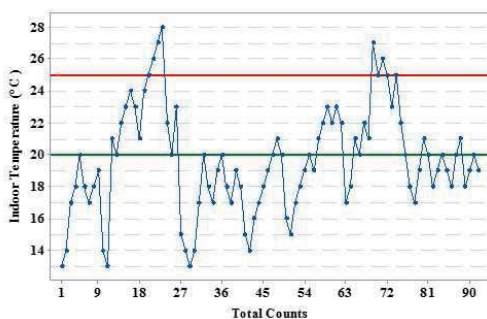
FIGURE 4. Mean indoor temperature: a – Jesus Pentecostal Church building; b – St. Joseph's Cathedral church building

ditioning Engineers (ASHRAE). Mean indoor relative humidity was measured as 41.61% and the corresponding range was 56.00% (such that 75.00 – 19.00 = = 56.00%). According to the Figure 5, it was established that the relative humidity conforms with the ASHRAE standards which take a range of 30–60%.

The mean CO_2 values were determined as 1,459.5 ppm and the corresponding range was 2,410 ppm such that (2,900 – 490 = 2,410 ppm). As per findings of Figure 6, for short-term expo-

sure, the acceptable CO_2 concentration is 1,000 parts per million (ppm). It is observed that the mean CO_2 value is above the ASHRAE standards. Consequently, the air quality standards in St. Joseph's Cathedral church building was more aggressive than that of Jesus Pentecostal Church building. In this regard, human respiration and combustion are joint sources of CO_2 ranks. St. Joseph's Cathedral church is also a prevalent destination for tourists. Due to its prime location and historical background, the church build-
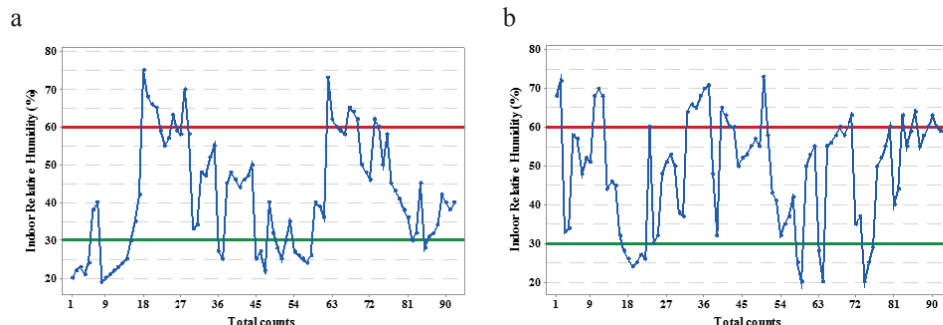
FIGURE 5. Mean indoor relative humidity: a – Jesus Pentecostal Church building; b – St. Joseph's Cathedral church building
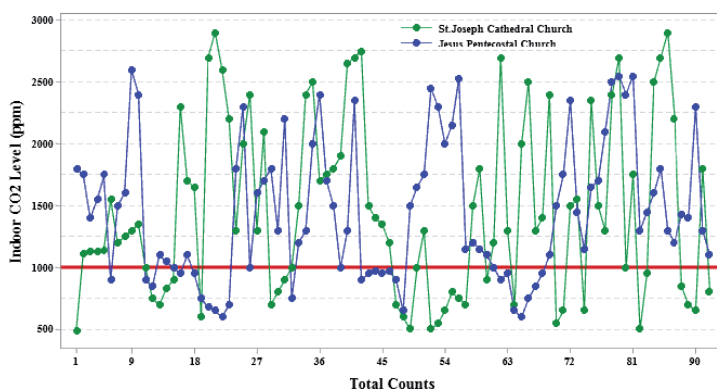
FIGURE 6. Carbon dioxide indoor concentration comparison

ing receives fairly a massive number of visitors every year. As a result, the CO_2 concentration for St. Joseph's Cathedral church building is much higher and extra polluted as compared to the indoor air quality of carbon dioxide for Jesus Pentecostal Church building.

The mean NO_2 values were determined as 200 $\mu g \cdot m^{-3}$ and the corresponding range was 195 $\mu g \cdot m^{-3}$ such that (300 – 105 = 195 $\mu g \cdot m^{-3}$). Based on Figure 7 rendering to the WHO, for a short-term exposure for an hour, the acceptable NO_2 concentration is 200 $\mu g \cdot m^{-3}$. It is noticeable that both church buildings had surpassed the acceptable range of concentration. How-

ever, the NO_2 concentration for St. Joseph's Cathedral church building is much greater and more contaminated compared to indoor air quality levels for Jesus Pentecostal Church building. Due to its central location, a heavy traffic flow is observed all the time. Moreover, the church building is much closer to the main road while Jesus Pentecostal Church building is located about 250 m from the main road. Hence it is confirmed that the distance of building from the roadway can affect the quality of air with respect to the levels of NO_2.

The mean SO_2 values were determined as 125 $\mu g \cdot m^{-3}$ and the corresponding range was 345 $\mu g \cdot m^{-3}$ (such
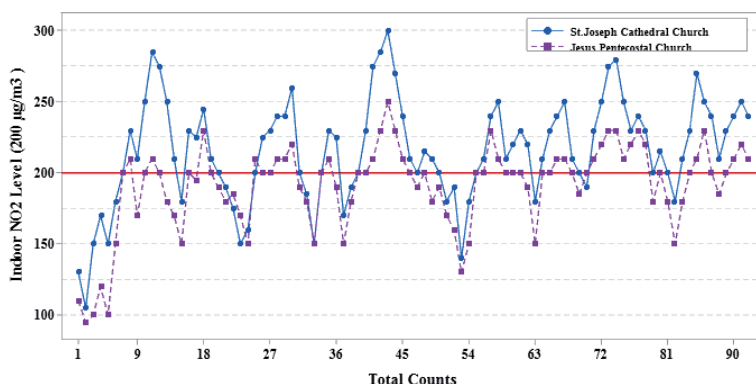
FIGURE 7. Nitrogen dioxide indoor concentration comparison

that $350 - 5 = 345$ μg·m^{-3}). According to the WHO and based on Figure 8 for a short-term SO$_2$ exposure is 10 min, the acceptable concentration for SO$_2$ is 500 μg·m^{-3}. It is observed that both the church buildings are quiet safe and deliver a well indoor atmosphere. It is due to the fact that the church buildings are located in the city area where no power generation stations and industries are located close to these buildings. Conversely, there still exists the presence of SO$_2$ pollutants in the indoor atmosphere owing to the means of transporta-

tion factor. Considering the distance of the church buildings from roadside and different means of transportations, it is confirmed that the SO$_2$ concentration at St. Joseph's Cathedral church building are higher compared to indoor air quality levels of SO$_2$ at Jesus Pentecostal Church building because a heavy flow of traffic is experienced throughout the day due its prime location in central part of the Faisalabad city.

The mean indoor PM$_{2.5}$ concentration values were determined as 69.04 μg·m^{-3} and the correspond-
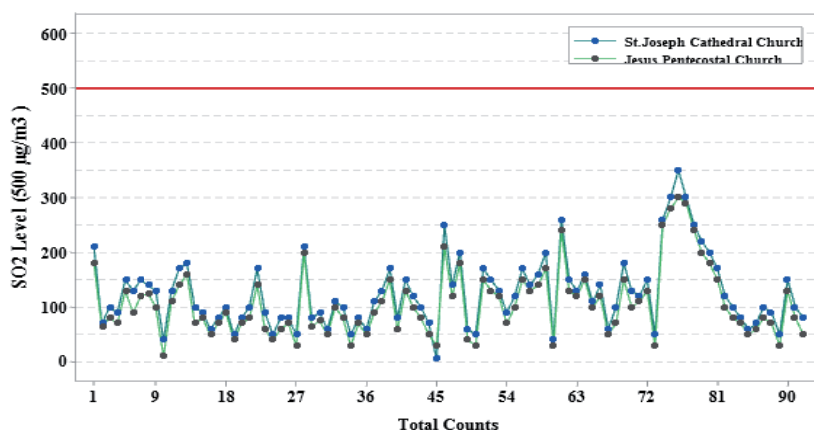
FIGURE 8. Sulphur dioxide indoor concentration comparison

Z. Hussain et al.
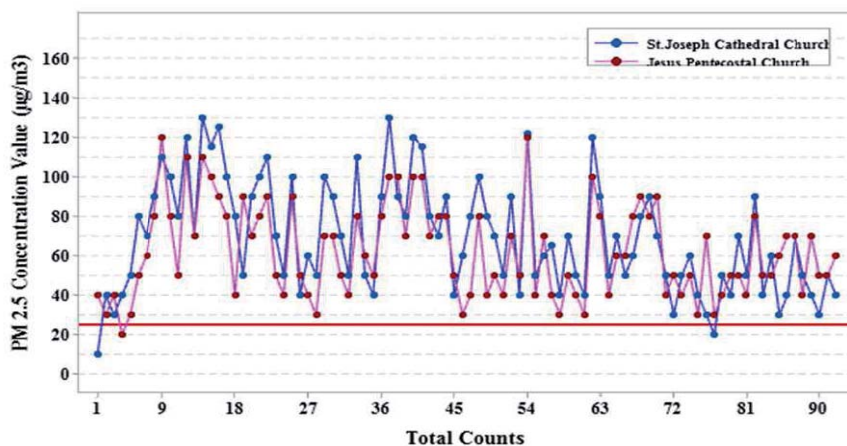
FIGURE 9. Particulate matter PM2.5 concentration comparison

ing range was 120 µg·m^{-3} (such that $130 - 10 = 120$ µg·m^{-3}). According to the WHO and based on Figure 9, for a limited PM$_{2.5}$ vulnerability for a 24-hour period of the adequate PM$_{2.5}$ concentration is 25 µg·m^{-3}. However, it observed that the PM$_{2.5}$ concentration for both the church buildings is higher than the satisfactory level. Rendering to the WHO, there are several bases of particulates matter connected with natural means which differ in conformation, concentration, and size. Still, there are human activities, for example, source gain from manufacturing, infrastructure, construction spots, landfills, agricultural fields and transportation means which intensely affect human health, visibility, climate, and biogeochemical cycling. Indoor air quality levels of environmental pollutants are usually a function of outdoor and indoor causes, where great outdoor portions are initiating from different combustion means and indigenous traffic sources impact indoor air quality. This factor and also considering the distance of church buildings from roadside, it revealed that

PM$_{2.5}$ concentration for St. Joseph's Cathedral church building are higher and more contaminated compared to indoor air quality levels of PM$_{2.5}$ for Jesus Pentecostal Church building because a heavy flow of traffic is experienced throughout the day due its prime location in central part of the Faisalabad city. Yet, there was some likelihood that indoor PM$_{2.5}$ may be generated through inadequate ventilation, combustion events such as the use of fireplaces, burning of candles, use of unvented and space-heaters and pulverized dust that added to indoor air quality levels of PM$_{2.5}$ in both church buildings.

Establishing statistical significance of parameters

To confirm whether the correlation among variables is significant, comparing the *p*-value to the significance level (α). The significance level (α) is chosen as 0.05 which will show that the risk of concluding that a correlation occurs while,

essentially, no correlation exists is 5%. Similarly, the *p*-value confirms whether the Pearson correlation coefficient (*r*) is significantly different from 0. Pearson correlation coefficient (*r*) between indoor CO_2 extent and general public is 0.640 which indicates a strong positive correlation between the two variables. It is observed that since door and windows are closed especially in the winter season, there is a substantial growth in CO_2 concentration reliant on the number of people. Pearson correlation coefficients (*r*) between the number of people and indoor $PM_{2.5}$ values is 0.278. It can be understood that different actions of people and their movement increase the percentage of particulates matter. It means that the church buildings are not ventilated adequately. Pearson correlation coefficients (*r*) between indoor CO_2 extent and indoor temperature is –0.567. It is because there is normal ventilation when the doors and windows are open. There is a slight increase in temperature generally in spring season hence carbon dioxide concentration declines which generates graphical instabilities. Pearson correlation coefficients (*r*) between indoor air temperature and indoor relative humidity is –0.6332. It is because as the concentrated humidity extent increases with an increase in air temperature, relative humidity rate decreases when air temperature increases. These different correlations among the parameters are given in Figure 10.
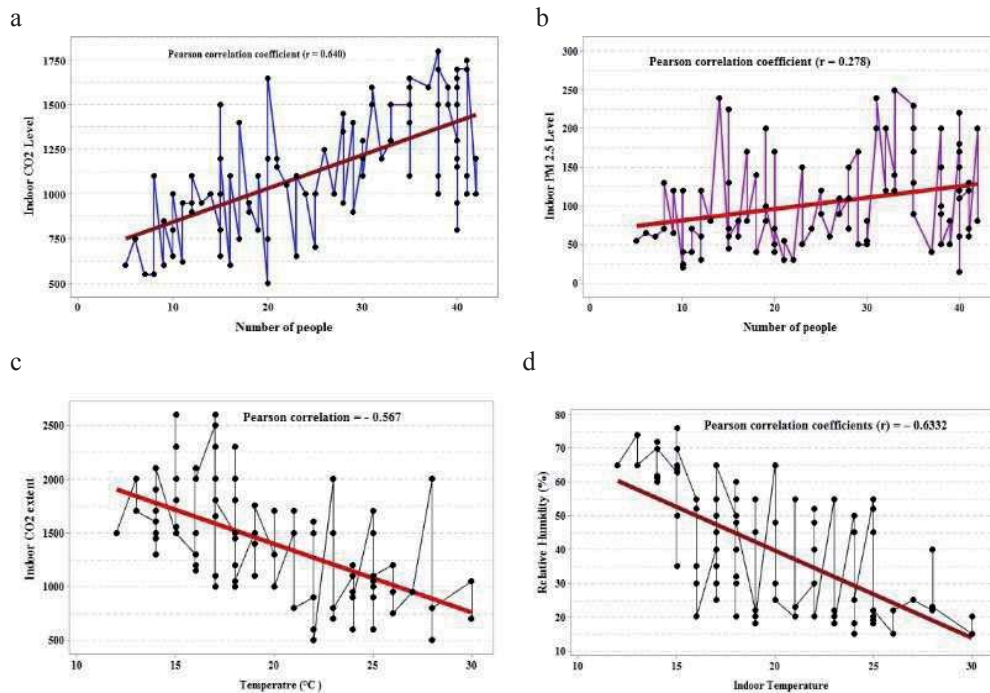
a

b

c

d

FIGURE 10. Parameters comparison: a – carbon dioxide indoor concentration and number of public; b – particulate matter $PM_{2.5}$ indoor concentration and number of public; c – carbon dioxide indoor extent and indoor temperature; d – indoor relative humidity and indoor temperature

Conclusions

This study seems to be innovative in Pakistan because the air quality of church buildings under study was not safe to the public as it may take harmful impact towards them. The result of this study specified that the distance of building from roads performs to have an impression on indoor air quality levels, particularly for CO_2, SO_2, NO_2, and $PM_{2.5}$. It was recognized that only gaseous particulates matter such as SO_2 did not surpass the satisfactory level compared to other particulates matter. It can be established that St. Joseph's Cathedral church building is more contaminated for indoor air quality parameters of CO_2, SO_2, NO_2, and $PM_{2.5}$ compared to Jesus Pentecostal Church building since location of St. Joseph's Cathedral church building is much nearer to the main road compare to Jesus Pentecostal Church building. The average indoor CO_2 level is greater. This is normally affected due to closed doors and windows especially in winter. The reduction in CO_2 level in spring confirms that there is typical air ventilation in church buildings although it is not adequate, hence a proper ventilation system should be installed to stop the exceeding indoor CO_2 levels. For determining the relationships among indoor air quality parameters, Pearson correlation coefficients (r) and significance level ($\alpha = 0.05$) were considered. Pearson correlation coefficient (r) of 0.640 acknowledged that there is a solid progression between the indoor CO_2 level and number of people. Pearson correlation (r) coefficients between number of people and indoor $PM_{2.5}$ values of 0.278 confirmed a moderate positive relationship. It can be concluded that different activities of people upsurge the percentage of particulates matter. At present, the average $PM_{2.5}$ concentrations in Faisalabad city is 69.04 $\mu g \cdot m^{-3}$, hence for controlling the extent of indoor particulates matter some necessary measures of ventilation must be taken into consideration. A value of Pearson correlation coefficients (r) is -0.567 established that due to the increase in temperature in the spring season, the concentration of CO_2 decreased. Pearson correlation coefficients (r) value of -0.6332 indicated that as the air temperature increases relative humidity rate decreases as well. It is also noticeable that at significance level ($\alpha = 0.05$) the relationship between other parameters and radon values could not be established. Since the concentration of indoor radon is likely changing from place to place. Additionally, the radon concentration level is continuously below a definite value. This difference may be recognized as climatic conditions, temperature, humidity, air circulation, ventilation, and soil penetrability.

References

Ahmad, A. & Nizami, S.M. (2015). Carbon stocks of different land uses in the Kumrat valley, Hindu Kush Region of Pakistan. *Journal of Forestry Research*, *26*(1), 57-64.

Al-Dabbous, A., Khan, A., Al-Tamimi, S., Shalash, M., Bajoga, A. & Malek, M. (2019). Oxides of carbon, particulate matters and volatile organic compounds impact on indoor air quality during waterpipe smoking. *International Journal of Environmental Science and Technology*, *16*(6), 2849-2854.

Alvi, M.U., Kistler, M., Mahmud, T., Shahid, I., Alam, K., Chishtie, F., Hussain, R. & Kasper-Giebl, A. (2019). The composition

and sources of water soluble ions in PM_{10} at an urban site in the Indo-Gangetic Plain. *Journal of Atmospheric and Solar-Terrestrial Physics*, *196*, 105142. https://doi.org/10.1016/j.jastp.2019.105142

Aung, W.Y., Noguchi, M., Yi, E-E.P-N., Thant, Z., Uchiyama, S., Win-Shwe, T.T., Kunugita, N. & Mar, O. (2019). Preliminary assessment of outdoor and indoor air quality in Yangon city, Myanmar. *Atmospheric Pollution Research*, *10*(3), 722-730.

Behrooz, R.D., Esmaili-Sari, A., Bahramifar, N., Kaskaoutis, D., Saeb, K. & Rajaei, F. (2017). Trace-element concentrations and water-soluble ions in size-segregated dust-borne and soil samples in Sistan, southeast Iran. *Aeolian Research*, *25*, 87-105.

Chang, H., Zhao, Y., Tan, H., Liu, Y., Lu, W. & Wang, H. (2019). Parameter sensitivity to concentrations and transport distance of odorous compounds from solid waste facilities. *Science of the Total Environment*, *651*, 2158-2165.

Chang, T., Wang, J., Lu, J., Shen, Z., Huang, Y., Sun, J., Xu, H., Wang, X., Ren, D. & Cao, J. (2019). Evaluation of indoor air pollution during the decorating process and inhalation health risks in Xi'an, China: a case study. *Aerosol and Air Quality Research*, *19*(4), 854-864.

Colbeck, I., Nasir, Z.A. & Ali, Z. (2010). The state of ambient air quality in Pakistan – a review. *Environmental Science and Pollution Research*, *17*(1), 49-63.

Fernández, I.C. (2019). A multiple-class distance-decaying approach for mapping temperature reduction ecosystem services provided by urban vegetation in Santiago de Chile. *Ecological Economics*, *161*, 193-201.

Filbet, F. & Jin, S. (2010). A class of asymptotic-preserving schemes for kinetic equations and related problems with stiff sources. *Journal of Computational Physics*, *229*(20), 7625--7648.

Gao, C., Xiao, W., Ji, G., Zhang, Y., Cao, Y. & Han, L. (2017). Regularity and mechanism of wheat straw properties change in ball milling process at cellular scale. *Bioresource Technology*, *241*, 214-219.

Kelly, F.J. & Fussell, J.C. (2019). Improving indoor air quality, health and performance within environments where people live, travel, learn and work. *Atmospheric Environment*, *200*, 90-109.

Koo, T.K. & Li, M.Y. (2016). A guideline of selecting and reporting intraclass correlation coefficients for reliability research. *Journal of Chiropractic Medicine*, *15*(2), 155-163.

Larsen, R., Bell, J., James, P., Chimonides, P., Rumsey, F., Tremper, A. & Purvis, O. (2007). Lichen and bryophyte distribution on oak in London in relation to air pollution and bark acidity. *Environmental Pollution*, *146*(2), 332-340.

Mitcham, C. & Briggle, A. (2009). The interaction of ethics and technology in historical perspective. In *Philosophy of Technology and Engineering Sciences* (pp. 1147-1191). Amsterdam: Elsevier.

Muqaddas, H., Arshad, M., Ahmed, H., Mehmood, N., Khan, A. & Simsek, S. (2019). Retrospective study of cystic echinococcosis (CE) based on hospital record from five major metropolitan cities of Pakistan. *Acta Parasitologica*, *64*(4), 866-872.

Nawaz, M.Z., Bilal, M., Tariq, A., Iqbal, H.M., Alghamdi, H.A. & Cheng, H. (2020). Biopurification of sugar industry wastewater and production of high-value industrial products with a zero-waste concept. *Critical Reviews in Food Science and Nutrition*. https://doi.org/10.1080/10408398.2020.1802696

Ramírez, O., de la Campa, A.M.S., Amato, F., Moreno, T., Silva, L.F. & Jesús, D. (2019). Physicochemical characterization and sources of the thoracic fraction of road dust in a Latin American megacity. *Science of the Total Environment*, *652*, 434-446.

Ruffolo, S.A., Comite, V., La Russa, M.F., Belfiore, C.M., Barca, D., Bonazza, A., Crisci, G.M., Pezzino, A. & Sabbioni, C. (2015). An analysis of the black crusts from the Seville Cathedral: a challenge to deepen the understanding of the relationships among microstructure, microchemical features and pollution sources. *Science of the Total Environment*, *502*, 157-166.

Shahid, M.J., Arslan, M., Siddique, M., Ali, S., Tahseen, R. & Afzal, M. (2019). Potentialities of floating wetlands for the treatment of polluted water of river Ravi, Pakistan. *Ecological Engineering*, *133*, 167-176.

Soudagar, M.E.M., Nik-Ghazali, N.N., Kalam, M., Badruddin, I.A., Banapurmath, N., Khan, T.Y., Bashir, N.M., Akram, N., Farade, J. & Afzal, A. (2019). The effects of graphene oxide nanoparticle additive stably dispersed in dairy scum oil biodiesel-diesel fuel blend on CI engine: performance, emission and combustion characteristics. *Fuel*, *257*, 116015. https://doi.org/10.1016/j.fuel.2019.116015

Stamp, S., Burman, E., Shrubsole, C., Chatzidiakou, L., Mumovic, D. & Davies, M. (2020). Long-term, continuous air quality monitoring in a cross-sectional study of three UK non-domestic buildings. *Building and Environment*, *180*, 107071. https://doi.org/10.1016/j.buildenv.2020.107071

Sultan, M., Waheed, S., Ali, U., Sweetman, A.J., Jones, K.C. & Malik, R.N. (2019). Insight into occurrence, profile and spatial distribution of organochlorine pesticides in soils of solid waste dumping sites of Pakistan: Influence of soil properties and implications for environmental fate. *Ecotoxicology and Environmental Safety*, *170*, 195-204.

Van den Heede, P. & De Belie, N. (2012). Environmental impact and life cycle assessment (LCA) of traditional and 'green' concretes: literature review and theoretical calculations. *Cement and Concrete Composites*, *34*(4), 431-442.

Wang, N., Ling, Z., Deng, X., Deng, T., Lyu, X., Li, T., Gao, X. & Chen, X. (2018). Source contributions to $PM_{2.5}$ under unfavorable weather conditions in Guangzhou City, China. *Advances in Atmospheric Sciences*, *35*(9), 1145-1159.

Yin, X., de Foy, B., Wu, K., Feng, C., Kang, S. & Zhang, Q. (2019). Gaseous and particulate pollutants in Lhasa, Tibet during 2013–2017: Spatial variability, temporal variations and implications. *Environmental Pollution*, *253*, 68-77.

Summary

Assessment of integrated indoor environmental air quality parameters in selected church buildings of Faisalabad city: a statistical based comparative study. The objective of this study is to control the air quality parameters for a selected range of different particulate matters. A comprehensive experimental approach is established to regulate the quality of air about a selected range of different air pollutants being investigated in the indoor atmosphere of the church building. Relative humidity, temperature, carbon dioxide, particulate matter and radon were considered as the factors of air quality extents. For establishing the association among the selected parameters, the data were mathematically analyzed. The correlation coefficient confirmed a strong relationship between the indoor CO_2 level and the number of public. A negative relationship between the indoor CO_2 extent and indoor temperature confirmed that due to the increase in temperature the concentration of CO_2 decreased as well. A solid adverse connection among indoor relative humidity and indoor air temperature showed that due to the increase in air temperature, the level of the relative humidity decreased. Some recommendations were proposed for the treatment of air quality in church buildings for human well-being.

Authors' address:
Zahid Hussain
(https://orcid.org/0000-0002-5671-7030)
Sarhad University of Science and Information Technology
Peshawar 25000
Pakistan
e-mail: zahid.btech@suit.edu.pk

Haneen Q. ADEEB, Yaseen K. Al-TIMIMI

Mustansiriyah University, College of Sciences

Change on detection of vegetation cover and soil salinity using GIS technique in Diyala Governorate, Iraq

Introduction

Salinization is a serious environmental risk and is the main factor leading to land degradation and desertification. Soil surface salinity occurs as a result of superfluous irrigation and increased agricultural vitality (Machado & Serralheiro, 2017). As a result of the irrigation process in excess of the need, this increase led to the dissolution of salts in the soil, which after the water evaporates, the salts accumulate in the ground or spread out on the surface of the earth (Rafiq, Blaschke & Ur Rehman, 2014).

Provides remote sensing by satellite, an opportunity to discover the soil affected by salinity and sediments for specific features using reflected and emitted electromagnetic energy. The spectral reflection of the salt properties studied on the soil surface was addressed and mapped. In addition, it provides an indirect indication of vegetation in order to detect soil salinity and mapping (Al-Khakani & Sa'ad, 2019). It has become possible to estimate the changes by salinity land affected by and the vegetation cover through the use of multispectral satellite imagery (Allbed & Kumar, 2013).

Saline soils can be detected in two ways. The first method is directly from the multi-spectral image bands, which can be applied through high spectral reflection in the visible and near infrared range of the electromagnetic spectrum and the second method, indirectly through changes in the state of crops and loss of agricultural productivity in the agricultural lands (Taghadosi & Hasanlou, 2017).

Rapid improvements in remote sensing technologies in recent decades through integration with the geographic information system (GIS), greatly enable assessment and mapping of salinity processes, and thus are considered

the most beneficial economic methods (Azabdaftari & Sunarb, 2016). Many vegetation indices are using in several studies, such as the normalized difference vegetation index (*NDVI*), the enhanced vegetation index (*EVI*), and the soil adjusted vegetation index (*SAVI*). The *NDVI* is the index most common assessment and control of differences in vegetation cover (Ke, Im, Lee, Gong & Ryu, 2015).

In this paper, image differencing technology was used to generate a difference image in order to capture changes in the study area. This study aimed to develop an effective change detection method for assessing vegetation change and soil salinity in measured the *NDVI* and the *SI* values, to estimate the relationship between the *NDVI* and the *SI*. In order to know the damages caused by increasing salinity, which have a great role in reducing the economic losses caused by increased salinity in Diyala Governorate.

Material and methods

Study area and data acquisition

Diyala Governorate is located in the central part of eastern Iraq, which is located at latitude (33°46′23″ N) and longitude (45°08′58″ E) and covers an area of about 17,685 km^2 as shown in Figure 1. It is bordered to the northeast by Sulaymaniyah Governorate, to the west by Salahuddin, to the east by Iran, to the south by Baghdad Governorate, and to the southeast by Wasit Governorate. Diyala Province differs from other provinces of Iraq, as it is located within two different regions, the northeastern part is located within the semi-mountainous region, the southern and southwestern part, located within the sedimentary region, so it has climatic properties that combine the characteristics of the arid and semi-arid regions. This location makes Diyala climate transitional between the desert climate and the Mediterranean climate,
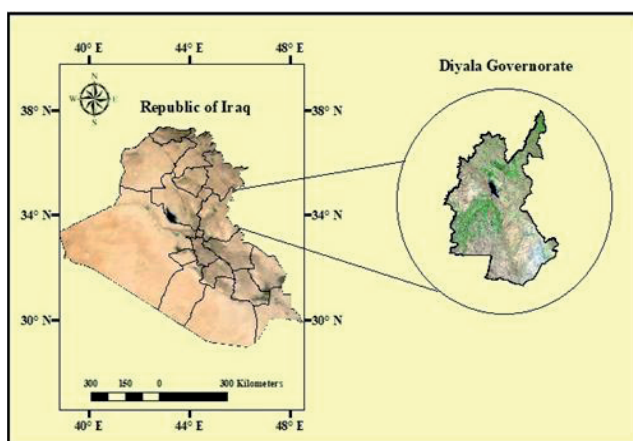

FIGURE 1. The geographical location of the study area (Diyala)

which is a continental climate characterized by drought and high temperatures in summer exceed 40°C and low with little rainfall in winter (Hussein, 2019).

The four images of Landsat, which path was 168 and row was 37, have been downloaded from the U.S. Geological Survey server (www.earthexplorer.com). The first image was Landsat 5 thematic mapper acquired on 14 March 2005, the second image was acquired on 29 April 2010, the third image was in 27 April 2015, while the fourth image was taken in 23 March 2020. The preprocessing of the images included geometric corrections. All images were geographically corrected to Universal Transverse Mercator (UTM) coordinate system utilizing the World Geodetic System (WGS) 1984 datum, Zone 38 by using ArcGIS 10.4 software. Including atmospheric correction for cloud pixel removal, and engineering data correction, while Excel 2010 software was used to achieve the Pearson correlation relationship between vegetation and salinity.

Differencing images technique

The change in the studied area can be detected using the image differences technique. Subtracting pixel values to the same position as two pictures includes two different time periods (Tan & Hao, 2017). The two images recorded jointly are compared to pixels, and pixels that indicate changing areas produce values that are distinctly different from those pixels accompanying regions that have not changed (Al-Khakani & Sa'ad, 2019). Mathematically, the image variation can be represented as follows:

$$ID = I(T_1) - I(T_2) \qquad (1)$$

Where ID represents difference image and $I(T_1)$ and $I(T_2)$ represents the captured images during two different time periods. Hence, the variable images are classified into three categories. The zero value is assigned to the areas of no change, and value range from 1 to −1 for the areas of increase and decrease, respectively.

The normalized difference vegetation index

The vegetation indicators are a great way to detect changes in land use by interpreting remote sensing images in multiple time data and assessing the density of vegetation (Al-Doski, Mansor & Shafri, 2013). In general, it is calculated as a ratio of the red and the NIR bands depending on the type of sensor, and is characterized by the following equation:

$$NDVI = \frac{NIR - R}{NIR + R} \qquad (2)$$

Vegetation are limited to values 0.1 and 1 of the *NDVI*. While non-vegetative surfaces such as water bodies, have negative *NDVI* values according to the ability of the water to absorb energy, whereas the bare soil regions have zero values for *NDVI*, due to the high reflection in the visible parts and the NIR (Usman, Yelwa & Gulumbe, 2012). In this study, the *NDVI* was used to monitor and evaluate changes in vegetation during the periods under study, in addition to the usage the value of the *NDVI* difference image that was calculated by subtraction of the *NDVI* image of the first date from the *NDVI* image of second date as follow:

$$DNDVI = NDVI(t_1) - NDVI(t_2) \qquad (3)$$

Salinity index

Among the various salinity indices, the *SI* was used to assess soil salinity based on two SWIR bands, because of the ability of these two ranges to completely distinguish in salinity areas, as follows:

$$SI = \frac{(SWIR_1 - SWIR_2)}{(SWIR_1 + SWIR_2)} \quad (4)$$

Soil salinity is calculated to enhance the spectral contribution of saline soils that cause the reduction and reduction of spectra associated with vegetation (Usman et al., 2012; Allbed & Kumar 2013; Al-Doski et al., 2013; Ke et al., 2015; Azabdaftari & Sunarb, 2016; Bannari, Guédon & El-Ghmari, 2016; Taghadosi & Hasanlou, 2017; Tan & Hao, 2017; Hussein, 2019). In the current search, the *SI* values were calculated for the different years 2005, 2010, 2015 and 2020, then the variation, the *SI* image (DSI) is calculated for the two change periods by subtracting the *SI* image for the first date from the *SI* image corresponding to the second date as shown in the following formula:

$$DSI = SI(t_1) - SI(t_2) \quad (5)$$

Positive and negative values of pixels are associated with increasing and decreasing salinity rates respectively, while zero values are indicated for salinity regions that do not change between the two change periods.

Results and discussion

Normalized difference vegetation index (*NDVI*) and salinity index (*SI*) were derived from Landsat images. Figure 2 illustrates the spatial variation of vegetation cover derived from the *NDVI* over the study area for the period 2005––2020. It can be seen that the vegetation cover varied from place to another, also from year to year in Diyala Province. The *NDVI* ranges between –0.6 and 1 in 2005, between –0.4 and 0.7 in 2010, between –0.7 and 0.5 in 2015, and also between –0.7 and 0.8 in 2020. The value more than 0.1 refers to vegetation cover, while the values from –1 to 0.1 represent the non-vegetation features as a bare surface, built-up area, and water body.

Table 1 data revealed the related statistics which included, the amount of area, and the percentage of area. The *NDVI* results showed that the vegetation cover in the year 2005, which was 10,454.796 km^2, accounted for 56% of the entire study area (17,685 km^2). On the other hand, the total coverage of the vegetation cover decreased in 2010 and 2015 to be 22% (4,066.21 km^2) and 19% (3,528.08 km^2), respectively. As for the year 2020, an increase in vegetation that cover most of Diyala regions of 41% (7,617.21 km^2) was seen.

Salinity index was applied to the TM and OLI images to extract the salinity information for the study area. Figure 3 shows the spatial variation of the soil salinity for the period from 2005 to 2020. Soil salinity analysis showed that estimated salinity lands were decreased gradually from 2005 to 2015, then it can be seen an increase in soil salinity in 2020.

Table 2 shows that area and percentage of soil salinity, in the year 2005 was 42.74% (7,940.74 km^2), while they decreased in 2010 and 2015 to be 22.5% (4,191.9 km^2) and 17.60% (3,270.1 km^2),
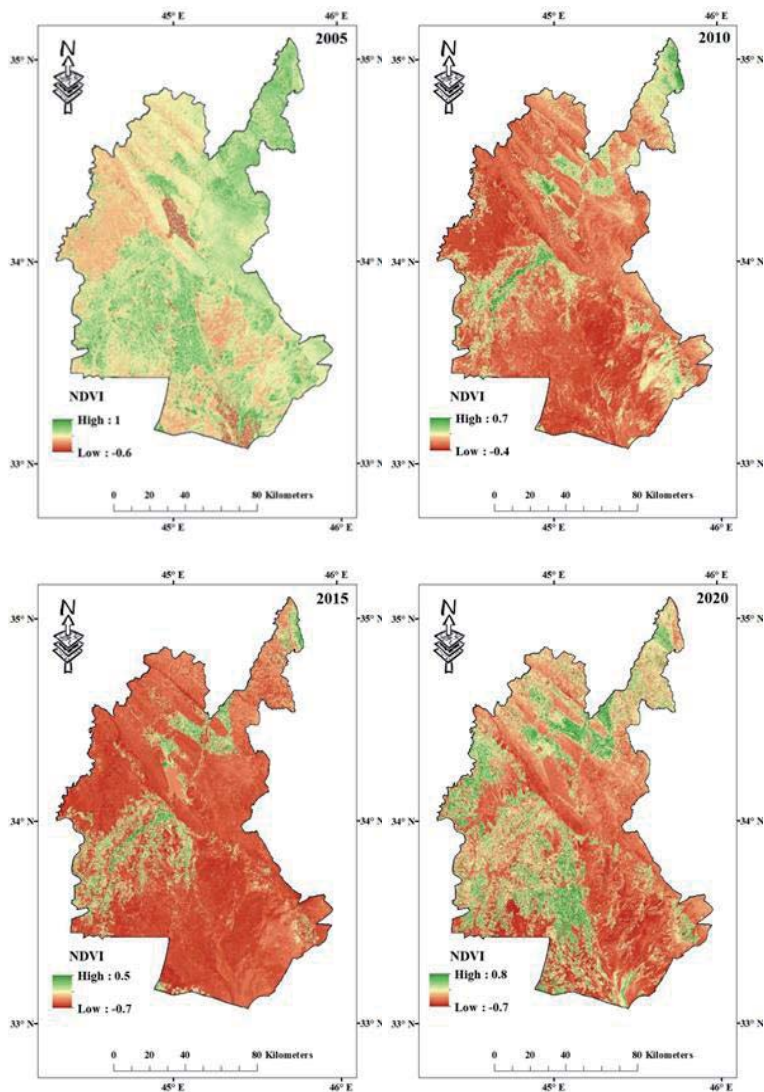
FIGURE 2. Spatial variation of the the normalized difference vegetation index based vegetation in 2005–2020 in Diyala Governorate

TABLE 1. Areas and percentages of change in the the normalized difference vegetation index values during for 2005–2020 periods

Classes	2005		2010		2015		2020	
	km	%	km	%	km	%	km	%
Non-vegetation	8 124.77	44	14 513.34	78	15 051.48	81	10 962.35	59
Vegetation	10 454.796	56	4 066.21	22	3 528.08	19	7 617.21	41

H.Q. Adeeb, Y.K. Al-Timimi
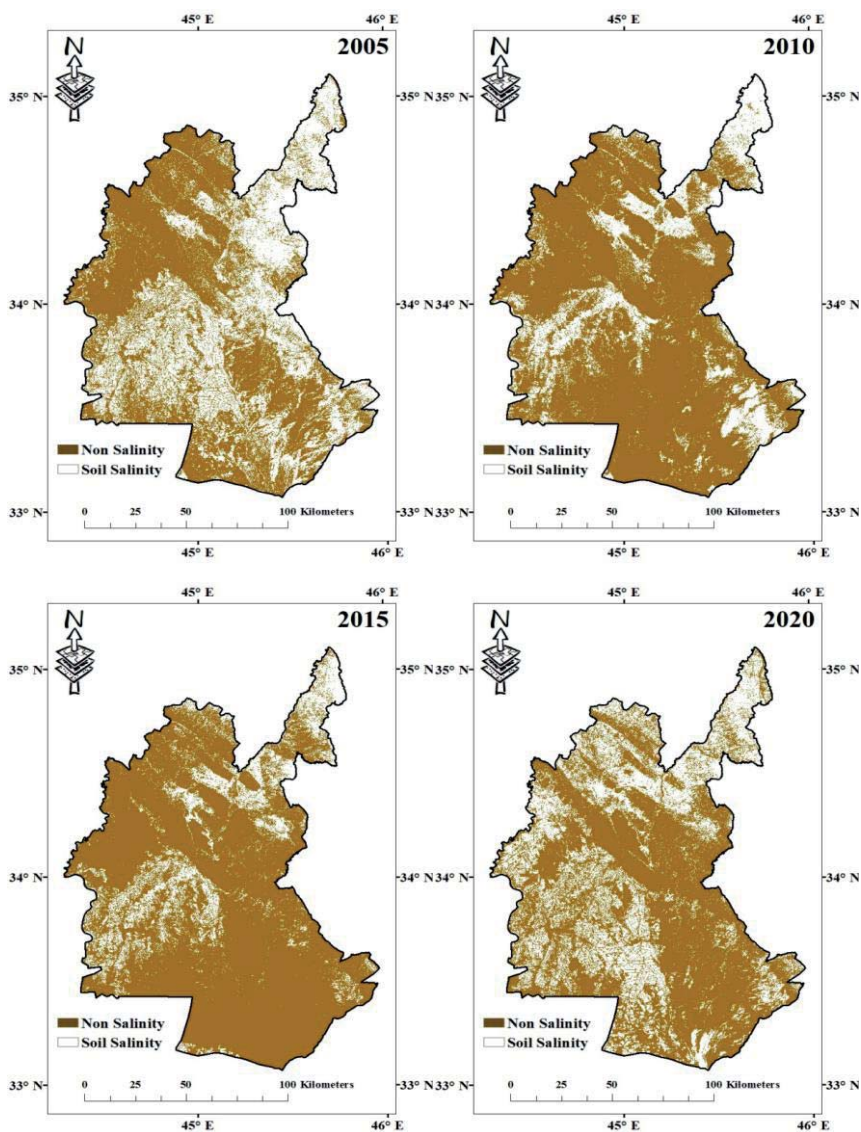
FIGURE 3. Spatial variation of the soil salinity in 2005–2020 in Diyala Governorate

TABLE 2. Areas and percentages of change in soil salinity index values during for 2005–2020 periods

Classes	2005		2010		2015		2020	
	km	%	km	%	km	%	km	%
Non-salinity	10 638.83	57.26	1 487.66	77.44	15 309.42	82.40	12 096.63	65.11
Salinity	7 940.74	42.74	4 191.90	22.56	3270.15	17.60	6 482.93	34.89

respectively. Then it can be seen an increase in coverage in soil salinity (6,482.9 km^2) about 34.89% stationed in the northwestern part of the study area in 2020. It can be seen that the highest salinity value was recorded in the year 2005 and the lowest salinity value recorded in the year 2015. Map of change detection for the *NDVI* and the *SI* illustrated in Figures 4 and 5. The change non-change maps of the DNDVI and DSI images for the change periods (2005–2010 and 2015–2020). The areas where changes occurred were displayed in red and blue to indicate the increase and decrease in vegetation or soil, respectively, while the areas that unchanged were shown in color yellow during the two study periods.

Figures 4 and 5 show a remarkable change in vegetation over a period of 20 years, mostly in the northern and southwestern regions of the study area between the two change periods. For the period 2005–2010, the increase in vegetation areas was clear in the small concentrated parts in the northern part of the study area. While, for the period 2015–2020, the increase in vegetation was more spread in the north and along the western side part of the study area. The decrease in vegetation has occurred in the southwestern and some eastern parts of Diyala Governorate for the period 2005–2020. Whereas, the decrease was mostly towards the northern part between in 2015–2020.

Table 3 summarizes the area and percentage change in the *NDVI* values between years 2005–2010 and 2015–2020. About 10% of the total study area experienced positive change that is increasing vegetation cover between 2005 and
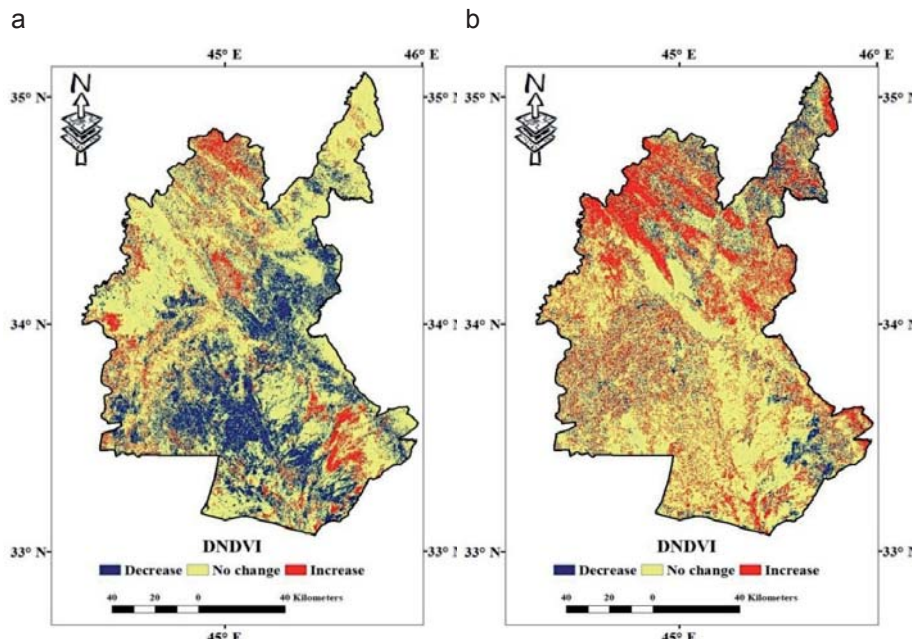
FIGURE 4. Change/no-change maps of the normalized difference vegetation index images: a – for 2005–2010 periods; b – for 2015–2020 periods
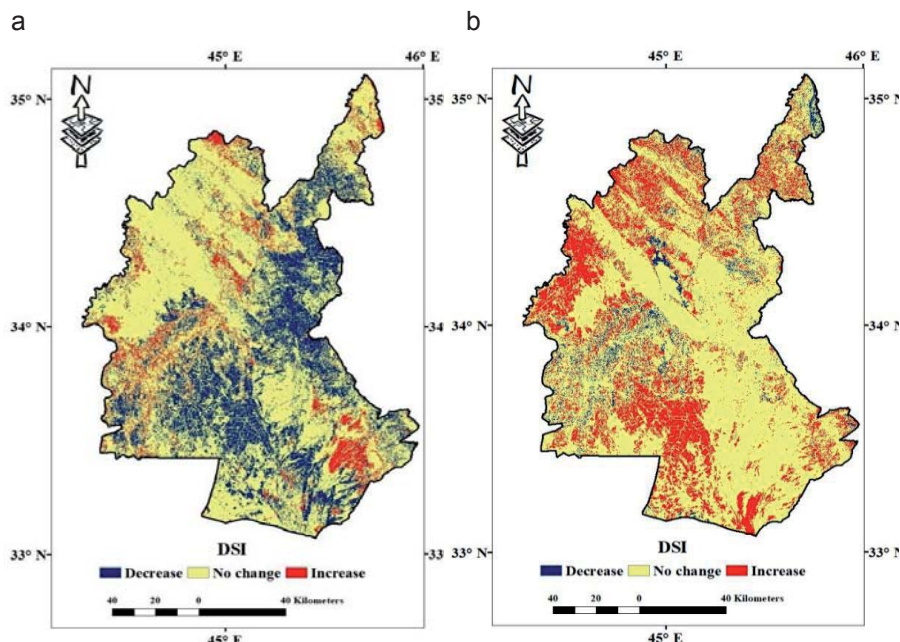
FIGURE 5. Change/no-change maps of the soil salinity index images: a – for 2005–2010 periods; b – for 2015–2020 periods

TABLE 3. Change area of the normalized difference vegetation index and the soil salinity index for the two change periods

Change classes	NDVI				SI			
	2005–2010		2015–2020		2005–2010		2015–2020	
	km	%	km	%	km	%	km	%
Change decrease	4 941.18	27	4 511.61	10	5 099	27.44	1 451	7.81
No change	11 751.85	63	12 229.18	66	12 131	65.29	12 107	65.16
Change increase	1 863.12	10	1 838.78	24	1 350	7.27	5 022	27.03

2010, whereas nearly 27% of showed negative change, that is decline in vegetation cover for the same period. However, in the 2015–2020 period, the positive changes increased to 24%, while the negative changes declined to 10%, indicating much vegetation increase during this period in the study area.

As for salinity changes, it can be observed that the period study attended a rise in saline areas from 7.2% in 2005––2010 to 27.03% in 2015–2020. It can be seen the increase in northwest and some southwestern parts of Diyala, while declining areas of salinity decreased from 27.4% in 2005–2010 to 7.8% in 2015––2020. This decrease is observed in southwestern and some eastern parts from Diyala Governorate. These results represent a significant increase in the sa-

FIGURE 6. The correlation between vegetation cover and soil salinity changes in 2005–2010 change period
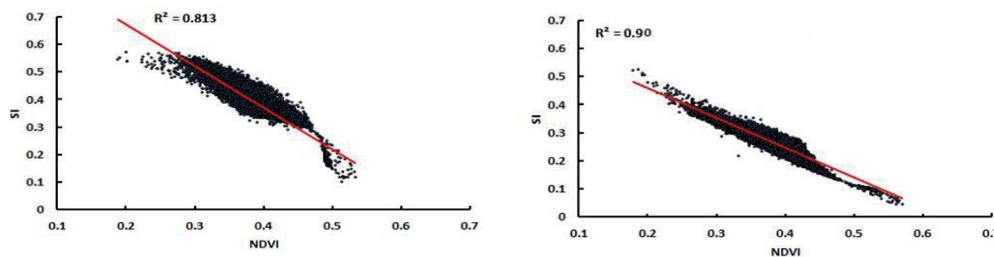
FIGURE 7. The correlation between vegetation cover and soil salinity changes in 2015–2020 change period

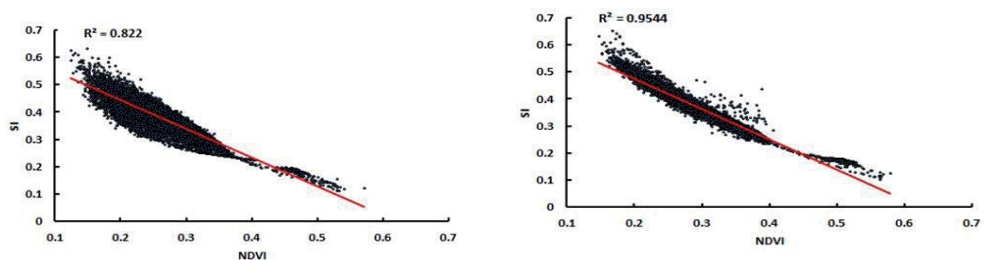linity of the soil and its negative effects on plant growth. In addition to higher temperatures, the study period (2005––2015) experienced a significant decrease in rainfall levels which led to an increase in evaporation rates (Al-Khakani & Sa'ad, 2019).

This has led to a reduction in the cultivated area and hence a rise in soil salinity levels. There are several reasons for vegetation degradation, such as the reluctance of a large number of farmers' to farm and practice in other works, as well as the conversion of some agricultural land into residential areas. Consequently, the study results showed that the decrease in vegetative regions often does not coincide with the increased salinity of the soil. The relationship between soil salinity and vegetation cover change has been calculated. Figures 6 and 7 show the

scatter plot between the *NDVI* and the *SI*. It can be seen that there is a high inverse correlation between the soil salinity and vegetation cover change for 2005–2010 and 2015–2020 periods. It is found the correlation coefficient between the *SI* and the *NDVI* at R^2 equal to 0.82, 0.95, 0.81 and 0.9 respectively.

Conclusions

Soil salinization is a complex process that changes over time and has adverse effects on agriculture, and so knowledge of the change in soil salinity dynamics over time and its impact on vegetation is required to help decision-makers working on the various steps needed to manage soil salinity and sustain vegetation. The purpose of this paper is to analyze

the possibility of salinity mapping and vegetation cover using different soil salinity and normalized vegetation difference indicators for part of Diyala Governorate. Overall, the soil salinity level has undergone remarkable changes in the study area over the past 20 years probably due to improper land use.

The findings suggest that the satellite imagery used in detection technologies can provide sufficient information on changes in vegetation and salinity in the soil. During the study period, it was discovered that there have been a strong changes in vegetation and soil salinity. The paper results showed a strong inverse correlation between the normalized difference vegetation index and salinity index values, and this confirms that changes in vegetation have a strong correlation with changes in salinity in the soil. Overall, during the research period the study region observed significant changes in soil salinity. This may be due to the high temperature and low average rainfall which, in addition to weak irrigation system and land misuse, all of which helped change the salinity levels in the soil.

References

Al-Doski, J., Mansor, S.B. & Shafri, H.Z.M. (2013). NDVI differencing and post-classification to detect vegetation changes in Halabja City, Iraq. *IOSR Journal of Applied Geology and Geophysics*, *1*(2), 1-10.

Al-Khakani, E.T. & Sa'ad, R.Y (2019). An assessment of soil salinity and vegetation cover changes for a part of An-Najaf governorate using remote sensing data. *Journal of Physics: Conference Series*, *1234*(1), 012023.

Allbed, A. & Kumar, L. (2013). Soil salinity mapping and monitoring in arid and semi-arid regions using remote sensing technology: a review. *Advances in Remote Sensing*, *2*(4), 373-385.

Azabdaftari, A. & Sunarb, F. (2016). Soil salinity mapping using multitemporal Landsat data. *The International Archives of the Photogrammetry, Remote Sensing and Spatial Information Sciences*, *7*, 3-9.

Bannari, A., Guédon, A.M. & El-Ghmari, A. (2016). Mapping slight and moderate saline soils in irrigated agricultural land using advanced land imager sensor (EO-1) data and semi-empirical models. *Communications in Soil Science and Plant Analysis*, *47*(16), 1883-1906.

Hussein, O.I. (2019). Impact of climate on human comfort in Diyala Governorate. *Journal of the University of Anbar for Humanities*, *1*(3), 305-331.

Ke, Y., Im, J., Lee, J., Gong, H. & Ryu, Y. (2015). Characteristics of Landsat 8 OLI-derived NDVI by comparison with multiple satellite sensors and in-situ observations. *Remote Sensing of Environment*, *164*, 298-313.

Machado, R.M.A. & Serralheiro, R.P. (2017). Soil salinity: effect on vegetable crop growth. Management practices to prevent and mitigate soil salinization. *Horticulturae*, *3*(2), 30. https://doi.org/10.3390/horticulturae3020030

Rafiq, L., Blaschke, T. & Ur Rehman, H. (2014). Satellite data based spectral indices for estimating surface salinity in Pakistan. *Journal of Agriculture and Environmental Sciences*, *1*, 6.

Taghadosi, M.M. & Hasanlou, M. (2017). Trend analysis of soil salinity in different land cover types using landsat time series data (case study Bakhtegan Salt Lake). *International Archives of the Photogrammetry, Remote Sensing & Spatial Information Sciences*, *XLII-4/W4*, 251-257.

Tan, M. & Hao, M. (2017). Change detection by fusing advantages of threshold and clustering methods. *International Archives of the Photogrammetry, Remote Sensing & Spatial Information Sciences*, *XLII-2/W7*, 897-901.

Usman, U., Yelwa, S. & Gulumbe, S. (2012). An assessment of vegetation cover changes across Northern Nigeria using trend line and principal component analysis. *Journal of Agriculture and Environmental Sciences*, *1*(1), 1-18.

Summary

Change on detection of vegetation cover and soil salinity using GIS technique in Diyala Governorate, Iraq. Soil salinity is one of the most important problems of land degradation, that threatening the environmental, economic and social system. The aim of this study to detect the changes in soil salinity and vegetation cover for Diyala Governorate over the period from 2005 to 2020, through the use of remote sensing techniques and geographic information system. The normalized difference vegetation index (*NDVI*) and salinity index (*SI*) were used, which were applied to four of the Landsat ETM+ and Landsat OLI satellite imagery. The results showed an increase in soil salinity from 7.27% in the period 2005–2010 to 27.03% in 2015–2020, as well as an increase in vegetation from 10% to 24% in the same period. Also the strong inverse correlation between the *NDVI* and the *SI* showed that vegetation is significantly affected and directly influenced by soil salinity changes

Authors' address:
Haneen Q. Adeeb
(https://orcid.org/0000-0003-3051-8110)
Mustansiriyah University
College of Science
Department of Atmospheric Sciences
Amreaa, 630 Baghdad
Iraq
e-mail: haneenq.alani@gmail.com

Yaseen K. Al-Timimi
(http://orcid.org/0000-0001-5820-0345)
Mustansiriyah University
College of Science
Department of Atmospheric Sciences
Palestine street, 46131, Baghdad
Iraq
e-mail: yaseen.altimimi.atmsc@uomustansiriyah.
        edu.iq

Ali Subhi ALHUMAIMA, Sanjar Mutalovich ABDULLAEV

South Ural State University, Department of System Programming

The sensitivity of vegetation in the lower Tigris basin landscapes to regional and global climate variability

Key words: climate variability, vegetation, global modulation, precipitation, temperature

Introduction

Global climate change has the potential to increase the frequency of ecosystem disturbances such as fire and drought, threatening the terrestrial ecological environment and food security (Yuan, Wu, Hou, Xu & Lu, 2019). Most of the Euphrates–Tigris basin, especially in southeastern Turkey as well as in northern Syria and Iraq (the lower Tigris basin), has a Mediterranean climate that is characterized by wet winters and dry summers (Food and Agriculture Organization of the United Nations [FAO], 2009). Hence, the vegetation of the region is highly sensitive to climatic variability (Alhumaima & Abdullaev, 2019).

Since the 1970s, monitoring vegetation has been improved using several remote sensing-based indices. The normalized difference vegetation index (*NDVI*) (Tucker, 1979), specifically, is the most popular and has been used successfully to detect vegetation and climate conditions interactions worldwide at various temporal and spatial scales (Wu et al., 2015; Xu, Yang & Chen, 2016; Yuan et al., 2019; Luo, Mao, Wen & Liu, 2020). In the study of Luo et al. (2020), the dynamic characteristics of drought characterized using the standardized precipitation evapotranspiration index (*SPEI*) and the *NDVI* were investigated and evaluated on an interannual scale from 1998 to 2015. Two *NDVI* datasets were used in the work of Xu et al. (2016) to study vegetation growth and its response to climate change reflected by the precipitation, minimum, maximum, and mean temperatures at yearly and monthly time scales from 1982 to 2013. Yuan et al. (2019) established the trend of *NDVI* vegetation change in the past three decades (1982–2013) and examined the effect of climate (monthly temperature and precipitation) and non-climate (population, gross domestic product, and live-

stock) factors on vegetation growth. Note that the temporal delay in the vegetation response to environmental changes should be considered when looking for the sensitivity of ecosystems to climate variability (Wu et al., 2015). However, in our recent work (Alhumaima & Abdullaev, 2019), found that the maximum biological productivity during the growing season for Diyala river basin, a tributary of Tigris, is controlled by seasonal winter precipitation and January–March mean temperatures. Also showed that the neural network-based prediction of the spatiotemporal *NDVI* can be improved by using additional zonal landscape input predictor or by constructing an individual predicting model for each one of the zonal landscapes.

The two main aims of this study are (a) to establish the temporal vegetation change during the maximum biological productivity season and (b) to explore the vegetation sensitivity to recent (2000–2016) climate variability. However, direct regional observations of precipitation and temperatures are very rare and sparse, i.e. they cannot provide the needed spatiotemporal series. A particularly attractive option is to use the available different climate factors from several global gridded datasets. In this work, we compared the *NDVI* response to precipitation and temperature time series derived from seven observational and reanalysis datasets. These data have rarely been used for the lower Tigris basin; therefore, it would be beneficial to assess their performance in reflecting the vegetation variability in the region. The significant differences in climatic conditions of the different datasets led us,

first, to use normalized versions of them, and second, to refuse the using of Köppen–Trewartha bioclimatic classification. Instead, landscapes were classified based on land cover/use categories and altitude levels. To compensate for the absence of some other factors on which the biological productivity of the landscapes depends, such as wind speed, cloudiness, etc., the impact of global weather-forming factors, expressed in global circulation indices, has been assessed also.

Materials and methods

Study area

The study area of approx. 251,400 km^2 (41°05′–48°07′E and 38°38′–48°07′N) illustrated in Figure 1; is distributed mainly between Iraq, Iran and Turkey and includes the basins of the five major tributaries of Tigris: Fesh Khabour, Greater Zab, Lesser Zab, Al-Adhaim and Diyala. The region has diverse landforms (Fig. 1b) and land cover patterns (Fig. 1c) that are expected to be very sensitive to climate variability. From the total study area, 22% are plains with heights of up to 300 m, 32% are foothills with elevations from 300 to 900 m and the remaining 46% are mountainous regions. From the land cover map, 47% of the study area is occupied by natural vegetation (NV: grasslands, trees, shrubs, and herbaceous vegetation), 33% is attributed to agricultural croplands which are classified into agricultural rainfed lands (AR: 25%) and agricultural irrigated lands (AI: 8%), and low vegetation lands (LV: sparse vegetation, barren, water bodies and urban).
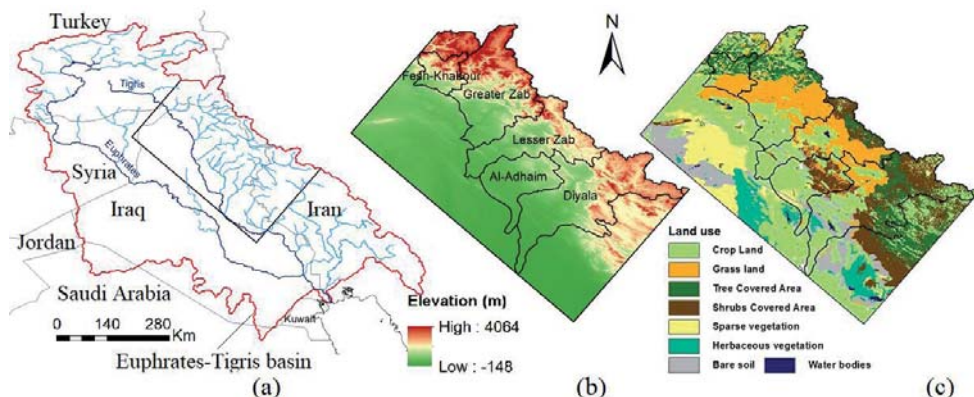
FIGURE 1. Study area (a) with elevation levels (b) and land cover map (c)

Datasets

Ten gridded datasets were used in this study. The MODIS 16-day *NDVI* maps of 250 × 250 m spatial resolution and 16 days temporal resolution (MOD13Q1) (Didan, 2015) for March and April growing months were directly downloaded from NASA's Earth Observing System. In addition, we used the ASTER GDEM version 2 (Ministry of Economy, Trade and Industry of Japan / United States National Aeronautics and Space Administration [METI/NASA], 2011) and FAO Global Land Cover-SHARE version 2014 (Latham, Cumani, Rosati & Bloise, 2014) datasets to delineate the different terrains and land cover types, and thus construct study area landscapes.

The monthly precipitation and temperature data used over the period 1981–2016 were obtained from two observational and five atmospheric reanalysis datasets: CRU-TS4.01 (Harris, Jones, Osborn, & Lister, 2014), UD-V5.01 (Willmott & Matsuura, 2019), ERA-Interim (Dee et al., 2011), Modern-Era Reanalysis 2 (Gelaro et al., 2017), NCEP-DOE AMIP-II Reanalysis

(Kanamitsu et al., 2002), JRA-55 (Kobayashi et al., 2015) and NCEP-CFSR (Saha et al., 2014), hereafter CRU, UD, ERA, MERRA, NCEP, JRA and CFSR, respectively.

In addition, non-gridded datasets of global circulation indices: El-Nińo-Southern Oscillation (*ENSO*), Atlantic Multidecadal Oscillation (*AMO*), North Atlantic Oscillation (*NAO*) and Dipole Mode Index (*DMI*), obtained from the National Oceanic and Atmospheric Administration (*NOAA*), were also used in this study.

Study area landscapes

From the above description, the study area has diverse ecosystems and land cover categories, and one could easily expect that their vegetation sensitivity to climate will be different. For this reason and in order to examine the effect of climate variability on the different *NDVI* landscapes, we classified our study area into 10 smaller landscapes (Fig. 2a): plains with NV, AR, AI and LV (PNV, PAR, PAI and PLV, respectively), foothills with NV, AR and LV (FNV,

FAR and FLV, respectively), and finally mountains with NV, AR and LV (MNV, MAR and MLV, respectively). The mean altitude and area percentage of each individual landscape are illustrated in Figures 2b and 2c. Note that, in our analysis, LV landscapes, urban, and water areas were not considered.

etated (Xu et al., 2016; Alhumaima & Abdullaev, 2019).

Standardized precipitation index and z-score

To minimize the significant variance in the original amplitudes of the climate factors between the different datasets, only normalized time series of monthly
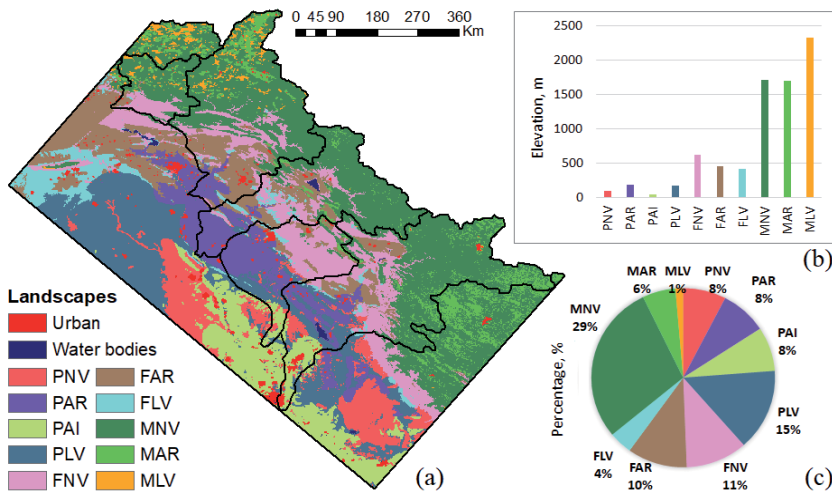
FIGURE 2. Study area landscapes (a) with their mean altitudes (b) and area percentages (c)

Methods

NDVI data processing

The maximum value compositing (MVC) method was used to produce monthly *NDVI* maps and minimize the effects of atmospheric, cloud contamination, and solar zenith angle (Alhumaima & Abdullaev, 2019). Additionally, *NDVI* pixels less than 0.1 were excluded from the analysis and considered as non-veg-

precipitation and temperatures have been used in this study. Therefore, we constructed for each individual landscape, seven pairs (based on the seven climate datasets) of 35-years (1981–2016) based time series of six-months (October––March) the standardized precipitation index (*SPI*) (Mckee, Doesken, & Kleist, 1993; Alhumaima & Abdullaev, 2018) and three-months (January–March) temperature *z*-score (Alhumaima & Abdullaev, 2018; Li, Li, Lu, Zhang & Kim, 2019).

Pearson correlation analysis

Since the indices time series for the *NDVI*, global circulations, precipitation and temperatures meet the basic assumptions of parametric linear analysis, we decided to use the Pearson correlation coefficient (*PCC*) (Luo et al., 2020) to give a clear picture of the strength of the relationships among them. The preliminary correlation analysis showed that the *NDVI* vegetation of both March and April, averaged over the entire region, have the highest correlation ($0.5 \leq PCC < 0.8$) to the same cumulative amounts of October–March period total precipitation and January–March period mean temperatures according to the seven climate datasets. Similarly, the coefficients of determination (Kamble, Kilic & Hub-

bard, 2013), denoted R^2, were to measure the proportion of variability in the landscapes' *NDVI* that can be explained by the other independent variables in the linear regression model.

Results and discussion

Landscapes' NDVI change

The *NDVI* time series for six regional landscapes during March and April growing months are illustrated in Figure 3. These time series are not regular over the study period with the presence of almost significant lack in vegetation during 2000, 2006, 2008, 2009, 2011 and 2012. In fact, many previous studies reported that the Euphrates–Tigris basin
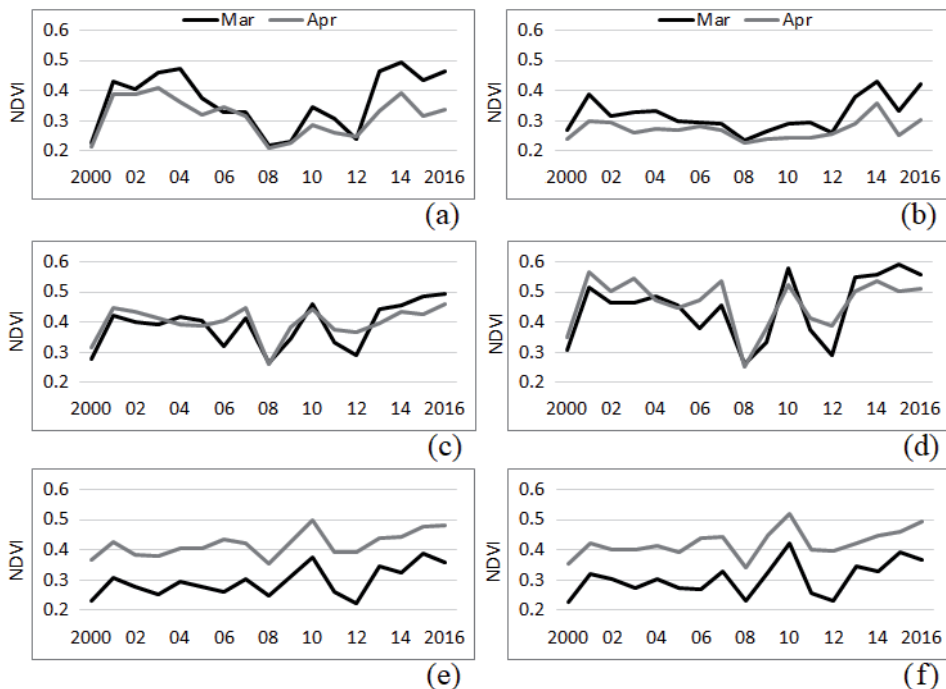
FIGURE 3. March and April mean *NDVI* of PAR and PAI (a and b), FNV and FAR (c and d), and MNV and MAR (e and f), respectively

experienced significant drought events during these years (Alhumaima & Abdullaev, 2018; Mathbout, Lopez-Bustins, Martin-Vide, Bech & Rodrigo, 2018). At the same time, the moderate–high correlations between March *NDVI* time series of all regional landscapes with each other ($0.5 \leq PCC < 1$), confirm the effect of drought on all landscapes simultaneously. The correlations between landscapes' March *NDVI* and those of April were moderate to high ($0.5 \leq PCC < 1$) also. On the other hand, these correlations indicate different responses from different landscape types.

The *NDVI* change in the agricultural rainfed landscapes (PAR for example, Fig. 3a) during both March and April were more prominent and less stable ($std = 0.103$ and 0.066) compared to that of the agricultural irrigated landscape (PAI, Fig. 3b) which was more stable but also observable ($std = 0.062$ and 0.032, respectively). This indicates that the croplands are also affected by climatic variability, but human management, such as; irrigation could mitigate the negative effects.

Landscapes sensitivity to climate

The 35-years based mean monthly precipitations averaged over the whole study area (Fig. 4a) show that UD, ERA, JRA, and CFSR, with annual precipitations of 451, 462, 620 and 470 mm, were wetter than CRU, MERRA and NCEP of 375, 257 and 395 mm, respectively. At the same time and with respect to the temperatures (Fig. 4b), the mean annual values were ranged between 17.8 and 18.4°C, except for NCEP and JRA datasets of only 12.8 and 14.3°C, respectively.

Several studies showed that significant differences exist in precipitation estimates between the different datasets and their performance may vary depending on the geographic location and climatic zone (Essou, Sabarly, Lucas-Pither, Brisette & Poulin, 2016; Chen, Gan, Tan, Shao & Zhu, 2019). We demonstrated in Alhumaima and Abdullaev (2018) that despite their relative simplicity, the *SPI* and *z*-score are good indicators of regional drought/wet and cold/warm cases, respectively. The 17 out of the 35-years based *z*-score time series of January–March period temperatures (ZJM) calculated over three of the regional landscapes and analogous six-month *SPI* time series of October–March period precipitation (SPIOM) are shown in Figures 4c, 4d, 4e, 4f, 4g and 4h.

However, we examined the correlations between *NDVI* in March and April of each individual landscape and the corresponding normalized climate factors and found that there are large variances in these relationships ($0.17 \leq PCC < 0.91$) depending on dataset used and landscape type. For example, March *NDVI* in of the foothills' natural vegetation landscape (FNV, Fig. 3e) has weak correlations ($PCC < 0.5$) with SPIOM according to UD and JRA datasets, moderate correlations ($0.5 \leq PCC < 0.75$) according to CRU, ERA, NCEP and CFSR datasets, and high correlation ($PCC \geq 0.75$) according to MERRA dataset. The correlations between March *NDVI* of the same landscape and ZJM were moderate (high) according to CRU, UD, ERA, MERRA, NCEP and CFSR (JRA).

To estimate how much March *NDVI* variability is associated with both SPIOM and ZJM according to the seven datasets,
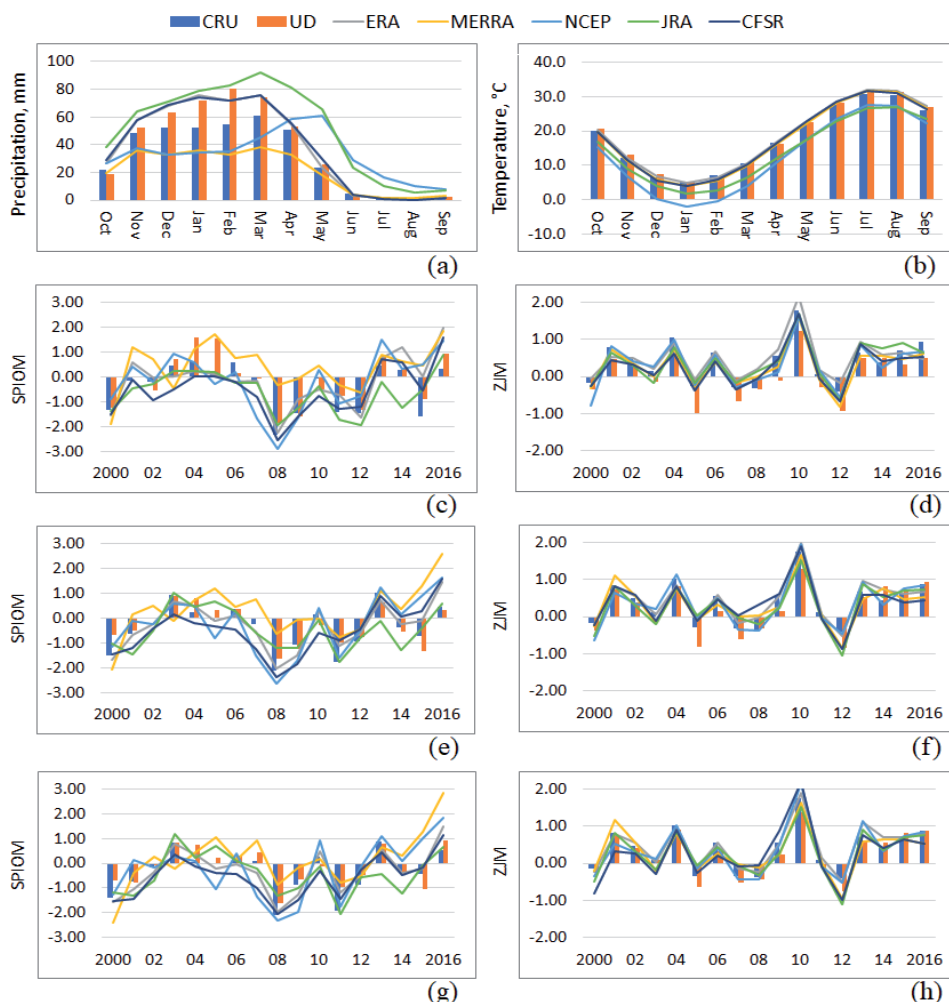
FIGURE 4. Study area mean annual precipitations and temperatures (a and b); normalized monthly precipitations and temperatures of PAR, FNV and MNV landscapes (c-d, e-f and g-h), respectively, according to seven datasets

we calculated the coefficients of determination (R^2). The R^2 values, presented in the table, are directly interpreted as follows. If the value of R^2 is 0.40, as in the case of PNV landscape (depending on SPIOM and ZJM of JRA reanalysis), this means that 40% of the original variability of *NDVI* can be explained by the corresponding hydrothermal regime,

and 60% of residual variability remains unexplained.

The table indicates that the variability of landscapes' *NDVI*, explained using two normalized climatic factors of the same dataset, is varied between 28 and 83% depending on the dataset used. However, using the time series of ERA and CFSR, we can explain from

TABLE. Relative part of landscapes' *NDVI* variability described by variations of normalized seasonal precipitation and temperatures

LS	Resulted R^2 values based on SPIOM/ZJM of the same dataset							Using mixed datasets	
	CRU	UD	ERA	MERRA	NCEP	JRA	CFSR	SPIOM/ZJM	R^2
PNV	0.48	0.62	0.80	0.45	0.48	0.40	0.69	ERA/CFSR	0.82
PAR	0.55	0.65	0.74	0.52	0.69	0.49	0.77	CFSR/UD	0.79
PAI	0.40	0.46	0.83	0.28	0.53	0.34	0.77	ERA/UD	0.86
FNV	0.54	0.56	0.65	0.78	0.61	0.61	0.72	MERRA/UD	0.80
FAR	0.61	0.71	0.71	0.77	0.72	0.67	0.75	CFSR/MERRA	0.83
MNV	0.54	0.58	0.63	0.78	0.61	0.69	0.69	MERRA	0.78
MAR	0.63	0.61	0.68	0.80	0.65	0.71	0.72	MERRA	0.80

77 to 83% of *NDVI* variability on lowland plains' landscapes and from 63 to 75% on higher landscapes. The MERRA dataset is poorest to describe the variability of the semi-desert plains' vegetation (28–45%) but it is the best predictor for foothills' and mountains' vegetation (77–80%). Thus, the consideration of the combined effects of normalized seasonal precipitation and temperature exposure to vegetation explains much of *NDVI* variability, regardless of geographic location and land cover type.

To obtain better predictions, we calculated R^2 for each individual landscape based on all possible combinations of SPIOM and ZJM time series from the different datasets. The results (the table) showed that the explanation of *NDVI* variability of four out of the five landscapes, located in plains and foothills (PNV, PAR, PAI and FNV), optimized by 2.4–3.5% using ZJM time series of CFSR and UD datasets, while the combination of SPIOM and ZJM time series of CFSR and MERRA datasets, respectively, to explain *NDVI* variability of the FAR landscape has increased R^2 by 7.2%. This clearly indicates that better

predictions of vegetation variability can be obtained when relying on more than one dataset simultaneously.

From the above analysis, vegetation of the region is highly dependent on climate. Therefore, it makes sense to link factors that affect the regional climate with the vegetation. On the other hand, these factors could compensate for the absence of other factors like wind speed, total cloud cover, evaporation, soil moisture and many others that have an effect on plant growth. However, in this work, we decided to verify from the states of *ENSO*, *AMO*, *NAO* and *DMI* as it has been found in several studies (Cullen, Kaplan, Arkin & de Menocal, 2002; Karabörk & Kahya, 2009; Khidher & Pilesjö, 2015; Pourasghar, Oliver & Holbrook, 2019) that they have a significant influence on climate and rivers' streamflow in the surrounding areas.

The analysis showed that the study area's averaged SPIOM according to all datasets are moderately correlated (0.55 ≤ *PCC* ≤ 0.7) to both: SON, OND, NDJ and DJF states of *ENSO* and December state of *DMI*, while the correlations were weak with both *NAO* and *AMO*.

We found that the ZJM temperatures are moderately correlated ($0.5 \leq PCC \leq 0.6$) to SON state of *AMO*, while the correlations were weak with other indices.

As expected, the correlation analysis between March *NDVI* and the four global circulation indices showed that the most positive responses of landscapes were also to the SON-DJF states of *ENSO* ($0.55 \leq PCC \leq 0.70$) and December state of *DMI* ($0.37 \leq PCC \leq 0.72$). With respect to the SON state of *AMO* and *NAO*, the responses of all landscapes were weakly positive ($0.17 \leq PCC \leq 0.36$) and weakly negative ($-0.34 \leq PCC \leq -0.1$), respectively. For the correlations with the next April, almost the same description above has noted but with less sensitivity compared to March.

As with the *NDVI*, SPIOM and ZJM, we calculated the coefficients of determination based on all possible combinations of the four circulation indices in order to find out the best predictors for each of the regional landscapes. The analysis showed that using the combined effect of three sets of circulation indices (*ENSO*, *AMO* and *NAO*; *ENSO*, *DMI* and *NAO*; *ENSO*, *DMI* and *AMO*) we can explain 30–55, 70–78, and 60–64% of landscapes' *NDVI* variability on plains, foothills, and mountains, respectively.

Thus, it can be concluded from the results that the consideration of the combined effects of the global circulation indices and climate factors can enhance the explanation of vegetation variation. To prove this, we recalculated R^2 based on five input predictors consisting of landscapes' best combinations of normalized climate factors (the table) and climate indices, and found that the relative explanations of *NDVI* variability for all

landscapes have increased by 4.5–9.5% compared to the values presented in the table. Here, R^2 of: plains' landscapes (PNV, PAR and PAI) have increased to be 86, 84 and 93% with increasing rates of 4.7, 6.0 and 7.5%, foothills' landscapes (FNV, FAR) have increased to be 88 and 89% with increasing rates of 9.1 and 6.7%, and finally, mountainous landscapes (MNV, MAR) have increased to be 86 and 88% with increasing rates of 9.3 and 9.1%, respectively.

Conclusions

In this work, the study area of the lower Tigris basin was classified based on the landforms (plains, foothills, and mountains) and land cover patterns (natural vegetation, agricultural rainfed, and agricultural irrigated) into 10 smaller natural and agricultural landscapes. The variation of remote sensing MODIS *NDVI* data was then examined during the maximum biological productivity season (March and April) as a response to the current regional and global climate variability. These latter are reflected by monthly precipitation and temperature time series derived from two observational and five reanalysis climate datasets (CRU, UD, ERA, MERRA, NCEP, JRA and CFSR) and four circulation indices (*ENSO*, *AMO*, *NAO* and *DMI*). The preliminary analysis showed the *NDVI* of both March and April are strongly correlated with the cumulative winter precipitation (October–March) and mean temperatures of January–March period. The significant differences in precipitation and temperature estimates between the different datasets led us to

use normalized versions of the climate factors (*SPI* and *z*-score) in searching for the landscapes' vegetation response to climate variability. The multiple correlation analysis showed that combining the normalized seasonal climate factors from different datasets can explain much of the landscapes' *NDVI* variability regardless of the geographic location and land cover category. It is also found that the predictability of landscapes' vegetation conditions can be enhanced by combining climate factors with global circulation indices that are found to influence the regional climate as well.

References

Alhumaima, A.S. & Abdullaev, S.M. (2018). Preliminary assessment of hydrothermal risks in the Euphrates–Tigris basin: Droughts in Iraq. *Bulletin of the South Ural State University, Series, Computational Mathematics and Software Engineering*, *7*(4), 41-58. https://doi.org/10.14529/cmse180403

Alhumaima, A.S. & Abdullaev, S.M. (2019). Landscape Approach to Normalized Difference Vegetation Index Forecast by Artificial Neural Network: Example of Diyala River Basin. *Bulletin of the South Ural State University, Series Computer Technologies, Automatic Control & Radioelectronics*, *19*(3), 5-19. https://doi.org/10.14529/ctcr190301

Chen, S., Gan, T.Y., Tan, X., Shao, D. & Zhu, J. (2019). Assessment of CFSR, ERA-Interim, JRA-55, MERRA-2, NCEP-2 reanalysis data for drought analysis over China. *Climate Dynamics*, *53*(1-2), 737-757. https://doi.org/10.1007/s00382-018-04611-1

Cullen, H.M., Kaplan, A., Arkin, P.A. & de Menocal, P.B. (2002). Impact of the North Atlantic Oscillation on Middle Eastern Climate and Streamflow. *Climatic Change*, *55*(3), 315-338. https://doi.org/10.1023/A:1020518305517

Dee, D.P., Uppala, S.M., Simmons, A.J., Berrisford, P., Poli, P., Kobayashi, S., Andrae, U., Balmaseda, M.A., Balsamo, G., Bauer, P., Bechtold, P., Beljaars, A.C.M., van de Berg, L., Bidlot, J., Bormann, N., Delsol, C., Dragani, R., Fuentes, M., Geer, A.J., Haimberger, L., Healy, S.B., Hersbach, H., Hólm, E.V., Isaksen, L., Kĺllberg, P., Köhler, M., Matricardi, M., McNally, A.P., Monge-Sans, B.M., Morcrette, J.J., Park, B.K., Peubey, C., de Rosnay, P., Tavolato, C., Thépaut, J.N. & Vitart, F. (2011). The ERA-Interim reanalysis: configuration and performance of the data assimilation system. *Quarterly Journal of the Royal Meteorological Society*, *137*(656), 553-597. https://doi.org/10.1002/qj.828

Didan, K. (2015). *MOD13Q1 MODIS/Terra Vegetation Indices 16-Day L3 Global 250m SIN Grid, V006* [Data set]. NASA EOSDIS Land Processes DAAC. https://doi.org/10.5067/MODIS/MOD13Q1.006

Essou, G.R.C., Sabarly, F., Lucas-Picher, P., Brissette, F. & Poulin, A. (2016). Can precipitation and temperature from meteorological reanalyses be used for hydrological modeling? *Journal of Hydrometeorology*, *17*(7), 1929-1950. https://doi.org/10.1175/JHM-D-15-0138.1

Food and Agriculture Organization of the United Nations [FAO] (2009). *AQUASTAT Transboundary River Basins – Euphrates-Tigris River Basin*. Rome: Food and Agriculture Organization of the United Nations.

Gelaro, R., McCarty, W., Suárez, M.J., Todling, R., Molod, A., Takacs, L., Randles, C.A., Darmenov, A., Bosilovich, M.G., Reichle, R., Wargan, K., Coy, L., Cullather, R., Draper, C., Akella, S., Buchard, V., Conaty, A., da Silva, A., Gu, W., Kim, G.K., Koster, R., Lucchesi, R., Merkova, D., Nielsen, J.E., Partyka, G., Pawson, S., Putman, W., Rienecker, M., Schubert, S.D., Sienkiewicz, M. & Zhao, B. (2017). The Modern-Era Retrospective Analysis for Research and Applications, Version 2 (MERRA-2). *Journal of Climate*, *30*(14), 5419-5454. https://doi.org/10.1175/JCLI-D-16-0758.1

Harris, I., Jones, P.D., Osborn, T.J. & Lister, D.H. (2014). Updated high-resolution grids of monthly climatic observations – the CRU TS3.10 Dataset. *International Journal of Climatology*, *34*(3), 623-642. https://doi.org/10.1002/joc.3711

Kamble, B., Kilic, A. & Hubbard, K. (2013). Estimating Crop Coefficients Using Remote Sensing-Based Vegetation Index. *Remote Sensing*, *5*(4), 1588-1602. https://doi.org/10.3390/rs5041588

Kanamitsu, M., Ebisuzaki, W., Woollen, J., Yang, S.K., Hnilo, J.J., Fiorino, M. & Potter, G. L. (2002). NCEP–DOE AMIP-II Reanalysis (R-2). *Bulletin of the American Meteorological Society*, *83*(11), 1631-1644. https://doi.org/10.1175/BAMS-83-11-1631

Karabörk, M.Ç. & Kahya, E. (2009). The links between the categorised Southern Oscillation indicators and climate and hydrologic variables in Turkey. *Hydrological Processes*, *23*(13), 1927-1936. https://doi.org/10.1002/hyp.7331

Khidher, S.A. & Pilesjö, P. (2015). The effect of the North Atlantic Oscillation on the Iraqi climate 1982–2000. *Theoretical and Applied Climatology*, *122*(3-4), 771-782. https://doi.org/10.1007/s00704-014-1327-4

Kobayashi, S., Ota, Y., Harada, Y., Ebita, A., Moriya, M., Onoda, H., Onogi, K., Kamahori, H., Kobayashi, Ch., Endo, H., Miyaoka, K. & Takahashi, K. (2015). The JRA-55 reanalysis: general specifications and basic characteristics. *Journal of the Meteorological Society of Japan. Ser. II*, *93*(1), 5-48. https://doi.org/10.2151/jmsj.2015-001

Latham, J., Cumani, R., Rosati, I. & Bloise, M. (2014). *FAO Global Land Cover SHARE (GLC-SHARE) Beta-Release* (version 1.0). Rome: Land and Water Division, Food and Agriculture Organization.

Li, F., Li, H., Lu, W., Zhang, G., & Kim, J.C. (2019). Meteorological Drought Monitoring in Northeastern China Using Multiple Indices. *Water*, *11*(1), 72. https://doi.org/10.3390/w11010072

Luo, N., Mao, D., Wen, B. & Liu, X. (2020). Climate Change Affected Vegetation Dynamics in the Northern Xinjiang of China: Evaluation by SPEI and NDVI. *Land*, *9*(3), 90. https://doi.org/10.3390/land9030090

Mckee, T.B., Doesken, N.J. & Kleist, J. (1993). The relationship of drought frequency and duration to time scales. *Proceedings of the 8th Conference on Applied Climatology, American Meteorological Society*, *17*(22), 179-184.

Mathbout, S., Lopez-Bustins, J.A., Martin-Vide, J., Bech, J. & Rodrigo, F.S. (2018). Spatial and temporal analysis of drought variability at several time scales in Syria during 1961–2012. *Atmospheric Research*, *200*, 153-168. https://doi.org/10.1016/j.atmosres.2017.09.016

Ministry of Economy, Trade and Industry of Japan / United States National Aeronautics and Space Administration [METI/NASA] (2011). *Advanced Spaceborne Thermal Emission and Reflection Radiometer Global Digital Elevation Model – ASTER GDEM* (version 2) [DEM data sets]. Retrieved from https://asterweb.jpl.nasa.gov/gdem.asp

Pourasghar, F., Oliver, E.C.J. & Holbrook, N.J. (2019). Modulation of wet-season rainfall over Iran by the Madden–Julian Oscillation, Indian Ocean Dipole and El Niño–Southern Oscillation. *International Journal of Climatology*, *39*(10), 4029-4040. https://doi.org/10.1002/joc.6057

Saha, S., Moorthi, S., Wu, X., Wang, J., Nadiga, S., Tripp, P., Behringer, D., Hou, Y.T., Chuang, H., Iredell, M., Ek, M., Meng, J., Yang, R., Mendez, M.P., van den Dool, H., Zhang, Q., Wang, W., Chen, M. & Becker, E. (2014). The NCEP Climate Forecast System Version 2. *Journal of Climate*, *27*(6), 2185-2208. https://doi.org/10.1175/JCLI-D-12-00823.1

Tucker, C.J. (1979). Red and photographic infrared linear combinations for monitoring vegetation. *Remote Sensing of Environment*, *8*(2), 127-150. https://doi.org/10.1016/0034-4257(79)90013-0

Willmott, C.J. & Matsuura, K. (2019). *Terrestrial Air Temperature and Precipitation: Monthly and Annual Time Series (1900-2017)*. Delaware: Department of Geography, University of Delaware.

Wu, D., Zhao, X., Liang, S., Zhou, T., Huang, K., Tang, B. & Zhao, W. (2015). Time-lag effects of global vegetation responses to climate change. *Global Change Biology*, *21*(9), 3520-3531. https://doi.org/10.1111/gcb.12945

Xu, Y., Yang, J. & Chen, Y. (2016). NDVI-based vegetation responses to climate change in an arid area of China. *Theoretical and Applied Climatology*, *126*(1-2), 213-222. https://doi.org/10.1007/s00704-015-1572-1

Yuan, W., Wu, S., Hou, S., Xu, Z. & Lu, H. (2019). Normalized Difference Vegetation

Index-based assessment of climate change impact on vegetation growth in the humid-arid transition zone in northern China during 1982–2013. *International Journal of Climatology*, *39*(15), 5583-5598. https://doi.org/10.1002/joc.6172

Summary

The sensitivity of vegetation in the lower Tigris basin landscapes to regional and global climate variability. This study investigates the lower Tigris basin's the normalized difference vegetation index (*NDVI*) sensitivity in 2000–2016 to regional climate variability reflected by the monthly precipitation and temperature time series of seven global datasets as well as to four global circulation indices. To examine the effect of climate variability on the different ecosystems, the study area has been classified into 10 smaller natural and anthropogenic landscapes based on landforms and land cover patterns. The preliminary analysis showed that the maximum biological productivity reflected by the *NDVI* of March and April has the highest correlation (0.5–0.8) to the same cumulative amounts of October–March period total precipitation and January–March period mean temperatures according to all datasets. In addition, this article showed there is a correlation between landscapes' *NDVI* and global modulation represented by the September–February state of El Niño--Southern Oscillation (*ENSO*) (0.55–0.70) and December state of the dipole mode index (*DMI*) (0.35–0.72). The significant differences in the original precipitation and temperature levels according to the different datasets have urged the use of normalized time series: *z*-score of temperatures and analogous six-months the standardized precipitation index (*SPI*). However, the multiple correlation analysis showed that using ERA--Interim and NCEP-CFSR (MERRA-2) based climate factors can explain from 77 to 83% of the *NDVI* variability on lowland plains (on higher foothills and mountainous lands). We found also that these prediction percentages can be increased by 2.4–7.2% when using time series of precipitation and temperatures derived from different datasets, in addition to 4.5–9.5% increasing rates when using the global circulation indices as additional predictors.

Authors' address:
Ali Subhi Alhumaima
(https://orcid.org/0000-0003-0895-6413)
Sanjar Mutalovich Abdullaev
(https://orcid.org/0000-0003-0405-704X)
South Ural State University
Department of System Programming
Lenin prospekt, 76, Chelyabinsk 454080
Russian Federation
e-mail: alhumaimaali@gmail.com
              abdullaevsm@susu.ru

Al-Zahraa A. MOHSEN, Monim H. Al-JIBOORI, Yaseen K. Al-TIMIMI
Mustansiriyah University, College of Science

Estimation of roughness and zero-displacement heights over Baghdad utilizing remote sensing and GIS techniques

Introduction

The determination of both zero-displacement height (Z_d) and roughness element height (Z_H) has special importance in micrometeorology when calculating surface roughness length (Z_o). These aerodynamic parameters in urban areas are important in many applications, such as air pollution modelling, wind-engineering activities, and can be considered as the main factors in describing the development of urban cities (Grimmond, King, Roth & Oke, 1998).

The surface roughness length is the height wind speed becomes zero in the logarithmic wind-speed profile, in the absence of Z_d (Al-Jiboori, 2010). Thus, any single object research that did not rely on the value of Z_d in estimating the values of roughness length was considered unacceptable. When the roughness elements (e.g. buildings, trees, bridges, etc.) are closely aligned to the surface it appears to have displaced the surface of the earth to some height. For example, some forests where trees are very close make a block of circumference size that blocks the wind when colliding with it (Hicks, Hyson & Moore, 1975).

The methods for analysing any natural and manmade surfaces can be classified into two major methods. The first classification requires observations of wind, and the second is based on the morphology and spatial arrangement of surface roughness elements, and this is referred to as morphometric analysis (Grimmond et al., 1998). The changes in the surface feature over a certain time can lead to changing micrometeorological parameters, such as Reynolds stresses and heat fluxes for the mean wind speed profile; and consequently, alter the vertical wind shear in both velocity and direction (Bradford, 2015).

The methods used in calculating the urban roughness that dependent on mor-

phometric parameters have improved radically because the anemometer equipment depends has limited observation in certain directions. These are considered the most accurate and active. However, installing the devices and designing the site experiment is complex and costly. On the other hand, morphometric methods are easy to operate and less costly. Remote sensing and geographic information system (GIS) techniques have reduced the complexity associated with these methods, and helps us to decrease time and exertion in calculating Z_d and Z_H (Jhaldiyal, 2015).

Remote sensing refers to various observation and exploration activities of the Earth's surface, through satellites and aircrafts fitted with sensors to capture images of Earth's surface. Those images are used to generate digital elevation model (DEM) and digital surface model (DSM), among others (Guo, Alessandro & Goodchild, 2019). Digital elevation model is defined as the altitude above mean sea level, measured in meters. When the surface is bare, the values of minimum and maximum elevation are equal. For scarce vegetation structures, the depth of the vegetation canopy results in the difference between the lowest and highest elevations. Therefore, it is possible to separate the land surface topography, represented by the DEM, from an elevation of the top of the vegetation canopy. Digital surface model refers to the altitude of features/objects on the surface of the earth. Both digital models have spatial resolution of 30 m (Desbarats, Logan, Hinton & Sharpe, 2002). The difference between DEM and DSM is that the first one is a land surface model that assuming the surface is bare

while the second is an elevation model that contains the top of surfaces or features on earth such as treetops, towers, buildings, and ground (Zhou, 2016).

Many researchers and authors have studied the surface roughness parameters of different sites. For example, Grimmond and Oke (1999) studied the characteristics of wind movement on the urban surface and analysed the shape of the surface by the morphometric method. The displacement height was defined using one of the methods for evaluating displacement height from velocity profile measurement (Petersen & Parce, 1994). Al-Draji & Al-Jiboori (2010) calculated Z_d for the Baghdad city center (Bab Al--Mhadham area) using the standard criteria and through the Bottema formula, found that Z_d ranged from 4 to 17.9 m with a mean value of 7.5 m.

In a recent study conducted by Haraj and Al-Jiboori (2019), utilizing three-dimensional ultrasonic anemometer installed at Mustansiriyah University to calculate zero-displacement length on eight sections, the results Z_H (9.2–13.8 m) and Z_d (4.3–8.1 m). Previous studies have focused on Z_d for most cities of the world, including Baghdad city centre and at Mustansiriyah University. However, no study has estimated the surface height of roughness element and zero-displacement height elements for the city. This study sought to estimate zero-displacement height and the height of roughness element over Baghdad, and for each municipality using GIS tools and techniques (ArcGIS 10.4.1 software). The study also analysed the relationship between Z_H and Z_d. The study estimated the roughness parameters for all municipalities of Baghdad.

Study area

Baghdad is the capital of the Republic of Iraq and is located in the central region on the banks of the Tigris river. Geographically, Baghdad is situated at latitude 33.22°–33.48° N, longitude 44.17°–44.50° E and 30–38 m above mean sea level. The area of the municipality of Baghdad city 877 km^2 (Al-Salihi, 2018). The borders of the municipality of Baghdad include 15 municipalities, seven in Karkh east of Tigris and eight in Rusafa west of Tigris as shown in Figure 1. The architecture of Baghdad ranges from traditional two or three story brick houses to modern steel, glass and concrete structures, and has about 12 bridges spanning the river-joining the east and west of the city (Hashim & Sultan, 2010). The climate of Baghdad can be described as subtropical, continental, and semiarid, characterized by cool winter, short springs as well as hot, dry and long summer. For the last 30 years, the average maximum temperature has been 31.95°C, and the average minimum temperature has been 18.05°C. The annual range of mean daily sunshine duration is about 10–14 h, with a mean of 7 h. Rainfall has never been recorded in summer and annual rainfall is almost restricted to the period of November–April (Saleh, 2011).

Data source

Data was acquired from three sources. Digital elevation model image for Baghdad, as shown in Figure 2, was acquired from the USGS earth explorer website, while DSM image for Baghdad, as shown in Figure 3, was obtained from the satellite global digital surface model "ALOS World 3D – 30M" (AW3D30) on 2 July 2019. Shapefile of the boundary of the municipality of Baghdad city, which comprises fifteen municipalities, was obtained from Baghdad municipality.
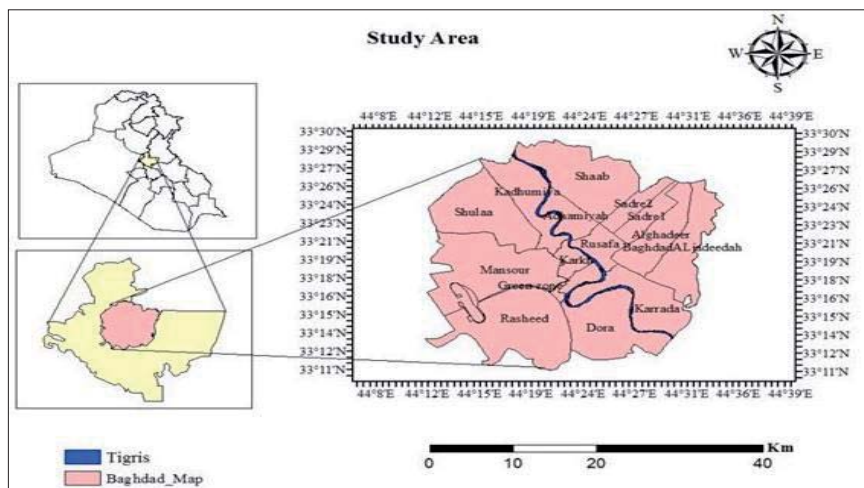

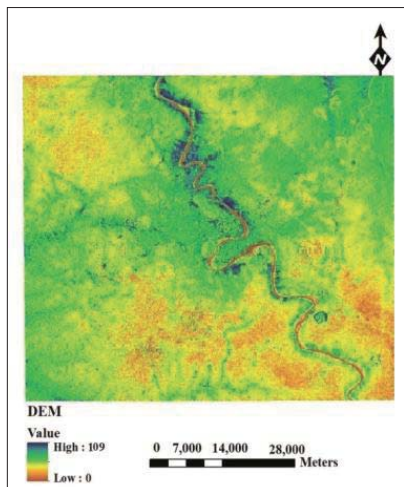FIGURE 1. Maps of Iraq, Baghdad city and the site of study

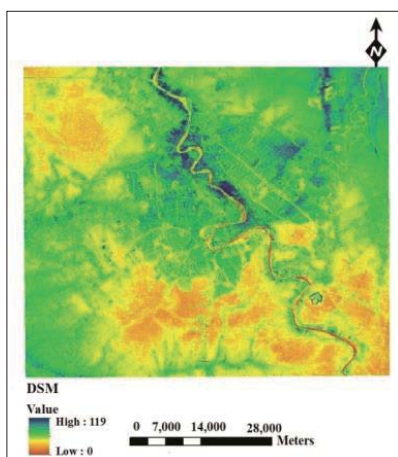FIGURE 2. Digital elevation model image of Baghdad city

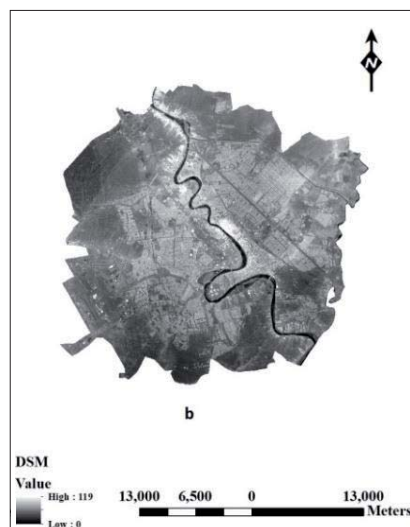FIGURE 3. Digital surface model image of Baghdad city
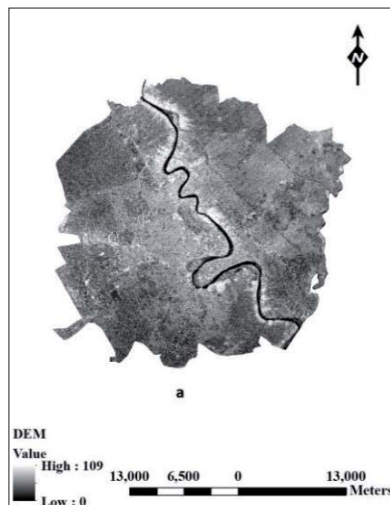
FIGURE 4. Baghdad city after extraction: a – digital elevation model; b – digital surface model

Pre-processing

Models of digital elevation and surface were extracted from the respective original images by masking them out using the shapefile for Baghdad city (Fig. 4).

The height was derived by computing the difference between DSM and DEM following Eq. (1) using GIS. The height is referred to as digital height model (DHM), and is shown in Figure 5. Digital height model represents the height of roughness element – Z_H (Dutra et al., 2006).

$$DSM – DEM = DHM \qquad (1)$$

A.A. Mohsen, M.H. Al-Jiboori, Y.K. Al-Timimi

FIGURE 5. Digital height model of Baghdad city

Processing

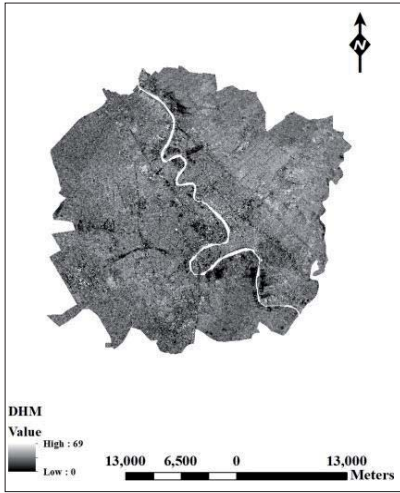There are several methods based on geometric analysis of the surface, which are related to the air dynamic scale. The method adopted in this study depends on the plan aerial index (λ_P), which describes the density of the fraction of the plan area. Plan aerial index is the ratio of the horizontal area occupied by roughness elements ('roof' or vegetative canopy) to the total area under consideration (Kent, Grimmond & Gatey, 2017), and is expressed using the following equation:

$$\lambda_P = \frac{A_P}{A_T} \qquad (2)$$

where:
A_P – plan surface of the roughness elements [m^2],
A_T – total surface area [m^2].

The plan area index is attached to the significance of interfering space between the roughness elements. For an array of

the equivalent height of roughness element, an excess of λ_P can lead to the excess of the displacement height and a reduction of the roughness of the obstacle array as λ_P, tends to 1. This means that the elements are so close that they merge to form a new surface (Chen, Fröhlich, Matzarakis & Lin, 2017). The ratio of displacement height over the roughness element height is given as:

$$\frac{Z_d}{Z_H} = 1 + \alpha^{-\lambda_P}(1 - \lambda_P) \qquad (3)$$

where:
Z_d – displacement height, which is mainly a function of λ_P [m],
Z_H – height of roughness element height [m],
α – empirical coefficient equal to 4.43 (Grimmond & Oke, 1999).

Figure 6 presents the flow chart of the calculation method for DHM ($= Z_H$) and Z_d.

Results and discussion

Average roughness height

The average height values for satellite image varies from one municipality to another, due to the presence of buildings, trees and towers, and their different spatial distributions in Baghdad. The height values of DSM are greater than DEM, where DEM includes the height of the land and does not take into consideration the height of the towers, trees and buildings, while DSM includes the height of the surface and everything on it. Digital height model is the result of
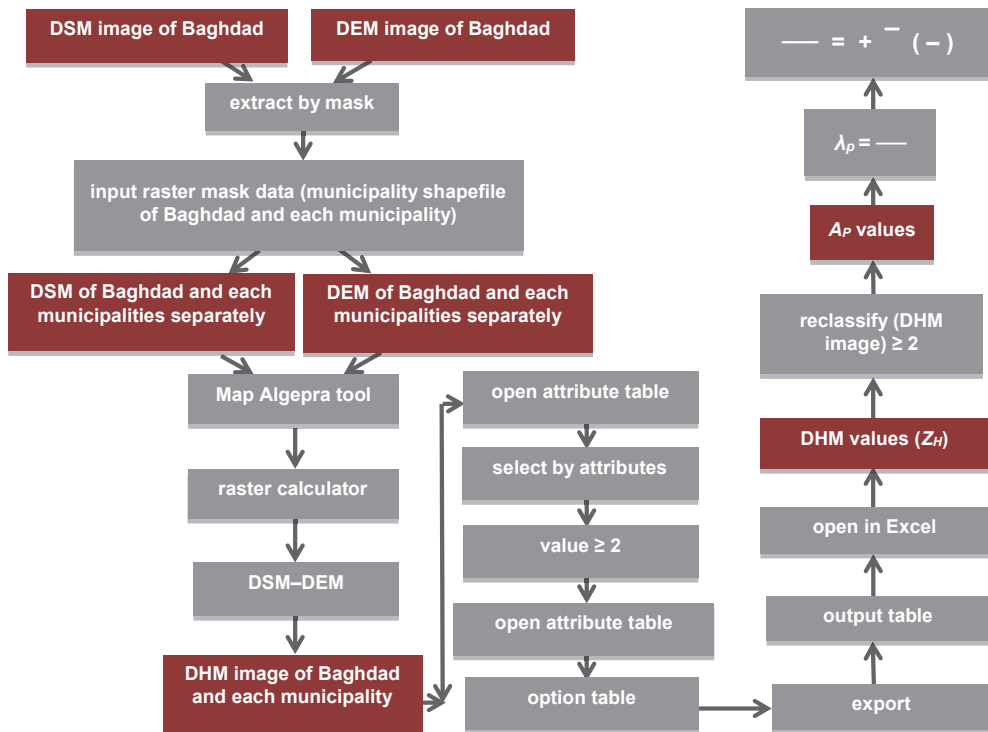
FIGURE 6. Flow chart of methodology

difference between them which represent Z_H.

Figure 7 and the values shown in Table 1 show the height of the roughness elements of every municipality were calculated from Eq. (1) by ArcGIS. It should be noted that the highest value was in Mansour with 28.7 m because of the many numbers of tall buildings and trees in this municipality, and the lowest value in Sader1 with 8.6 m due to the lack of tall buildings. It is also found that there are municipalities with almost similar values such as Sader 1 and

FIGURE 7. Average heights for each municipality of Baghdad

A.A. Mohsen, M.H. Al-Jiboori, Y.K. Al-Timimi

TABLE 1. Average of height values for satellite images of digital surface and elevation models and roughness element height

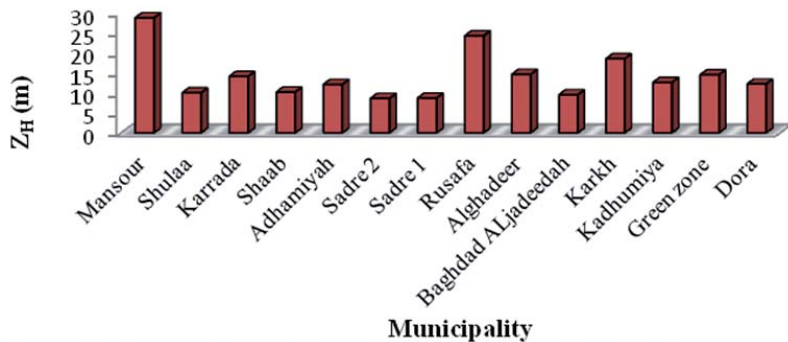| Municipality	DSM [m]	DEM [m]	Z_H [m]
Rasheed	35.8	35	18.4
Mansour	38.3	37.4	28.7
Shulaa	36.7	35.7	10
Karrada	37.2	36.5	14.1
Shaab	38.3	36.9	10.2
Adhamiyah	40.8	39.9	12.1
Sadre 2	39.2	37	8.6
Sadre 1	40.3	37.6	8.7
Rusafa	40.9	38.8	24.2
Alghadeer	39.1	36.8	14.6
Baghdad Aljadeedah	38.5	38	9.5
Karkh	39.8	39.5	18.5
Kadhumiya	40	39.1	12.6
Green zone	38.2	38	14.5
Dora	36.1	35.9	12.2

Sader 2, Dora, Adhamiyah and Kadhumiya. Shaab, Shulaa and Baghdad Aljadeedah municipalities are approximately similar in value, and finally Karrada, Algadeer and Green zone are found to close to the same values for roughness element heights.

Zero-displacement height

The zero-displacement values based on the Z_H and λ_P values are computed using Eq. (3) should previously calculated Z_H values and then λ_P. First step, the plan area (A_P) of roughness element which represents the area occupied by objects on the surface of the earth, such as buildings and trees calculated through ArcGIS. The height data was classified from DHM images for the roughness elements with heights greater or equal to 2. This classification was chosen ensuring that low-level street furniture (e.g. signage), vehicles, etc. are removed, to determine the plan area index consistent with the study of (Kent, Grimmond, Gatey & Hirano, 2019). Areas of pixels with heights equal to or greater than 2 were calculated for each municipality. This was followed by calculation of the total area (A_T) and packing density of the roughness elements λ_P for each municipality was determined by using Eq. (2).

Figure 8 shows the reclassified roughness heights for each municipality. The black colour shows areas of height values ≥ 2 which represents A_P distributions, and green colour shows the area of height values < 2.

As stated in Table 2, the values of A_P, A_T, and the results of both λ_P and Z_d shows that the values of λ_P ranged from 0.17 to 0.63. The largest value of λ_P was in Sader 1 which means it has high-density roughness elements and the lowest value was in the green zone. The average value of λ_P was 0.35 for the entire Baghdad. Zero-displacement height ranges from 4.5 to 15.8 m, with an average value of 8.4 m for the whole Baghdad.

Figure 9 shows the relationship between the length of zero-displacement and the average of the roughness elements height. There was a very strong positive correlation between the two parameters, with $R^2 = 0.7484$, $p < 0.05$. It was noted that the values of Z_d increases with increasing height of buildings in an area. The highest value of the length of the zero-displacement height Z_d was 15.8 m with Z_H of 24.2 m
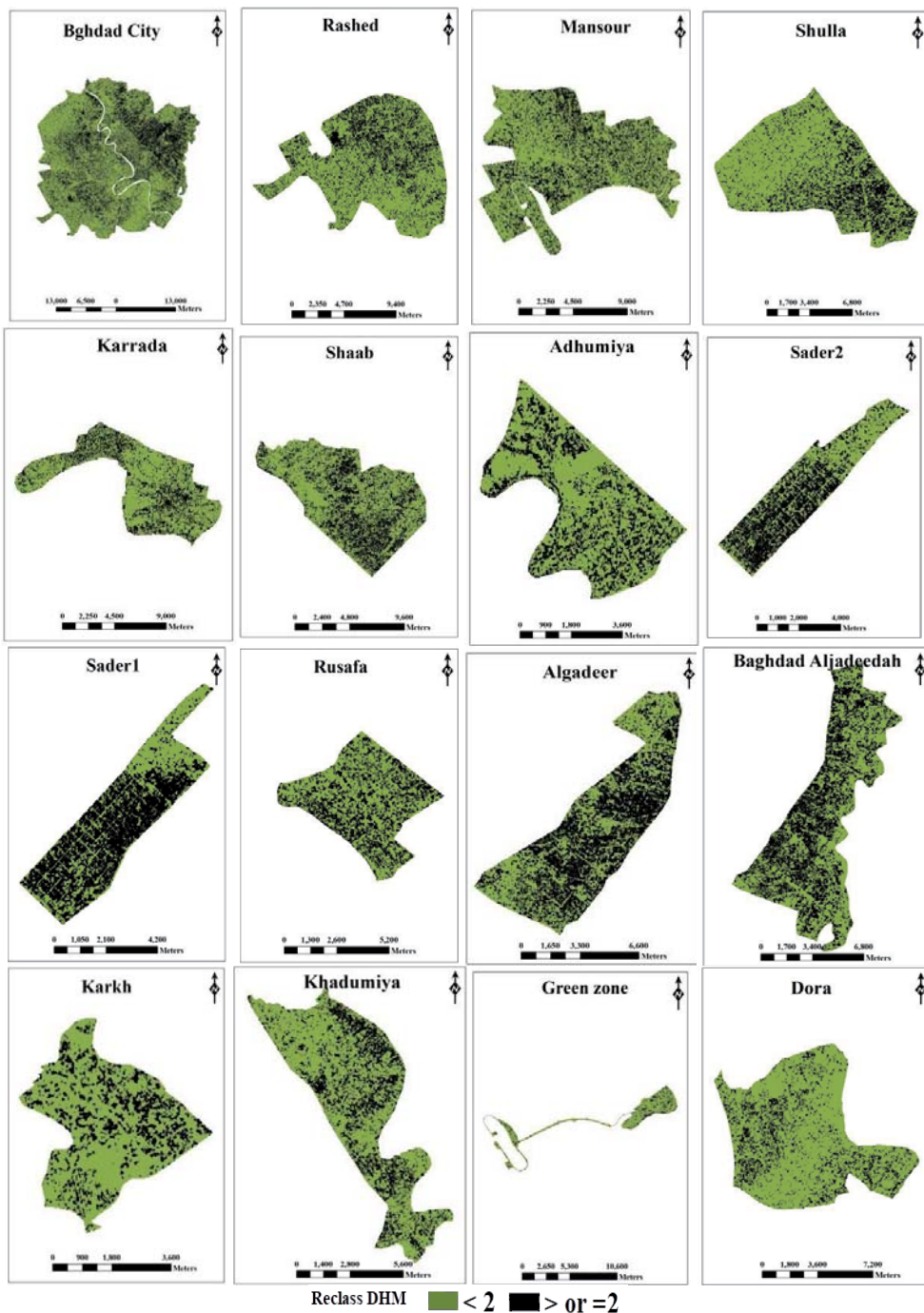
FIGURE 8. Maps present the distributions of plan area for Baghdad and each municipality

A.A. Mohsen, M.H. Al-Jiboori, Y.K. Al-Timimi

TABLE 2. Values of plan area, total area, plan aerial index and zero-displacement height for each municipality in Baghdad

Municipal	A_P [km^2]	A_T [km^2]	λ_P [-]	Z_d [m]
Rasheed	36.3	123.3	0.29	10.0
Mansour	36.3	123.3	0.29	15.6
Shulaa	4.6	90.2	0.27	5.1
Karrada	18.6	69.3	0.27	7.2
Shaab	35.6	99.2	0.36	6.3
Adhamiyah	8.3	27.3	0.3	6.7
Sadre 2	10.7	20.9	0.51	6.7
Sadre 1	14.5	23	0.63	7.5
Rusafa	9.1	23.7	0.38	15.8
Alghadeer	27.2	51.5	0.53	11.5
Baghdad Aljadeedah	29.9	65.3	0.46	6.9
Karkh	3.9	14.8	0.26	9.2
Kadhumiya	16.3	56.1	0.29	6.8
Green zone	2.8	16.7	0.17	5.1
Dora	15.2	82.1	0.19	4.7

Z_H values among all municipalities, the highest value is for Mansour (28.6 m), and the least value is for Sader 2 (8.6 m). This is due to the presence of high buildings in Mansour municipality, unlike in Sader 2 municipality. Zero-displacement height varies from 4.7 to 15.8 m across the municipality. The results of this research differ from the results of the previous two studies (Al-Draji & Al-Jiboori, 2010; Haraj & Al-Jiboori, 2019) which conducted for Bab Al-Muadham and Mustansiriya University, which these are part of the Rusafa municipality of Baghdad and with study areas of 1 km^2, while this study covered a very large area of 877 km^2 and 15 study points. Depending on the values of Z_d and Z_H, Baghdad city can be classified as having a medium height with a density of the urban surface consistent with results obtained by Grimmond and Oke (1999).

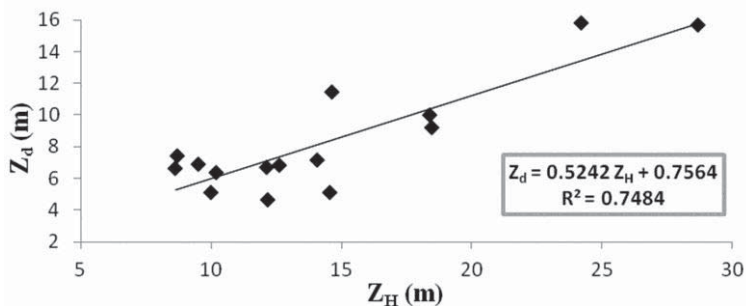FIGURE 9. Variation of zero-displacement height with roughness element height

in Rusafa, while least value of the length of zero-displacement was 4.7 m with 12.2 m Z_H in Dora.

The following observations were noted in the study. The average Z_H was 14.5 m and Z_d was 8.4 m. Comparing

Conclusions

The determination of urban surface aerodynamic parameters is an important question in the researches of urban wind

field characters, planning for vital areas, and microclimate. Using remote sensing and GIS resources and techniques, the study estimated zero-displacement height (Z_d) and roughness element height (Z_H) for each municipality in Baghdad city. Therefore, the importance of this study lies in the development of a simple method for estimating the roughness parameters (Z_H, Z_d). Besides, the use of GIS technology in this study contributed to obtaining more accurate results than the results of previous studies. According to our final results we recommended using another parameter such as frontal index to calculate zero-displacement and surface roughness lengths for municipalities of Baghdad.

References

Al-Draji, A.G. & Al-Jiboori, M.H. (2010). Aerodynamic surface roughness length of Baghdad City. *Al-Nahrain Journal of Science*, *13*(1), 96-102.

Al-Jiboori, M.H. (2010). Determining of neutral and unstable wind profiles over Baghdad city. *Iraqi Journal of Science*, *51*(2), 343-350.

Al-Salihi, A.M. (2018). Characterization of aerosol type based on aerosol optical properties over Baghdad, Iraq. *Arabian Journal of Geosciences*, *11*(20), 633. https://www.doi.org/10.1007/s12517-018-3944-1

Bradford, G.R. (2015). *Investigations of surface roughness length modification in Black Rock City, NV* (doctoral dissertation). San Francisco: San Francisco State University.

Chen, Y.C., Fröhlich, D., Matzarakis, A. & Lin, T.P. (2017). Urban roughness estimation based on digital building models for urban wind and thermal condition estimation – Application of the SkyHelios Model. *Atmosphere*, *8*(12), 247. https://www.doi.org/10.3390/atmos8120247

Desbarats, A., Logan, C., Hinton, M. & Sharpe, D. (2002). On the kriging of water table elevations using collateral information from a digital elevation model. *Journal of Hydrology*, *255*(1-4), 25-38.

Dutra, L., Dossantos, J., Frietas, C., Mura, J., Neeff, T., Elmiro, M. & Moura, P. (2006). Digital Height Modeling (DHM) of tropical forests using multi-frequency InSAR methodology. In *2006 IEEE International Symposium on Geoscience and Remote Sensing: Denver, CO, 31 July - 4 August 2006* (pp. 2190-2192). Piscataway Township, NJ: IEEE.

Grimmond, C. & Oke, T.R. (1999). Aerodynamic properties of urban areas derived from analysis of surface form. *Journal of Applied Meteorology*, *38*(9), 1262-1292.

Grimmond, C., King, I.S., Roth, M. & Oke, T.R. (1998). Aerodynamic roughness of urban areas derived from wind observations. *Boundary-Layer Meteorology*, *89*(1), 1-24.

Guo, H., Alessandro, A. & Goodchild, M.F. (eds.) (2020). *Manual of Digital Earth*. Berlin: Springer.

Haraj, S.A. & Al-Jiboori, M.H. (2019). Study of aerodynamic surface roughness for Baghdad City using signal-level measurements. *Baghdad Science Journal*, *16*(1 Supplement), 215-220.

Hashim, M.B. & Sultan, A.M. (2010). Using remote sensing data and GIS to evaluate air pollution and their relationship with land cover and land use in Baghdad City. *Iranian Journal of Earth Sciences*, *2*(1), 20-24.

Hicks, B., Hyson, P. & Moore, C. (1975). A study of eddy fluxes over a forest. *Journal of Applied Meteorology*, *14*(1), 58-66.

Jhaldiyal, A. (2015). *Automatic Estimation of Urban Roughness Parameters for Microclimatic Analysis* (unpublished master's thesis). Andhra University, Visakhapatnam.

Kent, C.W., Grimmond, S. & Gatey, D. (2017). Aerodynamic roughness parameters in cities: Inclusion of vegetation. *Journal of Wind Engineering and Industrial Aerodynamics*, *169*, 168-176.

Kent, C.W., Grimmond, S., Gatey, D. & Hirano, K. (2019). Urban morphology parameters from global digital elevation models: implications for aerodynamic roughness for windspeed estimation. *Remote Sensing of Environment*, *221*, 316-339.

Petersen, R. & Parce, D. (1994). *Development and testing of methods for estimating surface roughness length at refineries* (CPP Project, 92-0890). Ft. Collins: CPP.

Saleh, S.A. (2011). Air quality over Baghdad City using earth observation and Landsat thermal data. *Journal of Asian Scientific Research*, *1*(6), 291-298.

Zhou, Q. (2016). Digital elevation model and digital surface model. In *International Encyclopedia of Geography: People, the Earth, Environment and Technology: People, the Earth, Environment and Technology* (pp. 1-17). Hoboken, NJ: John Wiley & Sons.

Summary

Estimation of roughness and zero-displacement heights over Baghdad utilizing remote sensing and GIS techniques. The objective of this study was to estimate the height of roughness element (Z_H) and zero-displacement length (Z_d) for Baghdad city using remote sensing and GIS techniques and resources such as DEM, DSM, and shapefile. The difference between DEM and DSM produced digital height model which represents the height of the roughness element for the region, which was used to determine the zero-displacement height. The results showed that the variations in Z_d values depend strongly on Z_H. Rusafa had the highest Z_d (15.8 m) while Dora had the lowest values (4.7 m). Thus, Baghdad city has medium density classification according to the results of Z_d and Z_H values.

Authors' address:
Al-Zahraa A. Mohsen
Monim H. Al-Jiboori
Yaseen K. Al-Timimi
Mustansiriyah University
College of Science
Atmospheric Sciences Department
e-mail: alzahraa95adil@gmail.com
              mhaljiboori@gmail.com
              yaseen.k.abbas@gmail.com

Abdalrahman QUBAA[1], Saja Al-HAMDANI[2]

[1]University of Mosul, Remote Sensing Center
[2]University of Mosul, College of Computer & Mathematic Sciencese

Detecting abuses in archaeological areas using k-mean clustering analysis and UAVs/drones data

Key words: unmanned aerial vehicles, k-mean clustering, unsupervised classification, Pix4D, remote sensing, archaeological survey

Introduction

In recent years, new technologies in archaeology have emerged to get reliable data easily and at a lower cost. Unmanned aerial vehicles (UAVs) or drones have become advanced technological devices that archaeologists use and aim to add to their survey and gravure kits. Drones used for 3D documentation and analysis of landmarks and historical structures, aerial mapping, and forest archaeological analysis. Drones used now instead of the conventional field walking approach known as the pedestrian survey, which was historically used by archaeologists and archaeology students (Hill, Laugier & Casana, 2020). While satellite imagery offers wider coverage for any surveys (Bi, 2020), but at considerable expense and with little spatial precision compared to the cost and precision of drones' spatial discrimination, which flies at a relatively low altitude, providing a precise view of the archaeological region being surveyed. Satellite images vary in their spatial resolution and by the satellite used, which means they can cover an area of one kilometer per pixel in the image, or hundreds of meters, or at best tens of meters per pixel. This little precision has limited applications to uncover archaeologist's tiny archaeological features. Though these satellite images can be obtained free of charge, such as the satellite launched by the European Space Agency called Sentinel, which provides excellent spectral bands with a spatial accuracy of 10 m per pixel, it is not considered effective in the study of often small monuments and archaeological areas (Noor, Abdullah & Hashim, 2018). In addition to restrictions on the use of satellites such as the large height of the satellites and the distance between the satellites and the earth, this means that the emission signal entering the sen-

sor is affected by water vapor, the ozone layer, and clouds that adversely affect the quality and accuracy of the data (Agudo, Pajas, Pérez-Cabello, Redón & Lebrón, 2018). Therefore, drones images are the solution and providing archaeologists and students with very high capabilities, as they provide us with photos with a spatial resolution of up to a few centimeters per pixel and depending on the visual characteristics of the various sensors that these drones can bear. Furthermore, these drones offer a solution to the cloud problem and other weather effects induced by the satellite altitude on data quality, since drones fly at very low altitudes of 100 m or fewer. Besides the low cost of these planes, it has the possibility to repeat the survey process to record a higher time accuracy that reaches multiple times daily. However, it is still an up-to-date technology and as many formalities and security regulations have applied to its use, policy limitations on its use are growing (Brooke & Clutterbuck, 2019).

Unsupervised machine learning and classification techniques have been used in archaeological research (Jaimala & Sarita, 2020). In this research, the proposed approach uses a k-means clustering technique for image analysis which has been used broadly in image analysis. This unsupervised clustering does not use labels that define the classes. There are no information presents regarding the category or class label which differentiates the unsupervised classification concept. Clustering is a technique that analysis data objects then split them into a number of subgroups based on the information found in data that describes the objects and relationships among them

(Aggarwal & Aggarwal, 2012). k-Means algorithm firstly select k-objects as initial cluster centers, then calculate the distance between each cluster center and each object, and assign it to the nearest cluster, update the averages of all clusters, repeat this process until the criterion function converged (Vora & Oza, 2013).

The general objective of this research is to demonstrate the feasibility of using drones to maintain and track important archaeological sites that appeared to have been largely neglected and affected by thieves and looting in Iraq, as well as civil excesses and the random construction that occurs on the archaeological areas, particularly after 2003. An aerial surveillance system, which consists of modern DJI Phantom 4 drones in combination with the advanced Pix4D program, was used. The Pix4D's capabilities to analyze captured images, conduct processing operations, and generating image mosaics have been illustrated. k-Mean clustering algorithm was used to classify the resulting data to clarify the morphological changes and updates that happen in the archaeological sites. Expecting that this new system will be used and adapted by other local archaeological teams to protect our cultural heritage from neglect, damage, and theft.

Material and methods

Study area and devices used

The archaeological region of Nineveh was chosen as a case study, positioned in Mosul's city center and on the eastern side of the river Tigris (Fig. 1), near the University of Mosul, was chosen for its historical importance and be-
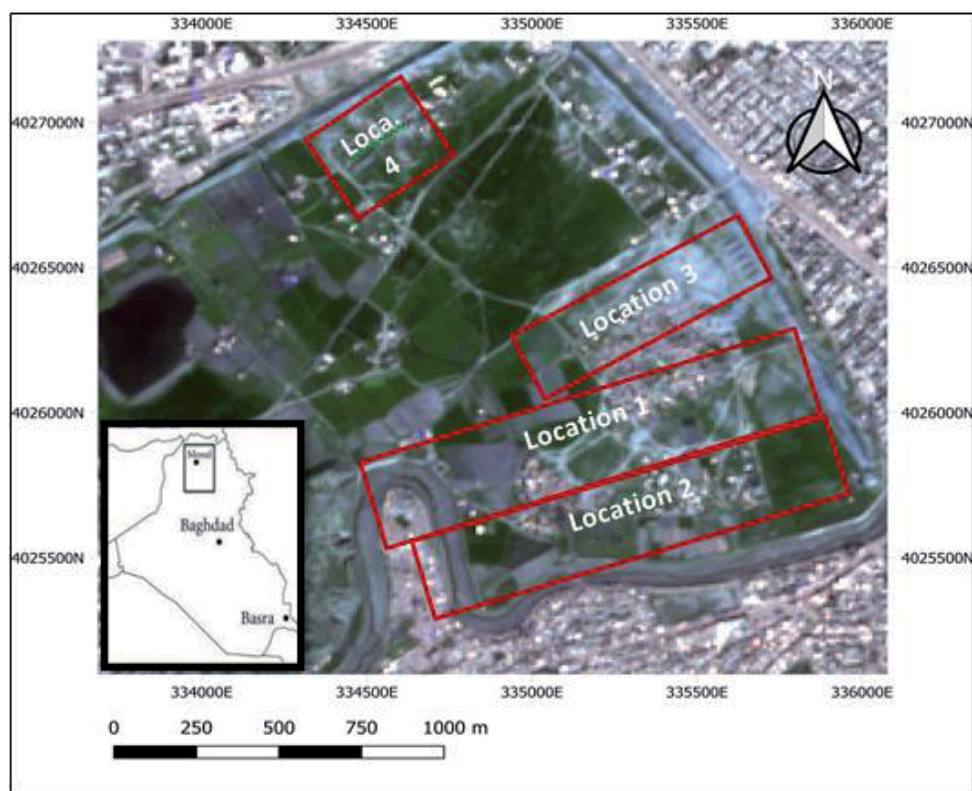
FIGURE 1. The study area, the Nineveh archaeological city, in the center of Mosul, the four survey locations were explained by red color

ing the capital of the ancient Assyrian Empire (Scardozzi, 2011). Where it was established during King Sennacherib's period and made it a defensive line to protect the empire from foreign military attacks. It also included archaeological evidence of weapons in several camps and stores (Ur, 2005).

Many drone flight trips were done in November 2018 after obtaining official approvals and in collaboration with the Nineveh Directorate of Archaeology and Heritage, security forces co-operation and accompaniment were necessary to cover the field experiment. An aerial survey was performed on four separate lo-cations throughout the region where the drone type DJI Phantom 4 Pro was used (Fig. 2), this drone is one of the modern drones that contains the autopilot's ca-pabilities and decides the GPS ground points that will be used in the mosaic picture collection phase (DJI, n.d.).

Despite the historical and archaeo-logical importance of the region, it has been noted in recent years that more and more abuses have taken place, such as the construction of residential areas, ce-ramic and stone warehouses (Fig. 3).

Utilizing the advanced Pix4Dfields software, drone images were upload-ed and analyzed. Where the software

FIGURE 2. DJI Phantom 4 Pro, the drone used in this research

Study area on 10/02/2002

Study area on 29/12/2004

Study area on 10/02/2013

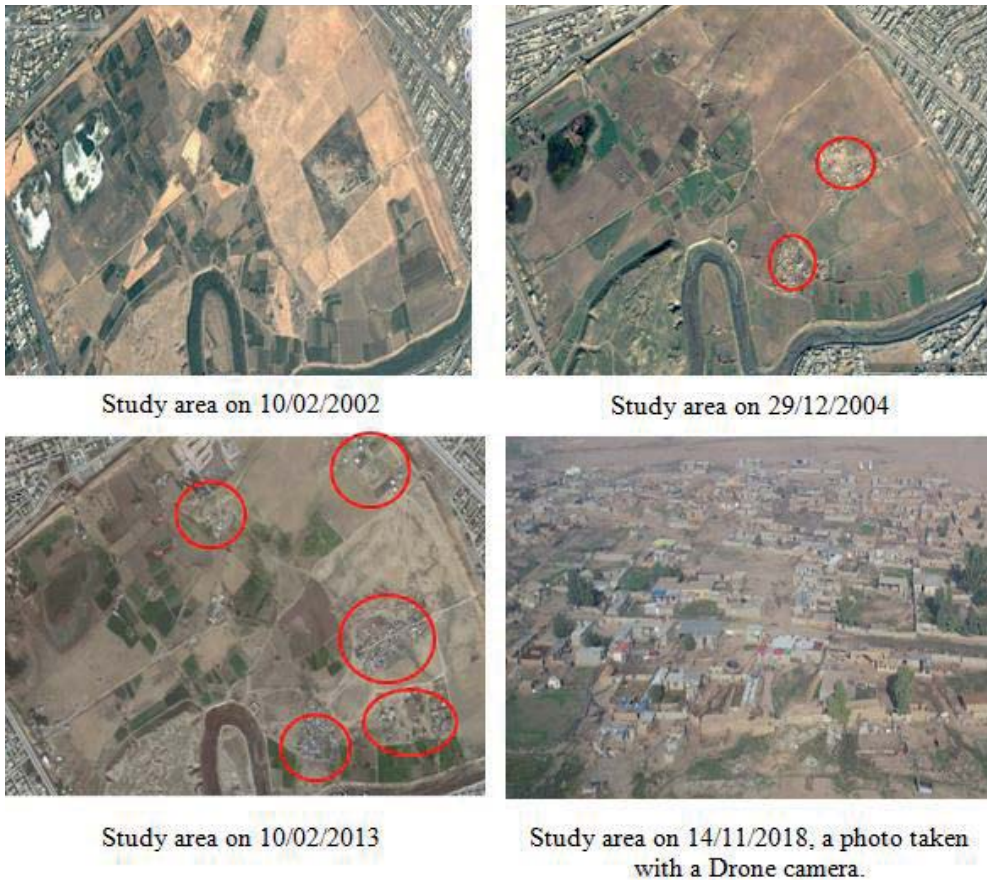Study area on 14/11/2018, a photo taken with a Drone camera.

FIGURE 3. An indicator of the violations in the field of research has risen over the years from 2003 to 2018 by using satellite and drone images

includes the possibilities for the use of geographical coordinates and the specific overlapping mosaic function for the region being surveyed. The software also includes the possibility of using mathematical equations to apply engineering indicators to gain more engineering measures from the images (Pix4D, n.d.).

Acquisition and processing pipeline for drone images

Every traditional drone air survey needs some main phases which sum up in this paragraph (Fig. 4) (Colomina, Blázquez, Molina, Paréz & Wis, 2004). The first stage is the planning stage, where this stage reflects the key preparation for the entire process, including deciding the devices available for the survey and choosing the optimal flight time and date.

The second step consists of the images-taken process, which includes the preparation and orientation of the camera,

its calibration, its location on the drone. After capturing the images, the stage of gathering these images begins, which is known as mosaic process, where we take advantage of the interference process that we mentioned in the previous stage in order to have a single visualization. All images taken from one location are included in one single visualization. In the final stage, the approach of extracting the information we need from the completed scene and the application of digital processing and photogrammetry processes to find measurements in engineering. For instance, areas and boundaries, characteristics extraction, 3D modeling, or digital and surface model extraction (Nex & Remondino, 2014).

At the mission planning stage, the flight parameter was adjusted and set at 100 m altitude for the control of a drone to achieve a resolution of approximately less than 10 cm per pixel. The pictures were taken in a serial manner and are
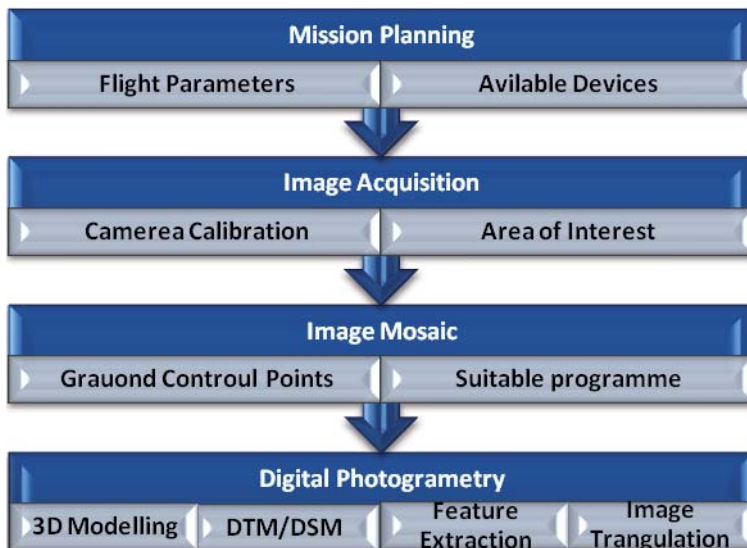

FIGURE 4. Typical acquisition and processing pipeline for drone images

stored in the memory accompanying the drone according to their digital sequence and with an interruption allowing the mosaic phase to be performed. In the information storage area for every image, the geographical location information and geographical coordinates are also stored. Figure 5 gives an example of the serial photos taken with a drone portable camera at the first location. After the scanning process was complete, the captured images will be moved to the computer for the preparation and processing of the entire location show.

Figure 6 shows the use of the proficient Pix4Dfields software to access

FIGURE 5. Sample of a serial picture captured using a drone

FIGURE 6. Processing of the collection images using a mosaic mechanism, projected onto its true geographical coordinates, the direction of route and number of flight lines is clarifies

the sample photos taken for the photography's first location, where the system performs the spatial return process according to the information stored in the pictures. The figure also demonstrates the direction of the route and number of lines covered by the survey (which were here eight lines). That covered nearly 30,000 m^2 in the field. The program also shows, to the left of Figure 6, the length of time taken by the survey, i.e. 22 min, in addition to the start time and date of the survey, which is 8.49 am on 14 November 2018. The four locations view captured by the scanning process are shown in Figure 7 following the completion of the mosaic and projection phase.
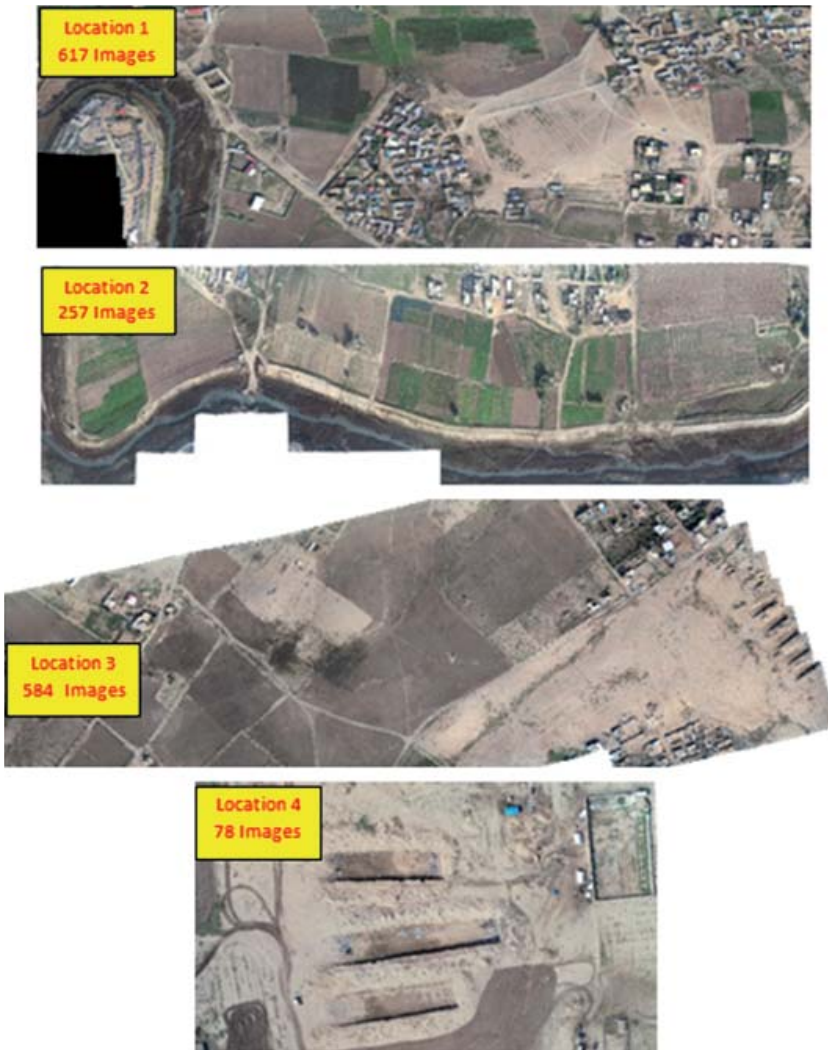

FIGURE 7. Shows the four aerial survey locations after the mosaic's operation

A. Qubaa, S. Al-Hamdani

Results and discussion

The stage of analysis and information generation

After completing the process of all locations, the Pix4D program was used to extract information from the surveying process and make comparisons, analyzing, and studying. In this paragraph, we provide examples of information that can be extracted from the drone's survey. Figure 8 shows the example of the amount of archaeological area overtaking in the river Al-Khosr curvature in the first location, where this location has become a group of large warehouses for ceramics that have overlooked, cut, and even sold for a high amount of money in the absence of oversight and confusion during the invasion of ISIS period. The high spatial resolution of drone images enables you to understand the boundaries and measure the areas, moreover small their size may be, decide their type, whether ceramic stores, residences or animal shelters are high-precision, and to punish those who crossed by their limits and range.

Figure 9 shows the excavations that took place between 2013 and 2018 at

FIGURE 8. Shows the amount of overtaking of the archaeological area in the curvature of the river Al-Khosr, where it has become large ceramic stores

FIGURE 9. The difference in the third survey location between 2013 and 2018 and an indication of the overtaking and drilling process that took in the site

the third location as a different example, which gives locations of archaeological excavations carried out by thieves to search for any relics or statues buried under the archaeological hill from the eastern side of the region. The figure also shows the use of large mechanisms for drilling and excavations, which is inconsistent with the mechanisms and laws of archaeologists.

Figure 10 shows the same method of drilling mechanism at the fourth site of the survey, which suggests that the excavators do not have any scientific back-ground in archaeology, and their aim is only to extract what can be extracted and benefit from it financially.

The Pix4Dfields software offers an extensive opportunity to apply mathematical equations to identify several agricultural indicators to track crop typology at archaeological sites and allow the cultivation of species only permitted under legal contracts with farmers under the Department of Antiquities, which are not extended to a specific land depth of land and that may have an impact on the relics. Figure 11 shows an example of the

FIGURE 10. Explanation of the difference at the fourth survey location between 2013 and 2018 and the drilling and overtaking process occurring at the location
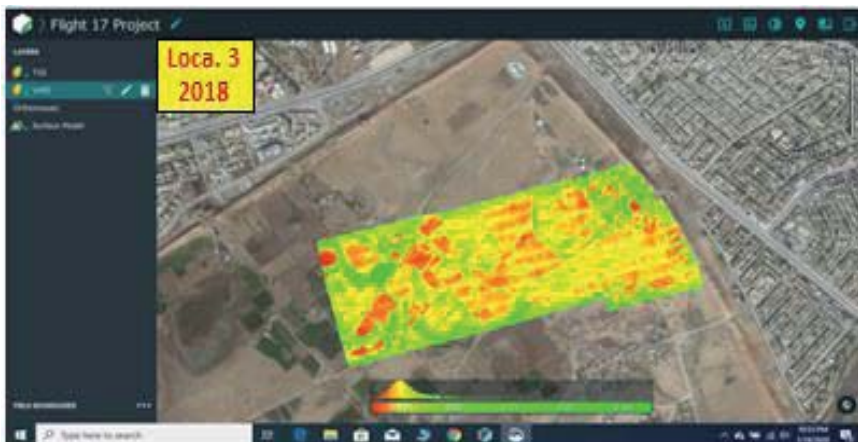

FIGURE 11. Implementation of the VARI at the third location of the survey

A. Qubaa, S. Al-Hamdani

application of one of the agricultural indicators at the third survey location. This indicator called the visible atmospheric resistant index (VARI) (Eng, Ismail, Hashim & Baharum, 2019), as shown in Eq. (1):

$$VARI = \min\{\max[-(GREEN - RED) / / (GREEN + RED - BLUE)]\} \qquad (1)$$

which relies on the visible spectrum of the RGB to use's as one of the indications for the existence of agricultural land.

Archaeological land classification using k-mean clustering

In this research, the archaeological lands were classified using an unsupervised k-mean clustering algorithm for one of the survey sites, as an example, the fourth site was chosen, during different periods of time to find out the extent of overtaking them and their impact on civil works that lead to the loss of their historical importance and heritage value. The proposed archaeological land classification framework showed in Figure 12. After reading the images in step one, the average color of the whole image was obtained, the normalized RGB values were calculated as normalization, which had been used to reduce the effect of illumination. The following normalization scheme was applied to the color index as in Eqs. (2), (3) and (4) (Saberioon et al., 2014):

$$R = R / (R + G + B) \qquad (2)$$

$$G = G / (R + G + B) \qquad (3)$$

$$B = B / (R + G + B) \qquad (4)$$

where R, G, and B are the digital numbers of the red, green, and blue bands, respectively.

In the third step, the VARI index was calculated, as an indicator that indicates the degree of the land change or any excavations that occurred, whether agricultural tillage or archaeological excavation. In the final step, the k-mean clustering algorithm was used, which is considered as one of the most used clustering algorithms due to its efficiency and simplicity. k-Mean clustering classified the land into three classes: archaeological lands; excavation lands; residential building and rocks lands.

The results of the classification in Figure 13 showed the great abuses of archaeological lands in the region, as it appeared that the percentage of archaeological lands in 2004 represented more than 90%, while the excavations and tilled lands did not exceed 3%. While in 2018, the percentage was completely different, as the percentage of archaeological lands appeared to be much less, approximately 25%, next to the large increase in excavations and tilled lands, which amounted to approximately 73%. The category of residential buildings and rocky lands varied from approximately 6.5 in 2004 and increased to 8.7 in 2013, then returned and decreased to approximately 1.6 in 2018 as a result of the Antiquities Department and

Input & Read Images → Calculated Color Index → Calculate VARI Index → Using k-means Clustering

FIGURE 12. Proposed archaeological land classification framework

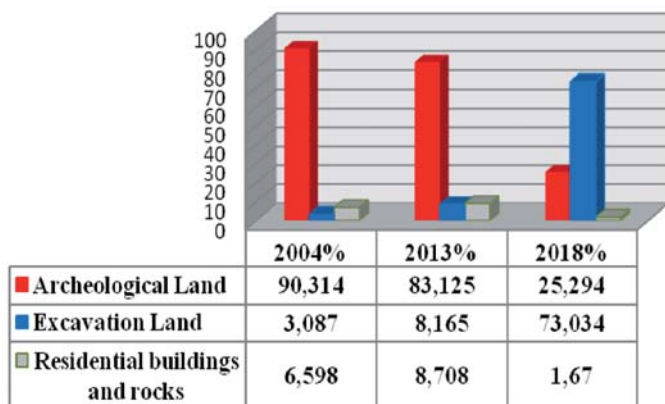|	2004%	2013%	2018%
■ Archeological Land	90,314	83,125	25,294
■ Excavation Land	3,087	8,165	73,034
■ Residential buildings and rocks	6,598	8,708	1,67

FIGURE 13. Classification results using k-mean clustering

Inspectorate beginning to lift some civil and building violations in this area.

Conclusions

Drones technology has rapidly become critical tools for use in archaeological remote sensing and may be limited compared to geophysical methods, but their cost-effectiveness, ease of use, and efficiency make them more widely used and useful for larger and larger surveys. In this study, for the first time in the governorate of Nineveh in Iraq, modern drones technology was used in the phase of surveying the archaeological region of Nineveh, firstly because of its historical importance and secondly because of the great losses that changed its characteristics during the invasion of ISIS. The software specializing in the image processing of this technique called Pix4D has also been used in this research. The UAVs data classification was adopted using a k-means clustering algorithm. The results of the data classification for three different time periods indicated that the percentage of archaeological lands decreased from 90.31% in 2004 to 25.29% in 2018. The research showed the importance and the great benefits of using these systems in the field of archaeology. It concluded that drones data collected provide additional benefits for researchers and policymakers interested in documenting damage to archaeological and heritage sites which will be of great help in preserving the important archaeological sites. Researchers also recommend that local authorities and antique directorates are encouraged to obtaining and use of such systems to protect our archaeological sites from overtaking, vandalism, and theft, as well as their cost, time, and effort savings.

References

Aggarwal, N. & Aggarwal, K. (2012). A Mid-point based k-mean Clustering Algorithm for Data Mining. *International Journal on Computer Science and Engineering*, *4*(6), 1174-1180.

Agudo, P.U., Pajas, J.A., Pérez-Cabello, F., Redón, J.V. & Lebrón, B.E. (2018). The potential of drones and sensors to enhance detection of archaeological cropmarks: A comparative study between multi-spectral and thermal imagery. *Drones*, *2*(3), 29. https://doi.org/10.3390/drones2030029

Bi, T. (2020). Optimal Allocation Algorithm of Geological and Ecological High-resolution Remote Sensing Monitoring Sampling Points. *Earth Sciences Research Journal*, *24*(1), 105-110.

Brooke, C. & Clutterbuck, B. (2020). Mapping heterogeneous buried archaeological features using multisensor data from unmanned aerial vehicles. *Remote Sensing*, *12*(1), 41. https://doi.org/10.3390/rs12010041

Colomina, I., Blázquez, M., Molina, P., Parés, M.E & Wis, M. (2008). Towards a new paradigm for high-resolution low-cost photogrammetry and remote sensing. *The International Archives of the Photogrammetry, Remote Sensing and Spatial Information Sciences*, *1*, 1201-1206.

DJI (n.d.). Phantom 4 Pro Specs. Retrieved from: https://www.dji.com/phantom-4-pro/info (access 14.09.2020).

Eng, L.S., Ismail, R., Hashim, W. & Baharum, A. (2019). The use of VARI, GLI, and VIgreen formulas in detecting vegetation in aerial images. *International Journal of Technology*, *10*(7), 1385-1394.

Hill, A.C., Laugier, E.J. & Casana, J. (2020). Archaeological remote sensing using multi-temporal, drone-acquired thermal and Near Infrared (NIR) Imagery: A case study at the Enfield Shaker Village, New Hampshire. *Remote Sensing*, *12*(4), 690. https://doi.org/10.3390/rs12040690

Jaimala, J. & Sarita, B. (2020). A novel approach for retrieval of historical monuments images using visual contents and unsupervised machine learning. *International Journal of Advanced Trends in Computer Science and Engineering*, *9*(3), 3563-3569.

Nex, F. & Remondino, F. (2014). UAV for 3D mapping applications: a review. *Applied Geomatics*, *6*(1), 1-15.

Noor, N.M., Abdullah, A. & Hashim, M. (2018). Remote sensing UAV/drones and its applications for urban areas: a review. *IOP Conference Series: Earth and Environmental Science*, *169*(1), 012003.

Pix4D SA (n.d.). Pix4Dfields. Retrieved from: https://support.pix4d.com/hc/en-us/categories/360000061343-Pix4Dfields (access 14.09.2020).

Saberioon, M.M., Amin, M.S.M., Anuar, A.R., Gholizadeh, A., Wayayok, A. & Khairunniza-Bejo, S. (2014). Assessment of rice leaf chlorophyll content using visible bands at different growth stages at both the leaf and canopy scale. *International Journal of Applied Earth Observation and Geoinformation*, *32*, 35-45.

Scardozzi, G. (2011). Multitemporal satellite images for knowledge of the Assyrian capital cities and for monitoring landscape transformations in the upper course of Tigris River. *International Journal of Geophysics*, 2011, 9172306. https://doi.org/10.1155/2011/917306

Ur, J. (2005). Sennacherib's northern Assyrian canals: new insights from satellite imagery and aerial photography. *Iraq*, *67*(1), 317-345.

Vora, P. & Oza, B. (2013). A survey on k-mean clustering and particle swarm optimization. *International Journal of Science and Modern Engineering*, *1*(3), 24-26.

Summary

Detecting abuses in archaeological areas using k-mean clustering analysis and UAVs/drones data. Unmanned aerial vehicles (UAVs) or drones have made great progress in aerial surveys to research and discover heritage sites and archaeological areas, particularly after having developed their technical capabilities to carry various sensors onboard, whether they are conventional cameras, multispectral cameras, and thermal sensors. The objective of this research is to use the drone technology and

k-mean clustering algorithm for the first time in Nineveh Governorate in Iraq to reveal the extent of civil excesses and random construction, as well as the looting and theft that occur in the archaeological areas. DJI Phantom 4 Pro drone was used, in addition to using the specialized Pix4D program to process drone images and make mosaics for them. Multiple flights were performed using a drone to survey multiple locations throughout the area and compare them with satellite images during different years. Drone's data classification was implemented using a k-means clustering algorithm. The results of the data classification for three different time periods indicated that the percentage of archaeological lands decreased from 90.31% in 2004 to 25.29% in 2018. Where the work revealed the extent of the archaeological area's great violations. The study also emphasized the importance of directing authorities of local antiquities to ensure the use of drone's technology to obtain statistical and methodological reports periodically to assess archaeological damage and to avoid overtaking, stolen and looted of these sites.

Authors' address:
Abdalrahman Qubaa
(https://orcid.org/0000-0001-6805-2200)
University of Mosul, Nineveh
Remote Sensing Center
Al-Hadbaa Street 16, 00964 Mosul
Iraq
e-mail: abdqubaa@uomosul.edu.iq

Saja Al-Hamdani
(https://orcid.org/0000-0003-4346-0587)
University of Mosul, Nineveh
College of Computer & Mathematic Science
Department of Computer Science
Aljamea Street 16, 00964 Mosul
Iraq
e-mail: sata@uomosul.edu.iq

Thaer O. ROOMI, Adel S. ABED

Mustansiriyah University, College of Science

Estimating gaseous pollutants in the air near Daura Refinery, Daura Power Plant and South of Baghdad Power Plant by calculating the fuel discharge

Introduction

Air is polluted when there are odd substances in it, and these substances become undesirable when their presence in a concentration may cause great harm to humans, their properties and their environment. These odd materials (pollutants) may be in the form of aerosols or gases (Vallero, 2014). The environmental pollution caused by the industrial facilities has become a global concern. Part of the complexity of this problem is the conflict between the economic benefits of these facilities and their risks to public health and the surrounding environment (Al-Jahdali & Bin Bisher, 2008). The industrial facilities emits several atmospheric pollutants including SO_2, H_2S, NO_X, CO, hydrocarbons and other poisonous materials (Damian, 2014).

Many diseases such as cancer, heart disease, pneumonia and premature death can occur because of exposure to gases from refineries, power plants and other industrial facilities (Shubbar, 2019). Sulfur dioxide gas dissolves rapidly in atmospheric water vapor, thus acid rain builds up in air, soil and plants around refineries and power plants (Zhao, Li, Xiao & Li, 2019). This gas caused primarily by refineries and power plants (Liu, Yang, Zhang Xiang & Wei, 2019). Many research works confirmed that NO_2 has serious problems to humans and contributing in agriculture degrading by affection on the chlorophyll (Camargo & Lombardi, 2018; Sheng & Zhu, 2019). Carbon monoxide resulting from incomplete combustion of carbon materials. It affects human health and plants due to its toxic nature (Cuinica, Abreu, Gomes & Esteves da Silva, 2013). One of the important factors in the dispersion and transmission of pollutants is the air stability. On diurnal to sub-diur-

nal timescales, variation in air stability can cause a comparable or greater influence on the variability of urban pollutant concentrations than the changes in source emission or advection (Wang et al., 2016). Wind speed and direction patterns plays an important role in dispersion and mitigation of the high concentration of gas pollutants. However, they distribute the pollutions to cover more remote regions (Manii & Al-Jumaylii, 2012). Many research works address the pollution problem and the environmental effects of refineries and power plants in Iraq. Al-Suhaili and Al-Khafaji (2015) built a mathematical model for integrated air pollution modelling around refineries and took Daura Refinery as a study case. The model demonstrates the influence of atmospheric stability, wind speed, emission rate, exit velocity, physical height, exit temperature and rural-urban area in reducing the concentrations of pollutants. Al-Dabbas, Ali and Afaj (2012) studied the concentrations of pollutants around Kirkuk Refinery by using low volume air sampler (a sniffer) in 2010 and 2011. The results revealed that the concentrations were higher than the permissible limits of the Iraqi national determinants. Al-Hassen, Al-Qarooni, Qassim, Al-Saad and Alhello (2015) determined the gaseous pollutants concentrations of CO, NO_2, and SO_2 emitted from selected emission sources at Basra city. The results revealed that the concentrations of the above pollutants exceeded the maximum permissible limits for Iraqi National Emission Standards. Shubbar, Suadi and Al-Jiboori (2018) studied the dispersion of SO_2 from Daura Refinery by using ScreenView model and checked the effect of the wind speed and direction

on the spread of pollutants. The three pollutants (CO, SO_2 and NO_2) have been also taken up by researchers from around the world. García-Gusano, Cabal and Lechón (2015) carried out a study to ease the lack of National Emission Ceilings (NEC) Directive assessments at country level for Spain. The amount of NOx and SO_2 emissions were analyzed using the TIMES-Spain energy optimization model. Abiye et al. (2016) provided model-based estimates of atmospheric dispersion for gaseous pollutants (SO_2 and NO_X) released from a scrap-iron recycling factory located in southwest of Nigeria. The study identified the pollutant concentrations increase by stable atmosphere, weak wind speed, low mixing height, and high relative humidity. A comprehensive Canadian study conducted by Ragothaman and Anderson (2017) presented a review of findings from different studies on air quality impacts of petroleum refining and petrochemical plants in several cities around the world. Kumar, Bhushan and Kishore (2018) applied a dispersion modeling approach to determine SO_2 and NO_2 concentrations in the surrounding air of the industrial and mining cluster in Keonjhar, India for one year 2015. Filonchyk, Hurynovich, Yan, Gusev and Shpilevskaya (2020) carried out a study focused on East China and attempted to assess comprehensively the environmental impact of the COVID-19 disease 2019 outbreak. The study analyzed satellite images of SO_2, NO_2, CO and aerosol optical depth in the period before and during the outbreak of the epidemic. The data then was compared with the data before the epidemic in 2019. The results showed that the COVID-19 lockdown improved air

quality in the short term, but as soon as power plants and refineries came back to normal work, pollution levels returned to their previous level.

In this study, the emitted pollutants of CO, SO_2 and NO_2 emerged from each of Daura Refinery (DR), South of Baghdad Power Plant (SBPP) and Daura Power Plant (DPP) was addressed. These three facilities uses the crude oil and are situated in a region of less than 3 km in diameter. Two of them (DR and BSPP) was established in 1950s, while DPP was established in 1981. In 1950s, these facilities where outside the city and no houses in around (Murtadah, Al-Sharify & Hasan, 2020). However, nowadays, these facilities are surrounded by inhabited cities, which are affected by the pollution of undesired gases. Therefore, the Iraqi committee of health and environment in the Iraqi parliament called for a decision to transfer DR to another place according to environmental and international regulations (Murtadah et al., 2020). However, due to the economic difficulties the country is going through, this option is no longer on the table now.

Gaussian plume model of dispersion

Gaussian dispersion models are extensively used to calculate local pollution levels. The accuracy of such models depends on stability determination (Awasthi, Khare & Gargava, 2006). This model utilizes an emissions rates, meteorological elements, and equations, which describe mathematically the physical process of turbulent transport of air pollutants in the boundary layer to calculate concentrations. Gaussian plume equation tells mathematically how to compute the concentration of a gas or any comparable in size, solid or liquid pollutant being emitted continuously from a single source (Weber, 1982), the equation can be written simply by (Leelőssy et al., 2014):

$$C(X,Y,Z,H) = \frac{Q}{2\pi\sigma_y\sigma_z U}\exp\left[-\frac{1}{2}\left(\frac{y}{\sigma_y}\right)^2\right]\left[\exp\left(-\frac{1}{2}\left(\frac{z-H}{\sigma_z}\right)^2\right)+\exp\left(-\frac{1}{2}\left(\frac{z+H}{\sigma_z}\right)^2\right)\right]$$

where:
C – concentration [ppm of kg],
X – horizontal distance in downwind direction [m],
Y – central line of pollutants dispersion [m],
Z – vertical altitude above surface [m],
H – effective height of chimney ($H = h + \Delta h$, in which h is chimney height and Δh is plume height) [m],
Q – emission rate [$kg \cdot s^{-1}$],
σ_y, σ_z – Gaussian plume standard deviations in horizontal (crosswind) and vertical directions,
U – wind speed at the effective height of chimney [$m \cdot s^{-1}$].

Our current study estimated the concentrations of by using the consumed fuel in three facilities: Daura Refinery (DR), Daura Power Plant (DPP) and South of Baghdad Power Plant (SBPP). The calculation implemented by using Gaussian dispersion model. The effects of the stability, wind speed and direction, chimneys height and diameter were also investigated. The most affected cities were determined, as well.

Material and methods

Location

Daura Refinery, Daura Power Plant are located in Daura District, south of Baghdad, while South of Baghdad Power Plant is located to the east of the refinery, 2 km away on the other side of the Tigris river. The area surrounding these facilities is urban areas of flat nature devoid of complex terrain as well as of tall buildings (Fig. 1).

on SBPP was obtained from the power plant. Data about DPP was obtained from the Environment Unit in the Department of Planning and Studies, Iraqi Ministry of Electricity. The meteorological data of 10 m wind speed and hourly 1.5 m air temperatures of year 2017 of Daura District were obtained from the European Center for Medium Weather Forecast (ECMWF) website. DR contains 12 units that have 35 chimneys, DPP has four units connected to four chimneys, while SBPP
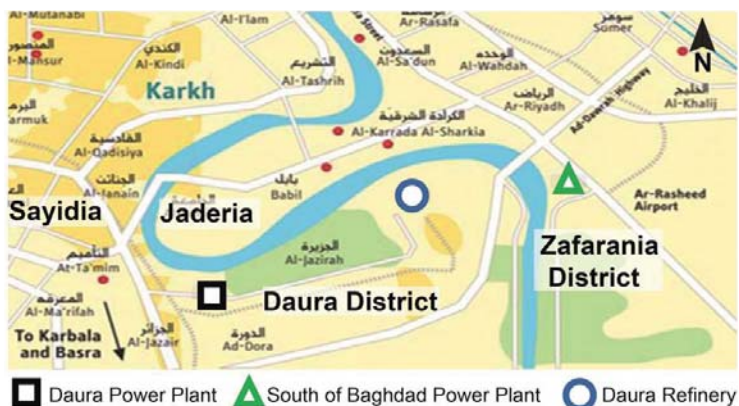

FIGURE 1. Location of examined emitters of air pollution

Data

The data were used for the monthly quantities of fuel discharged in each unit of DR for year 2017, and the data for the height, diameter, and temperature of the outgoing gas were used. These data were obtained from DR. Likewise, the data

has six units, three of which only are in operation, and each of the plant's units is connected to one chimney. To consider these units as a single point source, the height and diameter of the chimney and the temperature of the gas exiting from it were calculated as rates. Table 1 lists the information of the chimneys.

TABLE 1. Chimney characteristics of the pollutions sources

Specification	Daura Refinery (DR)	South of Baghdad Power Plant (SBPP)	Daura Power Plant (DPP)
Chimney average height [m]	29	54	100
Chimney average diameter [m]	1.5	2	2.5
Chimney exit gas temperature [K]	615	460	433

Concentrations of SO_2, CO and NO_2

Concentrations of SO_2, CO and NO_2 gases emitted from DR, DPP and SBPP were calculated for four months representing the seasons of 2017 (January, April, July and October) for a distance of 10 km from the source. The concentrations were calculated by using Gaussian plume model of dispersion, which requires gas emission rate, chimney's gas exit velocity in addition to the height, diameter, and gas exit temperature of the chimney. The method uses the data of consumed fuel. To calculate gas emission rates, the monthly fuel quantities data converted into hourly rates and then to convert volume units to mass units. Calculation of emission rates and gas exit velocity were computed by FORTRAN script.

Effect of stability and wind on pollutants concentrations

The concentrations were calculated for slightly stable (E) and moderately unstable air classes (B) for four months in 2017: January, April, July, October. Finally, a comparison among the three sources (DR, DPP, SBPP) of the emission rates and concentrations of pollutants was made to quantify the contribution of each source of the three pollutant gases (SO_2, CO, NO_2).

Results and discussion

Emission rates

The results of emission rates and gas exit speed were shown in Table 2. It is clear that DPP consumed more fuel and emitted more pollutants than the other sources.

TABLE 2. Emission rates and gas exit speed of Daura Refinery (DR), South of Baghdad Power Plant (SBPP) and Daura Power Plant (DPP)

Specification	Facility	January	April	July	October
Consumed fuel mass [kg·h^{-1}]	DR	41 428	45 056	51 997	47 964
	SBPP	25 629	24 189	25 164	20 680
	DPP	57 980	77 184	94 321	64 505
SO_2 emission rate [g·s^{-1}]	DR	904	1037	1 123	1 017
	SBPP	598	564	587	482
	DPP	1 352	1 800	2 200	1 505
CO emission rate [g·s^{-1}]	DR	862	863	1 023	930
	SBPP	660	623	648	533
	DPP	1 495	1 990	2 432	1 663
NO_2 emission rate [g·s^{-1}]	DR	84	89	97	84
	SBPP	61	58	60	49
	DPP	139	185	226	154
Gas exit speed [m·s^{-1}]	DR	5.5	6.1	7.2	6.9
	SBPP	18.8	17.7	18.4	15
	DPP	19.3	25.7	31.4	21.5

Concentrations of the pollutants at four months of slightly stable condition (E)

Figure 2 shows the pollutant concentrations emitted from DR for the four months when the atmosphere is slightly stable (E). The figures showed that the pollutant concentrations change with distance, as the pollutants concentrations at the surface level increase in the beginning with moving away from the point source and then decrease after that. It was observed that the highest concentration of pollutants is approximately at distance of 1,000 m. This high value can be justified due to the fact that the gas leaving the chimney is at a higher temperature than the surrounding temperature and therefore its density is lower than the surroundings' density. The gas rises higher due to the force of buoyancy and turbulence enhancing pollutants dispersion and reducing the concentrations. With increasing distance from the source, the plume mixes with the surrounding air. The temperature decreases gradually and the buoyancy force will be diminished and the vertical movement will be inhibited. Therefore, the concentrations of pollutants increase gradually in the distance less than 1,000 m. After this distance, pollutants concentrations begin to decrease gradually due to their departure from the source. Although the lowest emission rates of pollutants were during January, concentrations of pollutants at the surface level were the highest during this month. This may due to the lower wind speed in addition to the stratification of stable weather and inversion during this month. It was also noted that the concentration of SO_2 is slightly higher than CO and that the ratio of SO_2 to CO is greater in April. This may be due to the fact that the consumption of gaseous fuel is greater than that of liquid fuels in April when the need to electricity is the lowest. It is well known that the gaseous fuel releases more quantities of
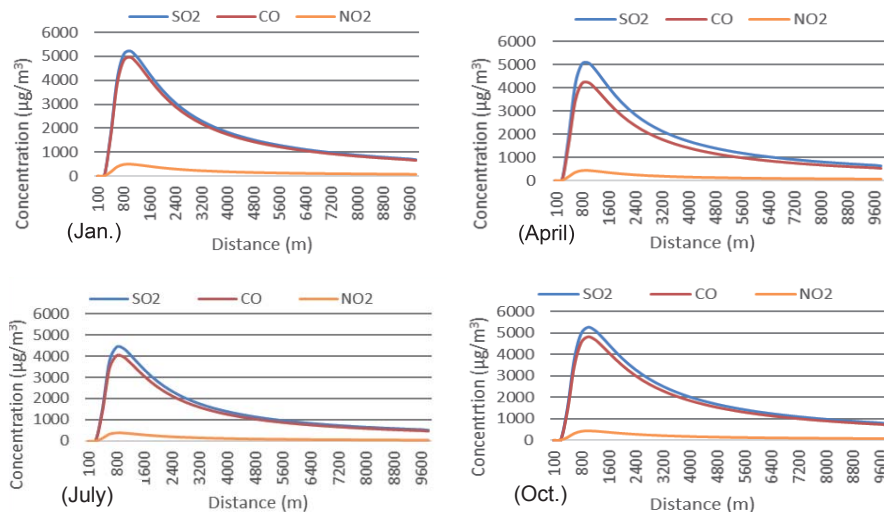

FIGURE 2. Pollutants concentration at stable conditions, at Daura Refinery

SO$_2$ than CO. On the other hand, it was observed that the concentrations of NO$_2$ gas was fewer compared to SO$_2$ and CO. This low value of NO$_2$ is normal for refineries (Nirel & Dayan, 2001).

Figure 3 shows the concentrations of pollutants emitted from SBPP at slightly stable condition (E). The highest concentration of pollutants was during January which might due mainly to the high quantities of fuel consumed during this month. Also, the wind speed during January was the least leading to an increase in concentrations. It was also observed that the concentration of CO was slightly higher than SO$_2$, while the concentrations of NO$_2$ were lowest.

Figure 4 shows the concentrations of pollutants emitted from DPP in a slightly stable weather condition. It was observed that the highest concentration of pollutants was during November, and the lowest was during January and July. Although the wind speed during July is higher than January, the emission rates of pollutants during July were also high and the values were close to January.

Moderately unstable condition (B)

Figure 5 shows the pollutant concentrations emitted from DR in moderately unstable condition (B). The highest concentration was approximately at distance of 200 m and then decreased greatly with the increase in the distance because the vertical movement was active, which led to mixing and dispersing of the pollutants, and thus the pollutant concentrations decreased. Hence, the pollutants concentration in this unstable condition was greater than in the case of moderately unstable atmosphere and with same wind speed.

In Figure 6, the dispersion of pollutants for SBPP at unstable conditions was very large and the concentrations were at their highest values at distances close
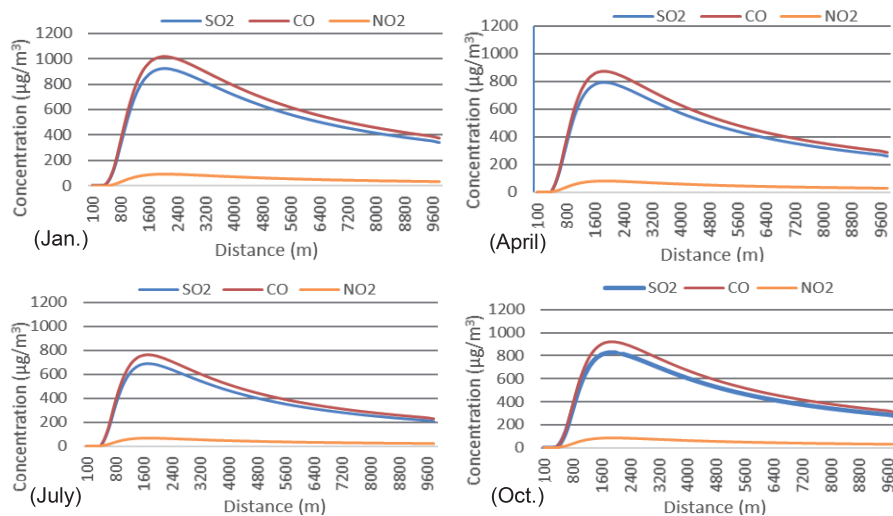

FIGURE 3. Pollutants concentration versus distance at stable conditions, at South of Baghdad Power Plant
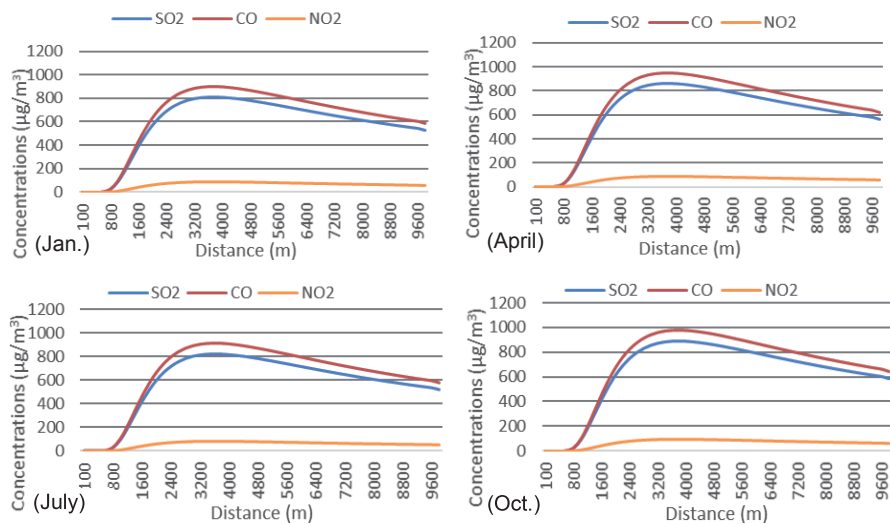
FIGURE 4. Pollutants concentration versus distance at stable conditions, at Daura Power Plant
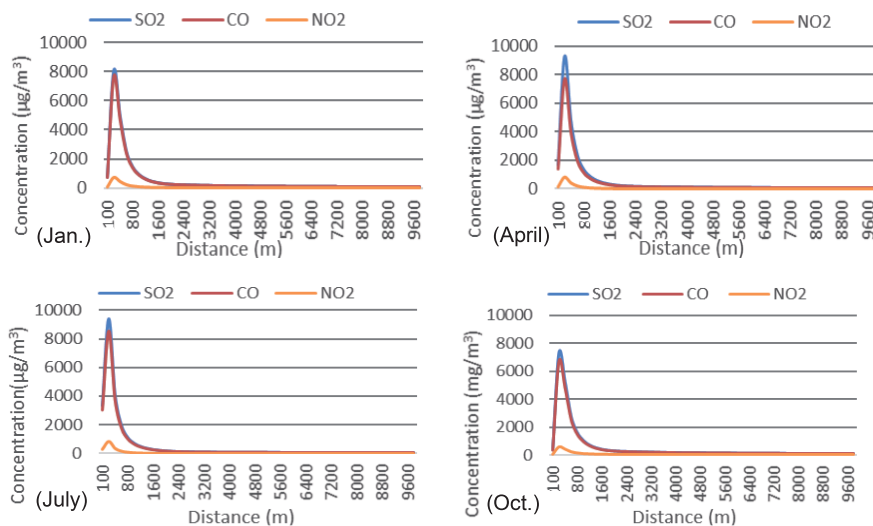

FIGURE 5. Pollutants concentration versus distance at unstable conditions, at Daura Refinery

to the plant. The highest concentration was approximately at 600 m. The concentration then decreases gradually with increasing distance.

Figure 7 shows that the dispersion of pollutants in unstable conditions is very large for DPP, where the concentrations are at their highest values at distances close to the plant. The highest concentration was approximately at distance of 700 m, then the concentration decreases with increasing distance.
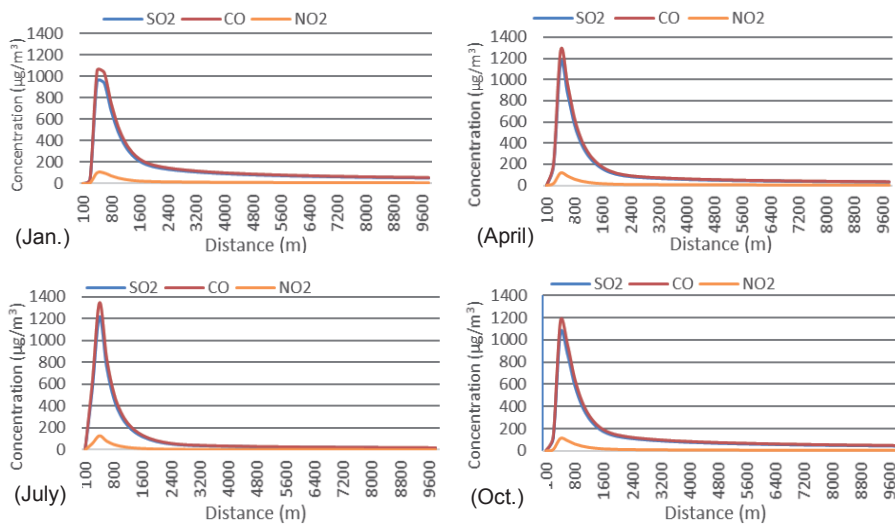
T.O. Roomi, A.S. Abed

FIGURE 6. Pollutants concentration versus distance at unstable conditions, at South of Baghdad Power Plant

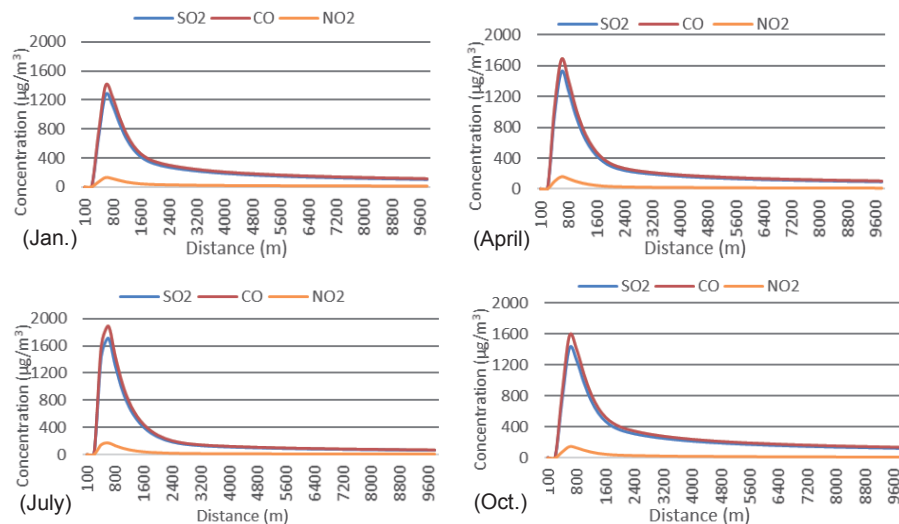FIGURE 7. Pollutants concentration versus distance at unstable conditions, at Daura Power Plant

Wind direction impact on pollutants dispersion

Table 3 shows that the prevailing wind is northwest. In stable conditions, high pollutants concentrations can reach greater distances than in unstable conditions since they maintain near the ground. During January and July, Daura District was the most affected by DPP, while Zafarania District was the most affected by DR and SBPP because it was affected by northwest winds. Dur-

TABLE 3. Prevailing wind in the study area for January, April, July, and October 2017

Month	Wind speed [m·s⁻¹]	Direction							
		N	NE	E	SE	S	SW	W	NW
January	0–5	28	9	11	20	7	7	16	135
	6–10	0	0	0	6	0	3	1	5
April	0–5	72	17	11	10	5	6	11	70
	6–10	6	2	3	4	3	0	1	20
July	0–5	25	4	0	0	5	6	16	70
	6–10	18	0	0	0	0	0	2	103
October	0–5	53	37	30	31	5	4	10	66
	6–10	0	0	0	6	4	0	0	3

ing April, one can notice that along with the northwest winds, there were eastern winds that contribute to the transfer of pollutants emitted from DR and SBPP to Daura area, while Sayidia area was more affected by DPP. October had the most variable wind direction.

Comparison of the three sources

The emission rates and concentrations of pollutants emitted from DR, DPP and SBPP were visualized to make a comparison among them (Fig. 8). It is clear that the pollutants concentrations
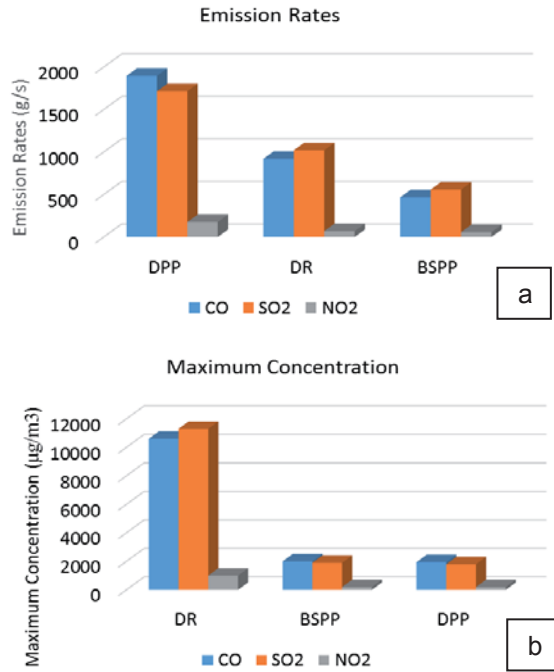
FIGURE 8. Facilities (a) emission rates and (b) maximum concentration

emitted from DR at the ground level are greater than those emitted from DPP. This may due to the difference in effective plume height, as the greater the effective height of the plume, the greater the dispersion of pollutants. This give indication that this facility has serious problems on the human health and even the plants. The height of the chimney, the gas exit velocity, and the gas temperature lead to an increase in the effective height of the plume. Considering the diameter, the larger the diameter, the faster the gas leaving the chimney, the lower effective height of plume. Because of the high altitude of DPP chimneys, the wind speed is greater at the top causing greater reduction of pollutants. The high altitude of the chimney does not mean it is environmentally friendly because pollutants will just spread for longer distances. In these three sources, it was observed that the effect of the height of the chimney as well as the velocity of the gas leaving the chimney were more clear on the dispersion of pollutants than the effect of diameter and the temperature of the gas leaving the chimney.

Conclusions

1. The concentrations of pollutants in DR, BSPP and DRR increase in stable conditions due to the less air turbulence. Hence, the unstable atmospheres are better at dispersing pollutants.
2. Since the prevailing wind direction is northwest, Zafarania District is the most affected by the pollutants emitted from DR and BSPP while Daura District is very affected by DPP.
3. Wind speed has a clear effect on the dispersion of pollutants, the higher wind speed, the lower pollutant concentrations.
4. Pollutant concentrations increase with increasing emission rates and chimney diameter, and decreasing with increasing chimney height, speed of the gas leaving the chimney.
5. DPP has higher emission rates than DR and SBPP. However, at the surface level, the concentrations emitted from DR are greater than those emitted from DPP and SBPP. Thus, DR is the most affecting source on the health of people in the areas surrounding the refinery.
6. Although increasing the height of the chimney contributes to reducing the concentrations of pollutants at the surface level that does not mean it is environmentally friendly because pollutants will just spread for longer distances.

Acknowledgements

References

Abiye, O., Sunmonu, L., Ajao, A., Akinola, O., Ayoola, M. & Jegede, O. (2016). Atmospheric dispersion modeling of uncontrolled gaseous pollutants (SO_2 and NO_X) emission

from a scrap-iron recycling factory in Ile-Ife, Southwest Nigeria. *Cogent Environmental Sciences*, *2*(1). 1275413. https://www.doi.org/10.1080/23311843.2016.1275413

Al-Dabbas, M.A., Ali, L.A. & Afaj, A.H. (2012). The effect of Kirkuk Oil Refinery on Air pollution of Kirkuk City-Iraq. *Proceeding of the 1st Conference on Dust Storms and their Environmental Effects*, *17*(18), 8-18.

Al-Hassen, S.I., Al-Qarooni, E.H., Qassim M.H., Al-Saad, H.T. & Alhello, A. (2015). An experimental study on the determination of air pollutant concentrations released from selected outdoor gaseous emission in Basra City, Southern Iraq. *Journal of International Academic Research for Multidisciplinary*, *3*(1), 88-98.

Al-Jahdali, M.O. & Bin Bisher, A.S. (2008). Sulfur dioxide (SO_2) accumulation in soil and plant's leaves around an oil refinery: A case study from Saudi Arabia. *American Journal of Environmental Sciences*, *4*(1), 84-88.

Al-Suhaili, R.H. & Al-Khafaji, M.S. (2015). Integrated system for air pollution around refineries. *Journal of Engineering*, *15*(4), 4204-4218.

Awasthi, S., Khare, M. & Gargava, P. (2006). General plume dispersion model (GPDM) for point source emission. *Environmental Modeling and Assessment*, *11*(3), 267-276.

Camargo, E.C. & Lombardi, A.T. (2018). Effect of cement industry flue gas simulation on the physiology and photosynthetic performance of *Chlorella sorokiniana*. *Journal of Applied Phycology*, *30*(2), 861-871.

Cuinica, L.G., Abreu, I., Gomes, C.R. & Esteves da Silva, J.C.G. (2013). Exposure of *Betula pendula* Roth pollen to atmospheric pollutants CO, O_3 and SO_2. *Grana*, *52*(4), 299-304.

Damian, C. (2014). Environmental pollution in the petroleum refining industry. *Analele Universitatii "Ovidius" Constanta. Chimie*, *24*(2), 109-114.

Filonchyk, M., Hurynovich, V., Yan, H., Gusev, A. & Shpilevskaya, N. (2020). Impact assessment of COVID-19 on variations of SO_2, NO_2, co and AOD over east China. *Aerosol and Air Quality Research*, *20*(7), 1530-1540.

García-Gusano, D., Cabal, H. & Lechón, Y. (2015). Evolution of NO_x and SO_2 emissions in Spain: Ceilings versus taxes. *Clean Technologies and Environmental Policy*, *17*(7), 1997-2011.

Kumar, D.S., Bhushan, S.H. & Kishore, D.A. (2018). Atmospheric dispersion model to predict the impact of gaseous pollutant in an industrial and mining cluster. *Global Journal of Environmental Science and Management*, *4*(3), 351-358.

Leelőssy, Á., Molnár, F., Izsák, F., Havasi, Á., Lagzi, I. & Mészáros, R. (2014). Dispersion modeling of air pollutants in the atmosphere: a review. *Central European Journal of Geosciences*, *6*(3), 257-278.

Liu, Z., Yang, J., Zhang, J., Xiang, H. & Wei, H. (2019). A bibliometric analysis of research on acid rain. *Sustainability*, *11*(11), 3077. https://www.doi.org/10.3390/su11113077

Manii, J.K. & Al-Jumaylii, A.K. (2012). Monthly variation of some air pollutants in Hilla City – middle of Iraq. *Journal of University of Babylon*, *22*(1), 1-12.

Murtadah, I., Al-Sharify, Z.T. & Hasan, M.B. (2020). Atmospheric concentration saturated and aromatic hydrocarbons around Dura refinery. *IOP Conference Series: Materials Science and Engineering*, *870*(1), 012033. https://www.doi.org/10.1088/1757-899X/870/1/012033

Nirel, R. & Dayan, U. (2001). On the ratio of sulfur dioxide to nitrogen oxides as an indicator of air pollution sources. *Journal of Applied Meteorology*, *40*(7), 1209-1222.

Ragothaman, A. & Anderson, W.A. (2017). Air quality impacts of petroleum refining and petrochemical industries. *Environments – MDPI*, *4*(3), 1-16.

Sheng, Q. & Zhu, Z. (2019). Effects of nitrogen dioxide on biochemical responses in 41 garden plants. *Plants*, *8*(2), 1-15.

Shubbar, R. (2019). *Numerical simulation of air pollutants using CALPUFF model at an urban area in Baghdad-Iraq* (unpublished PhD thesis). Pukyong National University, Busan.

Shubbar, R.M., Suadi, A.J. & Al-Jiboori, M.H. (2018). Study the concentration of SO_2 emitted from Daura refinery by using screen view model. *Al-Mustansiriyah Journal of Science*, *29*(3), 7-15.

Vallero, D. (2014). *Fundamentals of air pollution*. Amsterdam: Elsevier.

Wang, F., Chambers, S.D., Zhang, Z., Williams, A.G., Deng, X., Zhang, H., Lonati, G., Crawford, J., Griffiths, A.D., Ianniello, A. & Allegrini, I. (2016). Quantifying stability influences on air pollution in Lanzhou, China, using a radon-based "stability monitor": Seasonality and extreme events. *Atmospheric Environment*, *145*, 376-391.

Weber, E. (1982). Fundamentals for the application of a Gaussian Plume Model. In E. Weber (eds.), *Air Pollution: Assessment Methodology and Modeling* (pp. 101–128). Berlin: Springer.

Zhao, X., Li, K., Xiao, D. & Li, X. (2019). Experimental study of the mechanism of acid rain-gabbro Interaction. *E3S Web of Conferences*, *98*, 01053. https://doi.org/10.1051/e3sconf/20199801053

Summary

Estimating gaseous pollutants in the air near Daura Refinery, Daura Power Plant and South of Baghdad Power Plant by calculating the fuel discharge. This study addresses estimation of emission rates and concentrations of SO_2, CO and NO_2 gases emitted from Daura Refinery (DR), Daura Power Plant (DPP) and South of Baghdad Power Plant (SBPP) by calculating the fuel discharge. The estimations were made by using the Gaussian plume model of dispersion at distances within 10 km from the pollution source for January, April, July and October 2017 under two stability conditions, slightly stable and moderately unstable. The effect of wind speed and direction as well as the ambient temperature of the surrounding air on the dispersion and transmission of air pollutants were also investigated. It was found that the unstable conditions are better for dispersing out atmospheric pollutants. The results showed that Zafarania District was the most affected by pollutants emitted from DR and BSPP while Daura District was more affected by DPP due to the prevailing wind direction. It was also found that an increase in wind speed leads to a decrease in the concentration of pollutants. The concentration of pollutants is inversely proportional to the height of the chimney, the speed of the gas leaving the chimney, while it is directly proportional to the diameter of the chimney. DPP has higher emission rates than DR and SBPP while at the surface level, the pollutants concentrations emitted from DR are greater than those emitted from DPP and SBPP.

Authors' address:
Thaer O. Roomi – corresponding author
(https://orcid.org/0000-0002-5764-5075)
Adel S. Abed
(https://orcid.org/0000-0001-5175-904X)
Mustansiriyah University
College of Science
Department of Atmospheric Science
Palestine Street, 46131 Baghdad
Iraq
e-mail: th.roomi.atmsc@uomustansiriyah.edu.iq
a.adelsaad96@gmail.com

Ezekiel Kaura MAKAMA[1, 2], Hwee San LIM[1]

[1]Universiti Sains Malaysia, School of Physics
[2]University of Jos, Department of Physics

Inter-annual and seasonal patterns of precipitable water vapour over Malaysia from 1990–2019 based on MERRA-2 reanalysis

Key words: total precipitable water vapour, MERRA-2, monsoon, reanalysis

Introduction

Total precipitable water vapour (*TPW*) is the integration of water vapour in a column of atmosphere from the surface of the Earth to space with the potential of being precipitated. *TPW* is not only the most important greenhouse gas, it is the main source of moisture for precipitation that plays an important feedback role in climate system (Randel et al., 1996). Unlike other greenhouse gases, *TPW* has high variability both at the spatial and temporal scales, with higher values found equatorward against lower values poleward. The parameter exhibits seasonal patterns, with higher values during summer and lower during winter in the Northern Hemisphere.

Although *TPW* is influenced by land-sea convection, its value is significantly affected by orography over continental lands since the concentration is mostly within the lower layer of the atmosphere. Its regional variability is also affected by wind circulation like El Niño-Southern Oscillation (ENSO), which are common signatures in the equatorial belt (Numata et al., 2013).

Knowledge of the spatial and temporal variations of *TPW* is extremely important in climate models (Ccoica--López, Pasapera-Gonzales & Jimenez, 2019), the forecast of precipitation, and in the determination of moisture flow over an area (Tuller, 1977). Despite its importance and familiarity to meteorologists, only limited attempts have been made to evaluate the distribution and variability of mean *TPW* over Malaysia. Most of the published data on *TPW* values are found only as a minor element in

dealing with its quantitative forecasting or moisture flow in the area of concern (Peng, Li, Chen, Norizan & Tay, 2006; Salihin, Musa & Radzi, 2013; Suparta, Rahman & Singh, 2014; Suparta and Al-hasa, 2016; Makama, Lim & Abdullah, 2018). Malaysia, being a tropical region with overlapping seasonality and complex orography, is an important area for climate study. Moreover, global and regional phenomena like ENSO also characterize the climate of the region in addition to rising temperature occasioned by global warming. For instance, using twelve coupled Atmospheric-Oceanic General Circulation Models, the Malaysian Meteorological Department projected respective temperature increases of 1.0–3.5°C and 1.1–3.6°C for East and West Malaysia (Malaysian Meteorological Department [MetMalaysia], 2009). In this study temporal and spatial variations, as well as trend in *TPW* over Malaysia from 1990 to 2019 are evaluated using the Second Modern-Era Retrospective Analysis for Research and Applications (MERRA-2) data.

Data and methods

Study area

Malaysia lies between longitudes 99°–120°E and latitudes 1°–7°N in Southeast Asia. The Country consists of three federal territories namely; West Malaysia (or Peninsular Malaysia), Sabah, and Sarawak (jointly called East Malaysia). These two regions, which are separated by the South China Sea, share a largely similar landscape characterized by coastal plains rising to hills and mountains. The climate of Malaysia classified as tropical rainforest and monsoon in which high and constant precipitation is exhibited. Most of the region is made up of maritime continents with different topography. The mountains and the complex land-sea configuration strongly influence both the weather and climate of the Country. The Northeast Monsoon (NEM) and the Southwest Monsoon (SWM) also define the climate of Malaysia.

Datasets

MERRA-2 reanalysis data from the National Aeronautic and Science Administration (NASA) for the satellite era replaces MERRA reanalysis data using a three-dimensional upgraded version of Goddard Earth Observing System Model (GEOS) with Atmospheric Data Assimilation System (ADAS) ver. 5.12.4. All data products from MERRA-2 are provided at the same resolution of $0.5° \times 0.625°$ (latitude and longitude), unlike in MERRA. The data was accessed from the website https://nasa.gov/reanalysis/MERRA-2 (last accessed 2 May 2020). In this study, monthly mean *TPW* data derived from MERRA-2 reanalysis for the period 1990 to 2019 have been used. A collocation box of longitude-latitude grid closest to each of the World Meteorological Organization (WMO) station in the study area was averaged and compared directly with radiosonde *TPW*. Seasonal means were obtained for NEM (November–April) and SWM (May–October) for spatial and temporal patterns (Note: Though two inter-monsoon seasons are also involved in describing the weather of Malaysia, these are not separately considered in the current study).

Radiosonde data, primarily used to evaluate MERRA-2 product, were freely obtained from Integrated Global Radiosonde Archive (IGRA) ver. 2 of the National Climatic Data Centre (NCDC), available at www.ncdc.noaa.gov (Durre, Vose & Wuertz, 2008). The requisite *TPW* data were extracted from twice-daily sounding from WMO stations at Kota Bharu, Penang, Kuantan, and Changi (Singapore), Kota Kinabalu, Tawau, Bintulu, and Kuching for the period 1 January 1990 to 31 December 2019. Quality control was imposed on the daily data to rid it of obvious errors and outliers from the time series of the station data. For homogeneity test, at least 18 daily observations were used to calculate the mean monthly values and 10 valid months were used in deriving the annual mean values of *TPW*. Data from stations with a consistent time series of 18 years between 1990 and 2019 were considered for the validation of MERRA-2 data. Finally, the daily value was derived as the mean of the night and daytime and then converted into monthly means to conform with those of MERRA-2 for direct comparison.

Trend computation

Annually averaged monthly mean MERRA-2 precipitable water vapour time series was used to evaluate long-term variability of *TPW* over each of the three regions in recent decades. Least square regression (LSR) method (Eq. 1) (Zhai & Eskridge, 1997) was used to detect trend in the MERRA-2 *TPW* data.

$$y(t) = a + bx \qquad (1)$$

where:
y – total precipitable water vapour (*TPW*) [mm],
a – intercept [mm],
b – slope of the line of fit represents the regional water vapour trend [mm·decade^{-1}],
x – corresponding time [year].

The constants a and b were estimated from (Zhai & Eskridge, 1997):

$$a = \frac{1}{n} \sum y_i - \left(\frac{1}{n} \sum x_i \right) b \qquad (2)$$

$$b = \frac{S_{xy}}{S_{xx}} \qquad (3)$$

where: $\quad S_{xx} = \sum x_i^2 - \frac{1}{n} \left(\sum x_i \right)^2 \quad$ and $S_{xy} = \left[\sum x_i y_i - \frac{1}{2} \left(\sum x_i \right) \left(\sum y_i \right) \right], \quad n \quad$ is the total number of years in the study period while the summation is from $i = 1$ to $i = n$. The standard error was obtained from Eq. (4):

$$\sigma_b = \sqrt{\frac{S_{yy} - bS_{xy}}{S_{xx}(n-2)}} \qquad (4)$$

where: $S_{yy} = \sum y_i^2 - \frac{1}{n} \left(\sum y_i \right)^2$. In this study, the uncertainty of the trend estimate was taken as $S_{yy} = \sum y_i^2 - \frac{1}{n} \left(\sum y_i \right)^2$ at the 95% interval. The significance of the trend was determined by the Student's t-test with the following hypotheses: H_0: $b = 0$ and H_1: $b \neq 0$, in which the null

hypothesis avers that no trend while the alternative hypothesis holds existence of trend. The test statistic was obtained from Eq. (5):

$$Z = \frac{|b|\sqrt{S_{xx}}}{\sqrt{\dfrac{S_{yy} - bS_{xy}}{n-2}}} \qquad (5)$$

with the acceptance region for the null hypothesis being $-t_\alpha/2 < Z < t_\alpha/2$, where α is the significance level (0.05). If Z is non-zero, the null hypothesis is rejected in favour of the alternative hypothesis, and therefore, enough to say trend exist.

Results and discussion

Temporal variation of TPW

To discern mean *TPW* across Malaysia, eight radiosonde stations were adopted as sub-regional representatives

(Fig. 1). These locations are WMO stations that have long-term homogenous radiosonde data. The in-situ data from these stations were used to validate *TPW* from MERRA-2 for climatological application in Malaysia. The two sets of data agree well in the study area, with a correlation coefficient of range 0.88––0.92 and root mean squared error of between 2.05 and 2.61 mm across the different regions (not shown). Figure 1 is a map of the study area, showing regional locations as well as seasonal fluctuations of *TPW* in each of the sub-regions represented by radiosonde stations, marked as filled circles.

From Figure 1, double oscillations are seen throughout the stations, with the first and second depressions in February and August. This period is characterized by the lowest amount of rainfall in West Malaysia (Wong, Venneker, Uhlenbrook, Jamil & Zhou, 2009). Corresponding
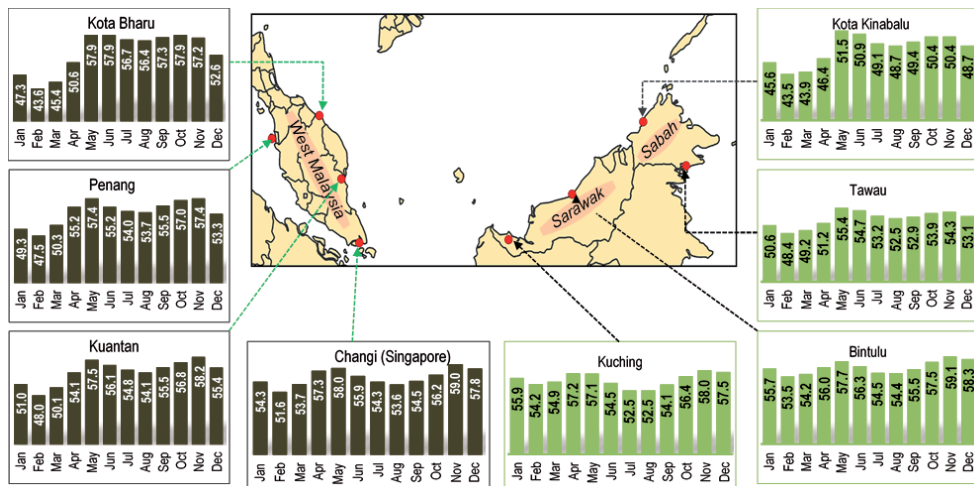

FIGURE 1. Monthly mean total precipitable water vapour (TPW, mm) for representative locations of West Malaysia and East Malaysia (Sabah and Sarawak) from MERRA-2 data from 1990–2019. Inset is the study area showing subregions and the World Meteorological Organization radiosonde stations in filled circles

peaks are obtained in May and November, which also fall within peak periods of precipitation in the region (Wong et al., 2009). Decreasing *TPW* is noticed northward in West Malaysia, with the northernmost station, Kota Bharu, presenting lowest mean moisture compared to the three others. Whereas this station provides the least amount of *TPW* between November and April (NEM season) in West Malaysia, the value is largest between May and October (SWM season). The high amount of *TPW* observed in the northern part during this period, is most probably due to moisture sheltering effect by high mountain ranges on the SWM winds, which arrive West Malaysia from Sumatra (Wong et al., 2009). The widening of the strait of Malacca northwards may also induce the land-sea breeze and convection that may exert local influence on precipitation in the region during the SWM season (Oki & Musiake, 1994). Additionally, higher temperature in the northern parts of West Malaysia during this period could induce evaporation rate and consequently produce more moisture content aloft. For instance, MetMalaysia (2009) projected higher mean temperature increases for West Malaysia against lower values for East Malaysia. Changi, which is in the southmost tip of West Malaysia displays reversed mean *TPW* compared to Kota Bharu with higher and relatively lower values obtained in NEM and SWM respectively. Similarly, synchronous double oscillations were obtained in East Malaysia, though the pairs of dips and peaks are not as conspicuous compared to those observed in West Malaysia. However, unlike the northmost station in West Malaysia, the corresponding sta-

tion (Kota Kinabalu) in East Malaysia maintained a consistently lowest amount of *TPW* all year round, just as the value in the southmost station (Kuching) dominated throughout.

Plots of the annual means of *TPW* for the three federated regions (Peninsular Malaysia, Sabah, Sarawak) from 1990 to 2019 are depicted in Figure 2a. Sarawak maintains a consistently higher *TPW* compared to West Malaysia and Sabah. Consistent temporal variation in annual mean *TPW* was, however, recorded for all the regions. This is consistent with the projected temperature and precipitation trends for the study area (MetMalaysia, 2009). Some obvious spikes noticed in the temporal regime of the annual mean *TPW* may be linked to ENSO (El Niño[1] and La Niña[2]), a common event in the study area and surroundings. This impact is further observed in the monthly anomaly of annual time series in the subsequent section.

To reveal seasonal variability of *TPW*, standard deviations are calculated and depicted in Figure 2b, from which larger deviations were predominantly found during the NEM period in all the stations except for Kuching in East Malaysia. Kota Bharu and Kota Kinabalu presented respective highest deviations in West and East Malaysia, with corresponding least deviations in Changi and Kuching. The regional deviation during

---

[1]El Niño is a large-scale ocean-atmosphere climate interaction associated with the episodic warming in sea surface temperatures across the central and east-central Equatorial Pacific, which often results in warm and dry conditions.
[2]La Niña episodes represent periods of below--average sea surface temperatures across the east--central Equatorial Pacific.
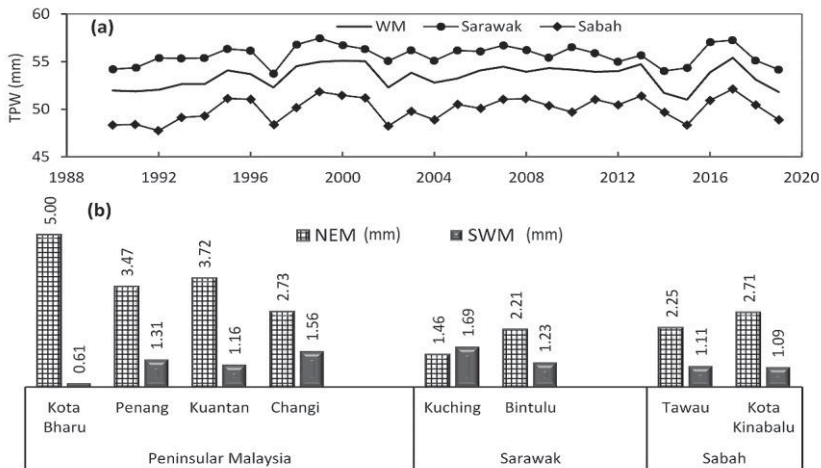
FIGURE 2. Total precipitable water vapour (*TPW*) from MERRA-2 for the period 1990–2019 for the three sub-regions: a – temporal fluctuation of annual means (WM – West Malaysia); b – standard deviations of seasonal means (NEM – northeast monsoon, SWM – southwest monsoon)

the NEM season is latitude-dependent, with the value falling from 5.00 mm at Kota Bharu to 2.73 mm at Changi in West Malaysia and from 2.71 mm at Kota Kinabalu to 1.46 mm at Kuching in East Malaysia. Similarly, during the SWM the deviation also trails a latitudinal pattern but with higher increases at lower latitudes. The largest deviations during this period were found in Changi (1.56 mm) and Kuching (1.69 mm), with Kota Bharu presenting the least value (0.61 mm) across all regions. The relatively small deviations (0.61–5.00 mm) obtained are to be expected since mean *TPW* ranges between 44 and 58 mm in both seasons across Malaysia. The mean seasonal deviations in the NEM (3.07 mm) and SWM (1.22 mm) across the study area are consistent with reported values of < 5 mm for global equatorial regions (Chen & Liu, 2016).

Spatial patterns of TPW

The mean seasonal distribution of *TPW* and its inter-annual variability for NEM and SWM is depicted in Figure 3a and b. From the left column of the figure, which presents maps of the means, it is observed that *TPW* decreases generally in a southeast-northwest orientation over Peninsular Malaysia, with regional maximum appearing over the southeastern tip of the area in both seasonal distribution of the means. The distribution over East Malaysia is, however, in a southwest-northeast orientation with regional maximum found in the southwestern area. The spread of *TPW* over Malaysia is dominated by latitude, topographical features, and the monsoons. The isopleths of *TPW* closely match the orographic features of Malaysia and reflect the influence of the monsoons. The atmospheric column is much shorter over

the central area of West Malaysia, the eastern part of Sarawak, and northwestern Sabah due to their high elevation, which explains the observed regional *TPW* minima. Although the elevation is lower in the northwestern part of West Malaysia, *TPW* values are relatively low due to the weakened influence of the SWM from the natural barrier formed by the mountains to the south. Complex and steep orography tends to shape intense horizontal gradient along the edges of West Malaysia and along the central and northeastern parts of East Malaysia. The rich horizontal gradients that manifest along the central regions of Sarawak and the entire Sabah are relatively uniform in the two seasons. Weak gradients are easily noticed over the southern and central parts of Peninsular Malaysia and west of Sarawak. More water vapour is accounted for during the SWM than in the NEM throughout Malaysia, which is consistent with the seasonal cycle shown in Figure 1. From the right column of Figure 3 (inter-annual variability of *TPW* in the two season) it is noted that larger variations found during the NEM season have higher values northwards. The variation in the SWM period has much lower amplitude which decreases with latitude. The spatial distributions of the mean and standard deviations of *TPW* are consistent with its temporal pattern discussed earlier in this work.

Long-term variability of TPW

For a better understanding of climate dynamics, it is important to investigate long-term trend in precipitable water vapour over a region (Durre, Williams, Yin & Vose, 2009). Linear trends between 1990 and 2019 in monthly anomalies from MERRA-2 *TPW* have, therefore, been performed for each region using LSR method. The statistical significance
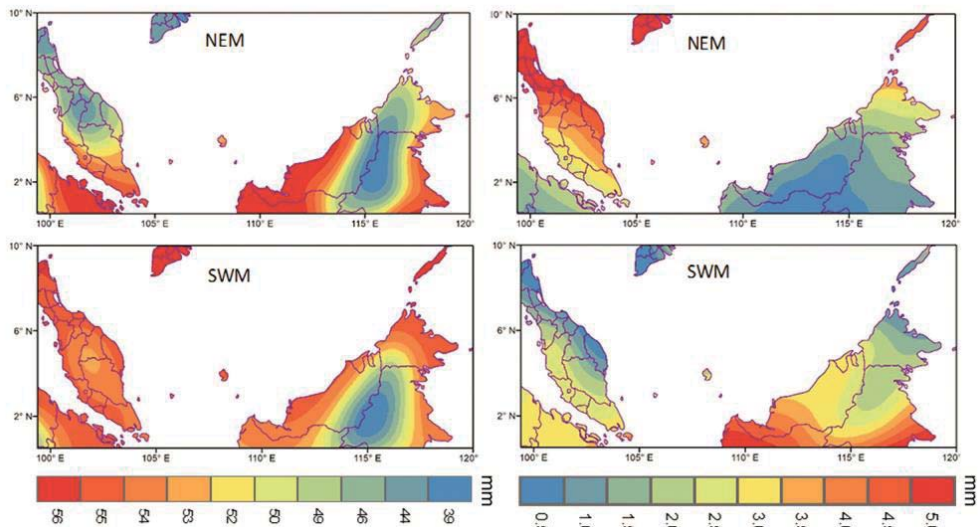

FIGURE 3. Mean total precipitable water vapour (*TPW*) from MERRA-2 in season 1990–2019: a – for northeast monsoon (NEM); b – for southwest monsoon (SWM); c – standard deviation of NEM; d – standard deviation of SWM

of the trends, the slope, and the probability (*p*-value) along with the trend direction for the annual time scales are presented in the table. Trends of *TPW* estimated from MERRA-2 over the regions are positive but very low, though the values are statistically significant at the 95% level, except for Sarawak. The *Z*-scores are consistent with the *p*-values within the study period. Statistically significant upward trends of the rate 0.09 ±0.06 mm·decade^{-1} and 0.10 ±0.04 mm·decade^{-1} were obtained in West Malaysia and Sabah respectively. However, Sarawak turned in nonsignificant positive trend rate of 0.05 ±0.01 mm·decade^{-1}. The results are consistent with the very low upward trend obtained for the tropics (Chen & Liu, 2016; Parracho, Bock & Bastin, 2018). Moreover, this positive trend is consistent with reported temperature increases in Malaysia (MetMalaysia, 2009).

2016. Records from the Oceanic Niño Index (ONI) indicate the occurrence of very strong El Niño events within 1997/1998 and 2015/2016, with corresponding moderate/strong La Niña from 1998–2000 and also 2017 (https://origin. cpc.ncep.noaa.gov). These events, which are partly responsible for the drying and moistening of water vapour contents in the atmosphere around the South Pacific, are most likely to affect the trend in *TPW*. The high anomalies observed in 1998–2000 and 2017 are most likely due to La Niña, while the troughs from 1997 to 1998 and from 2015 to 2016 may be attributed to El Niño. Although most of these events may result in drier or wetter years, substantial frequency of relatively dry or wet periods in Malaysia are, however, not accounted for by them. This indicates that ENSO may not be solely responsible in regulating moisture amount in the study area.

TABLE. Decadal trend estimates in MERRA-2 total precipitable water vapour (*TPW*) over the three federated regions of Peninsular Malaysia for the annual time scale (*b*) from 1990–2019. *Z*-scores, *p*-values and trend directions are also given

Region	Z	b [mm·decade^{-1}]	p ($\alpha_{0.05}$)	Trend (at 95% significant level)
West Malaysia	2.17	0.09 ±0.06	0.014	positive
Sarawak	1.48*	0.05 ±0.01	0.086	positive
Sabah	2.61	0.10 ±0.03	0.009	positive

*Non-significant trend.

The domain means of monthly anomalies in annual time series from MERRA-2 *TPW* for the box area over each of the three federated regions in Malaysia is given in Figure 4. The figure depicts some curious sharp rises and falls in the annual anomaly of *TPW* particularly, from 1995 to 2000 and 2015 to

Conclusions

The implication of total precipitable water vapour (*TPW*) variability and trend on the Earth's radiation budget and precipitation calls for its regular and regional monitoring. This study evaluates the inter-annual and seasonal patterns
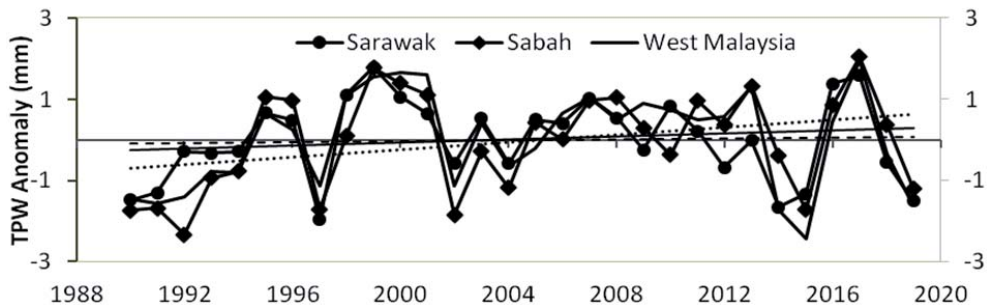
FIGURE 4. Domain mean of monthly anomalies in annual time series from MERRA-2 total precipitable water vapour (*TPW*) for the box areas of Sarawak, Sabah, and West Malaysia from 1990–2019

of *TPW* over Malaysia based on a 30-year data from the Second Modern-Era Retrospective analysis for Research and Applications (MERRA-2). Bimodal oscillations of *TPW* were discernible at the seasonal time scale, with a pair of maxima found in May and November, coinciding with the respective starts of the NEM and SWM seasons in Malaysia. Corresponding pair of minima, which occurred in February and August, are more conspicuous in West Malaysia. The spatial patterns of the annual mean *TPW* were also characterized by a pair of high and low with marked geographical differences as complex and steep orography shaped intense horizontal gradient along the edges of West Malaysia, western part of Sarawak, and southeastern area of Sabah. More moisture was found during the SWM period in all the regions, with higher values in the western part of the Country. Kota Kinabalu and Tawau, in the northeastern part of East Malaysia were the driest all year round. Generally, *TPW* was observed to decrease northward with slight upward significant trends of approx. 0.09 mm·decade^{-1} at the 95% level, found in West Malaysia for the annual time scale, which is consistent with reported global tropical

positive trend (Chen & Liu, 2016). Trend of *TPW* within the study period is most likely affected by ENSO, which is a common events in Malaysia and surrounding areas. It is, therefore, suggestive to isolate periods of severe ESNO events in order to decern actual decadal variability in *TPW* over the study area.

Acknowledgement

References

Ccoica-López, K., Pasapera-Gonzales, J. & Jimenez, J. (2019). Spatio-temporal variability of the precipitable water vapor over Peru through MODIS and ERA-Interim time

series. *Atmosphere*, *10*(4), 192. https://doi.org/10.3390/atmos10040192

Chen, B. & Liu, Z. (2016). Global water vapor variability and trend from the latest 36 year (1979 to 2014) data of ECMWF and NCEP reanalyses, radiosonde, GPS, and microwave satellite. *Journal of Geophysical Research: Atmospheres*, *121*(19), 11442-11462. https://doi.org/10.1002/2016JD024917

Durre, I., Vose, R.S. & Wuertz, D.B. (2008). Robust Automated Quality Assurance of Radiosonde Temperatures. *Journal of Applied Meteorology and Climatology*, *47*(8), 2081-2095. https://doi.org/10.1175/2008JAMC1809.1

Durre, I., Williams, C.N., Yin, X. & Vose, R.S. (2009). Radiosonde-based trends in precipitable water over the Northern Hemisphere: An update. *Journal of Geophysical Research Atmospheres*, *114*(5), 1-8. https://doi.org/10.1029/2008JD010989

Makama, E.K., Lim, H.S & Abdullah, K. (2018). Parameterization of the middle and upper tropospheric water vapor from ATOVS observations over a tropical climate region. *Journal of Atmospheric and Solar-Terrestrial Physics*, *167*, 190-199. https://doi.org/10.1016/j.jastp.2017.12.005

Malaysian Meteorological Department [MetMalaysia] (2009). *Climate change scenarios for Malaysia 2001–2099*. Petaling Jaya: Malaysian Meteorological Department.

Numata, S., Yasuda, M., Suzuki, R.O., Hosaka, T., Noor, N.S.M., Fletcher, C.D. & Hashim, M. (2013). Geographical pattern and environmental correlates of regional-scale general flowering in peninsular Malaysia. *PLOS ONE*, *8*(11), e79095. https://doi.org/10.1371/journal.pone.0079095

Oki, T. & Musiake, K. (1994). Seasonal Change of the Diurnal Cycle of Precipitation over Japan and Malaysia. *Journal of Applied Meteorology*, *33*(12), 1445-1463. https://doi.org/10.1175/1520-0450(1994)033<1445:SCOTDC>2.0.CO;2

Parracho, A.C., Bock, O. & Bastin, S. (2018). Global IWV trends and variability in atmospheric reanalyses and GPS observations. *Atmospheric Chemistry and Physics*, *18*(22), 16213-16237. https://doi.org/10.5194/acp-18-16213-2018

Peng, G., Li, J., Chen, Y., Norizan, A.P. & Tay, L. (2006). High-resolution surface relative humidity computation using MODIS image in Peninsular Malaysia. *Chinese Geographical Science*, *16*(3), 260-264. https://doi.org/10.1007/s11769-006-0260-6

Randel, D.L., Harr, T.H.V., Ringerud, M.A., Stephens, G.L., Greenwald, T.J. & Combs, C.L. (1996). A new Global Water Vapor dataset. *Bulletin of the American Meteorological Society*, *77*(6), 1233-1246.

Salihin, S., Musa, T.A. & Radzi, Z.M. (2013). Spatio-temporal estimation of integrated water vapour over the Malaysian peninsula during monsoon season. *International Archives of the Photogrammetry, Remote Sensing and Spatial Information Sciences – ISPRS Archives*, *42*(4W5), 165-175. https://doi.org/10.5194/isprs-archives-XLII-4-W5-165-2017

Suparta, W. & Alhasa, K.M. (2016). Modeling of Precipitable Water Vapor Using an Adaptive Neuro-Fuzzy Inference System in the Absence of the GPS Network. *American Meteorological Society*, *55*, 2283-2300. https://doi.org/10.1175/JAMC-D-15-0161.1

Suparta, W., Rahman, R. & Singh, M.S.J. (2014). Monitoring the variability of precipitable water vapor over the Klang Valley, Malaysia during flash flood. *IOP Conference Series: Earth and Environmental Science*, *20*(1), 012057. https://doi.org/10.1088/1755-1315/20/1/012057

Tuller, S.E. (1977). The relationship between precipitable water vapor and surface humidity in New Zealand. *Archiv Für Meteorologie, Geophysik Und Bioklimatologie. Serie A*, *26*(2-3), 197-212. https://doi.org/10.1007/BF02247163

Wong, C.L., Venneker, R., Uhlenbrook, S., Jamil, A.B.M. & Zhou, Y. (2009). Variability of rainfall in Peninsular Malaysia. *Hydrology and Earth System Sciences Discussions*, *6*(4), 5471–5503. https://doi.org/10.5194/hessd-6-5471-2009

Zhai, P. & Eskridge, R.E. (1997). Atmospheric Water Vapor over China. *Journal of Climate*, *10*(10), 2643-2652. https://doi.org/10.1175/1520-0442(1997)010<2643:AWVOC>2.0.CO;2

Summary

Inter-annual and seasonal patterns of precipitable water vapour over Malaysia from 1990–2019 based on MERRA-2 reanalysis. In this study seasonal and inter-annual patterns as well as trend in the total precipitable water vapour (*TPW*) over Malaysia, based on a 30-year data from MERRA-2, have been evaluated using least square regression method. Indicator *TPW* revealed a pair of minima in February/August and maxima in May/November with highest and lowest long-term means found in East Malaysia. Long-term seasonal variability of *TPW* exhibited latitudinal dependency in both the NEM and SWM seasons. Indicator *TPW* showed respective southeast-northwest and southwest-northeast spatial distribution in West and East Malaysia, with the highest statistically significant positive trend found in the former.

Authors' address:
Ezekiel Kaura Makama
(https://orcid.org/0000-0001-7074-0037)
University of Jos
Department of Physics
PMB 2084, Jos
Nigeria
Universiti Sains Malaysia
School of Physics
11800 USM, Pulau Pinang
Malaysia
e-mail: makamae@unijos.edu.ng

Hwee San Lim – corresponding author
(https://orcid.org/0000-0002-4835-8015)
Universiti Sains Malaysia
School of Physics
11800 USM, Pulau Pinang
Malaysia
e-mail: hslim@usm.my; makama@usm.my

Instruction for Authors

The journal publishes in English languages, peer-reviewed original research, critical reviews and short communications, which have not been and will not be published elsewhere in substantially the same form. Author of an article is required to transfer the copyright to the journal publisher, however authors retain significant rights to use and share their own published papers. The published papers are available under the terms of the principles of Open Access Creative Commons CC BY-NC license. The submitting author must agree to pay the publication charge (see Charges).

The author of submitted materials (e.g. text, figures, tables etc.) is obligated to restricts the publishing rights. All contributors who do not meet the criteria for authorship should be listed in an Acknowledgements section of the manuscript. Authors should, therefore, add a statement on the type of assistance, if any, received from the sponsor or the sponsor's representative and include the names of any person who provided technical help, writing assistance, editorial support or any type of participation in writing the manuscript.

Uniform requirements for manuscripts

Manuscript should be sent with tables, graphs and abstract on separate pages by e-mail: iks_pn@sggw.edu.pl. All figures and tables should be placed near their reference in the main text and additionally sent in a form of data files (e.g. Excel, Visio, Adobe Illustrator, Adobe Photoshop, CorelDRAW). Figures are printed in black and white on paper version of the journal (color printing is combined with an additional fee calculated on a case-by-case basis), while on the website are published in color.

The size of the manuscript should be limited up to 10 pages including overview, summary, references and figures (the manuscript more than 13 pages is unacceptable); Please set the text format in single column with paragraphs (A4 paper format), all margins to 25 mm, use the font Times New Roman, typeface 12 points and line spacing one and half.

The submitted manuscript should include the following parts:

- name and SURNAME of the author(s) – up to 5 authors
- affiliation of the author(s), ORCID Id (optional)
- title of the work
- key words
- abstract (about 500 characters)
- text of the paper divided into: Introduction, Material and Methods, Results and Discussion, Conclusions, References and Summary
- references in APA style are listed fully in alphabetical order according to the last name of the first author and not numbered; please find the details below
- post and mailing address of the corresponding author:

  Author's address:
  Name, SURNAME
  Affiliation
  Street, number, postal code, City
  Country
  e-mail: adress@domain

- Plagiarism statement (http://iks.pn.sggw.pl/Szablony/PublEth.pdf)

Reference formatting

In the Scientific Review Engineering and Environmental Sciences the APA 6th edition style is used.

Detailed information

More information can be found: http://iks.pn.sggw.pl